博士論文

Precision Spectroscopy of Muonium Ground-State Hyperfine Structure at Very Weak Magnetic Field

(極小磁場におけるミューオニウム超微細構造の精密分光)

University of Tokyo

Yasuhiro Ueno
上野　恭裕

December 7, 2018

"It's always night, or we wouldn't need light."

Thelonius Sphere Monk[1]

[1] In the epigraph of "Against the Day" by Thomas Pynchon. See also http://chumpsofchoice.blogspot.com/2006/12/that-thelonious-monk-epigraph.html and http://aphelis.net/portrait-thelonious-monk-boris-chaliapin-1964/

Precision Spectroscopy of Muonium Ground-State Hyperfine Structure at Very Weak Magnetic Field

Yasuhiro Ueno

Abstract

Muonium is the bound state of a positively-charged muon and an electron, a hydrogen-like atom. Unlike hydrogen atom, muonium is free from the internal structure of the proton, and one can calculate its energy levels precisely. Hence muonium is one of the best probes to test the bound-state Quantum Electrodynamics (bound-state QED).

In this thesis, we present a new precision measurement of the muonium hyperfine structure interval (MuHFS) at the Japan Proton Accelerator Research Complex (J-PARC), Materials and Life science Facility (MLF). The new experiment is called Muonium Spectroscopy Experiment Using Microwave (MuSEUM). By using the intense pulsed muon beam at J-PARC, MuSEUM ameliorates the statistics. This thesis focuses on recent achievements in the measurement of MuHFS at a very weak magnetic field.

In this measurement, the shift of MuHFS frequency due to the collision with krypton atoms is one of the dominant sources of systematic uncertainty. We developed a new microwave cavity and succeeded in the measurement of MuHFS at lower krypton gas pressure (0.3 and 0.4 atmospheres) than the precursor experiments, without significantly losing statistics. Combined with the previous data at 1.0 atmosphere, we determined the MuHFS frequency in vacuo and the result is

$$\Delta\nu_{\mathrm{fit}} = 4.463\ 3055(23)\ \mathrm{GHz}.$$

The result is consistent with the results of precursor experiments and the theoretical calculation. This result is mainly limited by lack of statistics, and the measurement with unprecedented precision is feasible with improvements of the accelerator which is ongoing at J-PARC.

Contents

List of Figures

List of Tables

Chapter 1

Introduction and Overview

The observation of the Higgs boson in the experiments at the Large Hadron Collider (LHC) [1, 2] completes the hunt for the predicted particles in the Standard Model (SM) of particle physics. The discovery of the Higgs boson is another great triumph for the SM, experimentally verifying the mechanism of the spontaneous breaking of the electroweak symmetry. The SM is, however, known to be incomplete; it does not contain the gravitational interaction, and it fails to explain some observed facts such as the existence of the dark matter and the baryon asymmetry in the Universe. Many experiments searching for a sign of physics beyond the Standard Model are ongoing. A statistically significant sign of new physics, however, is yet unseen.

Quantum Electrodynamics (QED) is one of the most important pillars of the SM and has been tested most precisely. One of such tests is measurements of electron magnetic moment [3], with a precision of 0.28 ppt (parts per trillion, 10^{-12}). The combination of the experimental result and QED calculation extracts the fine structure constant, α with a precision of 4×10^{-10}, and the obtained result agrees reasonably well with the other measurements of α, although a recent measurement of α using the recoil frequency of Cs-133 atoms in matter-wave interferometry [4] found 2.5 σ discrepancy between its result and the result from the electron magnetic moment.

While the QED well describes the electron magnetic moment, muon anomalous magnetic moment (g-2) has taken researchers attention since the measurement at the Brookhaven National Laboratory (BNL) found more than 3σ discrepancy from the SM [5]. Despite the intensive effort made both from the experimental side and theoretical side since then, this discrepancy remains to be an unsolved problem. If this discrepancy is confirmed with further statistical confidence through new experiments, the result will be the key to understand the new physics. As described in the following section, this muon g-2 is of particular relevance with muonium hyperfine structure spectroscopy.

Speaking about bound states, hydrogen spectroscopy had been one of the essential aspects in the advent of modern physics, such as the confirmation of the Bohr

model [6], Dirac equation [7], and the observation of the Lamb shift as the first example of the pure-QED effect [8, 9]. Several experimental results with high precision had been published both in optical and microwave regime [10, 11, 12]. Although the test of the bound-state QED is limited by the internal structure of the proton, the extracted values of the proton charge radius and the Rydberg constant had agreed with each other, until the laser spectroscopic results of muonic hydrogen ($p + \mu^-$) emerged: the result indicates the proton charge radius is deviated from the average value of the electronic hydrogen results by 7σ [13, 14]. Many theorists have reexamined the QED calculations for both systems, and two improved spectroscopies of hydrogen [15, 16] have been published, but the definitive interpretation of the discrepancy has not been found and this "proton-radius problem" remains.

Unlike hydrogen atom, muonium is free from the internal structure of the proton, and it is one of the best probes to test the bound-state QED. In this chapter, we introduce a new precision measurement of the muonium hyperfine structure interval at the Japan Proton Accelerator Research Complex (J-PARC), Materials and Life science Facility (MLF). The new experiment is called Muonium Spectroscopy Experiment Using Microwave (MuSEUM). We also explain the historical background and the physical motivation for the new experiment.

1.1 Muonium Hyperfine Structure

Muonium (Fig. 1.1) is the bound state of a positive muon and an electron. In the Standard Model (SM) of particle physics, muon and electron are treated as structureless particles. Unlike ordinary atoms such as hydrogen, muonium is free from the finite size effect of nucleons, and its energy levels can be calculated very precisely. By comparing the experimental result of the muonium ground-state hyperfine structure (MuHFS) spectroscopy and the theoretical calculation, one can test the bound-state QED with high precision.

MuHFS is the energy according to the muonium spin state caused by the spin-spin interaction between the muon and the electron. We denote the frequency corresponding to MuHFS by $\Delta\nu$. The theoretical value of MuHFS has been calculated as [17]

$$\Delta\nu_{\mathrm{th}} = 4.463\ 302\ 868(271)\ \mathrm{GHz} \tag{1.1}$$

with a relative uncertainty of 61 ppb (parts per billion, 10^{-9})[1]. The uncertainty above mainly comes from the uncertainty of the input parameter m_μ/m_e for QED calculation.

[1]Recently, we noticed there is a paper claiming the uncertainty above is mistakenly estimated smaller [18]. They claim the correct uncertainty should be 523 Hz (120 ppb). Here, we use the value from [17] throughout this thesis, however, it does not affect the discussion below.

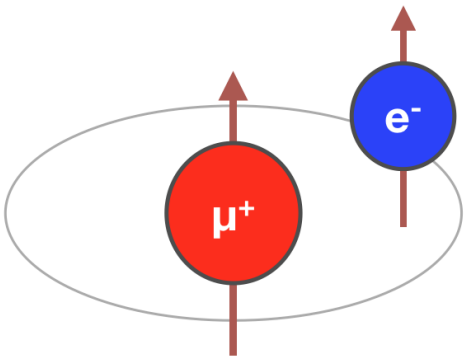

Figure 1.1: Muonium is the bound state of a positive muon and an electron.

There are two major ways of the MuHFS measurement, at a very low field and in a high field, as shown in Fig. 1.2. The most precise measurement in high field in 1999 [19] is

$$\Delta\nu_{\mathrm{HF}} = 4.463\ 302\ 776(51)\ \mathrm{GHz}\ (12\ \mathrm{ppb}). \tag{1.2}$$

For the very low field measurement, the result by a precursor measurement conducted in 1975 [20] is

$$\Delta\nu_{\mathrm{LF}} = 4.463\ 3022(14)\ \mathrm{GHz}\ (300\ \mathrm{ppb}). \tag{1.3}$$

The primal source of the uncertainties of both measurements comes from the statistics. Both measurements used the muon beam at the Los Alamos Meson Physics Facility (LAMPF). Note in passing that the two measurement methods have different sources of systematic uncertainties, thus combining these two measurements may claim a more reliable result. In this thesis, we focus on the measurement at a low field, as explained in the following sections.

1.2 Physical Motivations

There are several motivations for the new muonium hyperfine structure measurement. First, the MuHFS is one of the few ideal probes to test the bound-state QED, because muonium is free from the finite size of a nucleon. Second, through the spectroscopy of MuHFS, one can determine the muon magnetic moment, which is an important input parameter for muon g-2 experiments using a muon storage ring. The muon g-2 is known for a 3.5σ discrepancy between the theoretical calculation based on the SM and the experiment [5, 21]. Furthermore, since muonium is a clean system, the comparison between the theory and experimental result contributes to other searches for the beyond standard model physics.

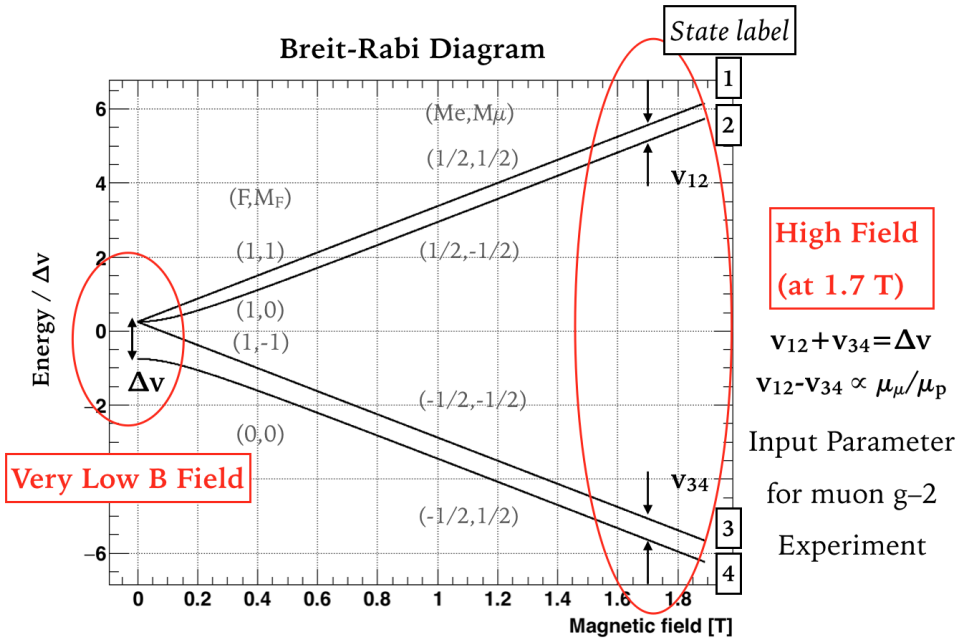

Figure 1.2: Breit-Rabi diagram of the ground-state muonium hyperfine structure. Muonium energy levels are labeled as 1, 2, 3, 4 in descending order from the highest energy to the lowest energy. This labeling is valid throughout this thesis. There are two measurement methods, high-field, and low-field, and we focus on the low-field measurement in this thesis.

1.2.1 Test of the Bound-State QED

The first motivation of the MuSEUM is a test of the bound-state QED. QED is one of the fundamental theories of the Standard Model, and testing its validity is one of the most important parts of the development of modern physics. Some systems can be used to test the bound-state QED as shown in Fig. 1.3. Here, we summarize the status of the experimental and theoretical values of HFS for these systems.

Such pursuit of the precision test of bound-state QED began with spectroscopy of the hydrogen atom, but despite the remarkable experimental precision of the hydrogen hyperfine structure, the precision of the theoretical calculation is limited by uncertainty which comes from the internal structure of the proton. The current experimental value of the hydrogen hyperfine structure with a notable precision of 2 ppt (parts per trillion, 10^{-12}) [10, 22] is

$$\Delta\nu_{\mathrm{H_{exp}}} = 1.420\ 405\ 751\ 7767(3)\ \mathrm{GHz} \tag{1.4}$$

and its theoretical calculation [23] is

$$\Delta\nu_{\mathrm{H_{th}}} = 1.420\ 405\ 11\ (97)(140)\ \mathrm{GHz} \tag{1.5}$$

where the first uncertainty comes from the internal structure of the proton and the second uncertainty is the combined uncertainty from all the other contributions.

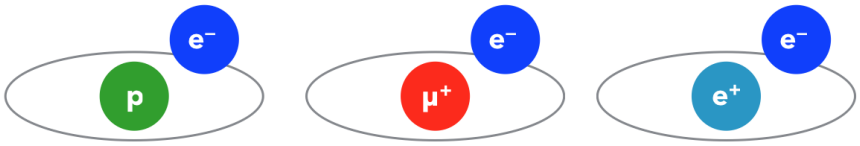

System	Precision	Comments
Hydrogen	The most precise experiment (2.1 ppt) Limited theoretical precision (1.2 ppm)	Theory is limited from proton structure
Muonium	**Precise experiment (12 ppb)** **Precise theory (61 ppb)**	Theory is limited by the uncertainty of an input parameter, m_μ
Positronium	The most recent experiment (10 ppm) Limited theoretical precision (1.2 ppm)	Theory is limited from recoil effect Experiment is limited from short lifetime

Figure 1.3: Current experimental and theoretical status of the hydrogen-like atoms in the view of bound-state QED test

The uncertainty of the theoretical calculation is 1 ppm (parts per million, 10^{-6}), which is a factor of 10^6 larger than the precision of the experimental value.

As mentioned above, muonium is the ideal system for testing the bound-state QED since it is made of only leptonic point-like particles. The theoretical calculation of the muonium hyperfine structure is

$$\Delta\nu_{\mathrm{th}} = 4.463\ 302\ 868(271)\ \mathrm{GHz} \tag{1.6}$$

and it is limited by the uncertainty of the input parameter, m_μ/m_e. Future experiments, for instance, muonium 1S-2S spectroscopy proposed at Paul Scherrer Institute [24] can improve the experimental precision of m_μ and also improve the theoretical calculation of the MuHFS.

Another purely-leptonic system for testing the bound-state QED is positronium, which is the bound state of a positron and an electron. The theoretical calculation [25] is

$$\Delta\nu_{\mathrm{Ps_{th}}} = 203.391\ 90\ (25)\ \mathrm{GHz} \tag{1.7}$$

with a relative uncertainty of 1 ppm, a factor of 15 larger than that of muonium.The theoretical precision is mainly limited by the recoil correction due to the equal mass of positron and electron. The result of the most recent experiment [26] is

$$\Delta\nu_{\mathrm{Ps_{exp}}} = 203.3942\ (16)(13)\ \mathrm{GHz} \tag{1.8}$$

where the first uncertainty is statistical and the second uncertainty is systematic.

The precision of the experimental and theoretical values of the hyperfine structure in the three systems mentioned above is summarized in Fig. 1.3. Muonium is the most suitable system for comparing the theory and the experiment due to the fairly high precision of both experiment and theoretical calculation.

1.2.2 Contribution to Muon g-2

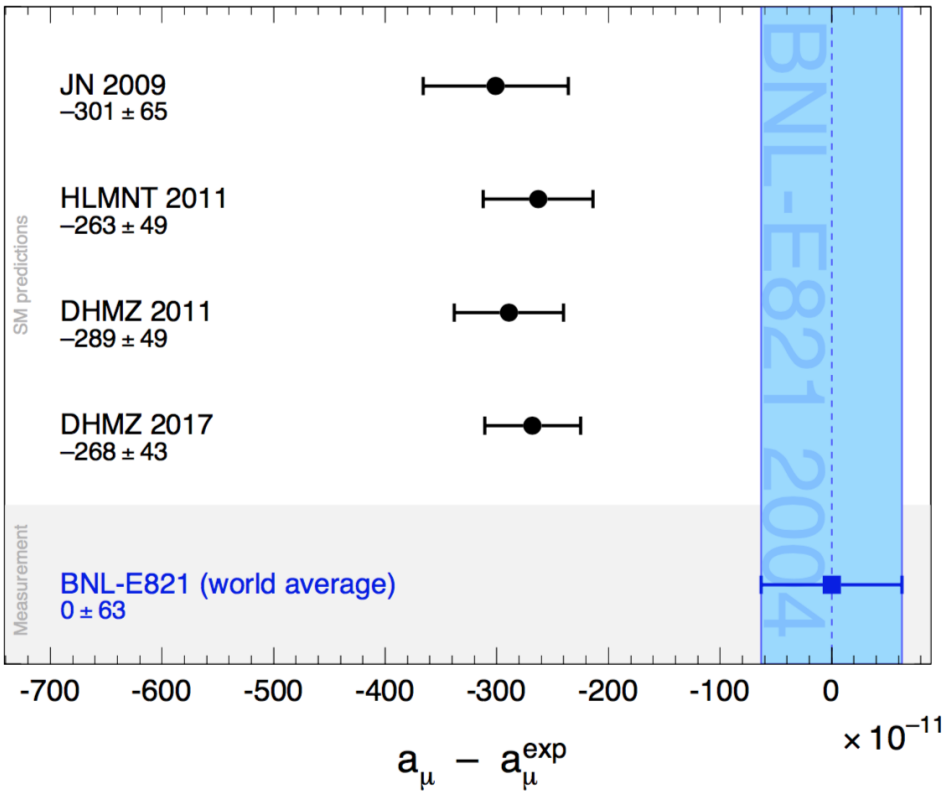

Figure 1.4: Comparison of the experimental and theoretical values for a_μ [21]. The SM predictions are taken from: JN 2009 [27], HLMNT 2011 [28], DHMZ 2011 [29], DHMZ 2017 [30].

Another important feature of the new muonium hyperfine structure measurement is an improved determination of the muon magnetic moment, μ_μ. This is an important input parameter of a muon storage ring experiment for determination of muon anomalous magnetic moment,

$$a_\mu = \frac{g-2}{2}. \tag{1.9}$$

The muon g-2 is known for the discrepancy between the experimental value [5] obtained at BNL and the theoretical value calculated from the SM [21, 27, 28, 29, 30]. The discrepancy corresponds to more than 3σ in terms of the uncertainty (Fig. 1.4), and the discrepancy has increased [31]. If the discrepancy is conclusive, it implies the existence of physics beyond the standard model.

To confirm the discrepancy at a more reliable level, two new experiments were proposed to measure a_μ with improved precision. One experiment has started to take data at Fermi National Accelerator Laboratory (Fermilab) [32] using the same magnet of the previous experiment at BNL. The other experiment at J-PARC employs a novel technique of ultracold muon beam to measure a_μ in a different way,

which can reduce systematic uncertainty [33]. The current precision from the BNL experiment is 540 ppb (parts per billion). The two experiments aim to measure a_μ with a precision of 100 ppb.

The key point of the future storage ring experiments is that they need an external parameter $\lambda = \mu_\mu/\mu_e$ to extract a_μ from the their experimental result, R, according to the relation

$$a_\mu = \frac{R}{\lambda - R}. \tag{1.10}$$

The λ parameter can be determined from the MuHFS measurement, and there are two different ways of determination. The first one is a determination under the assumption that the bound-state QED calculation of MuHFS is correct. By comparing the experimental result of $\Delta\nu$ and the theoretical expression of the $\Delta\nu$ including the muon-electron mass ratio m_μ/m_e, one can determine m_μ/m_e. Once m_μ/m_e is determined, $\lambda = \mu_\mu/\mu_e$ can be determined easily since the mass of the electron (muon) is related to the magnetic moment of the electron (muon) by the g-factor, which is precisely known.

The second way of the determination is to use the Zeeman effect of the muonium under an external magnetic field, and measure two different energy levels of the Zeeman sub-levels, namely ν_{12} and ν_{34}. The applied magnetic field can be precisely measured by Nuclear Magnetic Resonance (NMR) of a proton in pure water. The difference between the two is proportional to the ratio of the muon and proton magnetic moment,

$$\nu_{12} - \nu_{34} \propto \frac{\mu_\mu}{\mu_\mathrm{p}}. \tag{1.11}$$

The analysis of the recent g-2 experiment employed the magnetic moment ratio μ_μ/μ_e from the determination with the assumption of the bound-state QED calculation is correct. The value is cited from the most recent MuHFS experiment at LAMPF [19] in the high field, with a precision of 25 ppb. If one uses the determination without the assumption, the result obtained at the LAMPF experiment is

$$\frac{\mu_\mu}{\mu_\mathrm{p}} = 3.183\ 345\ 13\ (39) \tag{1.12}$$

with a precision of 120 ppb.

As mentioned above, future experiments aiming to measure the a_μ with a precision of 100 ppb are ongoing. In the situation of the existence of such contradicting values from the experiment and the SM theory, it is more secure to extract the a_μ from the new storage ring experiments without the assumption that the bound-state QED calculation is correct. The current precision of 120 ppb by the second way of determination without assumption is not sufficient to fully exploit the results of the two new experiments. The new spectroscopy of MuHFS can contribute to this program, by determining the μ_μ/μ_e with a precision of the order of 10 ppb.

1.2.3 Other Motivations

Test of Lorentz/CPT Invariance

There are several other motivations, except the two explained in previous sections, for the new measurement of the MuHFS. One is the test of Lorentz/CPT invariance using a theoretical framework called the Standard Model Extension (SME) [34, 35]. If there is a Lorentz violation, there is a Lorentz field in a certain direction in a celestial frame of reference. If there is a non-zero angle between the certain direction and the muon spin, the MuHFS frequency would be slightly shifted. Since the laboratory rotates with the Earth, the angle varies with time, as shown in Fig. 1.5. As a consequence, the MuHFS frequency oscillates as the Earth rotates. Therefore one can expect the oscillation of the frequency in one sidereal day (Fig. 1.6). Some parameters in the SME are constrained by the result of the precursor experiment (Fig. 1.7)[36]. The new precision measurement of MuHFS will improve this constraint and also make some new constraints on other unconstrained parameters by searching for the annual oscillation of $\Delta\nu$ due to the Earth's revolution, which the precursor experiment did not measure.

Exotic Particle Search

A new measurement of the MuHFS can contribute to the other exotic particle search. One such example of the search is a light Boson with an ultraweak coupling [37]. Spectroscopy of the hyperfine structures of various atoms can search for such a particle. Figure 1.8 shows the parameter space of the boson and the current constraint on the parameters. The horizontal axis shows the interaction length of a new particle and the vertical axis shows the coupling constant. The dashed lines are the constraint from 1S HFS from various atoms. As shown in the figure, muonium sets the current best limit, meaning a more precise result of MuHFS spectroscopy can constrain the broader range of the parameter space. There are also solid lines which indicate the constraint from the combination of the two different spectroscopic results of the same atom, D_{21}. Here, $D_{21} = 8f(\text{2S HFS}) - f(\text{1S HFS})$ where $f(\text{nS HFS})$ is the frequency of the nth-state HFS. D_{21} is a useful parameter for the comparison of the theoretical and experimental result by cancelling out the contribution from the internal structure of nuclei.

Recently, it is suggested that MuHFS is the best system for probing an exotic long-range force arising from the exchange of a pair of neutrinos [38]. A rough estimate suggests that MuHFS spectroscopy with a precision of 2 Hz (0.4 ppb) can distinguish such a force mediated by a pair of the SM neutrinos. The required precision is beyond the scope of the current status of the experiment, but a future facility with a more intense muon beam may be able to contribute to this program.

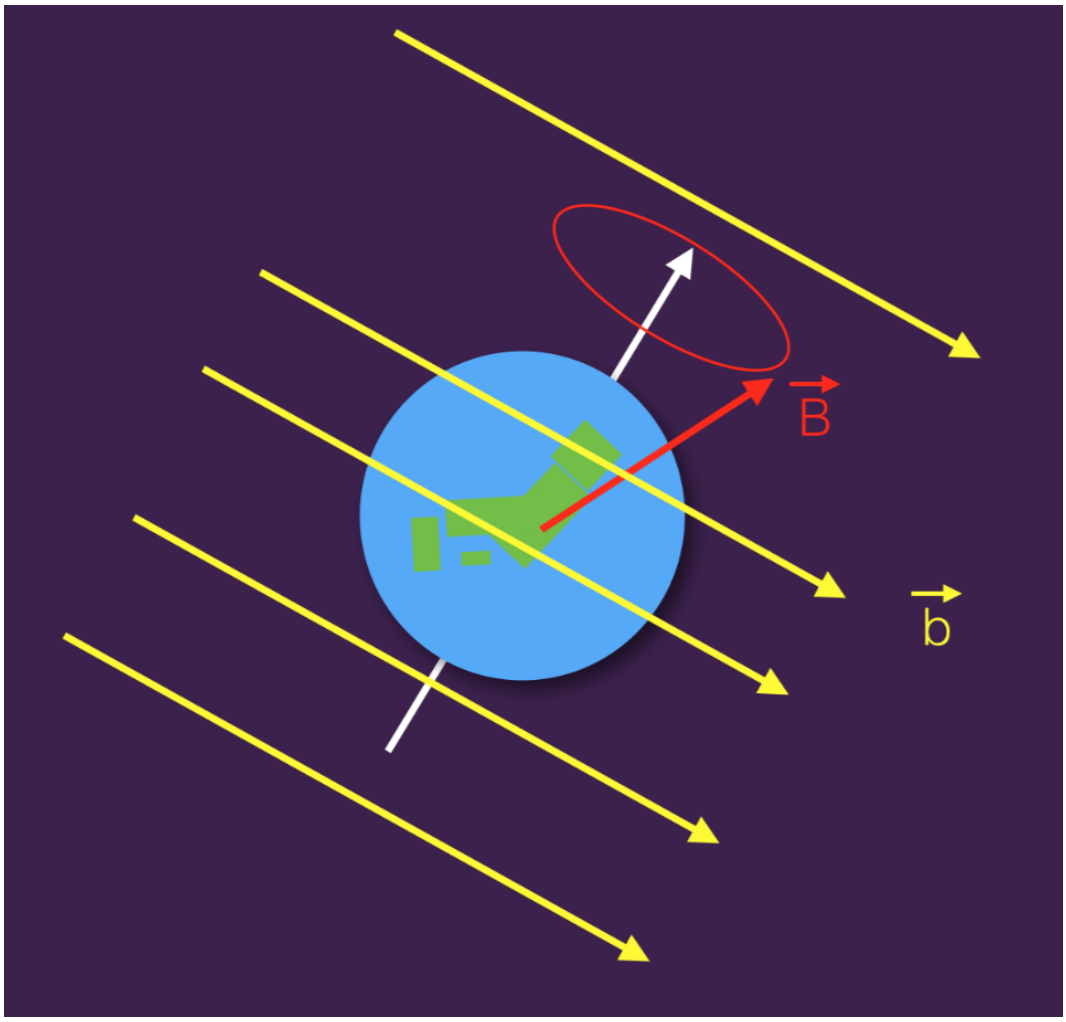

Figure 1.5: Search of CPT/Lorentz violation. The Lorentz violating field is expressed as $\vec{b}$. The angle between $\vec{b}$ and the spin direction $\vec{B}$ varies as the Earth rotates.

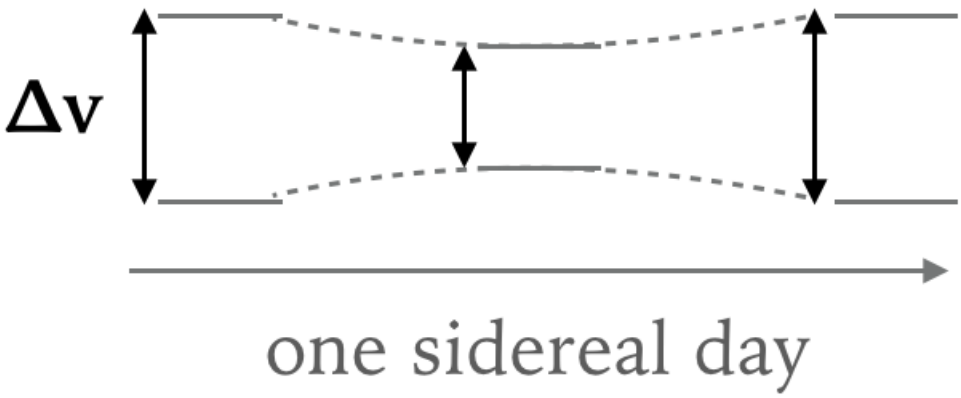

Figure 1.6: Expected sidereal oscillation of the MuHFS frequecny due to the Lorentz violation.

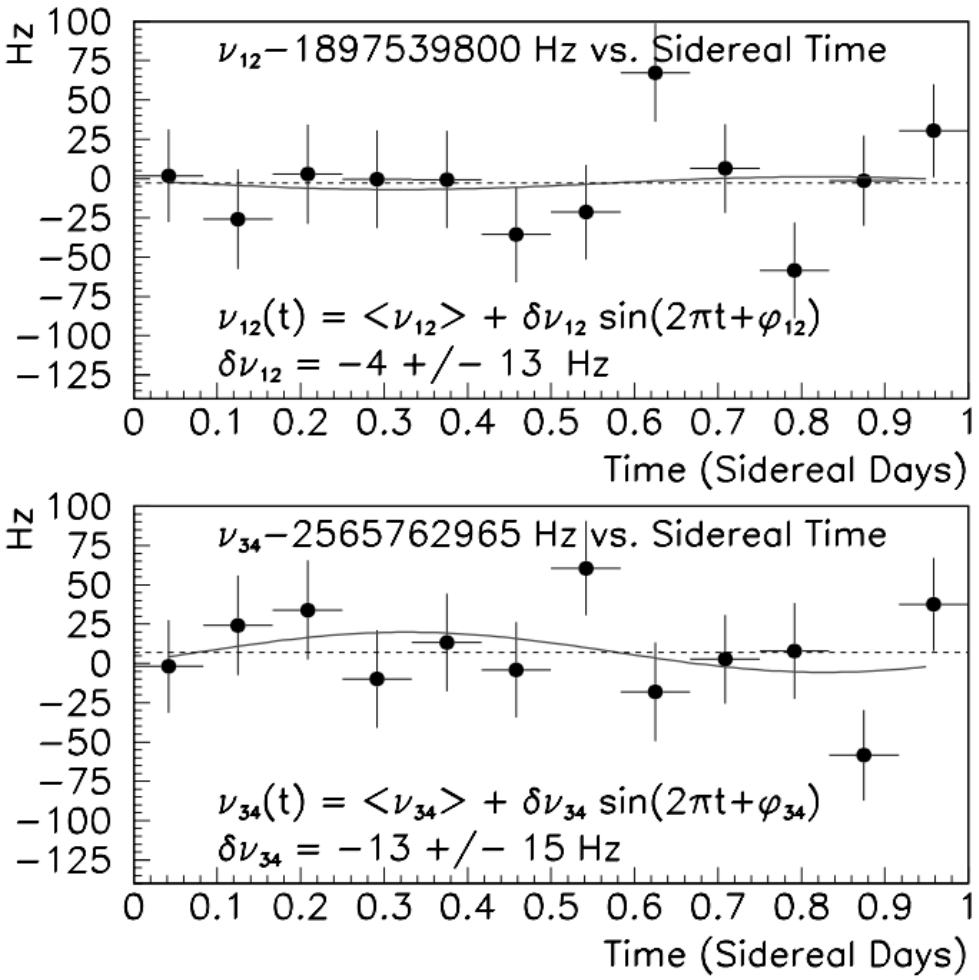

Figure 1.7: Signal obtained by the precursor experiment [36].

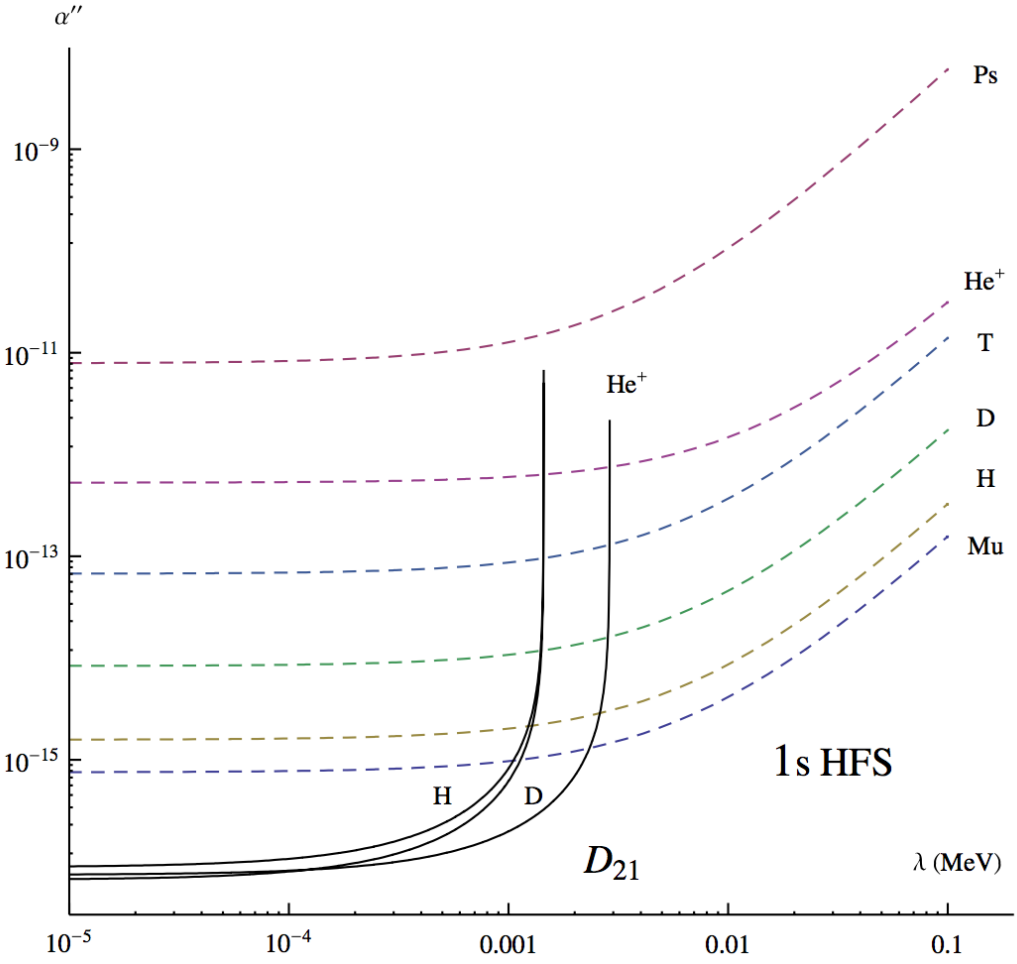

Figure 1.8: The constraint on the parameter space of a light boson with an ultraweak coupling [37]. Horizontal axis is the interaction length and the vertical axis shows the coupling constant. Muonium is the best probe in the case of the new particle mass is more than a few keV. Here, $D_{21} = 8f(\text{2S HFS}) - f(\text{1S HFS})$.

Muonium-antimuonium Conversion

This experiment also can be used for the search for the charged lepton flavor violation, which has never detected before. Potential muonium(μ^+e^-)-antimuonium(μ^-e^+) conversion would shift the MuHFS frequency due to the mixing of the ground states of the muonium and the antimuonium [39]. If there is no external field, the shift amounts to

$$\delta\nu_{\mathrm{Mu\overline{Mu}}}(nS) = \frac{519}{n^3} \times \left(\frac{G_{\mathrm{Mu\overline{Mu}}}}{G_{\mathrm{F}}}\right) \mathrm{Hz} \tag{1.13}$$

where $G_{\mathrm{Mu\overline{Mu}}}$ is the coupling constant for effective four-fermion interaction, and G_{F} is the Fermi coupling constant. Based on the present limit of $G_{\mathrm{Mu\overline{Mu}}}$ [40], the shift is less than 1.5 Hz, which is beyond the scope of the current precision but can be approached by the experiments with more statistics in the future. Note that if there is a strong external field the effect would be reduced [41], so a measurement in the low field is desirable for this purpose.

1.3 Overview of the Precursor Experiments

Since V. W. Hughes and his colleagues confirmed muonium formation and measured its Larmor precession frequency in 1960 [42], research groups at Yale and Chicago have made a series of measurements of the muonium ground-state hyperfine structure interval. The history of the measurements is summarized in Table 1.1. The most recent experiments in the high field and at the low field were conducted at the Los Alamos Meson Physics Facility (LAMPF). The experimental setup of the precursor experiments is shown in Fig. 1.9. The muon is injected into a noble gas such as krypton to produce muonium, and microwave in cavity induces the hyperfine transition. The summary plots of the experimental results by precursor experiments are shown in Fig. 1.10 and 1.11.

The dominant source of the uncertainty in the precursor experiment was the lack of statistics. LAMPF's muon beam intensity was 10^7 muons per second at the time of the experiment published in 1999. In order to use an effective analysis method called "old muonium" method, they chopped the muon beam. The discussion of the method in detail will be presented in the latter section. After the chopping, the beam intensity was 2×10^6 muons per second. The statistics can be improved by the muon beam at J-PARC. The maximum muon available in future is 10^8 muons per second, and the current intensity (5×10^6 muons per second) has already surpassed the LAMPF intensity.

As the statistical uncertainty is suppressed, systematic uncertainty becomes important for realizing more precise spectroscopy. One of the most important sources of systematic uncertainty is the collision between the muonium and Kr atom, which

Table 1.1: MuHFS determined from the precursor experiments. The items in boldface indicate the most recent measurements in high field and at low field.

published year	method	value [GHz]
1964[43]	low field	4.463 18(12)
1966[44]	high field	4.463 150(60)
1969[45]	low field	4.463 260(40)
1969[46]	high field	4.463 317(21)
1970[47]	high field	4.463 3022(89)
1973[48]	low field	4.463 3040(18)
1975[20]	**low field**	**4.463 3022(14)**
1977[49]	high field	4.463 302 35(52)
1982[50]	high field	4.463 302 88(16)
1999[19]	**high field**	**4.463 302 765(53)**

shifts the MuHFS frequency. Precursor experiments measured MuHFS at different Kr pressures, and extrapolated the results to obtain the MuHFS frequency in vacuo. The most recent measurement in the high field was conducted in 0.8 atmospheres (atm) and 1.5 atm (Fig. 1.12). The most recent experiment at low field measured the MuHFS with Kr gas pressures from 1.6 atm to 73 atm (Fig. 1.13). The measurement at low field also used Ar gas.

Measurements at lower gas pressures suppress the uncertainty caused by the gas pressure extrapolation. Such measurements at lower gas pressure have limitations. If gas pressure is lower, fewer muons can stop inside the microwave cavity, and less muonium is available for the spectroscopy, hence reducing the statistics. Lowering muon momentum may enhance the ratio of the muon stopped per injected muon, but in general, fewer muons can be extracted from a beamline when lowering the momentum.

In this research, a microwave cavity with larger volume realizes the measurement at lower gas pressures without the severe loss of the statistics. Adjusting a larger cavity to the MuHFS frequency (4.463 GHz) requires the use of higher resonance mode. In general, using a higher resonance mode in cavity causes more possibility of mode interference (unwanted another mode with a resonance frequency that is near MuHFS). This requires a careful design of the cavity for using a higher mode. Recent progress of computation and simulation of the cavity mode has made the design of the cavity with a higher mode available. This is the most important aspect of this research, and the details will be discussed in Chap. 3.

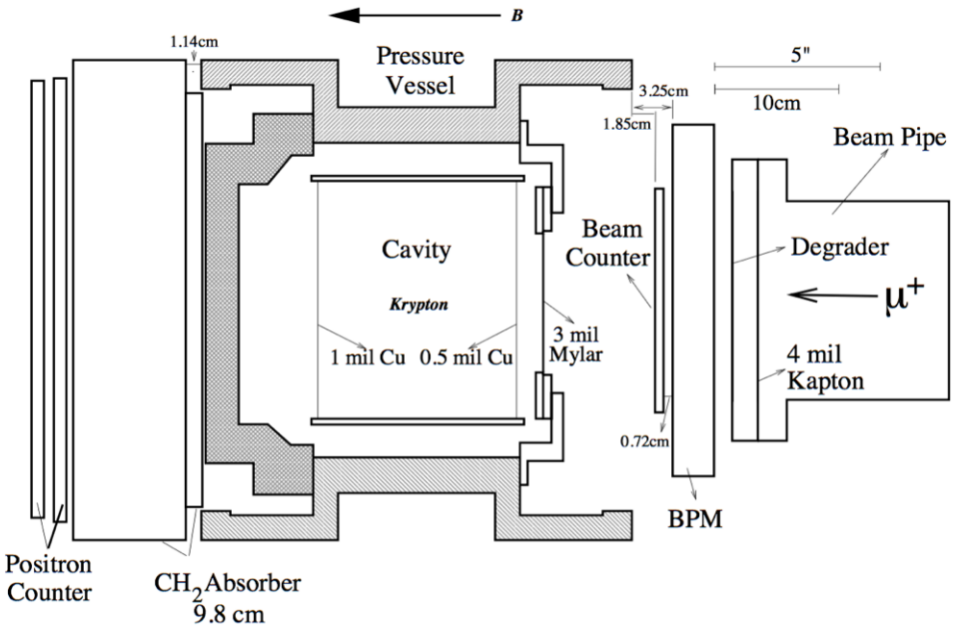

Figure 1.9: Experimental setup of the precursor high field measurement at LAMPF [51].

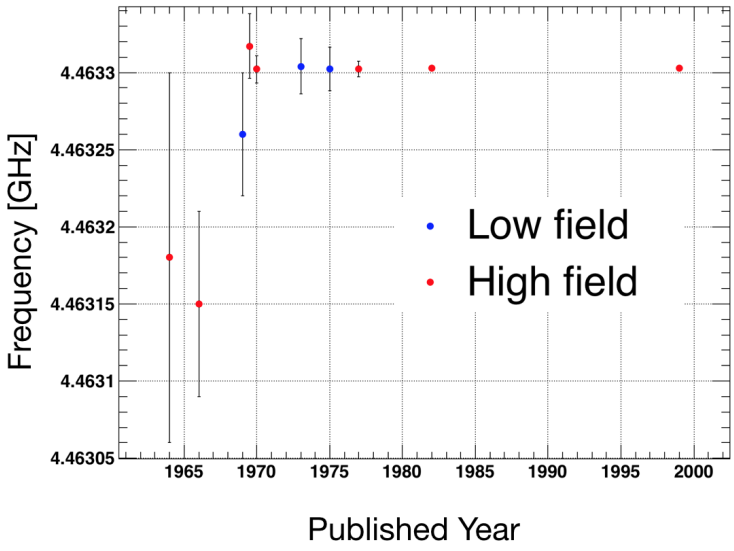

Figure 1.10: Obtained results from previous experiments. The red circles indicate the results from the measurements in the high magnetic field and the blue ones indicate the results from the measurements in the very low field.

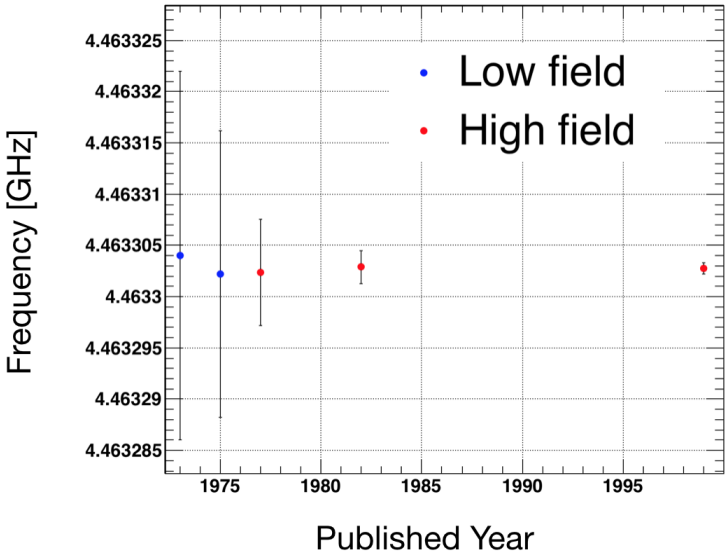

Figure 1.11: Zoomed view of the results from experiments. The red circles indicate the results from the measurements in high magnetic field and the blue ones indicate the results from the measurements in very low field.

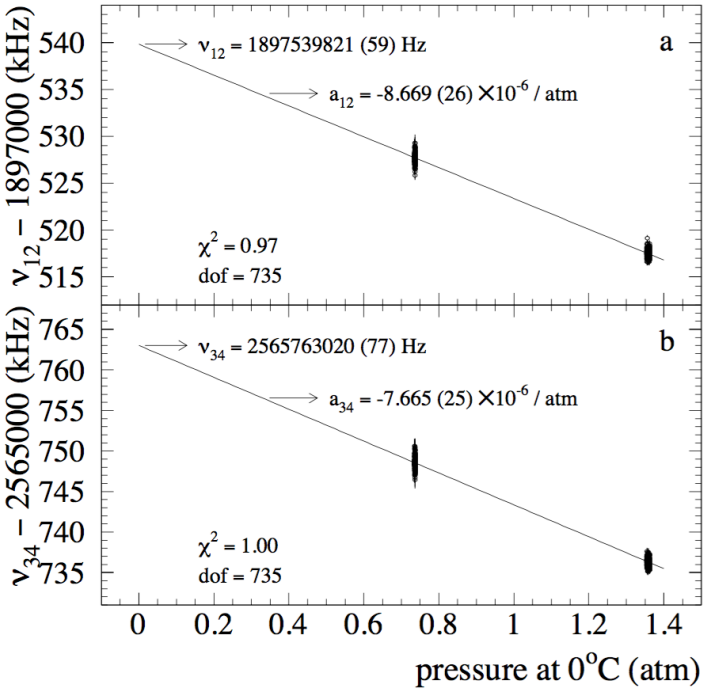

Figure 1.12: Gas pressure extrapolation of the precursor high-field measurement at LAMPF [51]. The experiment was done at 1.5 atm and 0.8 atm at room temperature.

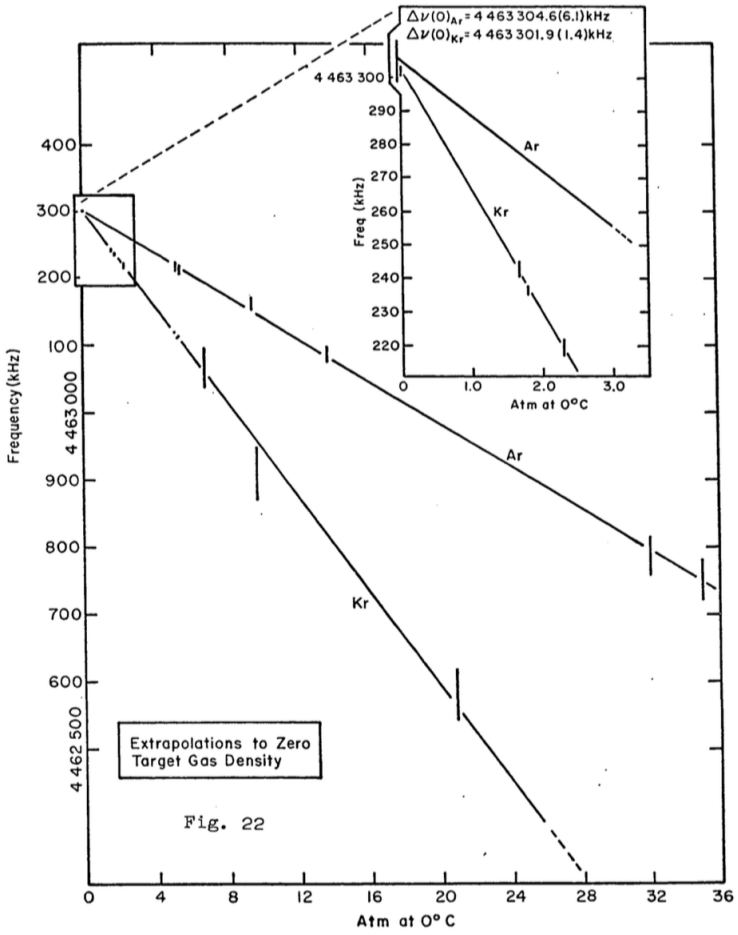

Figure 1.13: Gas pressure extrapolation of the precursor very low field measurement at LAMPF [52]. The experiment has been done with the Kr pressures varied from 1.64 atm to 72.6 atm.

1.4 MuSEUM Experiment

MuSEUM (Muonium Spectroscopy Experiment Using Microwave) is a newly proposed experiment to measure the muonium hyperfine structure with unprecedented precision using intense pulsed muon beams at J-PARC. As mentioned above, there are two different measurement methods, high-field, and low-field. They are complementary measurements since they have different sources of systematic uncertainty. MuSEUM aims a factor of ten improvements for both measurements.

Currently, a new beamline called H-Line is under construction at J-PARC, and ten times more intense muon beam will be available compared to the current beamline, D-Line. The measurement in a high field requires the superconducting magnet, but due to the limitation of the space in the experimental area D2 the installation of the magnet is currently not possible. MuSEUM started the measurement at a low field with existing Beamline D2. In order to conduct the high field measurement, MuSEUM needs an experimental area with more space for installation of the superconducting magnet. H-Line and its experimental area H1 with more space than D2 are under construction, so it will start the measurement in a high field once the H-Line is ready.

1.4.1 Strategy

One of the key components of the MuSEUM experiment is the improvement of the statistics. This improvement is available through the intense pulsed muon beam at J-PARC. The pulse structure of the muon beam is useful for efficient analysis.

Precursor experiments used LAMPF, which has DC (constant) muon beams. The experimental setup of the precursor experiments is shown. This is the case for the measurement in high field, but in the low field, they used a similar setup. They used a thin scintillator as a muon arrival timer. They used the information on how long muoniums feel the microwave to induce the transition. This information is useful for more efficient analysis, which will be discussed in detail in the latter section. The injected muon starts the timer, and forms a muonium in Krypton gas, then decay. Decay positrons are detected by a positron counter. If the second muon arrives before the first muon decay, it is difficult to identify how long each muonium feels the microwave, since one cannot distinguish from which muon the positron decay. This pile-up of the muon prevents them from using a more efficient analysis method. They hence chopped the beam to establish a quasi-pulsed structure of the beam, which enables them to suppress the pile-up. The chopping, however, reduces the available beam intensity. After the chopping, the intensity for the precursor experiment was 2×10^6 muons per second.

Compared to the DC beam at LAMPF, pulsed beam at J-PARC has no need to be chopped. The muon arrival is known as a trigger signal which is synchronized

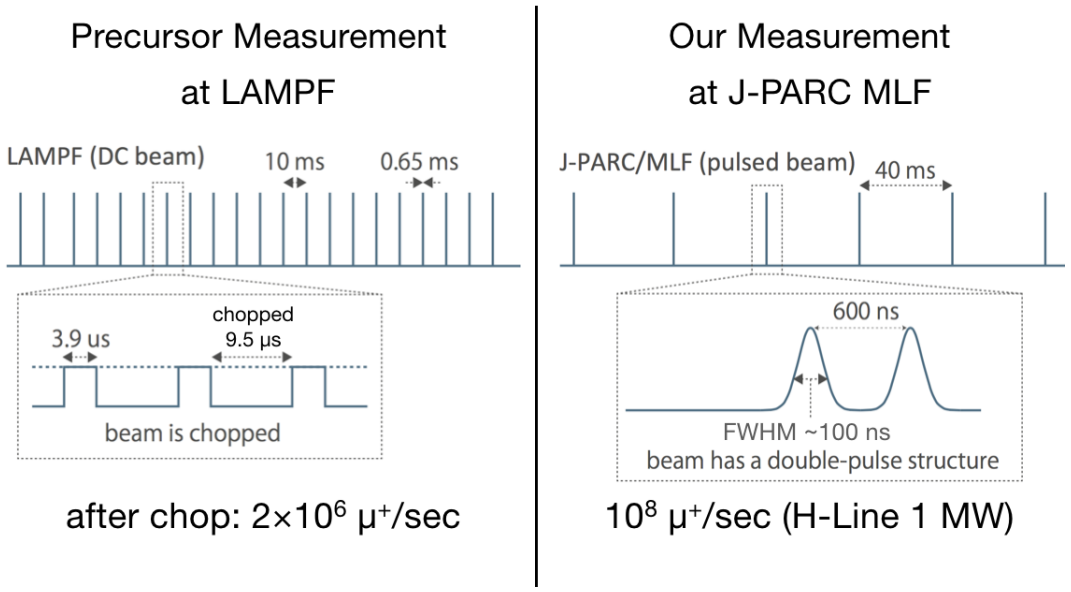

Figure 1.14: Time structure of the muon beam at LAMPF and J-PARC

with the RF (Radio Frequency) of the accelerator. The signal is used for the trigger of the data acquisition (DAQ) system. The current beam intensity at D-Line is 5×10^6 muons per second. In the near future, more proton beam power and a new beamline called H-Line enhance the muon beam intensity up to 1×10^8 muons per second. A comparison of the two beams at LAMPF and J-PARC is summarized in Fig. 1.14.

1.4.2 First Pilot Measurement

We conducted the first measurement trial in June 2016 [53, 54]. The resonance curve obtained from the first measurement is shown in Fig. 1.15. The statistical uncertainty was 22 kHz (5 ppm). The systematic uncertainty was evaluated to be 73 Hz. The main source of the systematic uncertainty is gas pressure extrapolation. The result was mainly limited by the lack of statistics. The statistics were limited mainly for two reasons.

First, at the time of the first measurement, the beam power at J-PARC MLF is limited to 150 kW. The maximum beam power planned at J-PARC is 1 MW and this can improve the statistics. At the time of June 2018, the beam power was enhanced to 500 kW. In the future, a new beamline (H-Line) can supply ten times more muons compared to the existing beamline, D-Line.

Second, the microwave cavity used in the first measurement was too small compared to the muon beam size. The cylindrical cavity has a diameter of 81 mm. The muon beam has a cross-sectional distribution which is similar to two-dimensional Gauss function. The 2σ of the typical beam profile is more than 60 mm (See Fig.

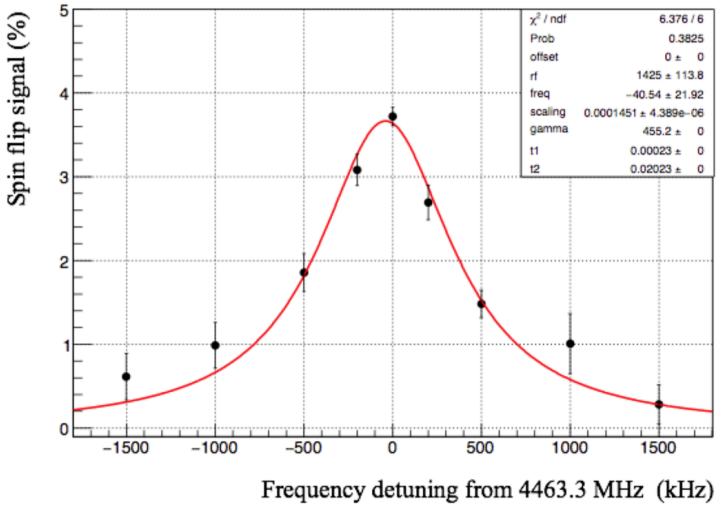

Figure 1.15: The resonance obtained in the first experiment at J-PARC [53, 54].

1.16). The beam width becomes larger by multiple scattering with Kr atoms in the gas chamber.

The cavity size is determined by the MuHFS frequency (4.463 GHz) and the resonance mode. In the case of the first cavity, Transverse Magnetic 110 (TM110) mode is used. The cross-sectional view of the muon beam has a diameter of 50 mm in the initial distribution. The muon beam distribution becomes broader due to the scattering with Kr gas atoms in the microwave cavity. Subsequently, most of the muon stop in the cavity wall and do not form muonium. This effect reduces the signal-to-noise ratio and makes the experiment statistically insensitive.

To reduce the number of the muon stop in the cavity wall and ameliorate the statistics, we develop a new microwave cavity with TM220 resonance mode. This new cavity has a diameter of 181 mm, which is sufficiently large to contain almost all the muon injected inside the cavity. This larger cavity also enables the measurement at lower Kr gas pressures without suffering severe loss of the statistics. The measurements at lower Kr pressure suppresses the systematic uncertainty related to the gas pressure extrapolation, which was the dominant systematic uncertainty at the first measurement at J-PARC.

1.4.3 Second Pilot Measurement

In July 2017, we made the pilot measurement with krypton pressure with 1.0 atm. The analysis in detail is discussed elsewhere [55]. In this measurement, we used a new microwave cavity discussed in Sec. 3.5.2. Measurements at lower krypton pressures change the resonance frequency of the cavity since the permittivity in krypton varies according to the krypton density, so we needed to modify the cavity antennae to adjust the resonance frequency of the cavity. Due to the limitation of

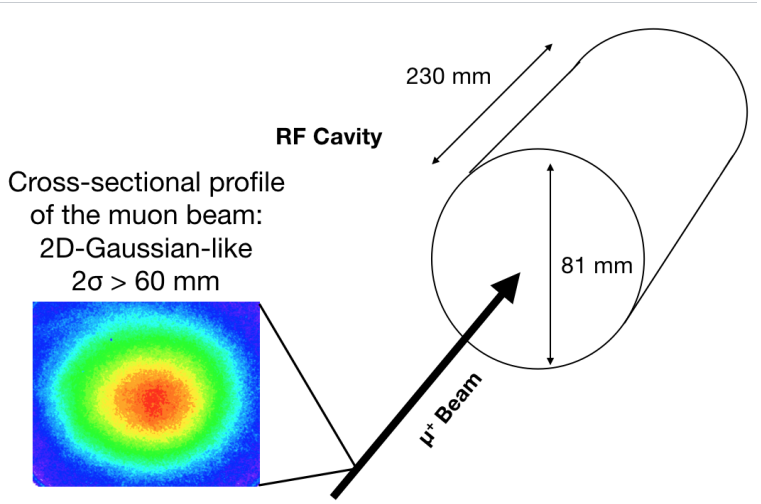

Figure 1.16: The dimension of the TM110 cavity and the cross-sectional profile of the muon beam. The muon beam has a cross-sectional distribution which is similar to the two-dimensional Gauss function. The 2σ of the initial beam profile is more than 60 mm. The diameter of the cavity is 81 mm and it is not sufficiently large to contain all the injected muons.

the time, there was no such time of the adjustment. The result in [55] will be used for pressure extrapolation in this thesis.

1.5 Structure of the Dissertation

In this dissertation, we present the development of the new microwave cavity with TM220 resonance mode and realization of the measurement at Kr pressure lower than 0.8 atmospheres (atm). We conducted the measurement at the low field using the existing beamline (D-Line) and the experimental area D2 in J-PARC. Combined with the previous result at 1.0 atm (Sec. 1.4.3), we extrapolate the results to obtain the MuHFS frequency at the zero Kr density. We present the basic theoretical discussion of the MuHFS in Chapter 2 and we explain our experimental setup as well as the development of the cavity in Chapter 3. We discuss the analysis in detail in chapter 4. In chapter 5, we show the result and discuss systematic uncertainty. We also address the future prospect for the MuSEUM project.

Chapter 2

Theoretical Discussion

2.1 Energy Diagram of Muonium

Fig. 2.1 indicates the energy diagram of the muonium. Each energy level splits into two different substates due to the spin-spin interaction between the muon and the electron. Throughout this thesis, the term "hyperfine structure" indicates the ground-state hyperfine structure, i.e., the energy difference between two 1S states.

2.1.1 Ground-State Hyperfine Structure of Muonium

In this section, we discuss the theoretical calculation of MuHFS[1]. The leading contribution for the ground-state hyperfine structure of the muonium can be written by the Fermi formula [56]:

$$\Delta\nu_{\mathrm{F}} = \frac{16}{3} Z^3 \alpha^2 R_\infty c \frac{m_{\mathrm{e}}}{m_\mu} \left[1 + \frac{m_{\mathrm{e}}}{m_\mu}\right]^{-3}, \tag{2.1}$$

where Z is the atomic number with $Z = 1$ for muonium, α is the fine structure constant, m_{e} (m_μ) is the electron (muon) mass, c is the speed of light, and R_∞ is the Rydberg constant. The higher order terms can be calculated from Lorentz covariant theories, such as the Bethe-Salpeter equation [57, 58, 59], non-relativistic QED (NRQED)[60, 61, 62].

The theoretical expression of the muonium hyperfine structure interval $\Delta\nu$ including QED, weak, and hadronic effect, is written as

$$\Delta\nu = \Delta\nu_{\mathrm{F}} + \Delta\nu_{\mathrm{QED}} + \Delta\nu_{\mathrm{weak}} + \Delta\nu_{\mathrm{had}}, \tag{2.2}$$

where the $\Delta\nu_{\mathrm{QED}}$ is the contribution from higher-order QED, $\Delta\nu_{\mathrm{weak}}$ is the contribution from weak interaction, and $\Delta\nu_{\mathrm{had}}$ is the contribution from hadronic interaction.

Furthermore, $\Delta\nu_{\mathrm{QED}}$ is also divided into smaller terms,

$$\Delta\nu_{\mathrm{QED}} = \Delta\nu_{\mathrm{D}} + \Delta\nu_{\mathrm{rad}} + \Delta\nu_{\mathrm{rec}} + \Delta\nu_{\mathrm{rad-rec}}, \tag{2.3}$$

[1]The discussion in detail can be found in [17].

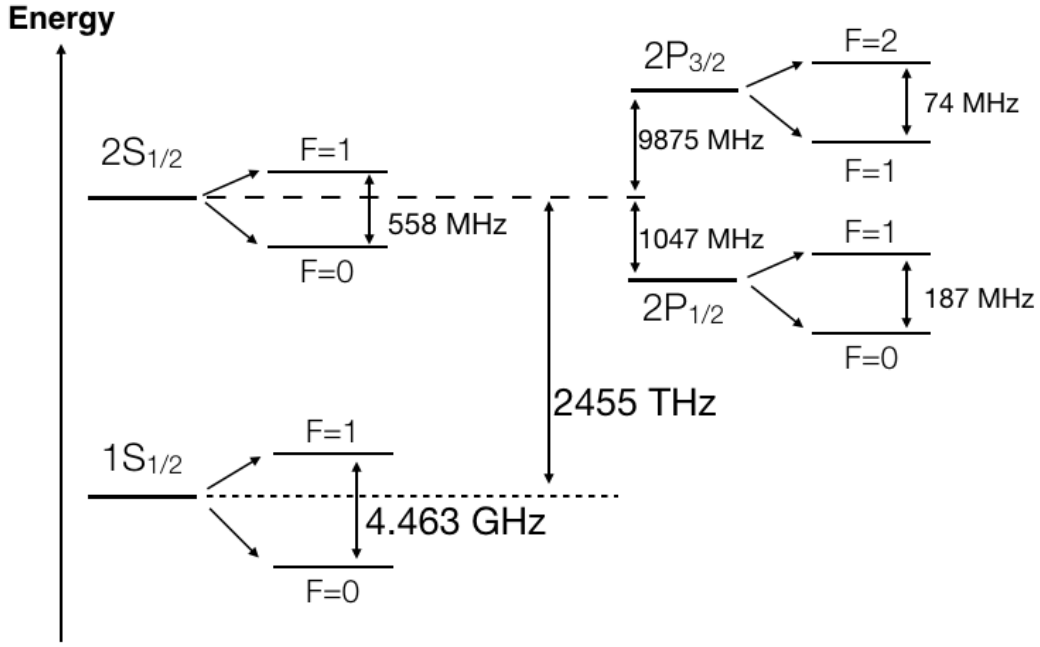

Figure 2.1: Muonium energy levels (not to scale)

where $\Delta\nu_{\rm D}$ is the Dirac contribution, $\Delta\nu_{\rm rad}$ is the radiative corrections, $\Delta\nu_{\rm rec}$ is the recoil corrections, and $\Delta\nu_{\rm rad-rec}$ is the radiative-recoil corrections.

QED: Dirac

The Dirac contribution is expressed as the following equation

$$\Delta\nu_{\rm D} = \Delta\nu_{\rm F}(1+a_\mu)\left[1+\frac{3}{2}(Z\alpha)^2+\frac{17}{8}(Z\alpha)^4+\cdots\right] \tag{2.4}$$

where a_μ is the muon anomalous magnetic moment.

QED: radiative

The radiative corrections are

$$\Delta\nu_{\rm rad} = \Delta\nu_{\rm F}(1+a_\mu)\left[D^{(2)}(Z\alpha)\left(\frac{\alpha}{\pi}\right)+D^{(4)}(Z\alpha)\left(\frac{\alpha}{\pi}\right)^2+D^{(6)}(Z\alpha)\left(\frac{\alpha}{\pi}\right)^3+\cdots\right] \tag{2.5}$$

where $D^{(n)}(Z\alpha)$ are the contributions from n virtual photons. The leading term is

$$\begin{aligned} D^{(2)}(Z\alpha) =& A_1^{(2)} + \left(\ln 2 - \frac{5}{2}\right)\pi Z\alpha \\ &+ \left[-\frac{2}{3}\ln^2(Z\alpha)^{-2} + \left(\frac{281}{360}-\frac{8}{3}\ln 2\right)\ln(Z\alpha)^{-2} + 16.9037\ldots\right](Z\alpha)^2 \\ &+ \left[\left(\frac{5}{2}\ln 2 - \frac{547}{96}\right)\ln(Z\alpha)^{-2}\right]\pi(Z\alpha)^3 + G(Z\alpha)(Z\alpha)^3 \end{aligned} \tag{2.6}$$

where $A_1^{(2)} = \frac{1}{2}$ is the contribution from a vacuum-polarization term in electron anomalous magnetic moment a_e. The function $G(Z\alpha)$ is for all higher-order contributions in powers of $Z\alpha$ and can be divided to self-energy and vacuum-polarization contributions, $G(Z\alpha) = G_{\rm SE}(Z\alpha) + G_{\rm VP}(Z\alpha)$. One loop self-energy has been calculated by Yerokhin and Jentschura [63];

$$G_{\rm SE}(\alpha) = -13.8308(43). \tag{2.7}$$

The vacuum-polarization part except Wichmann-Kroll contribution has been calculated as [64]

$$G_{\rm VP}(\alpha) = 7.227(9). \tag{2.8}$$

$D^{(4)}(Z\alpha)$ has been calculated as [65]

$$\begin{aligned} D^{(4)}(Z\alpha) =& A_1^{(4)} + 0.77099(2)\pi Z\alpha + \left[-\frac{1}{3}\ln^2 (Z\alpha)^{-2} \right. \\ & \left. - 6.390\ldots \times \ln (Z\alpha)^{-2} + 10(2.5) \right] (Z\alpha)^2 + \cdots \end{aligned} \tag{2.9}$$

where $A_1^{(4)} = -0.328\ 478\ 965\ 579\ldots$ is the next leading order vacuum-polariation term in a_e.

The next term $D^{(6)}(Z\alpha) = A_1^{(6)} + \cdots = 1.181\ 241\ 456\ldots + \cdots$ is only partially calculated, and for $n > 3$, the functions $D^{(2n)}(Z\alpha)$ are considered to be negligible.

QED: recoil

Recoil correction is expanded by a small parameter m_e/m_μ. Note that in positronium this parameter equals to unity and higher order contribution becomes larger. The leading term of the recoil correction comes from two-photon exchange [66]. The whole contribution can be written as below,

$$\begin{aligned} \Delta\nu_{\rm rec} =& \Delta\nu_{\rm F}\frac{m_e}{m_\mu}\left(-\frac{3}{1-(m_e/m_\mu)^2}\ln\left(\frac{m_\mu}{m_e}\right)\frac{Z\alpha}{\pi} + \frac{1}{(1+m_e/m_\mu)^2} \right. \\ & \left\{ \ln (Z\alpha)^{-2} - 8\ln 2 + \frac{65}{18} + \left[\frac{9}{2\pi^2}\ln^2\left(\frac{m_e}{m_\mu}\right) + \left(\frac{27}{2\pi^2} - 1\right)\ln\left(\frac{m_e}{m_\mu}\right) \right. \right. \\ & \left. \left. + \frac{93}{4\pi^2} + \frac{33\zeta(3)}{\pi} - \frac{13}{12} - 12\ln 2 \right] \frac{m_e}{m_\mu} \right\} (Z\alpha)^2 \\ & + \left\{ -\frac{3}{2}\ln\left(\frac{m_\mu}{m_e}\right)\ln (Z\alpha)^{-2} - \frac{1}{6}\ln^2 (Z\alpha)^{-2} + \left(\frac{101}{18} - 10\ln 2\right)\ln (Z\alpha)^{-2} \right. \\ & \left. \left. + 40(10) \right\} \frac{(Z\alpha)^3}{\pi} \right) + \cdots \end{aligned} \tag{2.10}$$

where ζ is the Riemann zeta function.

QED: radiative-recoil

The radiative effects in recoil diagrams are called radiative-recoil correction. The radiative-recoil contributions $\Delta\nu_{\mathrm{rad-rec}}$ are

$$\begin{aligned}\Delta\nu_{\mathrm{rad-rec}} =&\Delta\nu_{\mathrm{F}}\left(\frac{\alpha}{\pi}\right)^2\frac{m_{\mathrm{e}}}{m_\mu}\left\{\left[-2\ln^2\left(\frac{m_\mu}{m_{\mathrm{e}}}\right)+\frac{13}{12}\ln\left(\frac{m_\mu}{m_{\mathrm{e}}}\right)+\frac{21}{2}\zeta(3)+\frac{\pi^2}{6}+\frac{35}{9}\right]\right.\\&+\left[\frac{4}{3}\ln^2\alpha^{-2}+\left(\frac{16}{3}\ln 2-\frac{341}{180}\right)\ln\alpha^{-2}-40(10)\right]\pi\alpha\\&\left.+\left[-\frac{4}{3}\ln^3\left(\frac{m_\mu}{m_{\mathrm{e}}}\right)+\frac{4}{3}\ln^2\left(\frac{m_\mu}{m_{\mathrm{e}}}\right)\right]\frac{\alpha}{\pi}\right\}\\&-\Delta\nu_{\mathrm{F}}\alpha^2\left(\frac{m_{\mathrm{e}}}{m_\mu}\right)^2\left(6\ln 2+\frac{13}{6}\right)+\cdots\end{aligned}\tag{2.11}$$

where we omit the explicit dependence on Z for simplicity.

There are additional radiative-recoil terms from single-logarithmic and non-logarithmic three-loop contributions

$$\Delta\nu_{\mathrm{F}}\left(\frac{\alpha}{\pi}\right)^3\frac{m_{\mathrm{e}}}{m_\mu}\left\{\left[-6\pi^2\ln 2+\frac{\pi^2}{3}+\frac{27}{8}\right]\ln\frac{m_\mu}{m_{\mathrm{e}}}+68.507(2)\right\}=-30.99\text{ Hz}.$$

Hadronic

There is a correction from the hadronic vacuum polarization. The vacuum polarization term was calculated to be 232.7(1.4) Hz [67]. A negligible light-by-light scattering correction was calculated to be -0.0065(10) Hz [68].

Weak

There is a weak interaction term from the exchange of Z^0 boson. The term is expressed as [69]

$$\Delta\nu_{\mathrm{weak}} = -G_{\mathrm{F}}\frac{3\sqrt{2}m_{\mathrm{e}}m_\mu}{8\alpha\pi}\Delta\nu_{\mathrm{F}}\tag{2.12}$$

$$= -65\text{ Hz}\tag{2.13}$$

where G_{F} is the Fermi coupling constant. The next-leading order term was evaluated to be less than 1 Hz and negligible [70].

Total

As discussed in the Commitie on Data for Science and Technology [17, 71], they use a least-square adjustment of the fundamental constants (R_∞, α, $\frac{m_{\mathrm{e}}}{m_\mu}$, a_μ) using the theoretical expression for the MuHFS,

$$\Delta\nu_{\mathrm{Mu}}(th)=\Delta\nu_{\mathrm{Mu}}\left(R_\infty,\ \alpha,\ \frac{m_{\mathrm{e}}}{m_\mu},\ a_\mu\right)+\delta_{\mathrm{Mu}}\tag{2.14}$$

where $\delta_{\mathrm{Mu}} = 0(85)$ accounts for the theoretical uncertainty (85 Hz).

The adjustment above yields the theoretical value of MuHFS as [17]

$$\Delta\nu_{\mathrm{th}} = 4.463\ 302\ 868(271)\ \mathrm{GHz} \tag{2.15}$$

where the main source of the uncertainty is the muon-electron mass ratio m_μ/m_e. Purely theoretical uncertainty is 85 Hz [17]. Each contribution will be briefly reviewed below, and the summary table is shown in Table 2.1. Note that the CODATA does not open the adjustment result for each contribution of the theoretical value, so the values for contributions were cited from the other sources, and the square of the quadrature sum of the uncertainties of the contributions does not equal to the total uncertainty.

Table 2.1: Contributions to muonium hyperfine structure and its theoretical values.

Contribution	Theoretical value [kHz]
Fermi Energy and a_μ	4 459 031.816(253)
a_e	5 170.926
Radiative	−104.901(39)
Recoil	−791.714(80)
Radiative-Recoil	−3.427(70)
Electroweak	−0.065
Hadronic	0.233(1)
Total	4 463 302.868(271)

2.1.2 The Zeeman Effect

In this section, we discuss the shift of the hyperfine frequency due to the external magnetic field, the Zeeman effect. The effect is mainly relevant to the measurement in a high field, but also important to the measurement at the low field when we consider the systematic effect of the residual magnetic field.

The Hamiltonian of muonium under magnetic field is written as

$$\mathcal{H} = h\Delta\nu \boldsymbol{I}\cdot\boldsymbol{J} + \mu_B^e g_\mathrm{J} \boldsymbol{J}\cdot\boldsymbol{B} + \mu_B^\mu g_\mu^{'} \boldsymbol{I}\cdot\boldsymbol{B} \tag{2.16}$$

where h is the Planck constant, $\Delta\nu$ is the hyperfine structure interval of the muonium, $\boldsymbol{I}$ and $\boldsymbol{J}$ are the spin of the muon and the electron, μ_B^e and μ_B^μ are the Bohr magneton and muon Bohr magneton, g_J ($g_\mu^{'}$) is the bound g-factor of the electron (muon) in muonium, and the $\boldsymbol{B}$ is the applied magnetic field.

The quantities g_J and $g_\mu^{'}$ are related to the free g values, g_e and g_μ [56, 72][2]:

$$g_\mathrm{J} = g_e\left(1 - \frac{\alpha^2}{3} + \frac{\alpha^2}{2}\frac{m_\mathrm{e}}{m_\mu} + \frac{\alpha^3}{4\pi} - \left(\alpha^2\left(\frac{m_\mathrm{e}}{m_\mu}\right)^2 + \frac{5\alpha^3}{12\pi}\frac{m_\mathrm{e}}{m_\mu} + \alpha^4\left(\frac{1}{12} + \frac{0.289}{\pi}\right)\right)\right), \tag{2.17}$$

[2]Note that the expression of $g_\mu^{'}$ in [72] has a typographic error in the 3rd order term.

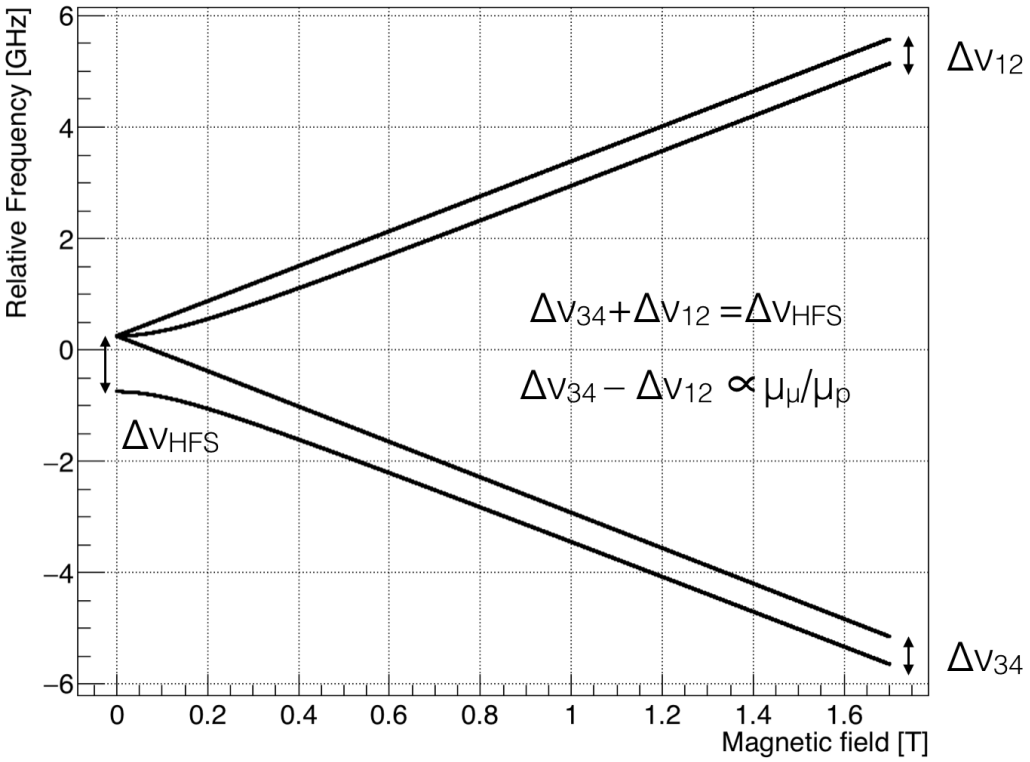

Figure 2.2: Zeeman effect on the ground-state muonium hyperfine structure

and

$$g_\mu^{'} = g_\mu \left(1 - \frac{\alpha^2}{3} + \frac{\alpha^2}{2}\frac{m_\mathrm{e}}{m_\mu} - \left(\alpha^2\left(\frac{m_\mathrm{e}}{m_\mu}\right)^2 - \frac{\alpha^3}{12\pi}\frac{m_\mathrm{e}}{m_\mu} + \frac{97}{108}\alpha^4\right)\right). \tag{2.18}$$

The energy eigenvalues of the Hamiltonian are given by the Breit-Rabi equation,

$$W_1 = +\frac{1}{4}h\Delta\nu + \frac{1}{2}(g_\mathrm{J}\mu_\mathrm{B}^\mathrm{e} + g_\mu^{'}\mu_B^\mu)B \tag{2.19}$$

$$W_2 = -\frac{1}{4}h\Delta\nu + \frac{1}{2}h\Delta\nu\sqrt{1+x^2} \tag{2.20}$$

$$W_3 = +\frac{1}{4}h\Delta\nu - \frac{1}{2}(g_\mathrm{J}\mu_\mathrm{B}^\mathrm{e} + g_\mu^{'}\mu_B^\mu)B \tag{2.21}$$

$$W_4 = -\frac{1}{4}h\Delta\nu - \frac{1}{2}h\Delta\nu\sqrt{1+x^2} \tag{2.22}$$

where

$$x = \frac{(g_\mathrm{J}\mu_B^e - g_\mu^{'}\mu_B^\mu)B}{h\Delta\nu} \tag{2.23}$$

is a dimension-less quantity, H is the magnetic field strength, F is the quantum number for the total angular momentum, and M_F is the quantum number for the z-component of the total angular momentum. The graph of the energy eigenvalues in frquency is shown in Fig. 2.2. Here, we number the four states starting from the one with the highest energy, and the transition frequency between the i-th state and the j-th state is called $\Delta\nu_{ij}$, *e.g.*, $\Delta\nu_{12} = (W_1 - W_2)/h$. The magnetic field dependence of the transition frequencies $\Delta\nu_{12}$ and $\Delta\nu_{34}$ is shown in Fig. 2.3.

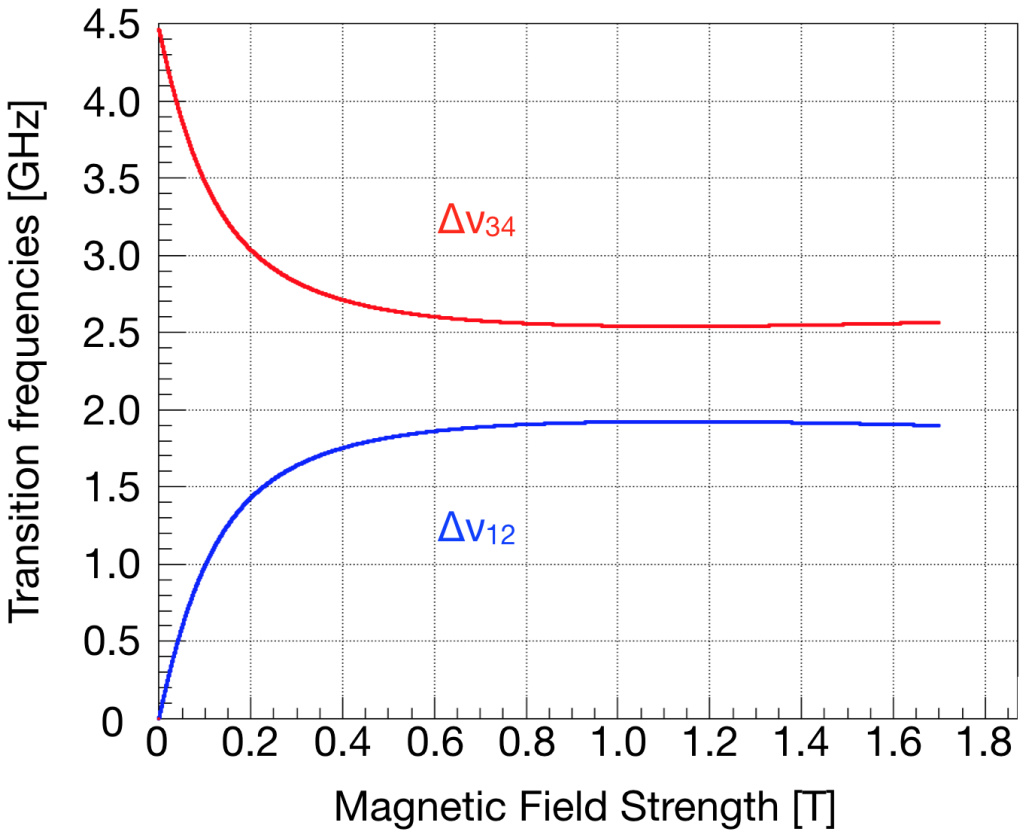

Figure 2.3: Transition frequencies and the applied magnetic field. The blue line indicates $\Delta\nu_{12}$ and the red line indicates $\Delta\nu_{34}$.

The spin eigenfunctions are

$$\chi_{1,1} = |1\rangle = \alpha_e \alpha_\mu \tag{2.24}$$

$$\chi_{1,0} = |2\rangle = c\alpha_e \beta_\mu + s\beta_e \alpha_\mu \tag{2.25}$$

$$\chi_{1,-1} = |3\rangle = \beta_e \beta_\mu \tag{2.26}$$

$$\chi_{0,0} = |4\rangle = s\alpha_e \beta_\mu - c\beta_e \alpha_\mu \tag{2.27}$$

where the α_μ and β_μ are the normalized spin eigenfunction of the muon. α_μ (β_μ) corresponds to the spin orientation in the positive (negative) z direction. In the case of this thesis, the positive z direction is set to be the initial muon spin orientation, antiparallel to the muon beam. The quantities s and c are field-dependent

$$s = \frac{1}{\sqrt{2}} \left(1 - \frac{x}{\sqrt{1+x^2}} \right)^{1/2} \tag{2.28}$$

$$c = \frac{1}{\sqrt{2}} \left(1 + \frac{x}{\sqrt{1+x^2}} \right)^{1/2} \tag{2.29}$$

which satisfy

$$s^2 + c^2 = 1.$$

In the limit of very low magnetic field, $x \ll 1$ and $s \approx c \approx 1/\sqrt{2}$, and the spin eigenfunctions become

$$\chi_{1,1} = |1\rangle = \alpha_e \alpha_\mu \tag{2.30}$$

$$\chi_{1,0} = |2\rangle \approx \frac{1}{\sqrt{2}} \alpha_e \beta_\mu + \frac{1}{\sqrt{2}} \beta_e \alpha_\mu = \frac{1}{\sqrt{2}} (\alpha_e \beta_\mu + \beta_e \alpha_\mu) \tag{2.31}$$

$$\chi_{1,-1} = |3\rangle = \beta_e \beta_\mu \tag{2.32}$$

$$\chi_{0,0} = |4\rangle \approx \frac{1}{\sqrt{2}} \alpha_e \beta_\mu - \frac{1}{\sqrt{2}} \beta_e \alpha_\mu = \frac{1}{\sqrt{2}} (\alpha_e \beta_\mu - \beta_e \alpha_\mu). \tag{2.33}$$

Also, in the limit of very low magnetic field, $\Delta\nu_{14}$, $\Delta\nu_{24}$, and $\Delta\nu_{34}$ all equal to $\Delta\nu$. This research is done at nearly zero magnetic field (≈100 nT or 1 mG) and approximate values of the transition frequencies are determined by expanding for small x:

$$\Delta\nu_{14} \approx \Delta\nu + \frac{1}{2h} (g_J \mu_B^e H + g_\mu^{'} \mu_B^\mu H) \tag{2.34}$$

$$\Delta\nu_{24} \approx \Delta\nu \tag{2.35}$$

$$\Delta\nu_{34} \approx \Delta\nu - \frac{1}{2h} (g_J \mu_B^e H + g_\mu^{'} \mu_B^\mu H) \tag{2.36}$$

The difference of $\Delta\nu_{14}$ and $\Delta\nu$ is 1.4 kHz/mG and at the measurement condition (B≈1 mG), it is unresolvable compared to the natural line width, 145 kHz.

2.2 Muonium Formation and State Population

2.2.1 Muonium Formation in Krypton Gas

Table 2.2: Muonium formation threshold energies E_{th} [51] and muonium formation ratio P_{Mu} measured by [74] for various gas atoms or molecule.

Atom or Molecule	E_{th}	P_{Mu} (Pressure [atm])
He	+11.04	0±1 (1.2-3.1)
Ne	+8.02	7±5 (1.2)
Ar	+2.22	74±4 (1.0-2.8)
Kr	+0.46	100±5 (0.4-0.95)
Xe	-1.41	100±4 (0.4-0.65)
N_2	+2.0	84 ±4 (1.0-2.4)

We use krypton as the muonium production target. Muonium is formed when a muon is stopped in gas target such as krypton, by electron capture

$$\mu^+ + \text{Kr} \rightarrow \text{Mu} + \text{Kr}^+. \tag{2.37}$$

Muonium formation in gas has been extensively studied [73]. Table 2.2 shows the experimental result of such studies on muonium formation threshold energies E_{th} and muonium formation ratio P_{Mu} for various atoms or molecules in gas phase [51] [74]. If the threshold energy is too high, muonium formation rate is low, and if the threshold energy is too low, the produced muonium becomes too energetic. Krypton is the ideal candidate in the sense of the threshold energy.

Muonium is an isotope of hydrogen and a highly reactive paramagnetic atom. In order to avoid chemical reactions and depolarization due to the collision, it is desirable to use an inert gas. By reasons above, we use krypton gas for the muonium production target.

The muonium spin state depends on the initial polarization P of the injected muon and parameters s and c which are related to the external magnetic field. The spin evolution during the muonium formation and subsequent hyperfine interaction is briefly summarized in Fig. 2.4. Here, we focus on the case of the initial muon is 100% polarized and the external magnetic field is low ($x \ll 1$ and $s \approx c \approx 1/\sqrt{2}$). Since the spin of the electron captured by muon is not polarized, there are equal probability of muonium in $|\alpha_\mu \alpha_e\rangle$ state and in $|\alpha_\mu \beta_e\rangle$ state right after the muonium formation. The latter state, however, is not the energy eigenstate thus evolves as the combination of the two energy eigenstates, namely $|2\rangle = \frac{1}{\sqrt{2}}(\alpha_e\beta_\mu + \beta_e\alpha_\mu)$ and $|4\rangle = \frac{1}{\sqrt{2}}(\alpha_e\beta_\mu - \beta_e\alpha_\mu)$. The interaction is sufficiently faster (4.463 GHz) than the muon decay rate and we treat the two states are equally occupied. This mixing effectively halves the muonium polarization.

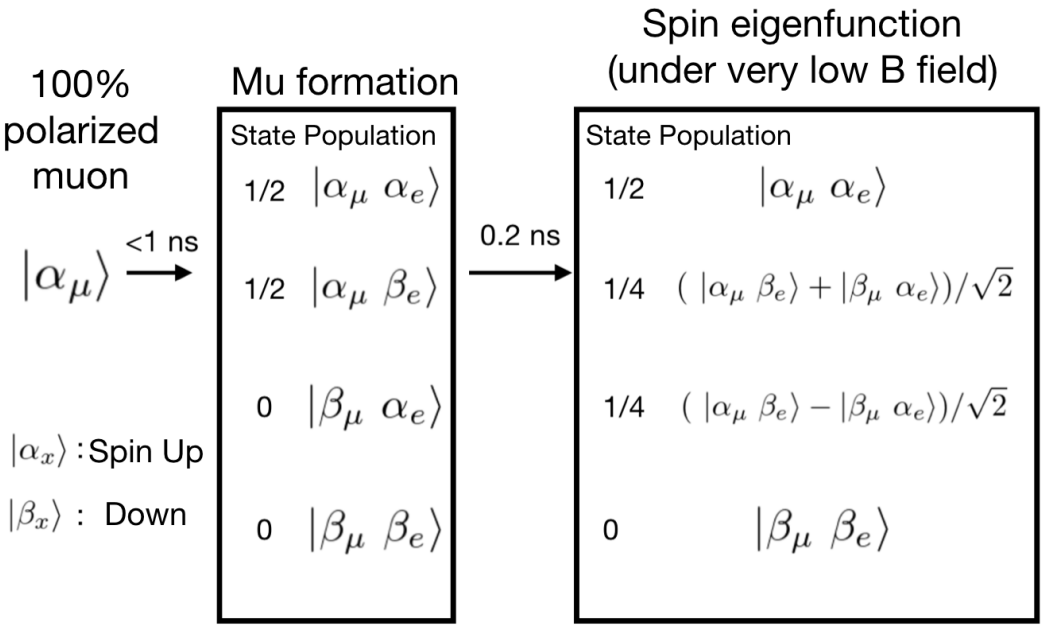

Figure 2.4: Muonium spin state evolution under low magnetic field. The initial muon spin polarization is 100% aligned to up, antiparallel to the muon beam.

2.2.2 State Population

2.3 Muon Decay

Muon decays with a lifetime of τ_μ =2.196 9811(22) μs [75]. The leading decay branch is so-called Michel decay,

$$\mu^+ \rightarrow \mathrm{e}^+ \ + \ \overline{\nu}_\mu \ + \ \nu_\mathrm{e}. \tag{2.38}$$

Since the chiralities of neutrino and antineutrino are fixed, the decay positron is emitted preferentially in the direction of the muon spin. This parity violation is an important aspect for analysing the muonium spin state. The distribution of the decay positron is

$$N(y,\theta,t)\mathrm{d}y\mathrm{d}\Omega = \frac{\gamma}{2\pi}y^2\Big[(3-2y)+(2y+1)P_{\mathrm{z}0}(t)\cos\theta\Big]\mathrm{e}^{-\gamma t}\mathrm{d}y\mathrm{d}\Omega \tag{2.39}$$

where y is the positron momentum normalized by its maximum $y = p/p_{\max}$, and

$$p_{\max} = \frac{m_\mu^2 - m_\mathrm{e}^2}{2m_\mu}c = 52.8\ \mathrm{MeV}/c, \tag{2.40}$$

θ is the polar angle between the positron momenta and the muon spin, γ is the muon decay rate, $\gamma = 1/\tau_\mu \approx 4.55 \times 10^5$ Hz, and $P_{\mathrm{z}0}(t)$ is defined to satisfy the following equation,

$$P_\mathrm{z}(t) = P_{\mathrm{z}0}(t)\mathrm{e}^{-\gamma t}. \tag{2.41}$$

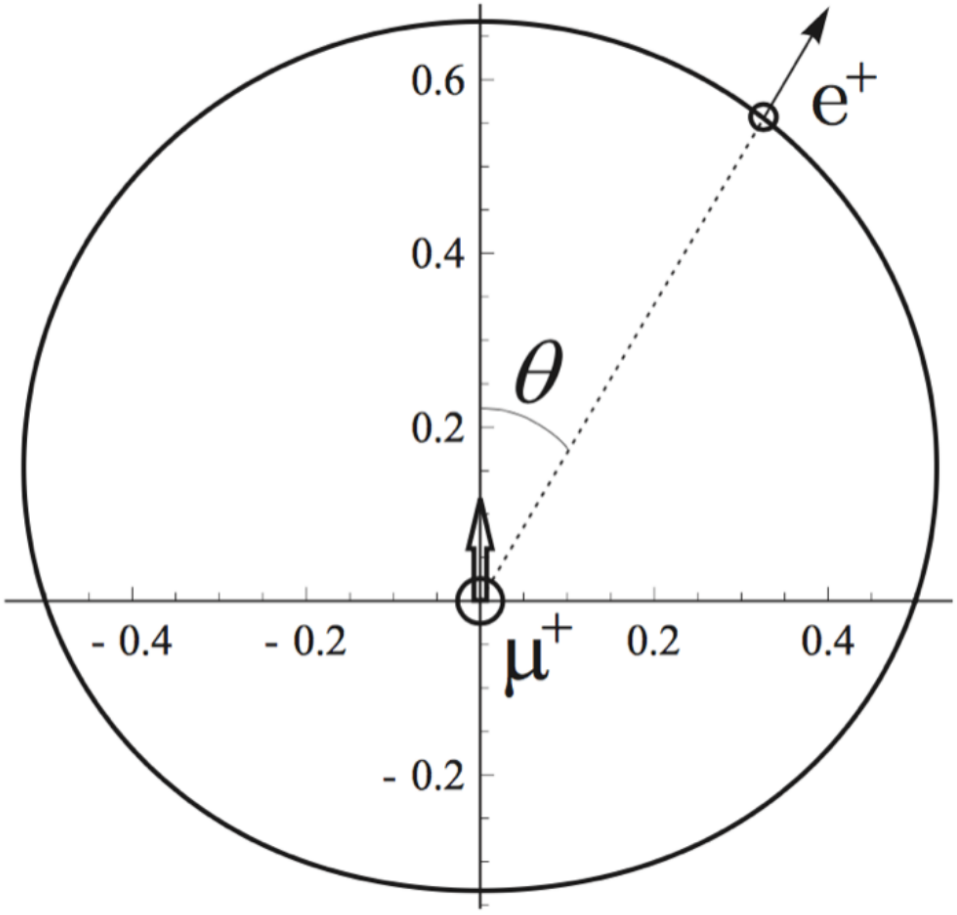

Figure 2.5: The distribution of the decay positron momentum direction in the Michel decay [76]. The spectrum is in the case for accounting all the decay positron energy.

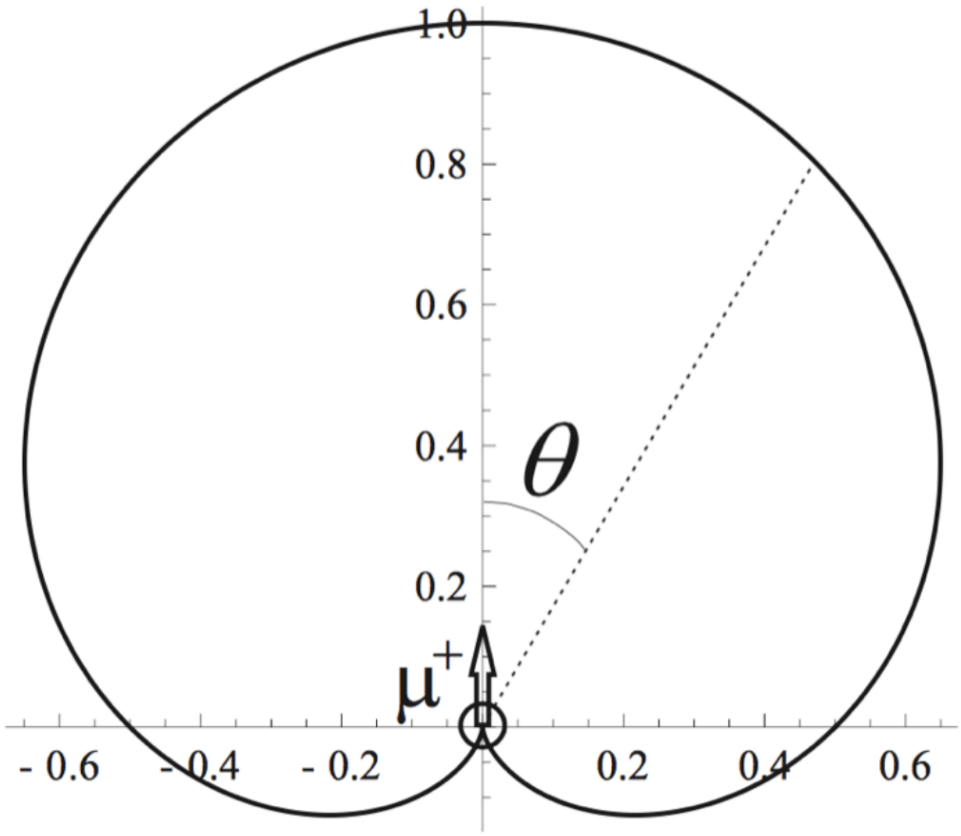

Figure 2.6: The distribution of the decay positron momentum direction in the Michel decay [76]. The spectrum is in the case for accounting only the positrons with the highest energy.

where $P_{\mathrm{z}}(t)$ is the z-component of muon polarization in muonium state. The decay positron spectrum is shown in Fig. 2.5 [76].

The higher momentum the decay positron has, the more likely it decays along the muon spin. So one can cut the low energy positrons and reduce the counting rate of the detectors, without losing the statistical sensitivity of the measurement. When the energy threshold is defined as y_0, the decay positron spectrum $N(y_0, \theta, t)$ is described as

$$N(y_0, \theta, t) = \int_{y_0}^{1} N(y, \theta, t)\mathrm{d}y\mathrm{d}\Omega \tag{2.42}$$

$$= \frac{\gamma}{4\pi}\Big[A_1(y_0) + A_2(y_0)P_{z0}(t)\cos\theta\Big]\mathrm{e}^{-\gamma t}\mathrm{d}\Omega \tag{2.43}$$

$$= \frac{\gamma}{4\pi}A_1(y_0)\Big[1 + a(y_0)P_{z0}(t)\cos\theta\Big]\mathrm{e}^{-\gamma t}\mathrm{d}\Omega \tag{2.44}$$

where

$$A_1(y_0) = 1 - (2y_0^3 - y_0^4) \tag{2.45}$$

$$A_2(y_0) = \frac{1}{3} - (y_0^4 - \frac{2}{3}y_0^3) \tag{2.46}$$

$$a(y_0) = \frac{A_2(y_0)}{A_1(y_0)}. \tag{2.47}$$

The probability of the direction of the decay positrons in case of the highest momentum is shown in Fig. 2.6.

2.4 Resonance Line Shape Theory

2.4.1 Hamiltonian and Eigenstate

Muonium has an initial population among Zeeman states as discussed above. Transitions between the states are induced by an applied microwave magnetic field. The transition probability depends on the detuning of the applied microwave frequency from the transition frequency as well as the power of the applied microwave. A resonance line can be observed by scanning the microwave frequency with a fixed magnetic field. Here, we discuss how resonance line shape is expressed.

The applied microwave field affixes an time-dependent term to the Hamiltonian,

$$\mathcal{H}' = (g_{\mathrm{J}}\mu_B^e\vec{J} + g_\mu'\mu_B^\mu\vec{I})\cdot\vec{B}_1\cos\omega t \tag{2.48}$$

$$\equiv \mathcal{H}_0'\cos\omega t \tag{2.49}$$

where $\vec{B}_1 = B_{\mathrm{x}}\hat{x} + B_{\mathrm{y}}\hat{y}$ is the vector amplitude of the applied microwave field and ω is its angular frequency.

The muonium wave function $\psi(\vec{r}, t)$ is expressed as follows

$$\psi(\vec{r}, t) = \phi(\vec{r})\sum_{\mathrm{k}=1}^{4} a_{\mathrm{k}}\left|\mathrm{k}\right\rangle \mathrm{e}^{-iW_{\mathrm{k}}t/\hbar} \tag{2.50}$$

in which $\phi(\vec{r})$ is the spatial component of the wavefunction, a_{k} is the coefficient of the kth spin eigenfunction $|\mathrm{k}\rangle$, W_{k} is the energy eigenvalue for the kth eigenstate, and $\hbar$ is the reduced Planck constant, $\hbar = h/2\pi$.

2.4.2 Time Evolution of State Amplitudes

There are two factors which change the muonium state amplitude: muon decay and the transition induced by the applied microwave field. By phenomenological treatment, one can write the muon decay as

$$\dot{a}_{\mathrm{k}} = -\frac{1}{2}\gamma a_{\mathrm{k}}(t) \tag{2.51}$$

in which γ is the muon deacy rate, $\gamma = 4.549(2) \times 10^5$ Hz. The induced transition by the applied microwave field is treated by

$$i\hbar\frac{\partial\psi}{\partial t} = (\mathcal{H} + \mathcal{H}^{'})\psi(t). \tag{2.52}$$

With the expressions above, the time evolution of the state amplitudes is written as

$$\dot{a}_{\mathrm{k}} = -\frac{1}{2}\gamma a_{\mathrm{k}}(t) - i\sum_{\mathrm{i}=1}^{4} a_{\mathrm{i}} b_{\mathrm{ki}} f_{\mathrm{ik}}(t) \tag{2.53}$$

where

$$b_{\mathrm{ik}} = \frac{1}{2\hbar}\left\langle i \left| \mathcal{H}_0^{'} \right| k \right\rangle \tag{2.54}$$

$$f_{\mathrm{ik}}(t) = \mathrm{e}^{-i(\omega_{\mathrm{ik}}-\omega)t} + \mathrm{e}^{-i(\omega_{\mathrm{ik}}+\omega)t} \tag{2.55}$$

$$\omega_{\mathrm{ik}} = \frac{W_{\mathrm{i}} - W_{\mathrm{k}}}{\hbar}. \tag{2.56}$$

The matrix elements of b_{ik} is summarized in Table 2.3.

Table 2.3: The matrix elements of b_{ik}. $K_{\mathrm{J}} = g_{\mathrm{J}}\mu_{\mathrm{B}}^{\mathrm{e}}/4\hbar$ and $K_{\mathrm{I}} = g_{\mu}^{'}\mu_{\mathrm{B}}^{\mu}/4\hbar$. $B_{\pm}$ is defined as $B_{\pm} = B_{\mathrm{x}} \pm iB_{\mathrm{y}}$.

i\k	1	2	3	4
1	$(K_{\mathrm{J}} + K_{\mathrm{I}})B_{\mathrm{z}}$	$(sK_{\mathrm{J}} + cK_{\mathrm{I}})B_{-}$	0	$(cK_{\mathrm{J}} - sK_{\mathrm{I}})B_{-}$
2	$(sK_{\mathrm{J}} + cK_{\mathrm{I}})B_{+}$	$(c^2 - s^2)(K_{\mathrm{J}} - K_{\mathrm{I}})B_{\mathrm{z}}$	$(cK_{\mathrm{J}} + sK_{\mathrm{I}})B_{-}$	$-2sc(K_{\mathrm{J}} - K_{\mathrm{I}})B_{\mathrm{z}}$
3	0	$(cK_{\mathrm{J}} + sK_{\mathrm{I}})B_{+}$	$-(K_{\mathrm{J}} + K_{\mathrm{I}})B_{\mathrm{z}}$	$(-sK_{\mathrm{J}} + cK_{\mathrm{I}})B_{+}$
4	$(cK_{\mathrm{J}} - sK_{\mathrm{I}})B_{+}$	$-2sc(K_{\mathrm{J}} - K_{\mathrm{I}})B_{\mathrm{z}}$	$(-sK_{\mathrm{J}} + cK_{\mathrm{I}})B_{-}$	$(s^2 - c^2)(K_{\mathrm{J}} - K_{\mathrm{I}})B_{\mathrm{z}}$

Using the expression in Table 2.3, the time evolution of the state amplitude is

rewritten as

$$\begin{pmatrix} \dot{a}_1 \\ \dot{a}_2 \\ \dot{a}_3 \\ \dot{a}_4 \end{pmatrix} = \begin{pmatrix} -\gamma/2 & -ib_{12}e^{i(\omega_{12}-\omega)t} & 0 & -ib_{14}e^{i(\omega_{14}-\omega)t} \\ -ib_{12}^{*}e^{-i(\omega_{12}-\omega)t} & -\gamma/2 & -ib_{23}e^{i(\omega_{23}-\omega)t} & -ib_{24}e^{i(\omega_{24}-\omega)t} \\ 0 & -ib_{23}^{*}e^{-i(\omega_{23}-\omega)t} & -\gamma/2 & -ib_{34}e^{i(\omega_{34}-\omega)t} \\ -ib_{14}^{*}e^{-i(\omega_{14}-\omega)t} & -ib_{24}^{*}e^{-i(\omega_{24}-\omega)t} & -ib_{34}^{*}e^{-i(\omega_{34}-\omega)t} & -\gamma/2 \end{pmatrix} \begin{pmatrix} a_1 \\ a_2 \\ a_3 \\ a_4 \end{pmatrix}. \tag{2.57}$$

The equation 2.57 above ignores the time-dependent Bloch-Siegert terms, involving the factors $e^{\pm i(\omega_{ij}+\omega)t}$. The effect of neglecting these terms will be discussed in Sec. 5.1.5.

In this experiment, the muon is fully polarized initially and magnetic field is applied to perpendicular to the muon spin, i.e., $B_z = 0$ in the experiment thus all the diagonal elements and b_{24} and b_{24}^{*} vanish (the diagonal elements have already been dropped in Eq. 2.57),

$$\begin{pmatrix} \dot{a}_1 \\ \dot{a}_2 \\ \dot{a}_3 \\ \dot{a}_4 \end{pmatrix} = \begin{pmatrix} -\gamma/2 & -ib_{12}e^{i(\omega_{12}-\omega)t} & 0 & -ib_{14}e^{i(\omega_{14}-\omega)t} \\ -ib_{12}^{*}e^{-i(\omega_{12}-\omega)t} & -\gamma/2 & -ib_{23}e^{i(\omega_{23}-\omega)t} & 0 \\ 0 & -ib_{23}^{*}e^{-i(\omega_{23}-\omega)t} & -\gamma/2 & -ib_{34}e^{i(\omega_{34}-\omega)t} \\ -ib_{14}^{*}e^{-i(\omega_{14}-\omega)t} & 0 & -ib_{34}^{*}e^{-i(\omega_{34}-\omega)t} & -\gamma/2 \end{pmatrix} \begin{pmatrix} a_1 \\ a_2 \\ a_3 \\ a_4 \end{pmatrix}. \tag{2.58}$$

There are terms with angular frequency $\omega_{mn} - \omega$. In the case the subscripts mn satisfies mn = 12, 13, or 23, ω_{mn} becomes sufficiently smaller than the microwave angular frequency $\omega \approx 2\pi \times 4.463$ GHz, satisfying $|\omega_{mn} - \omega| \approx \omega \gg 0$. In the case, the time average of $f_{mn}(t)$ in Eq. 2.55 becomes zero. We ignore such terms and the effect of ignoring those nonresonant states will be discussed in Sec. 5.1.5. The equation is simplified as

$$\begin{pmatrix} \dot{a}_1 \\ \dot{a}_2 \\ \dot{a}_3 \\ \dot{a}_4 \end{pmatrix} = \begin{pmatrix} -\gamma/2 & 0 & 0 & -ib_{14}e^{i(\omega_{14}-\omega)t} \\ 0 & -\gamma/2 & 0 & 0 \\ 0 & 0 & -\gamma/2 & -ib_{34}e^{i(\omega_{34}-\omega)t} \\ -ib_{14}^{*}e^{-i(\omega_{14}-\omega)t} & 0 & -ib_{34}^{*}e^{-i(\omega_{34}-\omega)t} & -\gamma/2 \end{pmatrix} \begin{pmatrix} a_1 \\ a_2 \\ a_3 \\ a_4 \end{pmatrix}. \tag{2.59}$$

Here, the state $|2\rangle$ is decoupled from the other states.

From now on, we choose the x axis parallel to the microwave field, $\vec{B}_1$, in order to simplify the expressions below. Introducing the linear combinations of the state amplitudes

$$a_+ = \frac{1}{2}\sqrt{2}(a_1 + a_3) \tag{2.60}$$

$$a_- = \frac{1}{2}\sqrt{2}(a_1 - a_3) \tag{2.61}$$

and defining microwave parameter b as follows,

$$b \equiv b_{14} = -b_{34}^{*}, \tag{2.62}$$

we simplify the equation further:

$$\begin{pmatrix} \dot{a}_+ \\ \dot{a}_- \\ \dot{a}_4 \end{pmatrix} = \begin{pmatrix} -\gamma/2 & 0 & 0 \\ 0 & -\gamma/2 & -i\sqrt{2}b\mathrm{e}^{i(\omega_0-\omega)t} \\ 0 & -i\sqrt{2}b^{*}\mathrm{e}^{-i(\omega_0-\omega)t} & -\gamma/2 \end{pmatrix} \begin{pmatrix} a_+ \\ a_- \\ a_4 \end{pmatrix}. \tag{2.63}$$

and obtain the equation where only a_- and a_4 are coupled. Therefore, we treat the equation as a two-state problem and obtain the solutions:

$$a_+(t) = \frac{a_1(0) + a_3(0)}{\sqrt{2}}\mathrm{e}^{-\gamma t/2} \tag{2.64}$$

$$a_-(t) = \left\{ \frac{a_1(0) - a_3(0)}{\sqrt{2}}\Big[\cos\frac{\Gamma t}{2} - \frac{i\omega^{'}}{\Gamma}\sin\frac{\Gamma t}{2}\Big] + a_4(0)\Big[-i\frac{2\sqrt{2}b}{\Gamma}\sin\frac{\Gamma t}{2}\Big] \right\}\mathrm{e}^{-\gamma t/2 + i\omega^{'}t/2} \tag{2.65}$$

$$a_4(t) = \left\{ \frac{a_1(0) - a_3(0)}{\sqrt{2}}\Big[-i\frac{2\sqrt{2}b}{\Gamma}\sin\frac{\Gamma t}{2}\Big] + a_4(0)\Big[\cos\frac{\Gamma t}{2} + \frac{i\omega^{'}}{\Gamma}\sin\frac{\Gamma t}{2}\Big] \right\}\mathrm{e}^{-\gamma t/2 - i\omega^{'}t/2} \tag{2.66}$$

where

$$\omega^{'} = \omega_0 - \omega \tag{2.67}$$

$$\Gamma = \sqrt{\omega'^2 + 8|b|^2}. \tag{2.68}$$

From the equations above, we can obtain the state amplitude $a_1(t)$ and $a_3(t)$ as follows,

$$a_1(t) = \frac{1}{2}\sqrt{2}[a_+(t) + a_-(t)] \tag{2.69}$$

$$a_3(t) = \frac{1}{2}\sqrt{2}[a_+(t) - a_-(t)] \tag{2.70}$$

2.4.3 Muon Spin Polarization

The total muon spin polarization P_z equals to the expectation value of the muon spin operator $I_{\mu z}$ in terms of the state amplitudes and the spin eigenfunctions

$$P_z(t) = \langle \Psi(t) \,|\, 2I_{\mu z}/\hbar \,|\, \Psi(t) \rangle \tag{2.71}$$

$$= \sum_{i,j=1}^{4} a_i^{*} a_j \langle \chi_i^{*} \,|\, 2I_{\mu z}/\hbar \,|\, \chi_j \rangle \, \mathrm{e}^{i\omega_{ij}t} \tag{2.72}$$

where $\Psi(t)$ is the time-dependent muonium wavefunction and χ is the spin eigenfunction. In the case of low magnetic field, the muon spin polarization is written as

$$P_z(t) = |a_1|^2 - |a_3|^2 + a_2^{*}a_4\mathrm{e}^{i\omega_{24}t} + a_4^{*}a_2\mathrm{e}^{-i\omega_{24}t}. \tag{2.73}$$

The last two terms have faster component ω_{24} compared to the muon decay rate, so by averaging we can neglect the terms and obtain

$$P_z(t) = |a_1|^2 - |a_3|^2 \tag{2.74}$$
$$= 2\mathrm{Re}(a_+^*(t)a_-(t)) \tag{2.75}$$
$$= \frac{1}{2}\left(\cos\frac{\Gamma t}{2}\cos\frac{\omega' t}{2} + \frac{\omega'}{\Gamma}\sin\frac{\Gamma t}{2}\sin\frac{\omega' t}{2}\right)\mathrm{e}^{-\gamma t} \tag{2.76}$$
$$= \frac{1}{4}\left(\frac{\Gamma+\omega'}{\Gamma}\cos\frac{\Gamma-\omega'}{2}t + \frac{\Gamma-\omega'}{\Gamma}\cos\frac{\Gamma+\omega'}{2}t\right)\mathrm{e}^{-\gamma t} \tag{2.77}$$

2.4.4 Resonance Line Shape

The resonance line shape is obtained from the time integration of the muon spin flip signal. We define the signal as the difference of the number of the positrons counted with and without microwave field, i.e.,

$$S = \frac{N_{\mathrm{ON}} - N_{\mathrm{OFF}}}{N_{\mathrm{OFF}}} \tag{2.78}$$

where N_{ON} (N_{OFF}) is the number of the counted positrons when the microwave is ON (OFF).

The differential signal for a resonance line shape is defined as follows

$$\mathrm{d}S = \frac{a(y_0)P}{2}\frac{\int_{t_1}^{t_2}\left\{\frac{\Gamma+\omega'}{2\Gamma}\cos\frac{\Gamma-\omega'}{2}t + \frac{\Gamma-\omega'}{2\Gamma}\cos\frac{\Gamma+\omega'}{2}t - 1\right\}\cos\theta\mathrm{e}^{-\gamma t}\mathrm{d}t}{\int_{t_1}^{t_2}\left(1+\frac{aP}{2}\cos\theta\right)\mathrm{e}^{-\gamma t}\mathrm{d}t} \tag{2.79}$$
$$= \frac{\frac{a(y_0)P}{2}\cos\theta}{1+\frac{a(y_0)P}{2}\cos\theta}L(|b|^2,\omega',t_1,t_2) \tag{2.80}$$

where L is the microwave dependent term,

$$L(|b|^2,\omega',t_1,t_2) = \frac{1}{\mathrm{e}^{-\gamma t_1}-\mathrm{e}^{-\gamma t_2}}\times \tag{2.81}$$
$$\left[\frac{\gamma\mathrm{e}^{-\gamma t}}{\Gamma}\left\{\frac{\Gamma+\omega'}{(\Gamma-\omega')^2+4\gamma^2}\left((\Gamma-\omega')\sin\frac{\Gamma-\omega'}{2}t - 2\gamma\cos\frac{\Gamma-\omega'}{2}t\right)\right.\right.$$
$$\left.\left.+\frac{\Gamma-\omega'}{(\Gamma+\omega')^2+4\gamma^2}\left((\Gamma+\omega')\sin\frac{\Gamma+\omega'}{2}t - 2\gamma\cos\frac{\Gamma+\omega'}{2}t\right)+\frac{\Gamma}{\gamma}\right\}\right]_{t_1}^{t_2}$$

The integration of dS gives the signal

$$S = \frac{a(y_0)P}{2\int_{\mathrm{V}}\rho(r)\left[\int_{\mathrm{D}}(1+\frac{a(y_0)P}{2}\cos\theta)\mathrm{d}\Omega\right]\mathrm{d}\tau}\int_{\mathrm{V}}\rho(r)L\left(\int_{\mathrm{D}}\cos\theta\right)\mathrm{d}\Omega\mathrm{d}\tau \tag{2.82}$$

where $\rho(r)$ is the spatial distibution of the muonium, V is the volume of the microwave cavity, $d\tau$ is the volume element, and D is the solid angle covered by the positron detector.

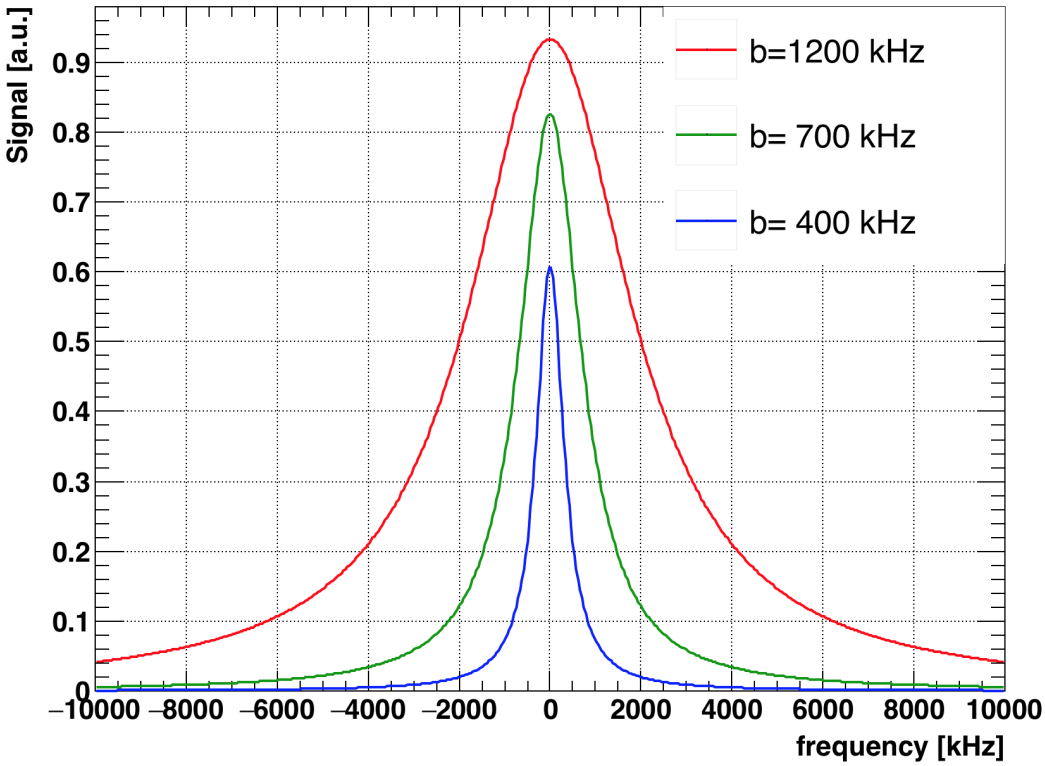

Figure 2.7: Lorentzian shaped resonance line. The lines with different colors indicate the resonance line with different values of microwave parameter b. The blue line is the resonance with $b = 400$ kHz. The green line is the resonance with $b = 700$ kHz, and the red line is the resonance with $b = 1200$ kHz. The red line has a wider width compared to the other lines, although the change in signal height is not large, deteriorating its statistical sensitivity to the determination of the resonance center. This broadening of the resonance is so-called saturated power broadening.

The integration of the microwave term L over the infinite time interval $(0, \infty)$ makes the resonance line shape a Lorentzian form as follows

$$L(|b|^2, \omega', 0, \infty) = \frac{2|b|^2(\gamma^2 + 2|b|^2)}{(\gamma^2 + 2|b|^2)^2 + \gamma^2\omega'^2} \tag{2.83}$$

Calculated resonance line is shown in Fig. 2.7. Red line corresponds to a resonance line shape with $|b| = 800$ kHz. Green and blue lines indicate the resonance when $|b| = 400$ kHz and $|b| = 1200$ kHz, respectively.

2.5 "Old Muonium" Method

The statistical sensitivity of spectroscopy of a state with a lifetime is limited by the natural line width. "Old Muonium" method is a line-narrowing technique by using the counts of the decay positron from long-lived muoniums. This method realizes a resonance line with a narrower width, at the expense of a reduced number of the

counted positrons.

The old muonium method was also applied in the precursor experiment at LAMPF [19]. The LAMPF DC beam structure forced them to chop the beam and make a quasi-pulsed beam, which reduced the statistics further. The pulsed muon beam at J-PARC enables us to use the old muonium method without chopping the beam and limiting the statistics.

We can obtain the resonance line shape from the Eq. 2.81,

$$\begin{aligned} L(|b|^2, \omega', t_1, t_2) =& \frac{1}{\mathrm{e}^{-\gamma t_1} - \mathrm{e}^{-\gamma t_2}} \frac{\gamma}{\Gamma} \times \\ & \left[A_+ \left\{ \mathrm{e}^{-\gamma t_2} (k_- \sin \frac{k_-}{2} t_2 - 2\gamma \cos \frac{k_-}{2} t_2) - \mathrm{e}^{-\gamma t_1} (k_- \sin \frac{k_-}{2} t_1 - 2\gamma \cos \frac{k_-}{2} t_1) \right\} \right. \\ & + A_- \left\{ \mathrm{e}^{-\gamma t_2} (k_+ \sin \frac{k_+}{2} t_2 - 2\gamma \sin \frac{k_+}{2} t_2) - \mathrm{e}^{-\gamma t_1} (k_+ \sin \frac{k_+}{2} t_1 - 2\gamma \sin \frac{k_+}{2} t_1) \right\} \\ & \left. + \mathrm{e}^{-\gamma t_2} - \mathrm{e}^{-\gamma t_1} \right], \end{aligned} \tag{2.84}$$

where

$$A_\pm = \frac{\Gamma \pm \omega'}{(\Gamma \mp \omega')^2 + 4\gamma^2} \tag{2.85}$$

and

$$k_\pm = \Gamma \pm \omega'. \tag{2.86}$$

Figure 2.8 shows the comparison of the line shapes when integrating all the positron signals ("conventional method") and when integrating positron signals from t_1=2 μs to t_2=6 μs. The microwave b parameter is set to be 400 kHz.

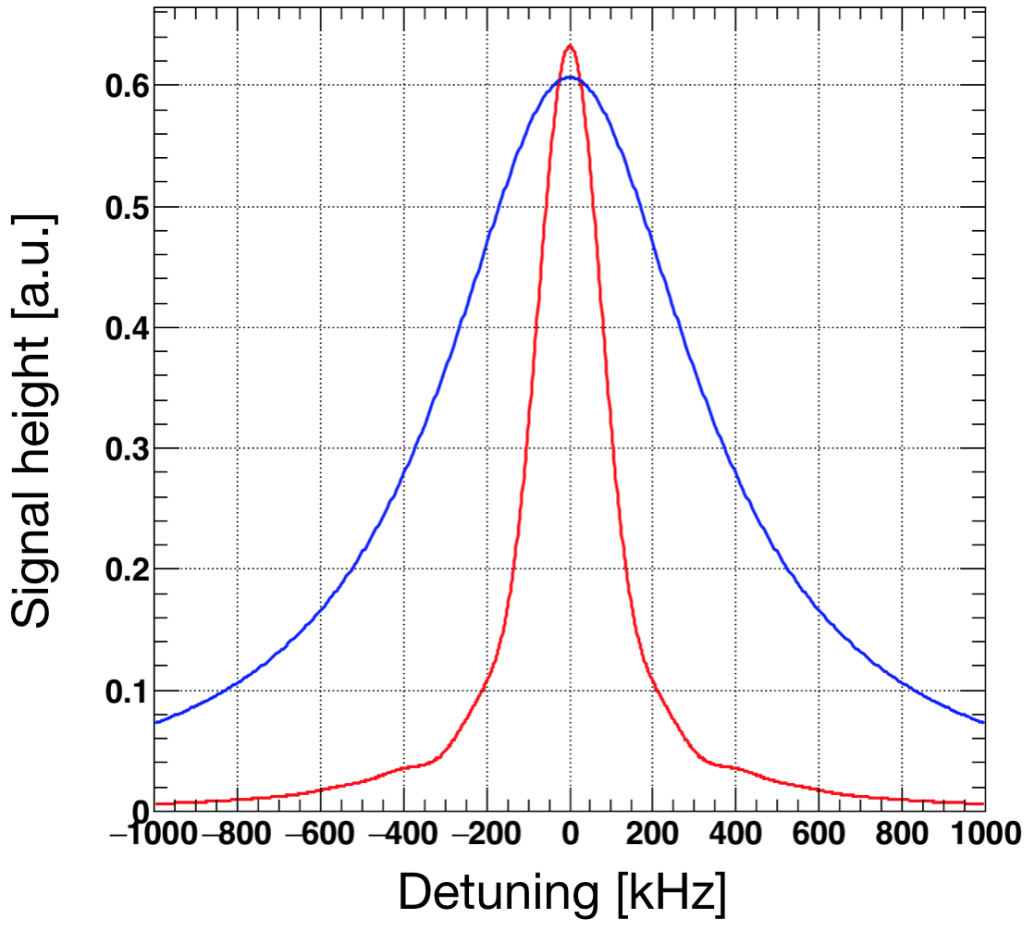

Figure 2.8: Resonance line shapes of the conventional method and the old muonium method. Blue line is the line shape of the conventional method, and the red line is the line shape from the old muonium method when t_1=2 μs and t_2=6 μs.
$|b|$ = 400 kHz.

Chapter 3

Experimental Procedure and Apparatus

In this chapter, we explain the apparatus and the procedure of the experiment. The experiment was performed at Materials and Life science Facility (MLF) of Japan Proton Accelerator Research Complex (J-PARC). We present a general overview of the experiment in the first section of this chapter, then we will present the details of each piece of the apparatus in the following sections. The section of the microwave cavity introduces the design and the development of a new microwave cavity.

3.1 General Principle

Figure 3.1 shows the schematic drawing of the experimental setup. The main components of the setup are a magnetic shield, a gas chamber, a microwave cavity, and positron detectors. The magnetic shield made of permalloy suppresses the magnetic field, which disturbs the precise spectroscopy of MuHFS. Nearly 100% polarized muon beam is injected into a gas chamber. The gas chamber contains either 0.3, 0.4, 0.7, or 1.0 atm of 99.97% pure krypton (Kr) gas. After the injection, the collisions with the Kr atoms decelerate the muon and in the end, the muon captures one electron from one of the Kr atoms, forming a muonium.

Muon in muonium decays with a lifetime of 2.2 μs. The leading decay branch (99%, [21]) is $\mu^+ \rightarrow e^+ + \overline{\nu}_\mu + \nu_e$. Since muon decay is a parity-violating decay, the decay positron is preferentially emitted in the direction of the muon spin. The initial direction of the spin of the injected muon beam is antiparallel to its momentum (upstream), so the decay positrons from muoniums also emitted toward upstream in the case of no MuHFS transition induced.

To induce the MuHFS transition, microwave is applied to a cavity which is situated in the gas chamber. If we apply microwave with a frequency corresponds to the hyperfine structure, muonium hyperfine transition occurs, and the muon spin

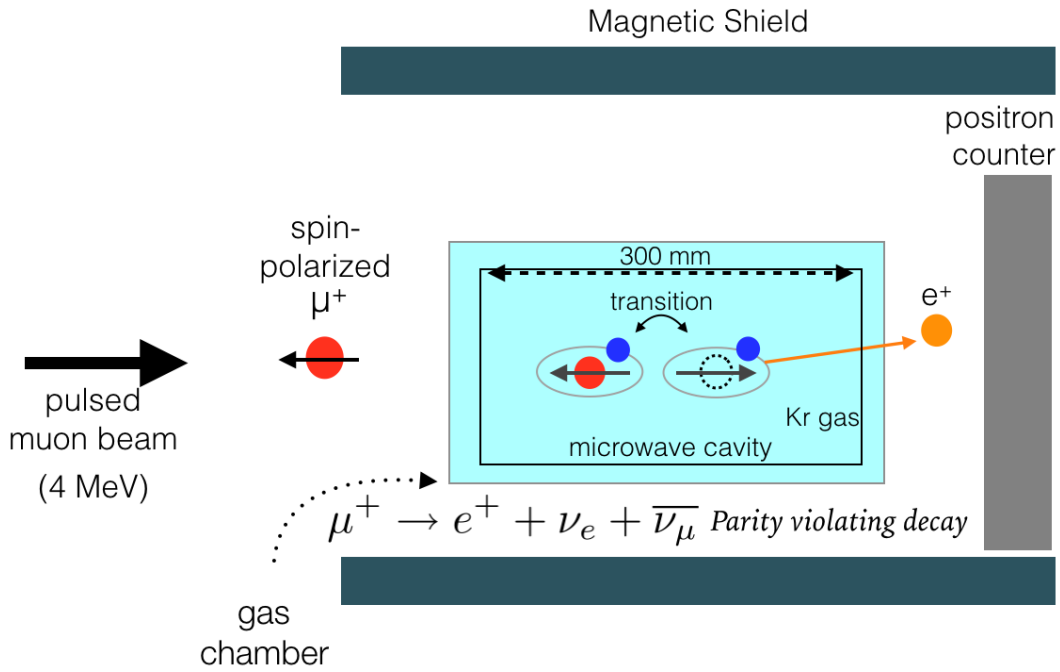

Figure 3.1: Schematic drawing of the experimental setup.

flips since the hyperfine structure is a spin-spin interaction. As a result, more decay positrons are emitted toward downstream, and the counts of the positron detectors increase. One can determine hyperfine structure frequency by counting the number of the detected positrons while sweeping the microwave frequency.

3.2 Muon Beamline

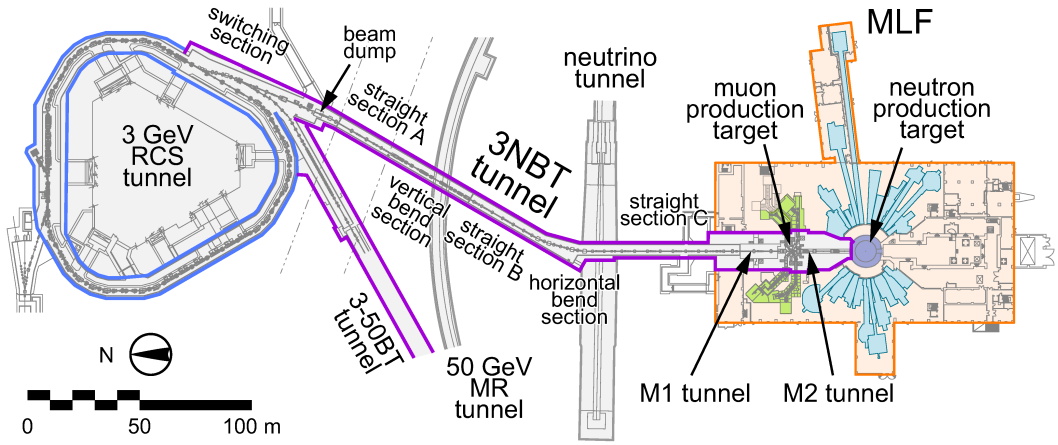

Figure 3.2: Synchrotron and MLF in J-PARC [77]. The proton beam from a linac is injected to the synchrotron, and it is accelerated up to 3 GeV before transported to the MLF hall.

In this measurement, statistics is one of the important factors for the improvement of precision. There are three major factors of muon beam which contribute to the statistics: intensity, polarization, and time structure. The first two factors are essential to increase the number of positrons and signal-to-noise ratio (S/N). The last factor is important when we try to utilize the time dependence of the muon spin flip signal, which can be used to reduce the statistical and the systematic uncertainties by the old muonium method described in the chapter 2.

We use an intense pulsed muon beam at J-PARC MLF (Fig. 3.2) [77]. A linac (not shown in the figure) and a synchrotron accelerate protons up to 3 GeV. The protons are transported to MLF. Detailed view of the beamline in the MLF hall is shown in Fig. 3.3. The repetition rate of the proton beam is 25 Hz. The proton beam from the synchrotron irradiates a muon production target made of graphite. As a consequence of nuclear spallation, positively charged pions are produced.

Some of the produced pions decay at rest on the surface of the muon production target. The two-body parity-violating pion decay

$$\pi^+ \rightarrow \mu^+ + \nu_\mu \tag{3.1}$$

emits a mono-energetic muon and the spin polarization of the muon is 100% opposite to their momenta since the helicity of neutrino is left-handed. This muon is called a "surface" muon since the muon decays from a pion at rest on the surface of the muon production target. The surface muons are transported through a solenoid and a series of magnets (indicated as D-Line in the figure) to an experimental area called area D2. The energy of the surface muon at the entrance of the experimental area depends on materials in the beamline such as a thin foil for blocking the flow of

radioactive materials from the production target. In the case of J-PARC MLF, the energy of the surface muon at the entrance of the experimental area is 3.50 MeV (momentum = 27.4 MeV/c). The operation power of the accelerator during the experiment was 500 kW.

Positrons resulting from muon decay or $e^- - e^+$ pair production by gamma rays contaminate the muon beam. To reduce the positrons, the beamline has a $\vec{E}\times\vec{B}$ separator (Wien filter, indicated as DSEP in Fig. 3.3). The directions of the static $\vec{E}$ and $\vec{B}$ fields are mutually perpendicular and both transverse to the beam. The separator only pass through particles with a velocity

$$v = \frac{E}{B}. \tag{3.2}$$

The beamline magnets are tuned for particles with 27.4 MeV/c momentum, so the positrons and the muons in the beam have different velocities. The strength of the fields is set to pass only muons while vertically bending the trajectory of the positrons.

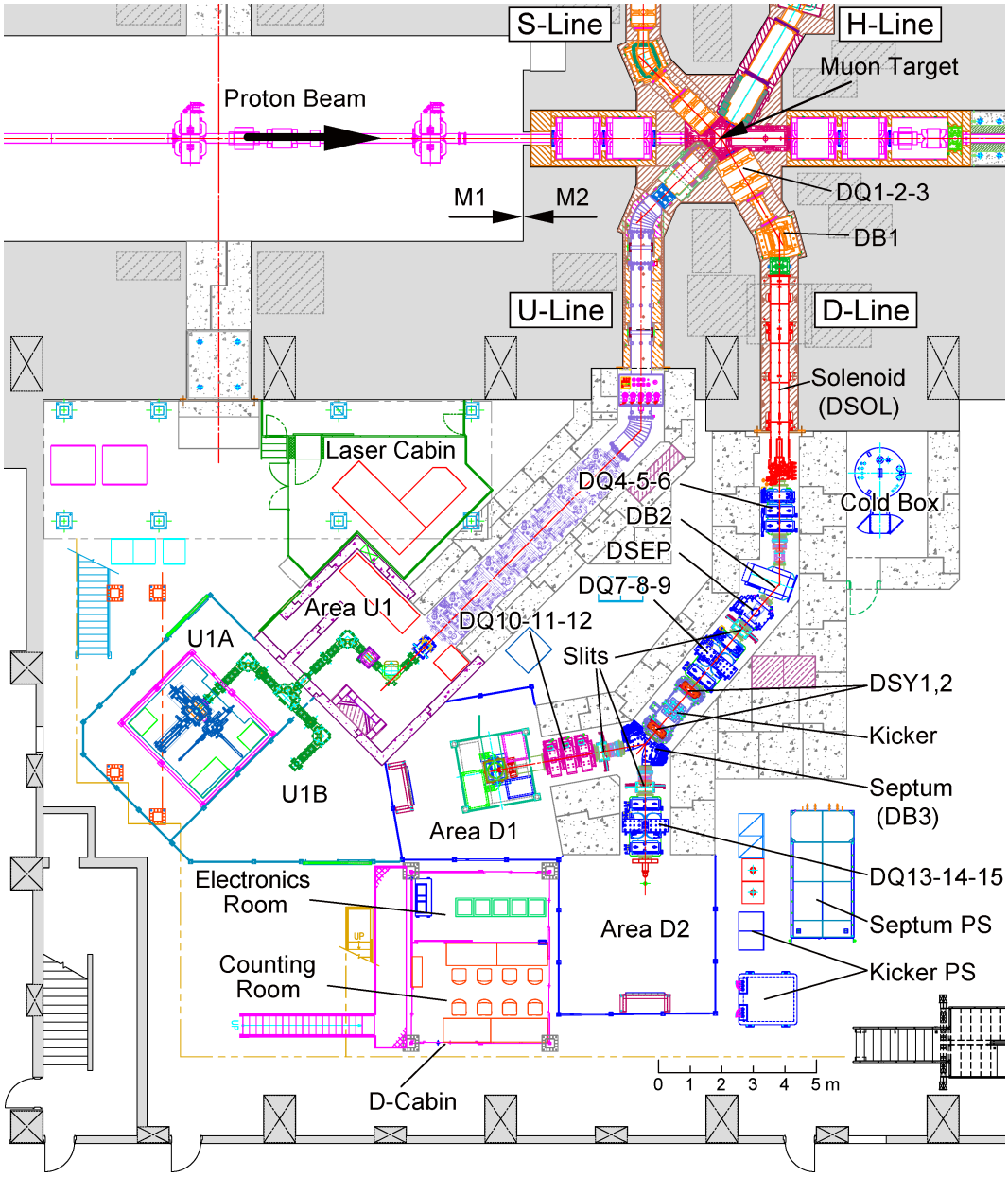

Figure 3.3: Detailed view of the beamline in the MLF hall [77]. The proton beam irradiates the muon production target (upper right), and four different beamlines extract produced muons. The beamline D has two branches and experimental areas, area D1 and area D2. The experiment was conducted at area D2.

3.3 Magnetic Field

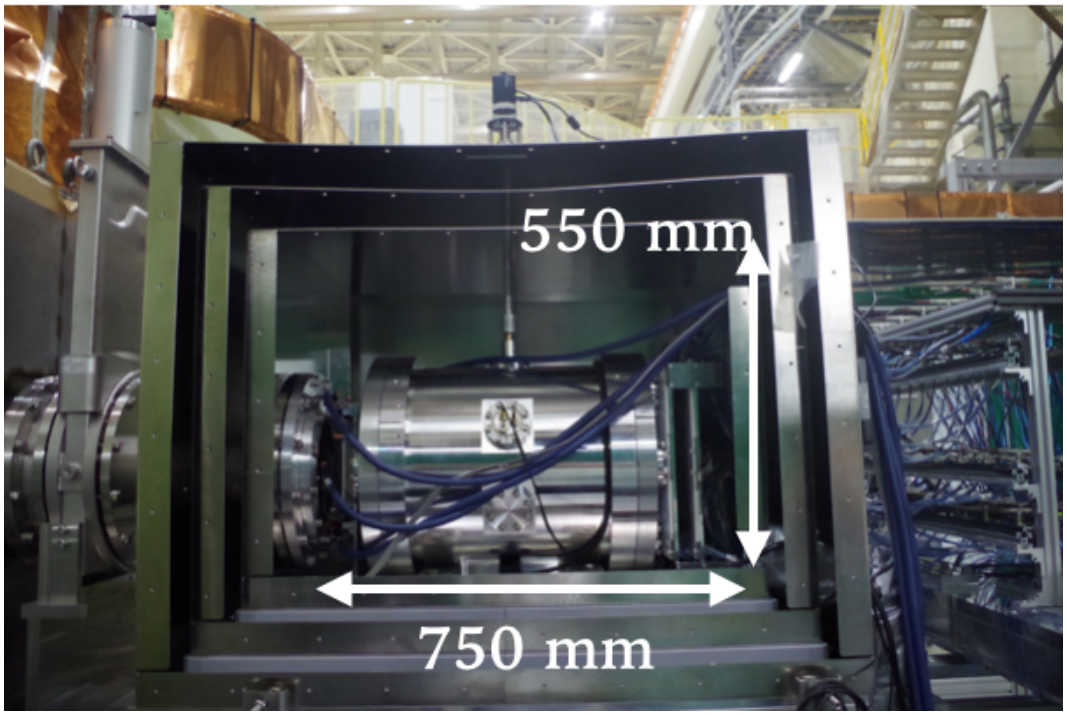

Figure 3.4: Magnetic shield made of three layers of permalloy box. The muon beam is injected from the left-hand side. The shield contains the gas chamber and the positron detectors. The dimension of the inner volume of the smallest box is 750 mm×550 mm×550 mm.

In the presence of an external magnetic field, the muonium spin rotates. The gyromagnetic ratio of the muonium is roughly a half of the gyromagnetic ratio of the electron,

$$\gamma_{\mathrm{e}} = 176 \text{ GHz/T}, \tag{3.3}$$

$$\gamma_{\mathrm{Mu}} = 88 \text{ GHz/T}. \tag{3.4}$$

Under the magnetic field of 1 mG = 100 nT, the muonium spin precess at the rate of $\gamma_{\mathrm{Mu}} \times 10^{-7}/2\pi = 1.4$ kHz. The rate corresponds to the rotation of muonium spin of 1° in the muon lifetime, 2.2 μs.

In the experimental area D2, the magnetic field was measured to be ≈ 100 μT, which is too strong for the measurement. The main sources of the magnetic field are the Earth's terrestrial magnetism, the beamline magnets and magnetized structures under the floor of the experimental area.

To suppress the background field in the experimental area, we place three layers of the permalloy box as a magnetic shield (Fig. 3.4). The high permeability of permalloy prevents the magnetic flux from entering inside the shield box. The box was designed to contain the whole apparatus, including the gas chamber and the

positron detectors. The size of the inner volume of the smallest layer is 750 mm × 550 mm × 550 mm. The shield has one through-holes with a diameter of 120 mm for a duct for extension of the beamline to extract the muon beam without losing muons due to the scattering with air. The duct is shown in Fig. 3.5. There are also four square-shaped apertures (100 mm square for each) for the cables of the detectors and the microwave system.

Before and after the installation of the shield, we measured the magnetic field inside the shield. Figure 3.6 [78] shows the results of the measurements. The blue triangle points indicate the magnetic field strength without the shield, measured at the center of the beamline axis. The red circle points are magnetic field strength in the cavity, measured at the center of the cavity (which is aligned to the center of the beamline axis). The field is well suppressed to a few of 100 nT, which is sufficient for the spectroscopy.

The magnetic field was measured by a three-axis fluxgate probe. We use a commercially available fluxgate probe (MTI FM-3500, Fig. 3.7). The probe is a cube with a side of 35 mm. It contains three coils inside. Each coil is 30 mm long and measures a field along one axis. The resolution (0.5 nT) and the linearity (0.5% for 1000 nT scale) of the probe are sufficiently precise for the measurement. The typical variation of the magnetic field inside the shield is ≈ 20 nT and it is negligible.

We scanned the residual magnetic field distribution inside the cavity by the fluxgate probe. Figure 3.8 shows the cross-sectional view of the measurement. We insert the probe in the cavity, and we scan the probe position by rotating the probe tilting angle theta. The result is shown in Fig. 3.9. The probability distribution of the residual magnetic field felt by muonium ensemble in the cavity is calculated by the field distribution and the muonium distribution in the cavity. The probability distribution is shown in Fig. 3.10. The magnetic field felt by the muoniums are mostly less than 300 nT, which is sufficient for the spectroscopy.

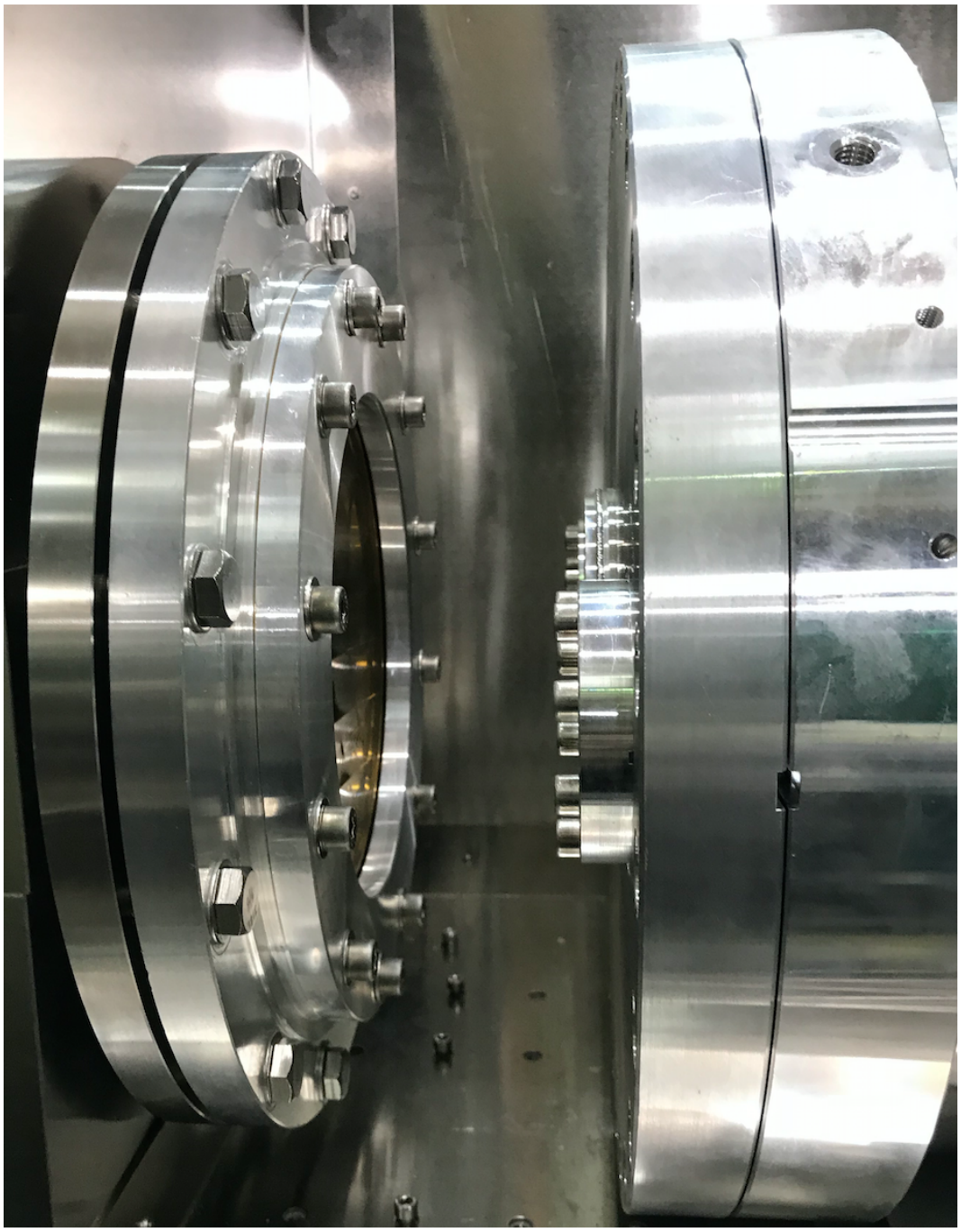

Figure 3.5: A pipe duct for beam extension (left). The duct end is covered by a sheet of 75 μm polyimide film. The distance between the duct end and the foil on the gas chamber (right) is 10 cm.

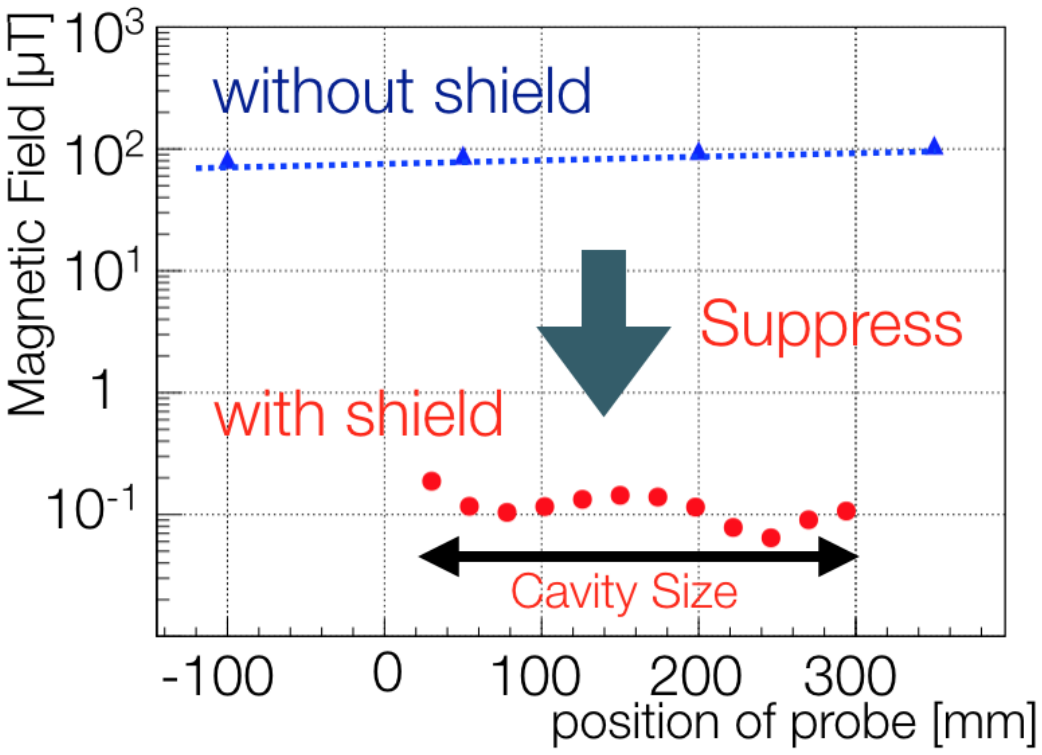

Figure 3.6: Comparison of the magnetic field in the experimental area with and without the shield [78]. The blue triangle points indicate the magnetic field strength without the shield, measured at the center of the beamline axis. The red circle points are magnetic field strength in the cavity, measured at the center of the cavity (which is aligned to the center of the beamline axis). The magnetic field is suppressed by approximately a factor of 1000.

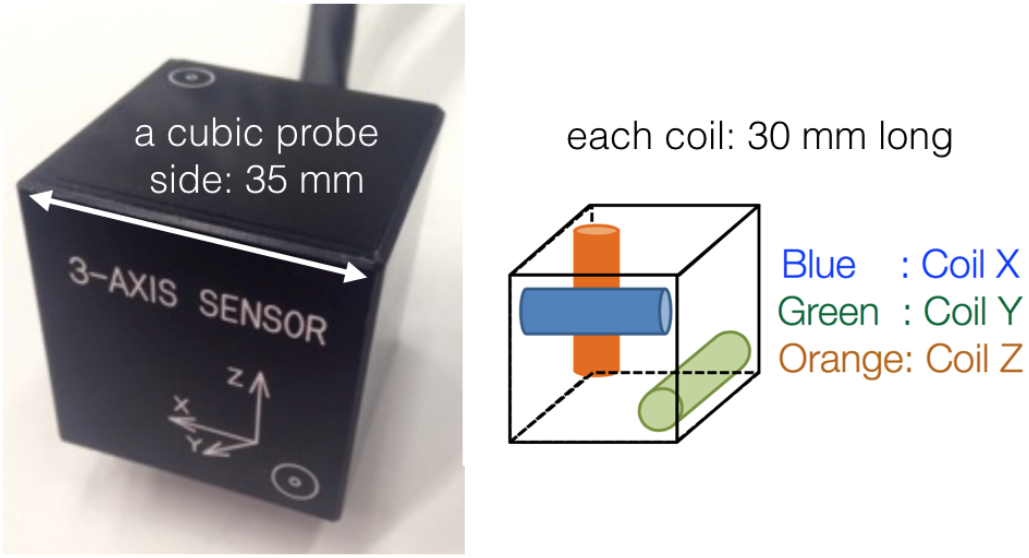

Figure 3.7: Fluxgate probe: a cubic probe with a side of 35 mm. Three coils for the measurement of magnetic flux for each axis. A coil is 30 mm long.

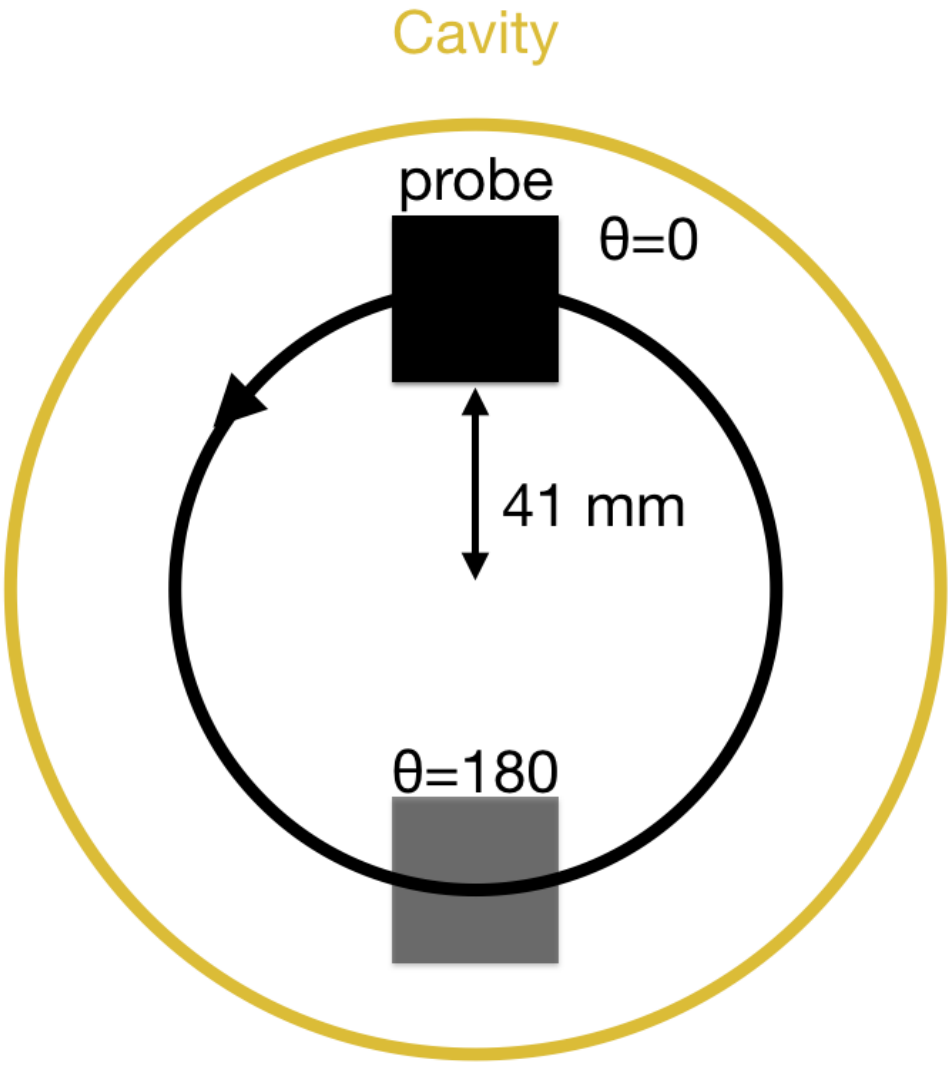

Figure 3.8: Schematic drawing of magnetic field measurement.

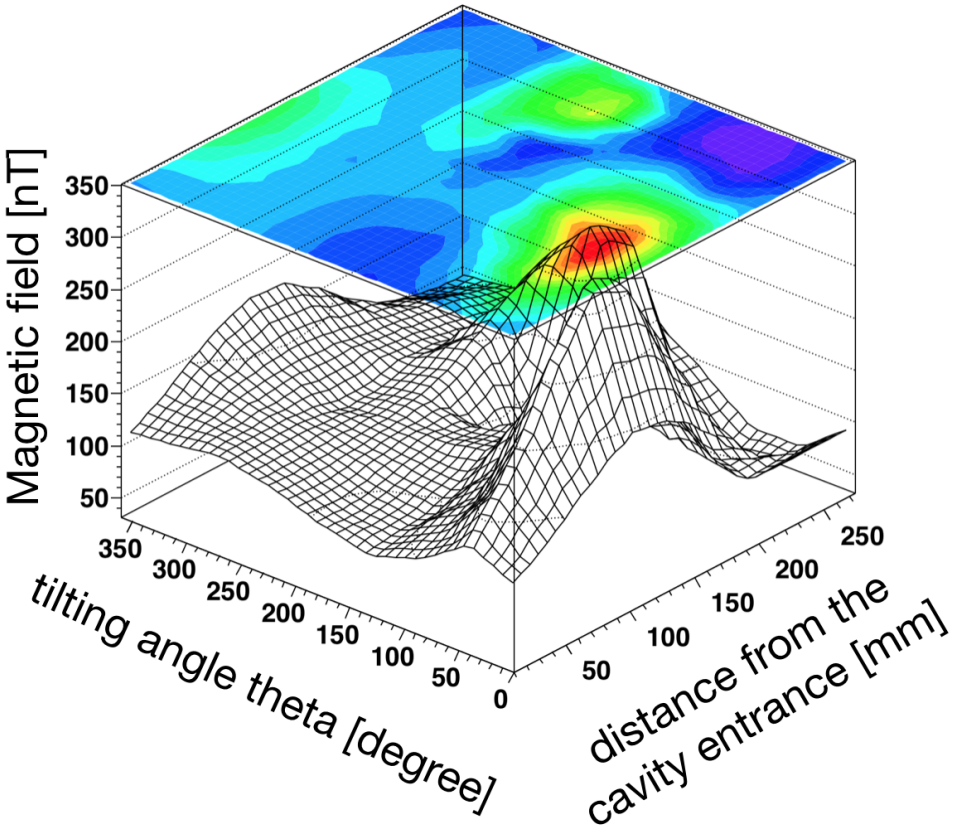

Figure 3.9: Magnetic field distribution in the cavity [78]. To scan the field in a broader volume, the probe was intentionally placed off from the beamline and the cavity center. The offset from the center was 41 mm. Tilting angle indicates the tilting angle of the probe position. When the probe is placed on the point 41 mm vertically above the center of the cavity, the angle is zero. When the probe is 41 mm under the center, the angle is 180 degree. The other horizontal axis shows the distance between the probe position and the cavity entrance, i.e., the cavity foil.

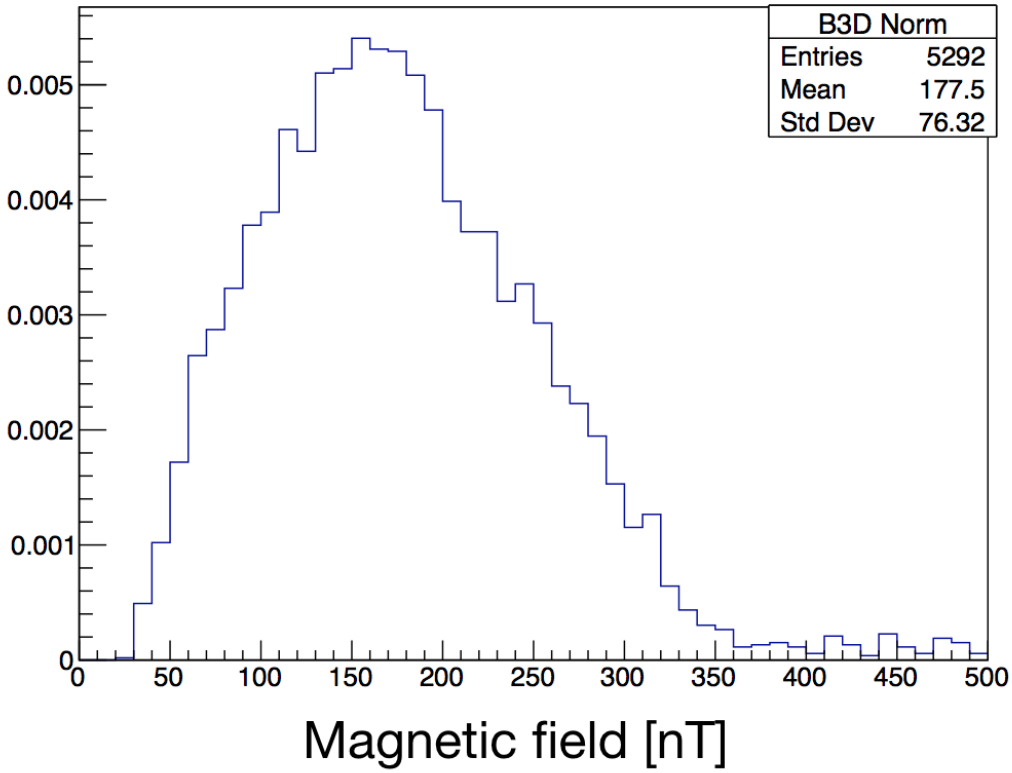

Figure 3.10: The probability distribution of the residual magnetic field felt by muonium in the cavity [78]. The horizontal axis is magnetic field in nT.

3.4 Gas System

The gas system is composed of a gas chamber, a gas handling panel, a mass spectrometer (Q-MASS), and ancillary apparatus. A layout of the gas system is shown in Fig. 3.11. The gas pressure is monitored by a capacitance gauge at the gas handling panel. The precision of the gauge is 0.2%. Inside the gas chamber, there are thermocouples to monitor the gas temperature.

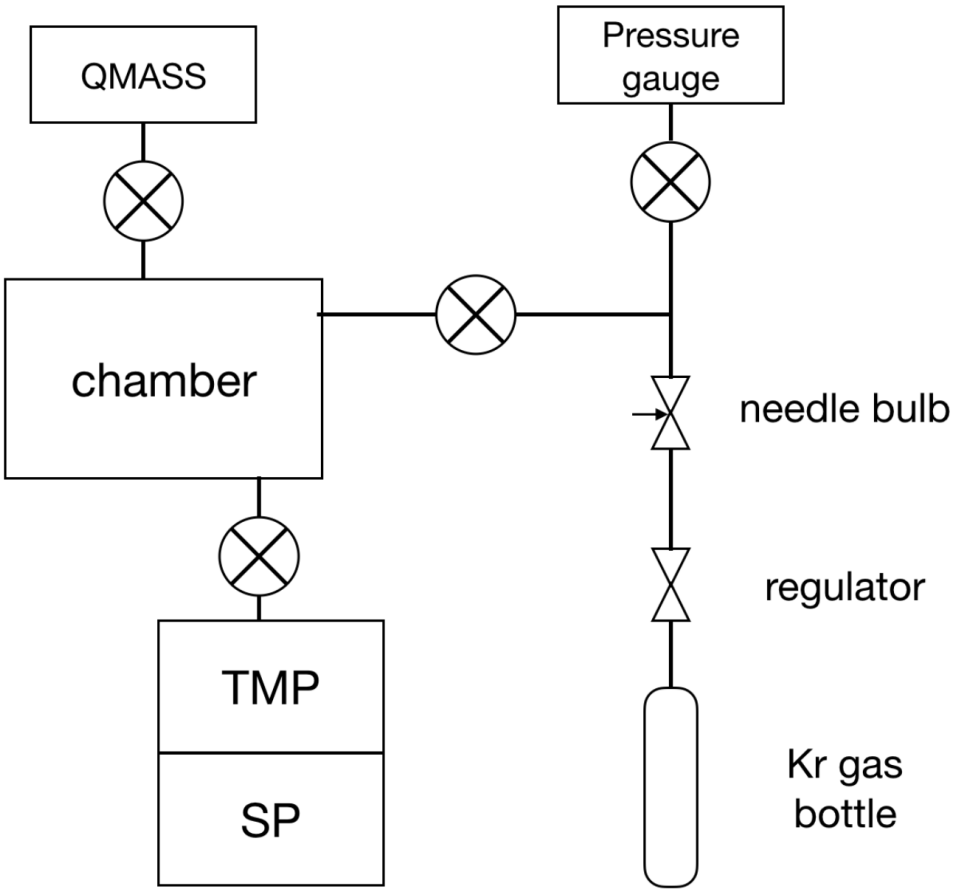

Figure 3.11: The diagram of the gas system. SP indicates a scroll pump and TMP is a turbo molecular pump. Kr gas is supplied to the chamber from a Kr gas bottle through a gas handling panel. The pressure is monitored by a gauge on the panel. QMASS measures the impurity in the gas.

The gas chamber is shown in Fig. 3.12. The cylindrical chamber is made of aluminum A2219, which is a less magnetic aluminum alloy. The chamber can be tolerable for various pressures from vacuum to 2.0 atm pressure. During this research, we use krypton gas with a pressure of either 0.3 atm, 0.4 atm, or 0.7 atm. For the muon beam entrance, there is a foil in the center of the upstream flange. The shape of the foil is a circle 10 cm in diameter and 0.1 mm in thickness (Fig. 3.13). The foil is made of aluminum A1050. The thickness of the other part of the upstream

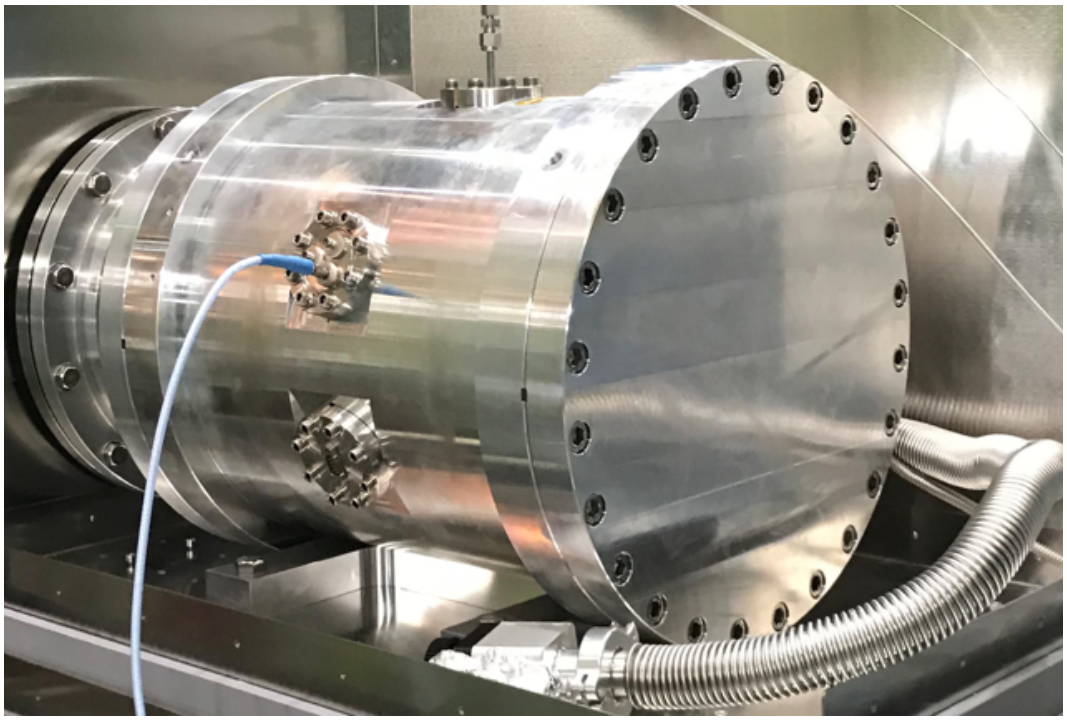

Figure 3.12: Gas chamber

flange is 40 mm. The downstream flange serves also as an absorber for background positrons contaminated in muon beam in order to improve the signal-to-noise ratio. The thickness of the downstream flange is 55 mm.

The polarization of the muonium is a key factor for the measurement. Spin exchange of the muonium and other paramagnetic impurities, such as oxygen molecule, depolarize the muonium. The contamination of O_2 at a level of a few ppm might destroy the resonance signal. To reduce the impurity, we bake the chamber and the panel with at 150 °C for 24 hours. After the baking, the chamber and the panel are evacuated first by a scroll pump (SP) and then by a turbo molecular pump (TMP) to $\approx 10^{-5}$ Pa. The whole gas system is then filled with krypton gas. To reduce the effect of the impurity, krypton gas in the chamber is exchanged once a day.

The temperature of the gas in the chamber is monitored by a thermocouple. Since there is no water cooling available for the current setup, over the scan of a resonance curve, the fluctuation of the temperature is about 1 °C. The systematic effect from the fluctuation of the temperature will be discussed in the chapter 5.

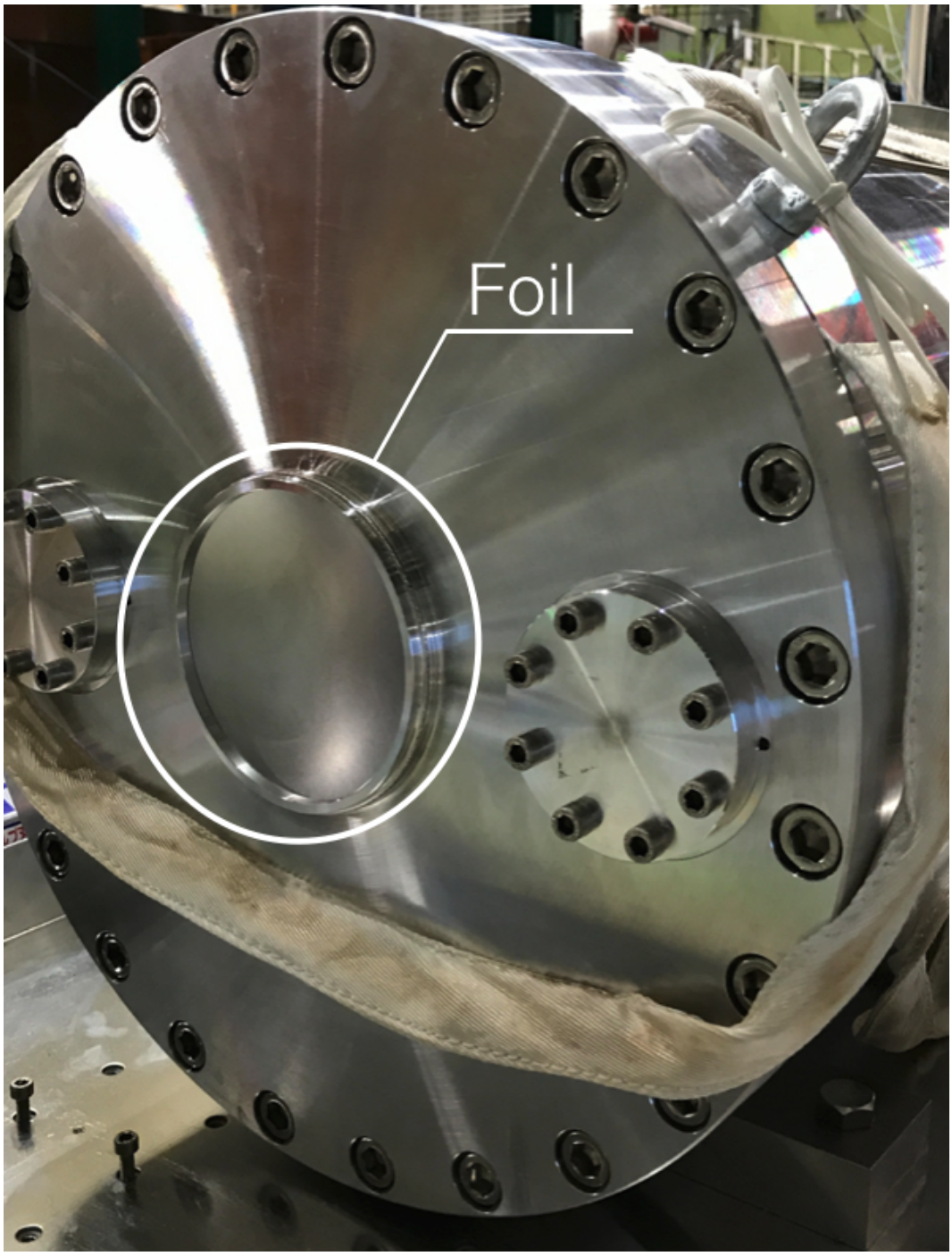

Figure 3.13: Aluminum foil for the forward flange of the gas chamber. The muon beam is injected through this foil. To avoid the loss of the muon from scattering, the thickness of the foil is suppressed to 0.1 mm.

3.5 Microwave System and Cavity

3.5.1 Microwave Circuit

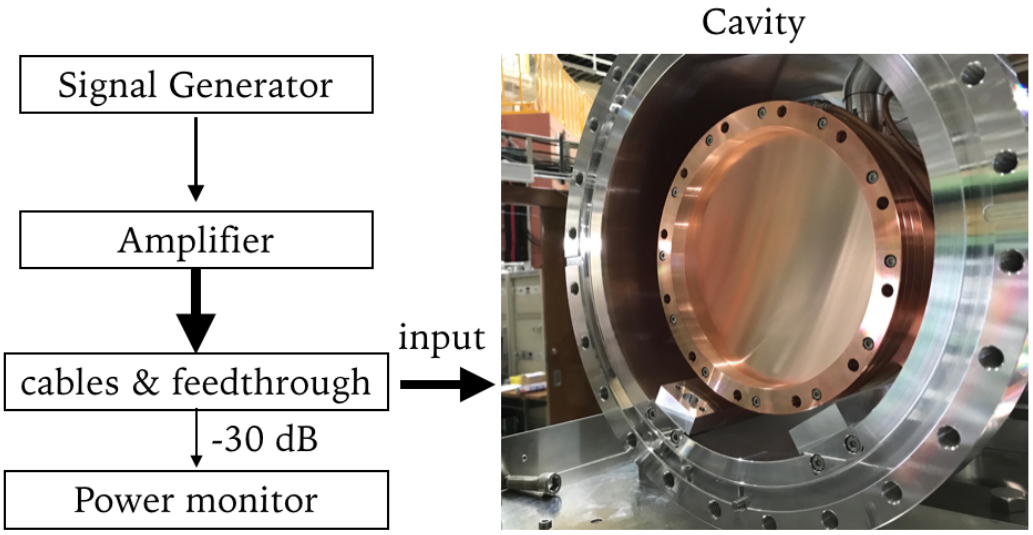

Figure 3.14: A schematic drawing of the microwave system. A microwave from a signal generator is amplified, then fed to the cavity. The small portion of the power is measured by a power monitor, and the total power induced at the cavity is determined.

To induce the hyperfine transition, microwave with a frequency near 4.46 GHz is used. A schematic view of the microwave system is shown in Fig. 3.14. The microwave is generated by a signal generator (R&S SMB 100A, with the option of SMB-B106) and amplified by four amplifiers (mini-circuit ZVE-8G+). The signal generator has an oven-controlled crystal oscillator (OCXO) as the frequency reference (frequency error is less than 10^{-8}). Each amplifier is attached to a heat sink to suppress the temperature increase of the amplifier. After the amplification, the microwave power is approximately 8 W.

After the amplification, the microwave was divided into a small fraction (-30 dB) using a directional coupler (PE2203-30) and the small fraction is monitored by a power detector (R&S NRP18T or mini-circuit ZX47-55-S+). The remaining microwave is supplied to the cavity through co-axial cables and a feedthrough flange on the chamber. We feed the microwave through a loop-antenna inside the wall of the cavity (Fig. 3.15). Due to the power loss during the propagation, the microwave power at the entrance of the cavity is approximately 1.0 W.

In order to reduce a systematic effect from the drift of the number of muons in one pulse, microwave is switched every pulse, as shown in Fig. 3.16. This switching

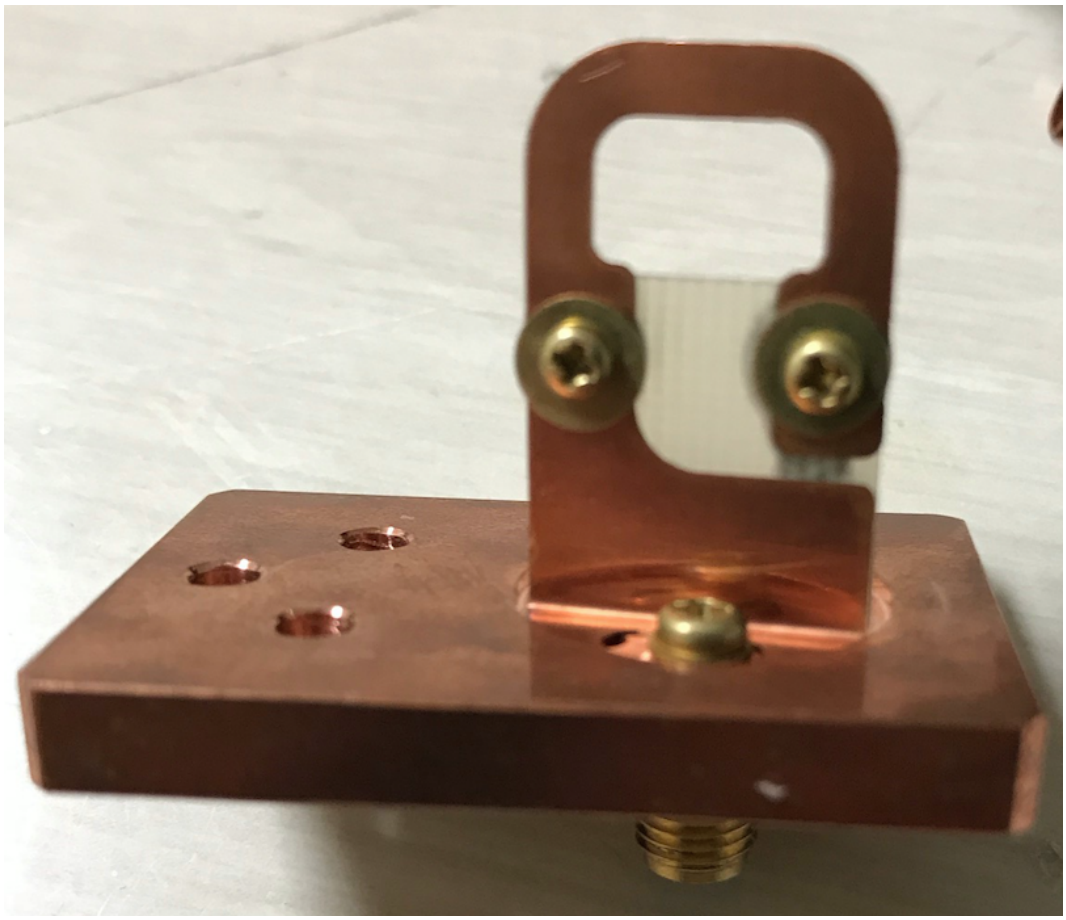

Figure 3.15: A loop-antenna for microwave input. The antenna is attached to the cavity by a supporting board also made of copper. The board also serves as a small portion of the cavity wall and can be fixed by three screws. We feed microwave through an SMA connector on the other side of the board.

sequence also reduces the heating of the cavity due to the energy loss at the cavity surface, compared to the case the microwave is always ON. The heating expands the cavity and changes the frequency characteristics of the cavity, and effective microwave energy stored in the cavity. The reduction of heating also suppresses the related systematic effect.

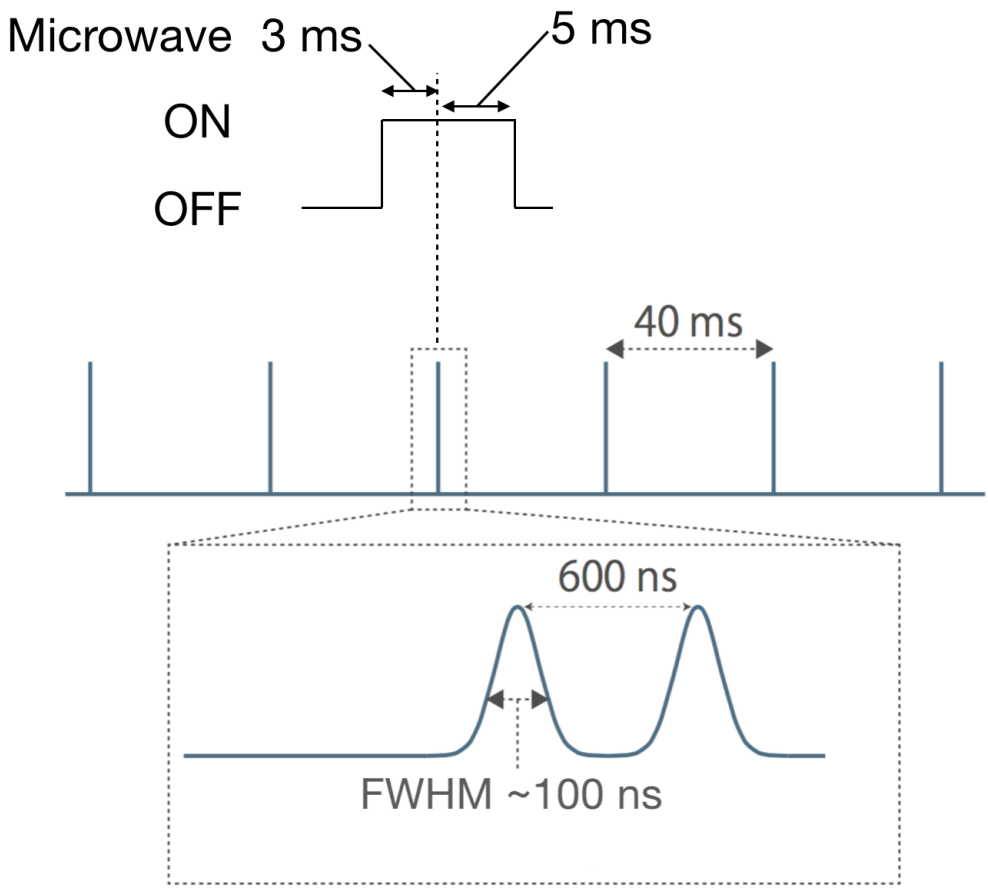

Figure 3.16: Schematic drawing of the microwave switching sequence. To reduce systematic effects, microwave is switched ON or OFF for every pulse. Also, this sequence reduces the heating of the cavity due to the microwave loss at the cavity surface.

3.5.2 Microwave Cavity

We will describe two different cavities, but they share some similarities. They are all cylindrical and they are made of oxygen-free copper with a purity of 99.97%. To suppress the injected muon loss while containing the microwave efficiently, a copper foil with a thickness of 25 μm is attached to each end of the cavities.

As mentioned in the Sec. 1.4.2, our pilot measurement found the loss of the statistical power since many muons stopped in the wall of the cavity. The old cavity with TM110 mode has a diameter of 81 mm. To prevent injected muons from stopping in the wall of the cavity and increase the statistical sensitivity of the experiment, we develop a larger cavity with TM220 mode.

The new cavity with TM220 mode was designed with another purpose, which is to enable us to measure MuHFS with lower Kr gas pressures. The old TM100 cavity has a longitudinal length of 230 mm. The lower the Kr pressure is, the wider the muon longitudinal distribution inside the cavity becomes. Consequently, more muons stop on the foils at each end of the cylindrical cavity. To achieve the measurement at lower gas pressures without losing the muons by stopping in the cavity foils, we decided to design the new cavity with a larger length.

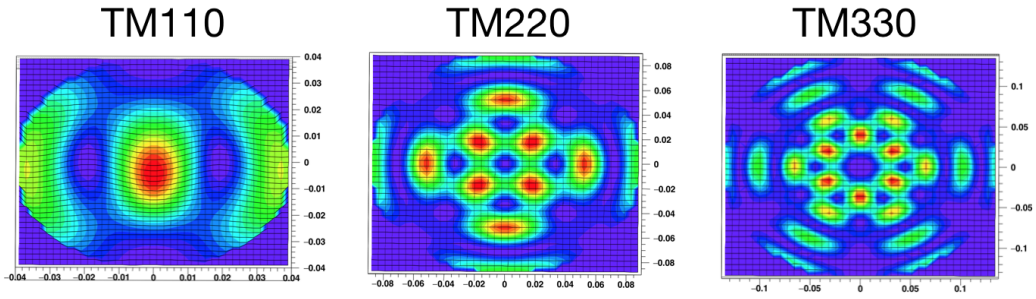

Figure 3.17: Magnetic field distribution for different TM modes calculated from analytical equation. The red color indicate strong magnetic field, and the blue color indicate weak magnetic field.

In general, a cavity with higher resonance mode and longer length suffers mode interferences from adjacent resonance modes. We have to confirm the frequency of the TM220 mode is well isolated from the frequencies of other modes before making a cavity. The resonance frequency of the TM mode in ideal case is written by

$$f_{nmp} = \frac{c}{n}\sqrt{(\frac{x_{mn}}{\pi D})^2 + (\frac{p}{2L})^2}, \tag{3.5}$$

where n, m, p are subscripts describing TM npm mode, c is the speed of light, D and L are the diameter and the longitudinal length of the cavity, and x_{mn} is the n-th root of the Bessel function $J_m(x)$. The magnetic field distributions for different TM modes are shown in Fig. 3.17. For our experiment, we need to vary the resonance

frequency in order to obtain the resonance curve. We insert a tuning rod made of aluminum and vary the position of the rod to effectively alter the diameter of the cavity. Therefore, we should also consider the effect of the tuning rod for various positions. We use CST microwave studio by Computer Simulation Technology to simulate the resonance frequency in order to determine the diameter and the length of the new cavity, and to confirm the frequency is tunable by the rod and the resonance frequency is isolated by other modes.

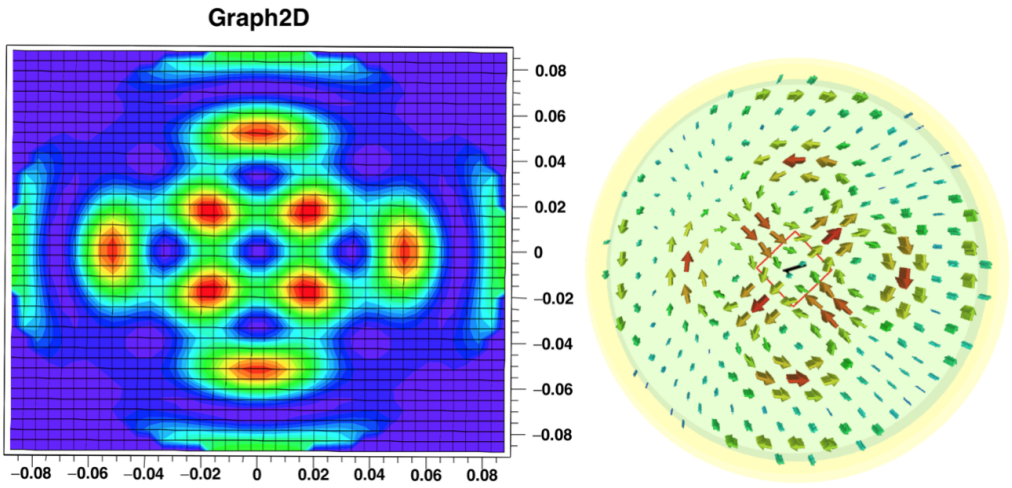

Figure 3.18: Magnetic field strength calculated from analytical equation for the ideal TM220 mode cavity (left) and the simulated magnetic distribution (right). For the left figure, the red color indicate strong magnetic field, and the blue color indicate weak magnetic field. For the right figure, larger arrow indicates stronger magnetic field.

We started the simulation with the ideal case, no tuning rod inside. The magnetic field simulation agrees the field calculated from the analytical equation, as shown in Fig. 3.18. Then we simulated the resonance frequencies of cavities with different diameters and lengths, varying the position of the tuning rod. The result in the case of $D = 93$ mm and $L = 300$ mm is shown in Fig. 3.19. The vertical axis shows the frequency offset from 4462 MHz and the horizontal axis indicates the relative position of the tuning rod, positive value meaning the rod is more inside the cavity. The red points indicate the resonance frequency of the TM220 mode, and the blue points indicate the resonance frequencies of the adjacent modes. The 4 MHz isolation in the worst case is sufficient for the measurement. The dashed black line indicates the frequency scan range (4 MHz), which is much larger than the natural linewidth (145 kHz) expected from the muon life. It was confirmed that we can tune the resonance frequency of TM220 mode and cover the required scan range by moving the tuning rod.

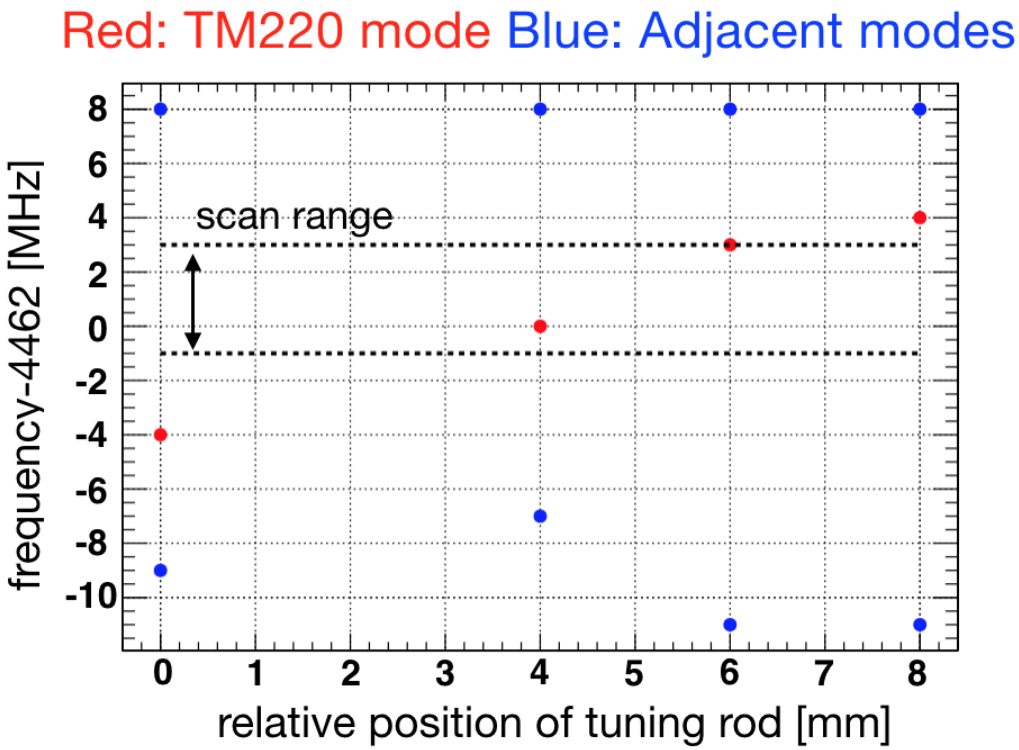

Figure 3.19: Simulation result of the mode isolation of a new cavity. The vertical axis shows the frequency offset from 4462 MHz and the horizontal axis indicates the relative position of the tuning rod, positive value meaning the rod is more inside the cavity. The red points indicate the resonance frequency of the TM220 mode, and the blue points indicate the resonance frequencies of the adjacent modes. The TM220 mode is isolated from the adjacent modes by more than 4 MHz. The dashed black line indicates the frequency scan range (4 MHz), which is much larger than the natural linewidth (145 kHz) expected from the muon life. The TM220 mode is isolated from the adjacent modes by more than 4 MHz.

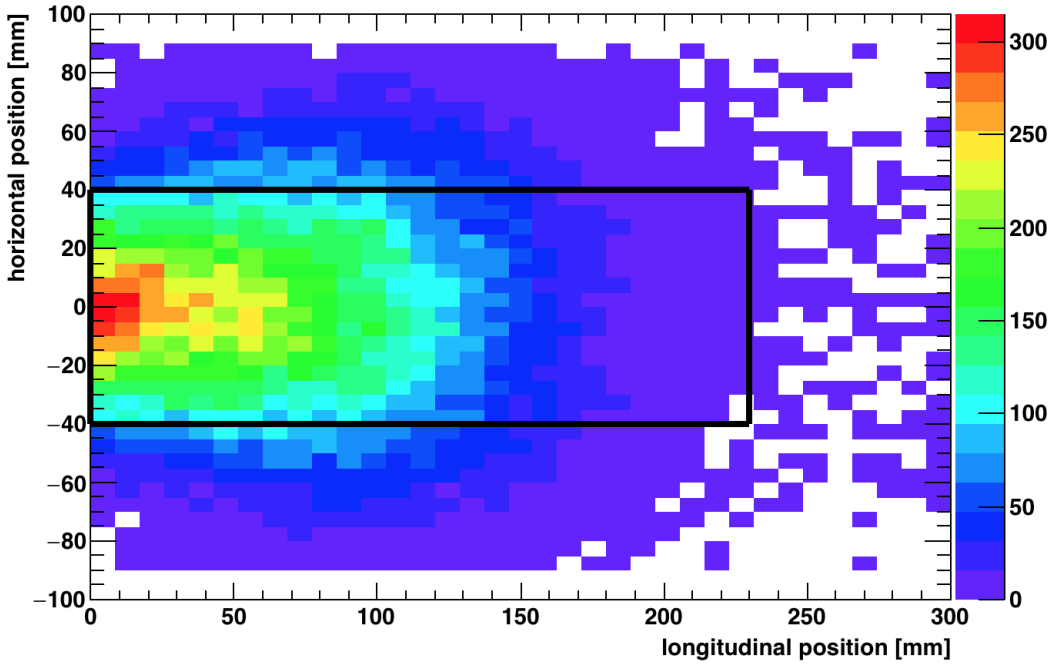

Figure 3.20: Simulated distribution of the muon stopping position inside the TM220 cavity using GEANT4 in the case of Kr pressure = 1.0 atm. The color spectrum indicates the number of the muon stopped at 1 mm × 1 mm area per pulse. The black line indicates the dimension of the old TM110 cavity.

We compare the stopping distribution of the muon inside the cavities using a simulation using GEANT4 [79]. The simulation is validated by the muon beam profile measurement, which will be described in Appendix A. Figure 3.20 shows the muon stopping distribution inside the TM220 cavity when the muon momentum is 27.4 MeV/c. The color spectrum in z-axis shows the number of the muon stopped at 1 mm × 1 mm area per pulse. The black line indicates the dimension of the old TM110 cavity. In the case of the old TM110 cavity, only 40% of the injected muon stop inside the cavity, while 90% of the muon stop inside the new TM220 cavity. Figure 3.21 is the muon distribution when Kr pressure is 0.3 atm and the muon momentum is 26.5 MeV/c. Only 21% of the injected muon stop in the TM110 cavity, while 61% stop inside the TM220 cavity.

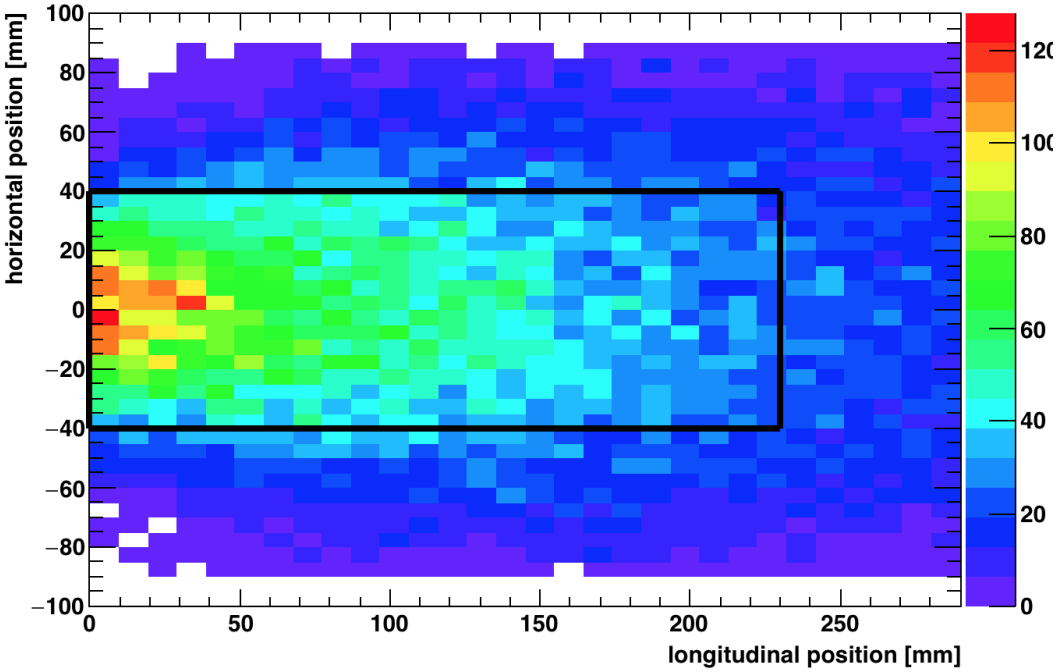

Figure 3.21: Simulated distribution of the muon stopping position inside the TM220 cavity using GEANT4 in the case of Kr pressure = 0.3 atm. The color spectrum indicates the number of the muon stopped at 1 mm × 1 mm area per pulse. The black line indicates the dimension of the old TM110 cavity.

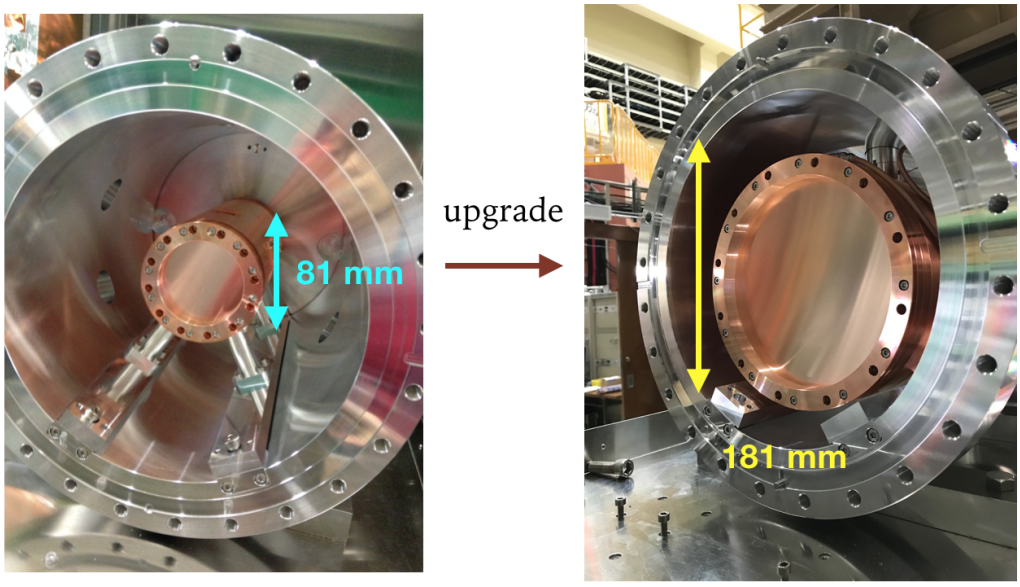

Figure 3.22: Comparison of the old TM110 cavity and the new TM220 cavity.

After the confirmation of the statistical improvement using GEANT4, we made the new TM220 cavity. The comparison of the two cavities is shown in Fig. 3.22. We measured the frequency characteristic of the new cavity using a Vector Network Analyzer (VNA). We tune the resonance frequency by varying the position of the tuning rod, which is attached to a piezo motor (Fig. 3.23). Figure 3.24 shows the inside of the cavity installed in the gas chamber. By measuring the reflections and transmissions of an input port and an output port, we can determine the frequency characteristics and the Q value of the cavity (Fig. 3.25). The Q value is an index which indicates how well the microwave energy is stored in the cavity. Figure 3.26 shows the resonance frequency of the cavity when the tuning rod is moved. The range covered by the resonance frequency is sufficiently broad to realize the MuHFS measurement.

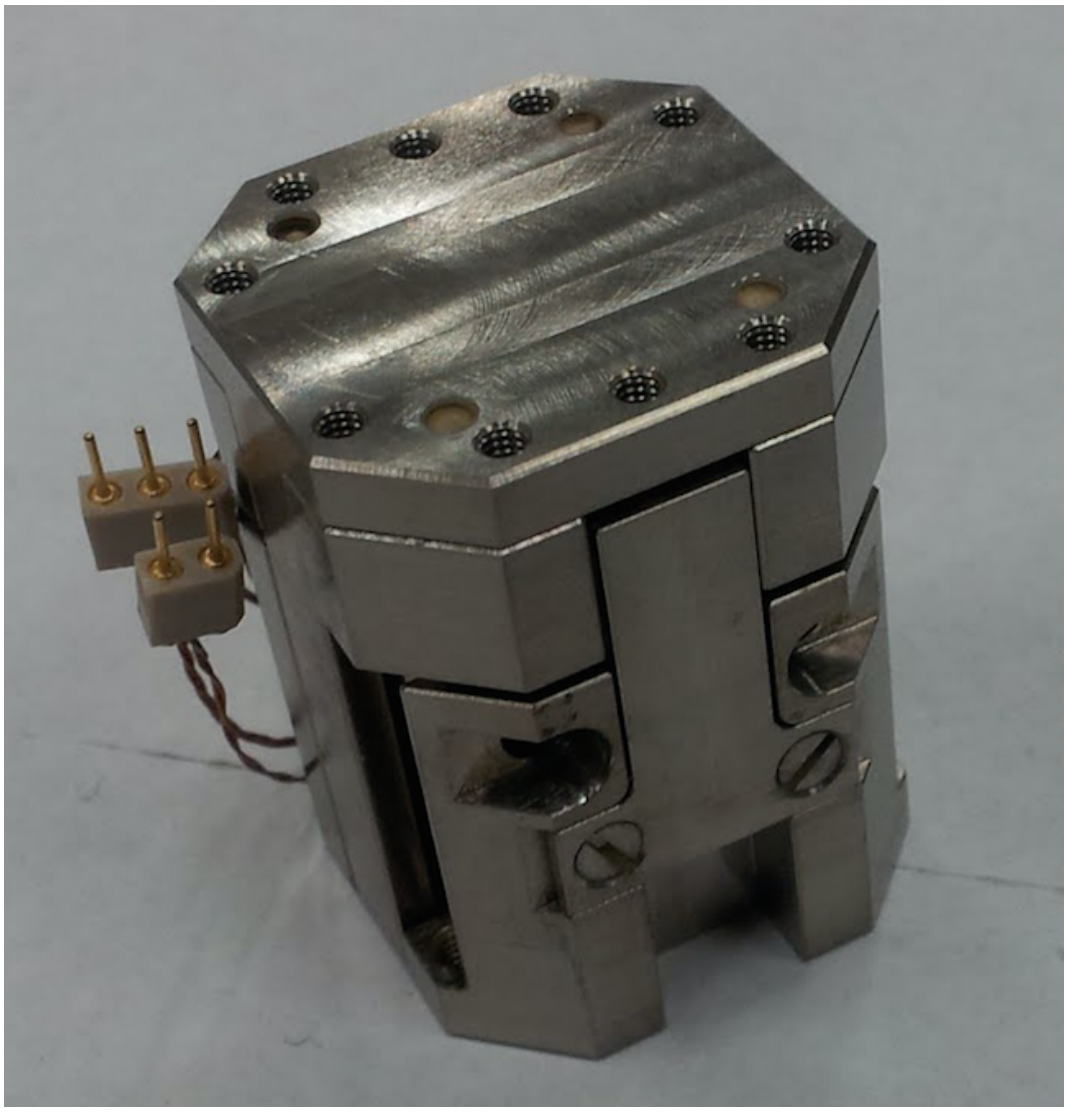

Figure 3.23: Piezo motor used for tuning the resonance frequency of the cavity

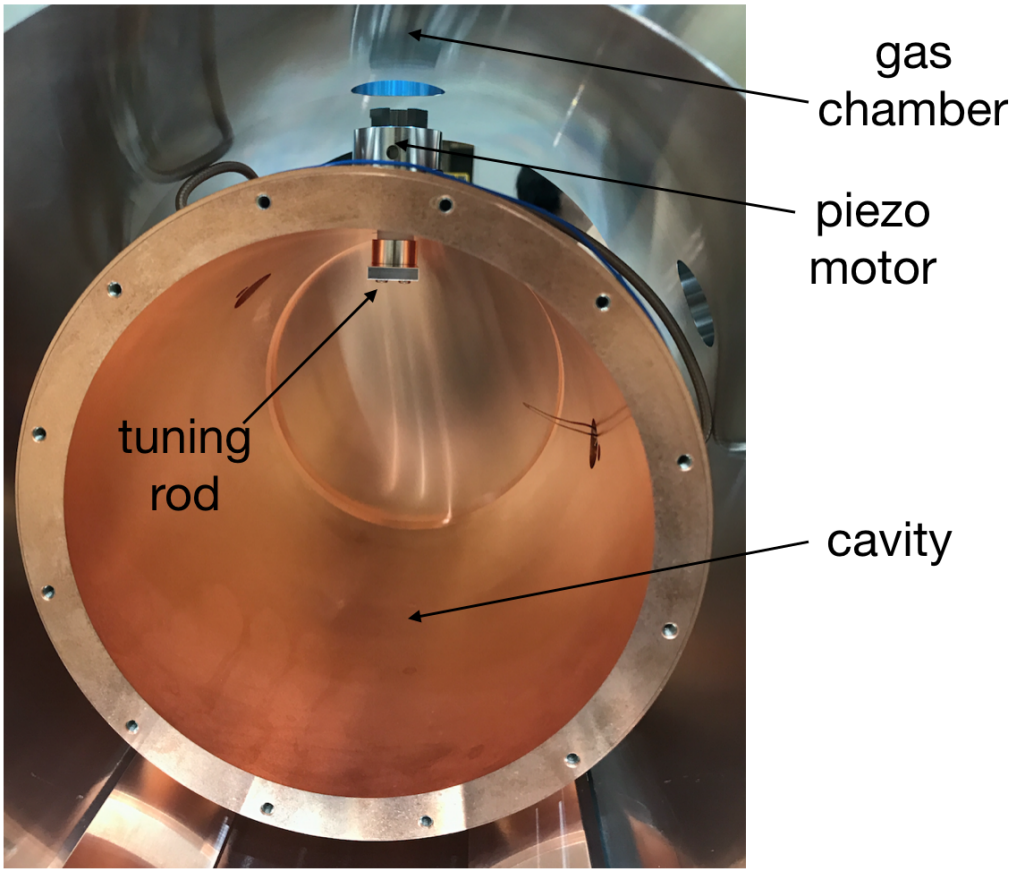

Figure 3.24: Inside of the cavity. The tuning rod is attached to the piezo motor which is cover by an aluminum container.

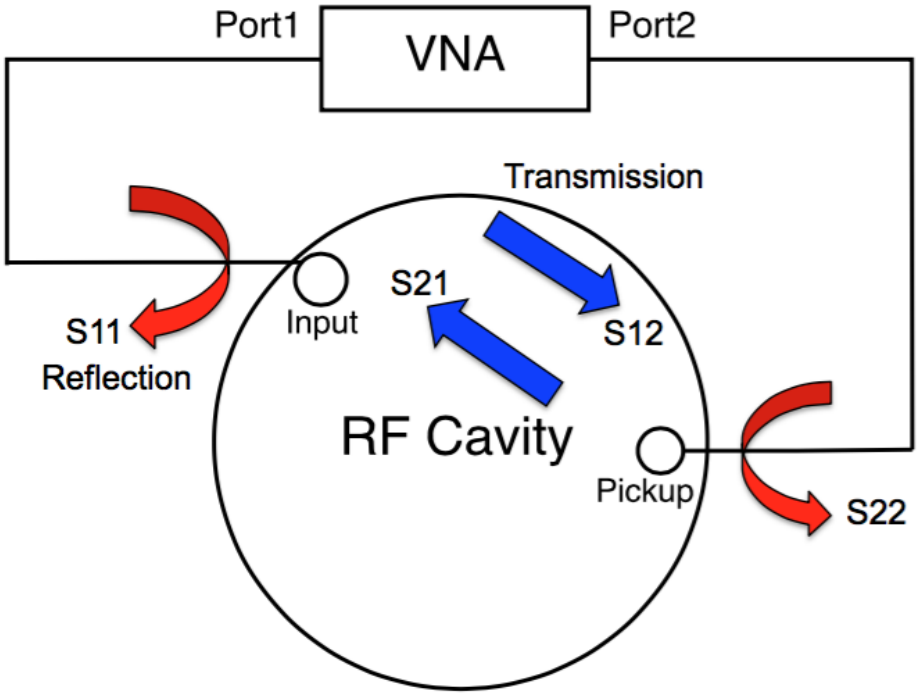

Figure 3.25: Schematic diagram of the Q factor measurement using Vector Network Analyzer (VNA).

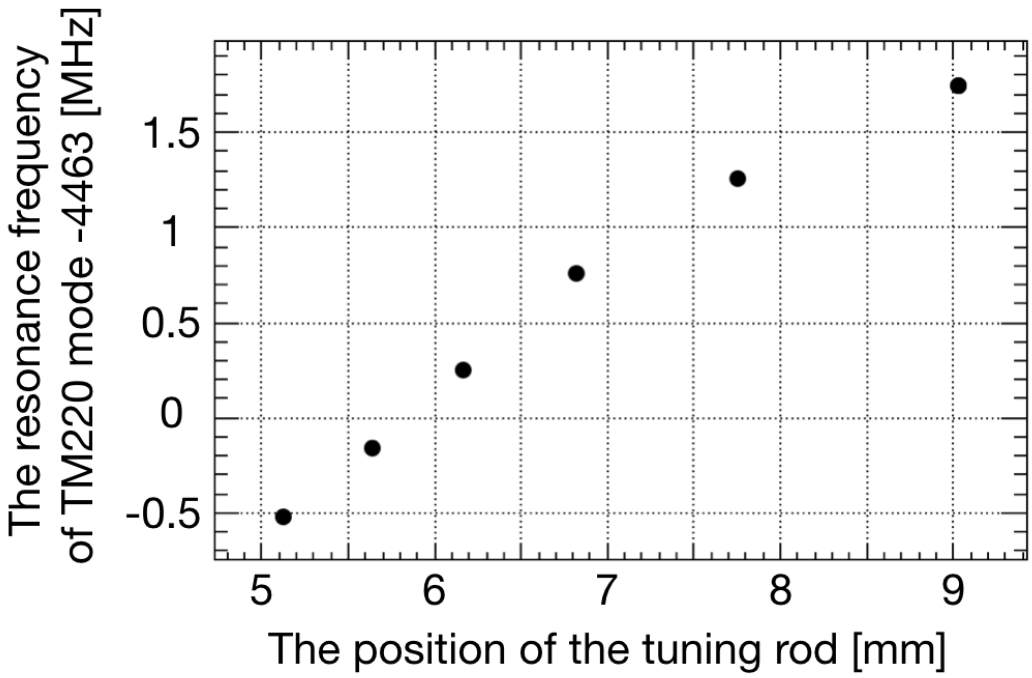

Figure 3.26: The resonance frequency of the TM220 mode for different tuning rod position measured by a VNA.

3.6 Positron Detector System and Data Acquisition System

Positron counters are made of pairs of a finely segmented scintillator and a silicon photomultiplier, Multi-Pixel Photon Counters (MPPC) by Hamamatsu Photonics K.K., S12825-050P-01. The scintillators are EJ212 by Elgen with a fast decay constant (2 ns) and emission wavelengths around 450 nm. Each scintillator pixel is 10 mm×10 mm square-shaped, with a thickness of 3 mm. For each scintillator segment, an MPPC is attached. One MPPC has 667 Avalanche Photodiodes (APD) in the 1.3 mm×1.3 mm square active area. Each pair of the scintillator and the MPPC consist one unit pixel. 24×24 pixels are aligned two-dimensionally in each layer of the detector, as shown in Fig. 3.27. We used two layers of the positron detector in this experiment. Between each pair of the adjacent scintillation pixels, a slice of the light-reflective film was inserted in order to suppress the optical cross-talk between the pixels.

The signal from MPPCs is read out by a KEK Kalliope board which consists of a fast read amplifier based on ASIC and multi-hit Time-to-Digital Converter (TDC) in FPGA. The diagram of the digital part of the readout is shown in Fig. 3.28. The digital part is used as multi-hit TDC with a time resolution of 1 ns. Once it starts taking the data, the timing window is open for 64 μs, which is sufficiently long compared to the muon lifetime (2.2 μs) and sufficiently short compared to the muon pulse interval, 25 ms. One Kalliope board has 24 channels, so we use 48 boards in total to read the signals from 24×24×2 = 1152 MPPCs. We employ the bitwise coincidence of the pulses from accelerators and the ready signal from the FPGAs on the Kalliope boards as the trigger signal.

The trigger system is shown in Fig. 3.29 [54]. The TDC data from Kalliope boards are sent to a data acquisition (DAQ) computer. Gas pressure gauge, magnetic field monitor and power sensor is also read out by another PC. The temperature data from the thermocouples are recorded by a data logger (Graphtec midi logger GL240).

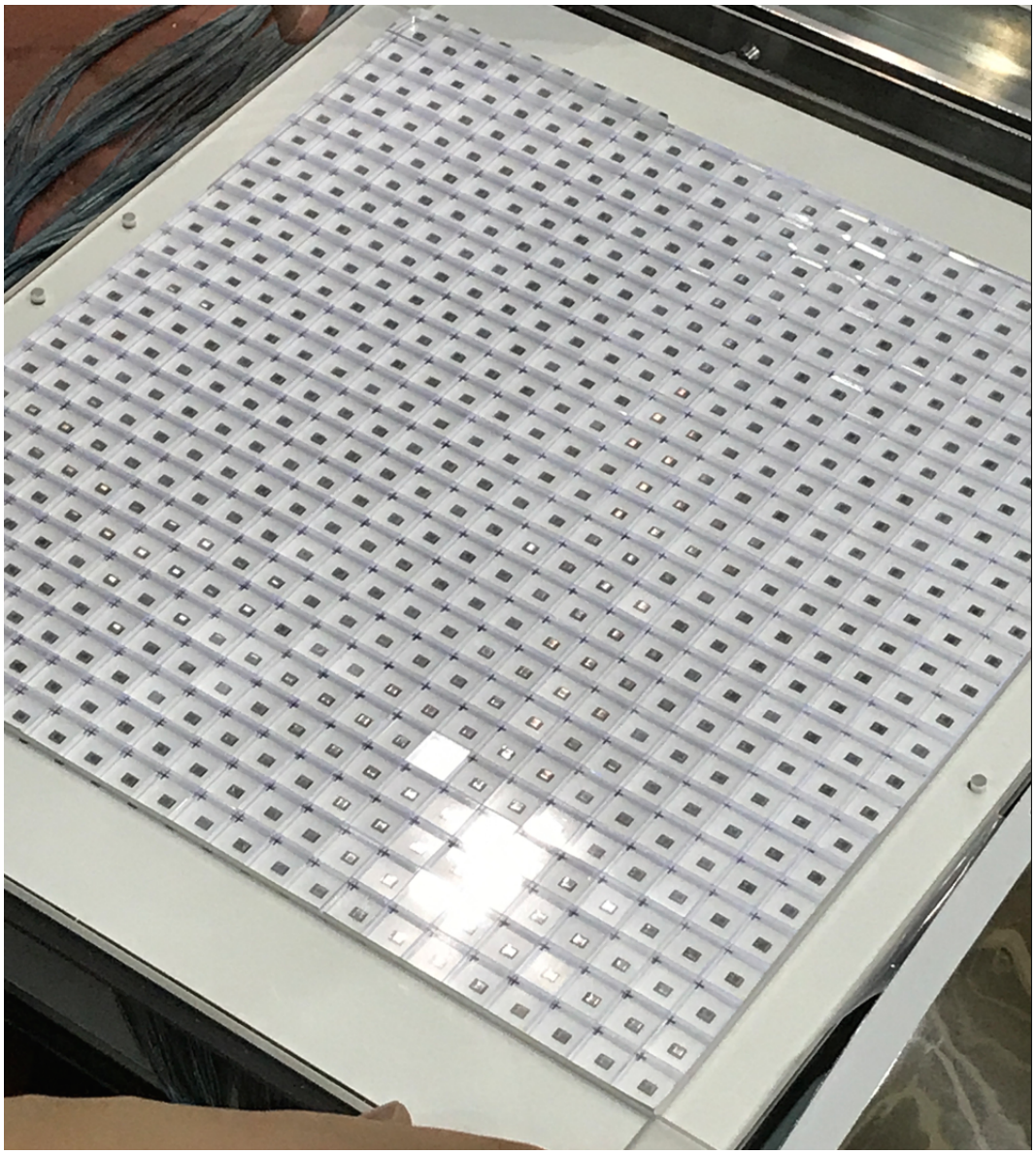

Figure 3.27: One layer of the positron counter. Each layer is made of 24×24 pixels. Each pixel is made of a pair of a 10 mm×10 mm scintillator and an MPPC.

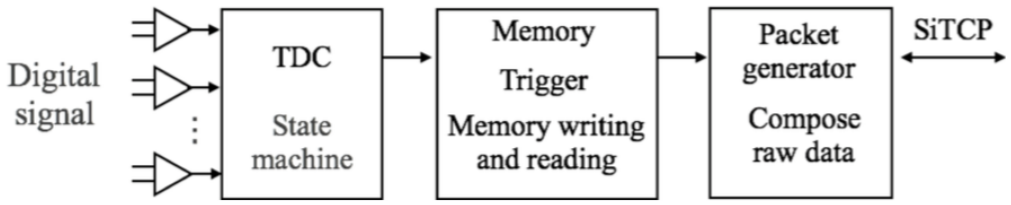

Figure 3.28: Diagram of the digital part of the readout [54]

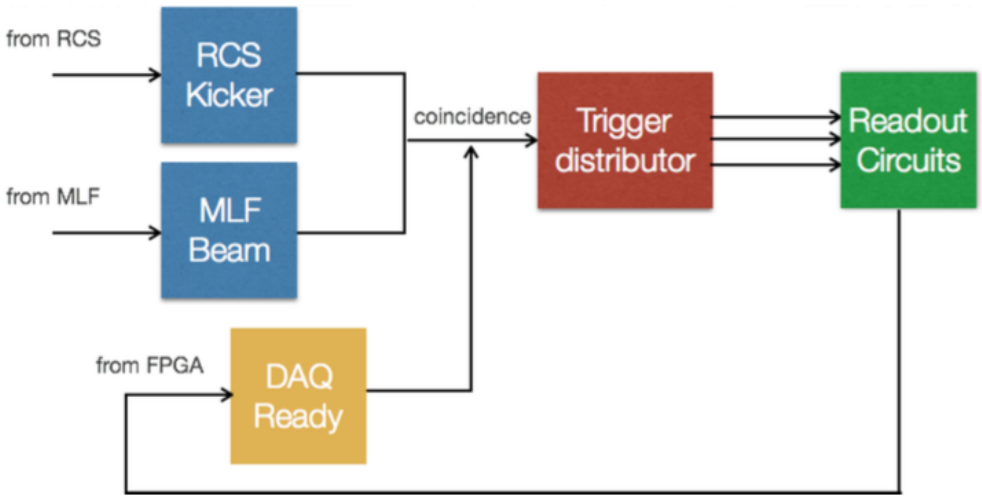

Figure 3.29: Schematic diagram of the trigger system [54]. The pulses synchronized with the accelerator is fed to the trigger distributor. The trigger is on by taking the coincidence of the accelerator signals and the ready signal from FPGA on the read-out board.

Chapter 4

Data Analysis

4.1 Data Set

In the allocated beam time of June 2018, we have measured MuHFS with Kr pressures from 0.3 to 0.4 atm at experimental area D2 in J-PARC MLF. In addition to these data in June 2018, the result obtained from the analysis of the data at 1.0 atm (June 2017) is used to take the extrapolation to the MuHFS value at zero Kr density.

We analyze the data for 3 days in June 2018. The proton beam power during the beam time was 500 kW. Figure 4.1 shows the number of positron counted per pulse for each layer of the detector. Figure 4.2 shows the zoomed view of the previous plot. There are some pulses with no positron hits recorded. This is due to the proton beam extraction to another accelerator ring, the Main Ring (MR), for other experiments on neutrinos or hadrons. The number of the extracted pulses are fixed to four. The interval of the extraction depends on the operation mode of the MR.

When there is some problem with the accelerator, the operation is halted. Figure 4.3 shows the positron hits when such a beam lost occurs. These pulses with no hit, because of either the beam lost or the MR injection, are omitted from the analysis.

4.2 Data Analysis

4.2.1 Workflow

Fig. 4.4 shows the workflow of the analysis. We employ a C++ based data analysis tool called ROOT CERN [80]. We obtaind raw data as binary files. To suppress the consumption time for the later process, we convert the data into a ROOT-friendly binary file (*.root) while omitting some of the background hits which reach the detector much earlier than the decay positrons from the muons. Most of these omitted background hits account to the prompt positron produced at the muon production target. During the extraction, we also rewrite the data structure to

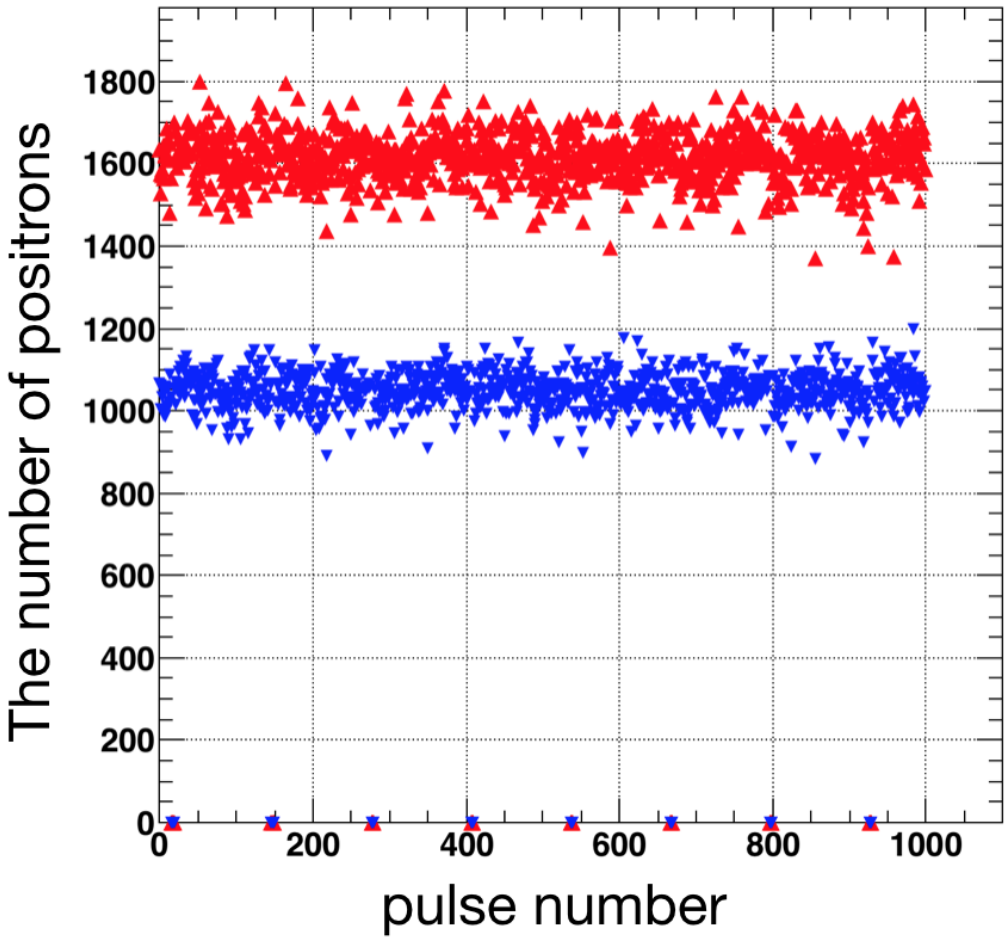

Figure 4.1: The number of hits per pulse for each layer of the detector. The red upper triangle indicates the number of hits in the first layer, and the blue one indicates the number of hits in the second layer.

make the time devoted to later analyses faster. We call this process "branching" which will be explained in detail later.

There are some hits make "clusters", meaning one positron causes signals at more than one pixel of the scintillator at the same time (see Fig. 4.5). One needs to combine these hit and count them as one hit, in order to avoid overcounting the number of hits. This combining process is called "clustering". After the clustering, the next step is taking the coincidence between the two layers of the positron counters to omit background hits. We do not have information such as time-over-threshold (TOT) to omit the background hits.

4.2.2 Extraction and Branching

The first step of the data analysis is the extraction and branching. This step is of importance for reducing the data size and the time consumption for later analyses.

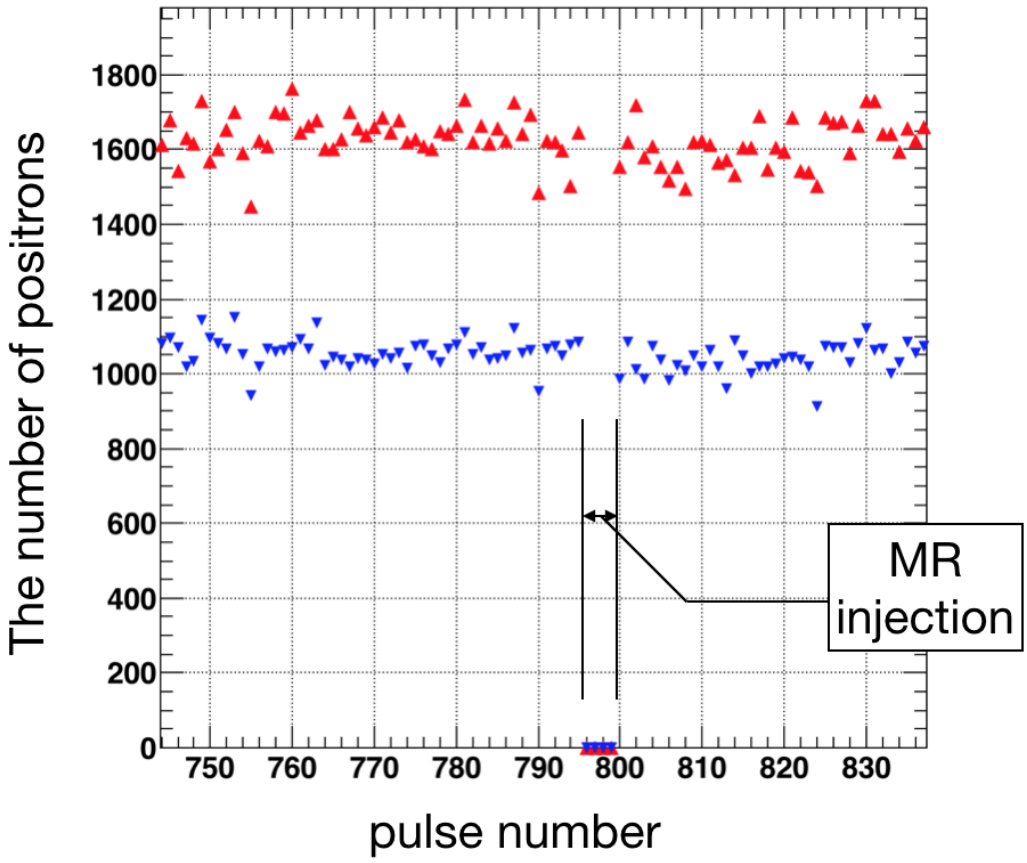

Figure 4.2: The change in the number of the hits due to the MR injection. Occasionally, the proton beam is extracted to the Main Ring (MR) in J-PARC for other experiments. The number of the extracted pulses are always four. The interval of the extraction depends on the MR operation mode. The pulses with no hits are omitted from the analysis.

Some of the hits are artificial and we need to omit those hits. In the process, we have to merge several hits into one hit ("clustering") or make a pair of hits penetrating the two layers of the detector ("coincidence"). When one searches pairs of hits from N candidate hits, the expected time to spend is proportional to N^2. The time consumption was not a serious problem in the pilot measurements: it was possible to analyze the data with a time comparable to the time we spent to collect the data. In the case of the current measurement, the number of the hits per pulse is larger since the proton beam power at J-PARC was 500 kW, at least 2.5 times higher than the previous measurements by MuSEUM. This means the time consumption for analysis becomes at least 5 times larger. This means the time for analyzing the data collected in several days now would amount to several weeks if there is no change in the analysis method. For the future experiment in H-Line, 20 times more muon per pulse is expected and the data taking is expected to last 100 days. The problem of reducing the analysis time becomes crucial for the measurement with

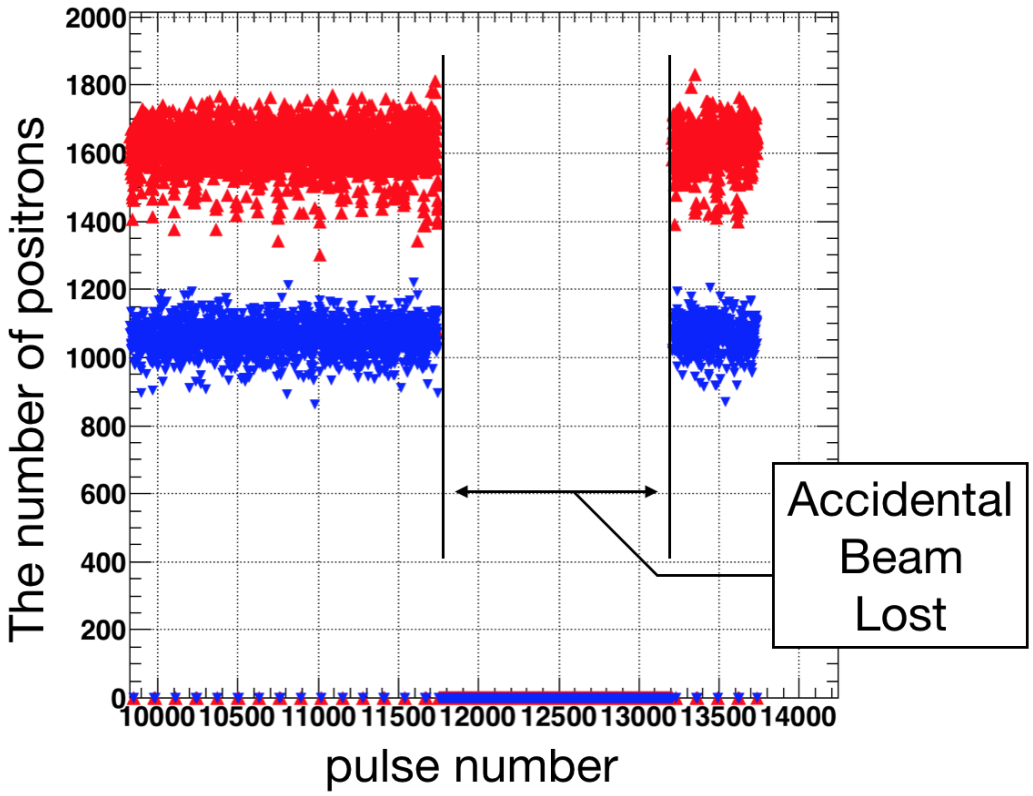

Figure 4.3: In additional to MR extraction, the beam pulses are sometimes lost due to the accident in the accelerator components. The pulses with no hits due to the beam lost are omitted from the analysis.

high statistics.

We obtain the data as a set of information of when a positron hits which channel of the detector. A typical raw time spectrum of the positron decay is shown in Fig. 4.6. The horizontal axis is the elapsed time from the trigger by the accelerator. There are two peaks due to the prompt positron bursts from the muon production target, which managed to penetrate the $\vec{E} \times \vec{B}$ filter. After the second peak, we the exponential decay of the hits, which corresponds to the muon lifetime. These hits are the decay positrons from the injected muons.

In order to make the later analyses faster, we need to select the hits only from muon decay. Figure 4.7 shows the zoomed view of the raw time spectrum. Most of the prompt positrons hit earlier than 10850 ns. Thus, we only extract hits after 10850 ns, to reduce the size of the new file smaller. The time spectrum after extraction is shown in Fig. 4.8.

By extraction, we can effectively omit the background hits but the number of hits is reduced to only 90% by this method. This corresponds to 19% reduction of the analysis time. The next step called branching is a method reducing the analysis time without reducing the data size itself.

Combined with the extraction, we rewrite the data structure into small branches

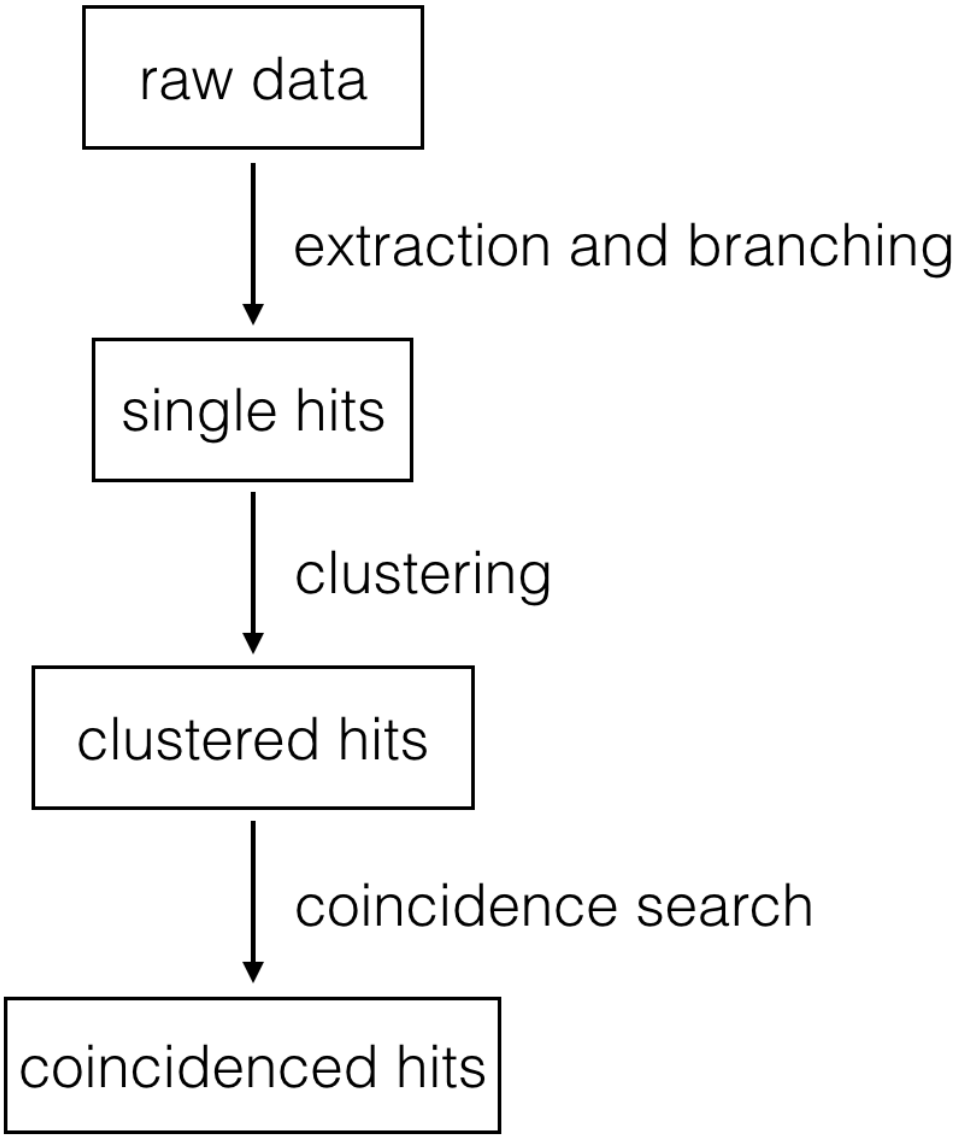

Figure 4.4: Workflow in the analysis

so that data analysis becomes faster. This process is called branching (Fig. 4.9). We prepare a branch for each detector channel, which indicates the x and y positions of a certain hit. Then each hit is attributed to one branch according to the channel. After the branching, we have 1152 branches and each branch is just a series of the number indicating the hit time. The nth number of a branch is the hit time of the nth hit in the corresponding channel.

A previous analysis method applied in the analysis of the pilot measurement was without branching, and all the hit was grouped into one stack. The stack is a long list of the hit information, the hit time and the hit positions. By branching, roughly 1/1152 of the hits are in one branch. This makes the number of the hits under pair search drastically small.

The hit position of the first layer is shown in Fig. 4.10. The number of the

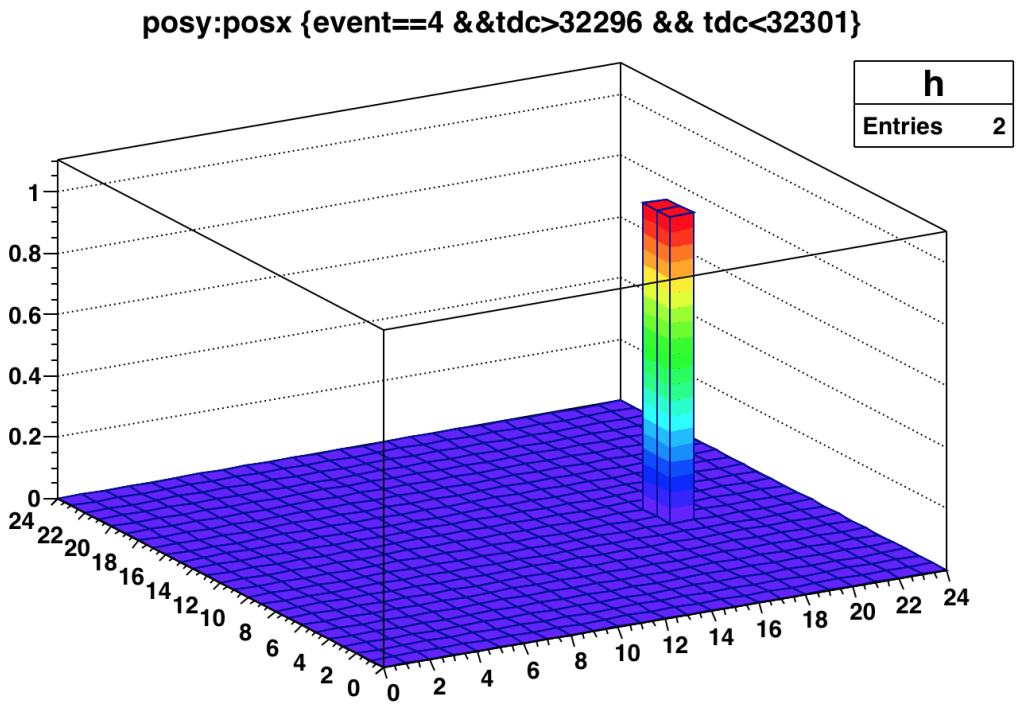

Figure 4.5: An example of a cluster. There are two hits in the two adjacent pixels in a short time interval (in this case the interval is 5 nsec). In this time region (approximately 22 μs after the muon arrival), the number of the hits expected during 5 nsec interval for one layer of the detector is 1 hit per 3000 pulses. Therefore, it is unlikely that these two hits were accidentally caused by two different positrons.

hit are normalized by the number of the beam pulse. There are several pixels not recording hits, which is an already-known problem in pilot measurements. Figure 4.11 shows the one-dimensional projections of the hit map.

For later analysis steps, the time resolution of the detector is important. We can check the time resolution from the time difference of the hits by a positron perpendicularly penetrating the two layers of the detectors. The second layer is 10 cm apart from the first layer, and a positron with a speed near the speed of light need less than a nanosecond to penetrate the layers. In order to avoid accidentally counting two hits due to two different positrons, we only consider the positron hits 15 μs later than the muon arrival. If there are two hits, satisfying the condition below, we consider them as the penetrating hits: first, they are from two different layers, second, they are from the same hit positions (hit position x and y are the same), and finally, their hit timing is within 50 ns range.

Figure 4.12 shows the time difference of such hits. The analysis is made for 20000 pulses. The time resolution is a Gaussian-like structure with $\sigma = 5$ ns. Most of the data are within $\pm$ 15 ns range. Thus in later analysis steps, we often set the time difference condition for pairing hits as $\pm$ 15 ns.

Figure 4.13 shows the time resolution for each detector channel. The resolution

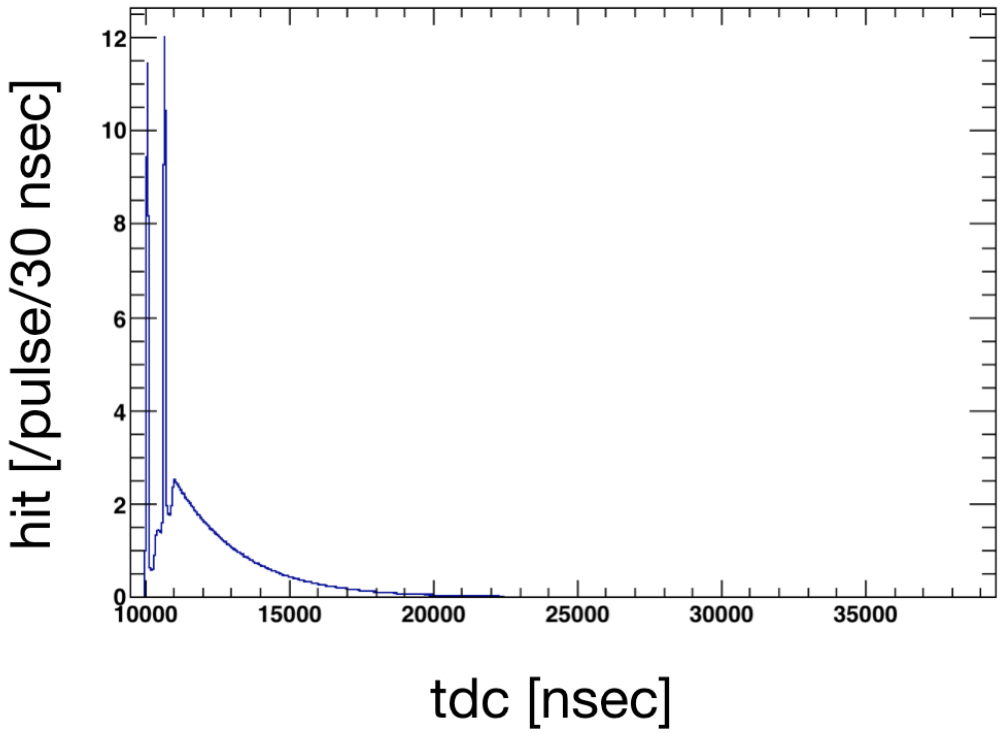

Figure 4.6: Raw time spectrum. The horizontal axis is the elapsed time from the trigger by the accelerator. The number of the hits is normalized by the number of the pulse. The two peaks are caused by the prompt bursts of the positrons.

is dependent on the channels, but the resolutions of most of the channels are in the region of from 3.5 ns to 5.5 ns, as shown in Fig. 4.14.

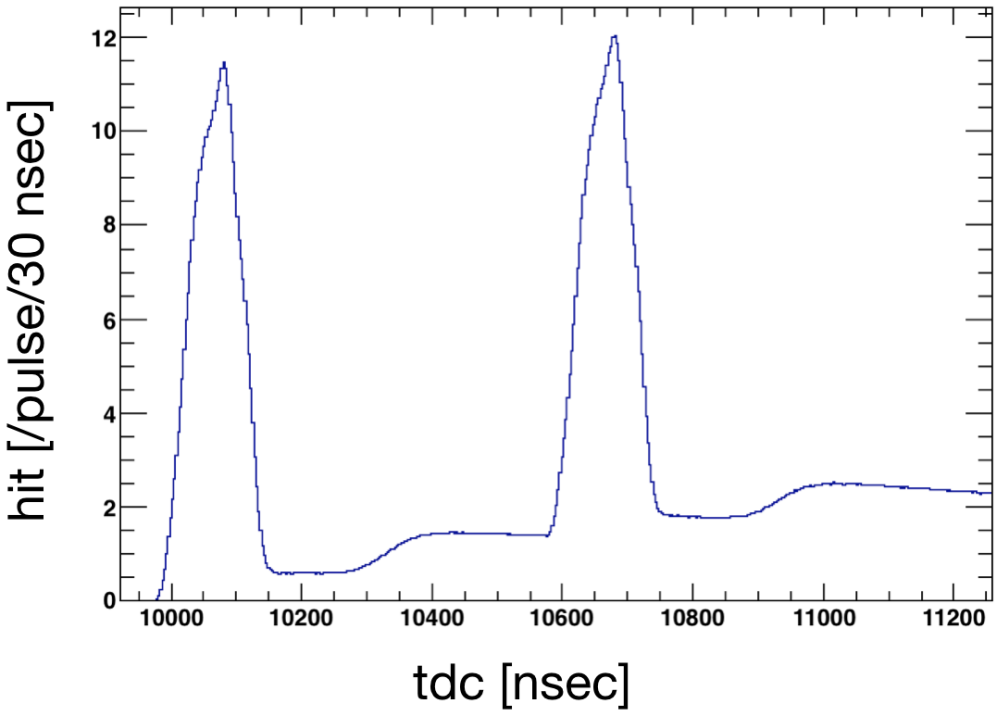

Figure 4.7: Raw time spectrum with a zoomed view. The horizontal axis is the elapsed time from the trigger by the accelerator. The number of the hits is normalized by the number of the pulse. The two peaks are caused by the prompt bursts of the positrons.

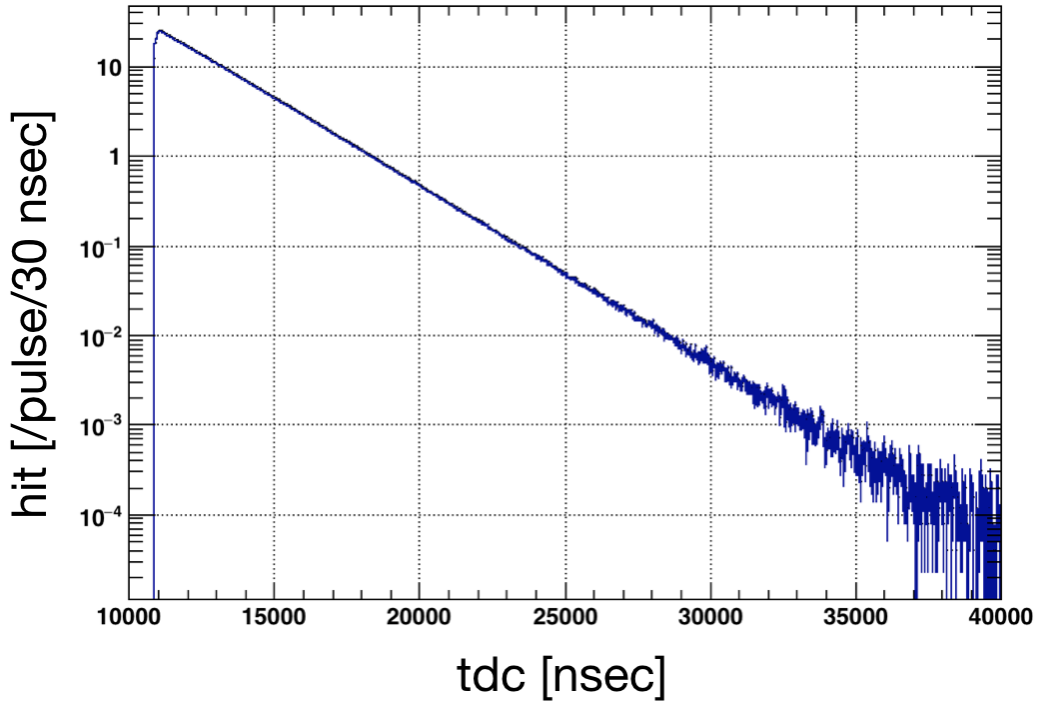

Figure 4.8: Typical time spectrum after data extraction.

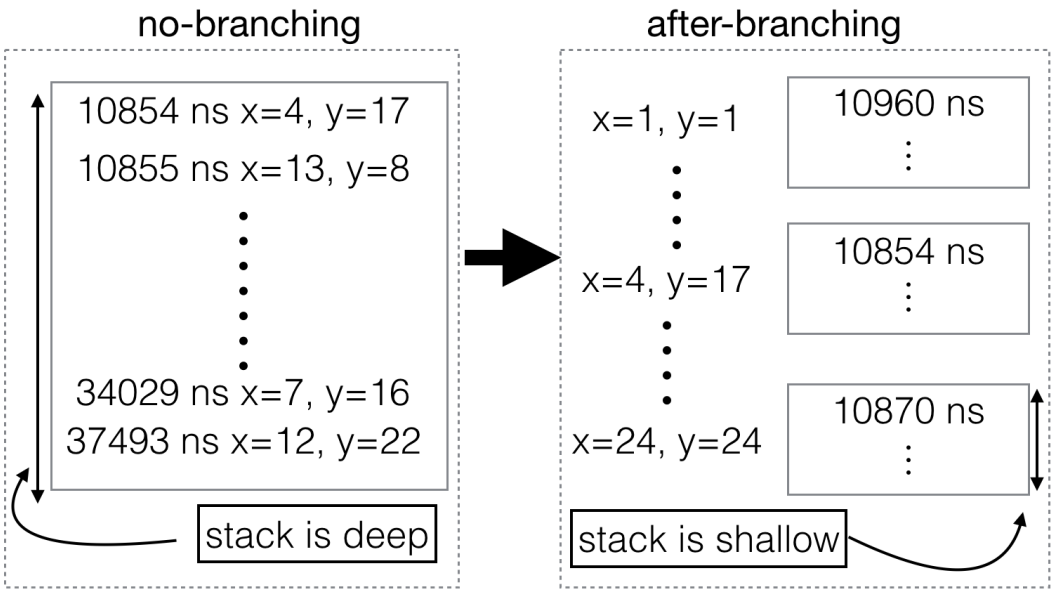

Figure 4.9: Branching. By branching, we redefine the data structure so that the later analyses become less time-consuming. Without branching, all the data is contained in one stack. The branching process allocate all the positron hits in one pulse into 1152 small stacks, according to their hit positions in the x-y plane of the detector layer.

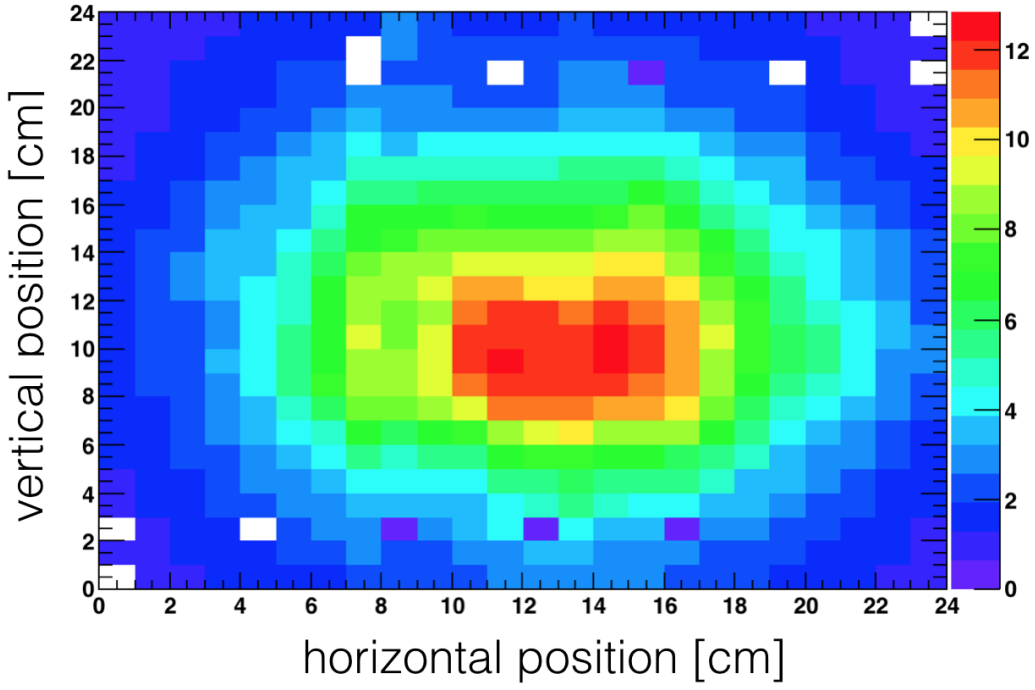

Figure 4.10: The hit position of the first layer of the detector. The number of the hit is normalized by the number of the beam pulse.

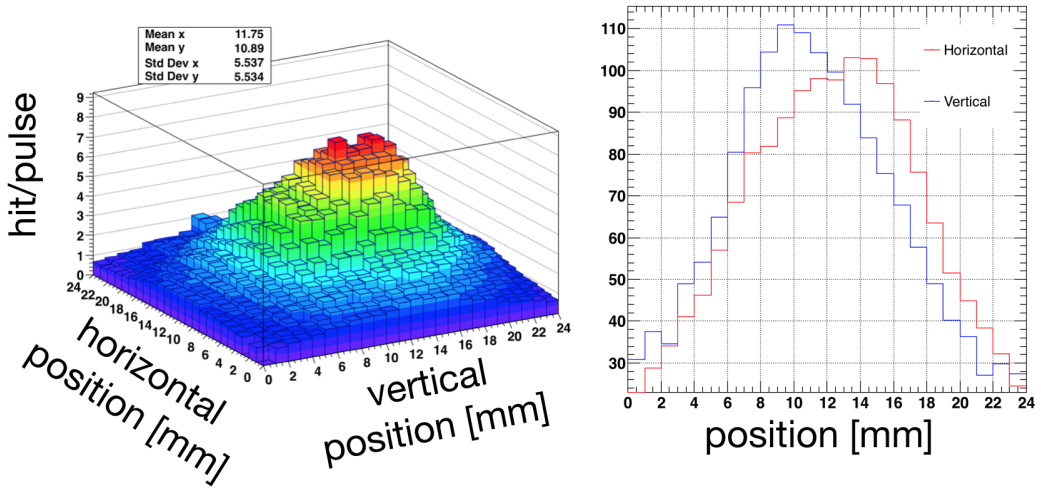

Figure 4.11: The hit position of the first layer of the detector and the projection to each axis. The number of the hit is normalized by the number of the beam pulse.

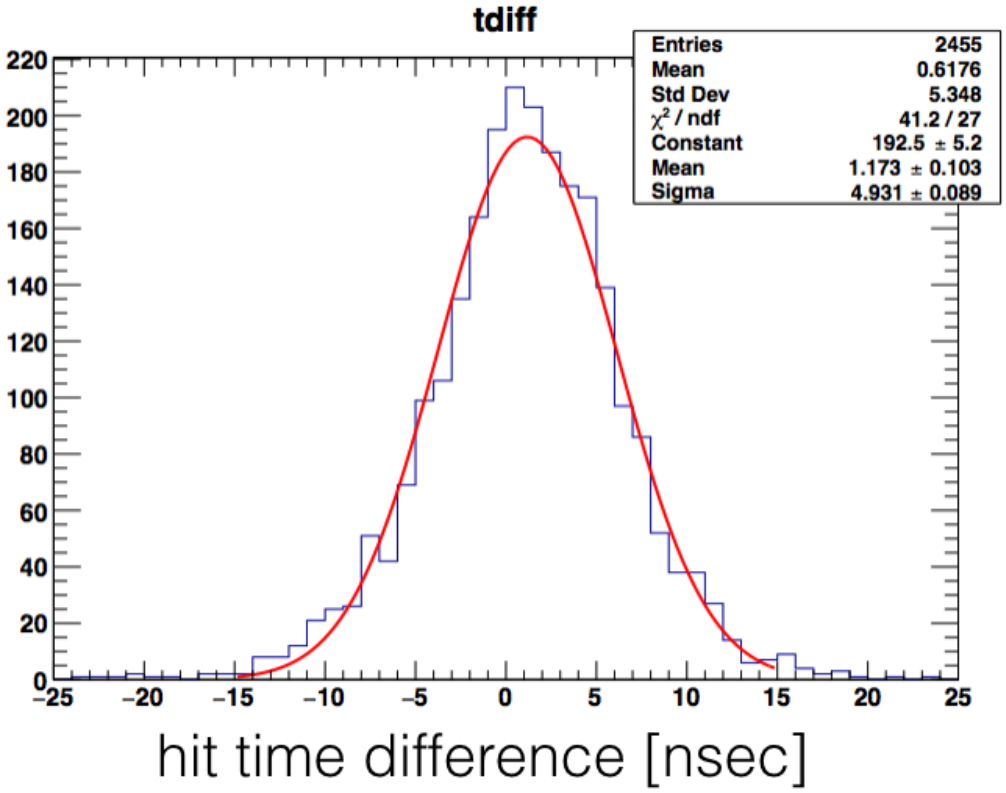

Figure 4.12: Time difference of the hits which are caused by a positron perpendicularly penetrating the two detector layers

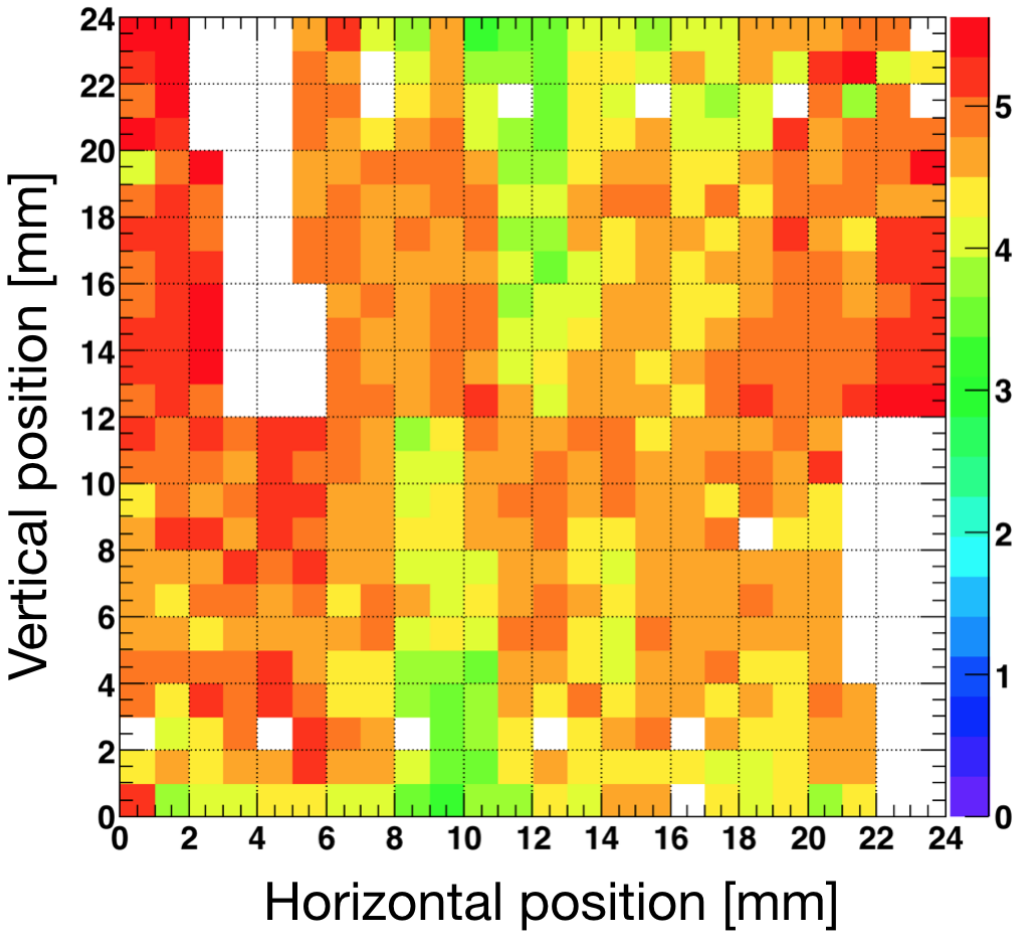

Figure 4.13: The time resolution for different scintillator positions. The resolution has a tendency that the resolution is narrower for the detector channels in the center of the detector. There is no significant deviation of the time resolution for different detector channels.

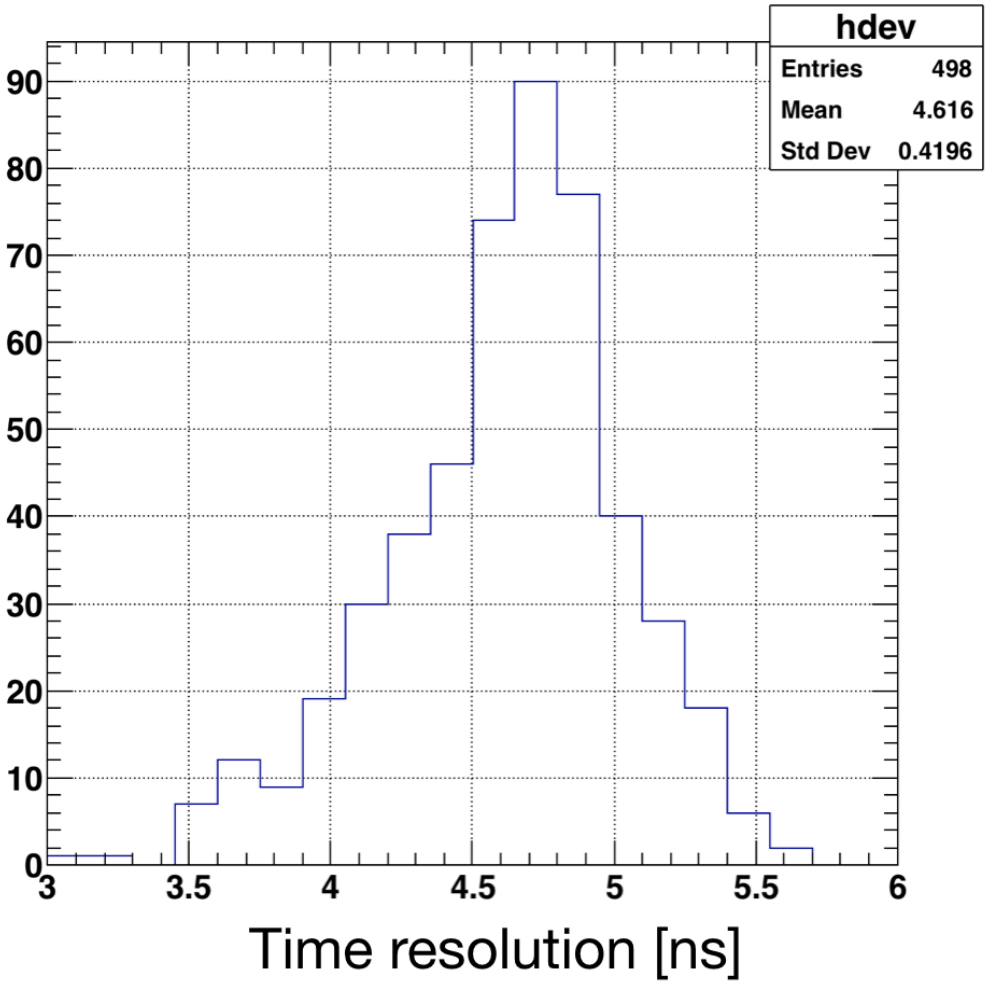

Figure 4.14: Histogram of the time resolution for different detector channels, i.e., the z-axis projection of the Fig. 4.13. There is no detector channel with a time resolution significantly deviated from the time resolutions of the other channels.

4.2.3 Clustering

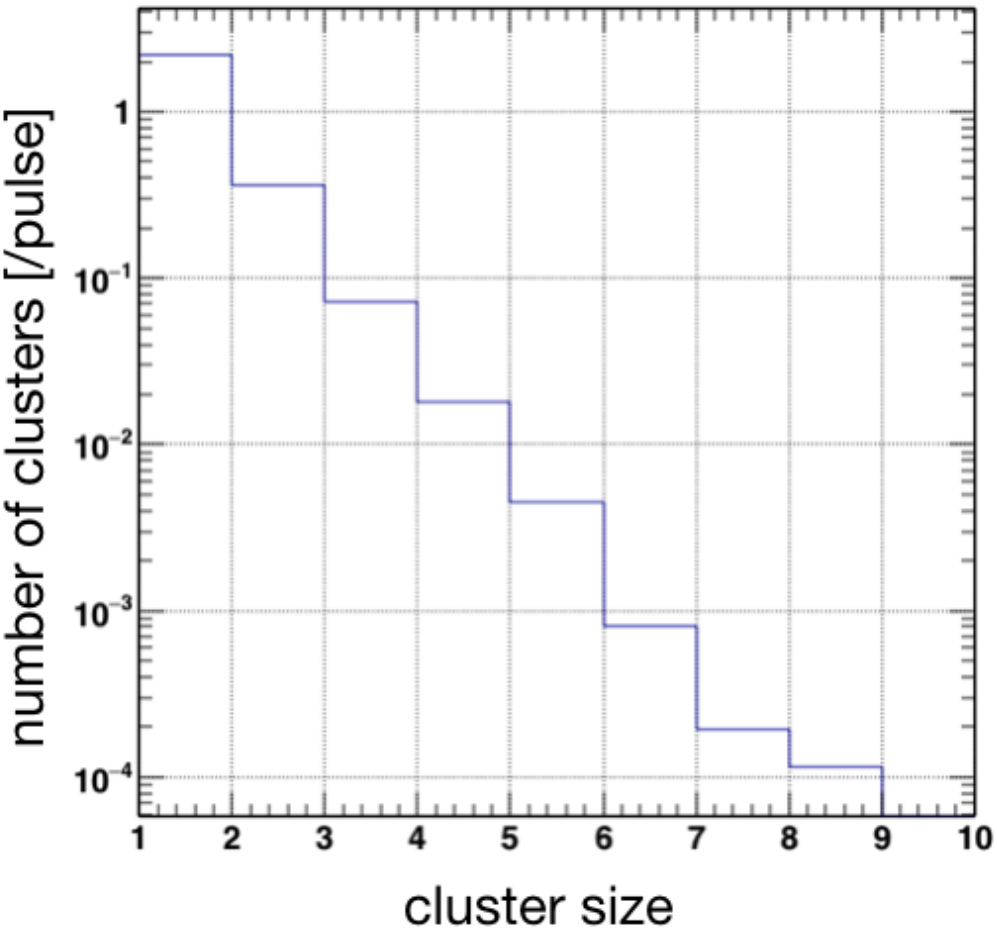

Figure 4.15: The size of clusters. The size of a cluster is defined to be the number of hits consisting the cluster. The vertical axis is normalized by the number of pulses. To avoid counting piled-up different true hits as one cluster, this size check has been done for the hits 16 μs after the muon arrival.

As mentioned earlier, there is a set of hits caused by one positron, which is called a "cluster". Such a cluster should be counted as one hit. The next step of the analysis is clustering, which checks the hits in one layer of the detector, and merges some of the hits into one cluster according to certain criteria.

To make the criteria for clustering, we first study the characteristic of the hits by a single positron. In the early time window, there are multiple positron hits due to the pulse structure of the muon beam. This is not desirable for studying hits from single positron, so we focus on the hits which are at least 16 μs later than the muon arrival. In this time region, the hit rate at one layer (576 pixels) in a 30 ns time interval is at most 0.03 hit/pulse, which is sufficiently low.

In this time region, the hit rate is sufficiently low and almost all the hits are from single positron. If there are multiple hits in 30 ns time interval, the hits are clusters.

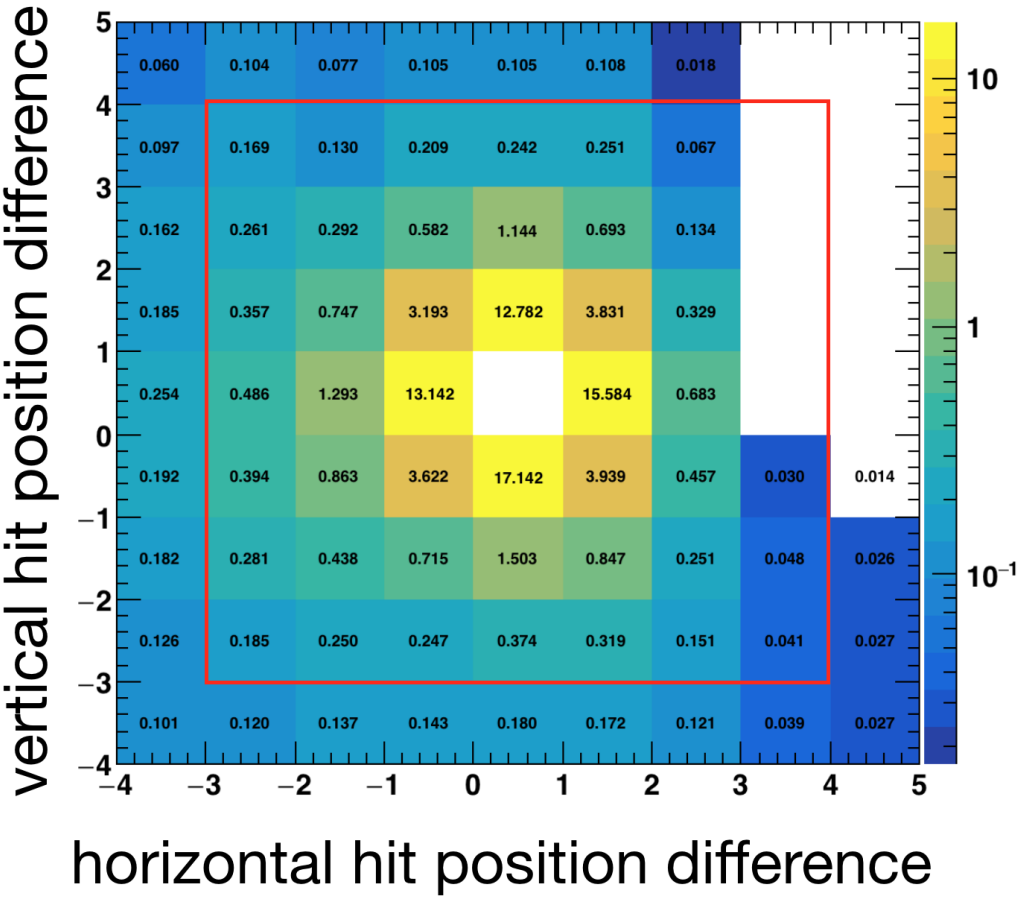

Figure 4.16: The hit positron difference of the hits consisting one cluster. The text in a cell indicates the probability of such pairs of hits in percentage. Most of the hits come adjacent hit positions. To avoid counting piled-up different true hits as one cluster, this hit position check has been done for the hits 16 μs after the muon arrival. We set the clustering condition is that the two hits are within 7×7 region, shown as the red rectangle.

We define the size of a cluster by the number of the hits consisting the cluster, and Fig. 4.15 shows the cluster size distribution. The cluster size one means they are made of only one hit, which is an ordinary hit. There are clusters with a size larger than 2, and the number of the clusters with size $N+1$ is approximately 0.2 times of the number of the clusters with size N. The size of the 96% of the clusters are one or two, and the size of the 99.1% of the clusters are less than or equal to three.

Next, we study the hit position differences between hits making a cluster. As mentioned before, we select hits 16 μs after the muon arrival. Figure 4.16 is a two-dimensional histogram of the hit position difference between two hits making a cluster. The color and the text in a cell indicates a probability in percentage. Most of the pairs of hits come adjacent positions. The probability of 3×3 area around the center, however, is small and amounts to 73% of the clusters in total. 5×5 area has

83% of probability, 7×7 area has 90% of probability, and 9×9 area has 91%. Thus, we set the condition of clustering such that if two hits are within 15 ns and within the 7×7 area.

We define the hit position of a cluster as the center of gravity of the consisting hits, i.e. if we have a pair of the hits and the first hit A has a position of (x_A,y_A) and the second hit B has a position of (x_B,y_B), then the cluster position (x_{cl},y_{cl})is defined as

$$(x_{cl}, y_{cl}) = \left(\frac{x_A + x_B}{2}, \frac{y_A + y_B}{2}\right). \tag{4.1}$$

The hit timing of a cluster is also defined as the average of the hit timing of the consisting hits.

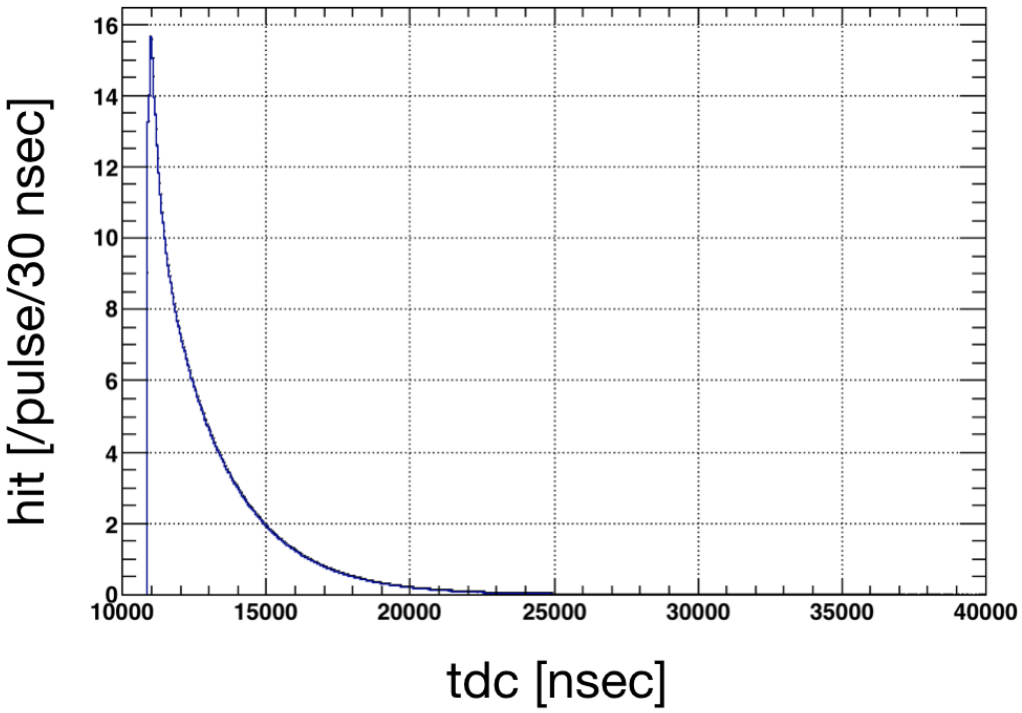

Figure 4.17: Time spectrum after clustering.

Figure 4.17 shows the time spectrum after the clustering. The hits are normalized by the number of the pulse. The bin width is 30 ns. The hit positions of the clusters are shown in Fig. 4.18. Here, the term cluster also includes those made of only one hit (cluster size one). Note that the cluster hit position was defined as the center of gravity of the consisting hits, therefore there is a small but non-zero number of hits in a pixel which had no hits before the clustering.

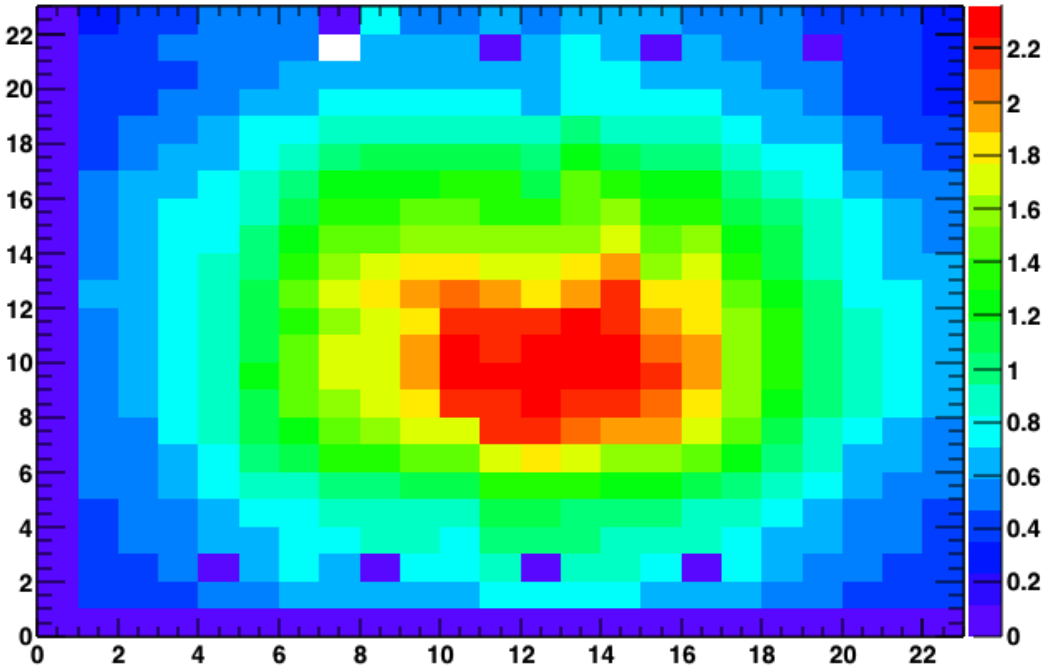

Figure 4.18: hit position distribution after clustering. The hit is normalized by the number of the muon pulse.

4.2.4 Coincidence

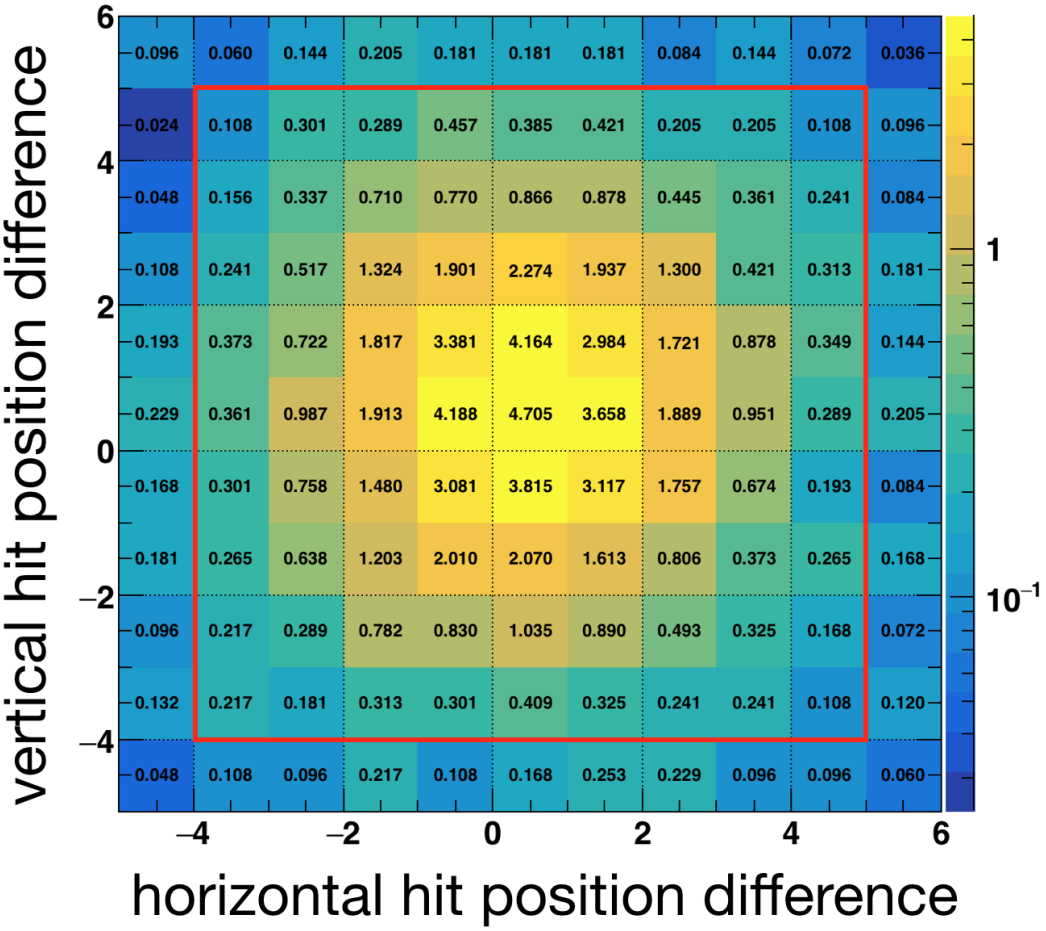

Figure 4.19: The hit positron difference betweeing the hits making one coincidence hit. The texts in a cell indicates the probability of such hits in percentage. To avoid counting piled-up different true hits as one coincidence hit, this hit position check has been done for the hits 16 μs after the muon arrival. We set the coincidence condition is that the two hits are within 9×9 region, shown as the red rectangle.

After the clustering, we have to take a coincidence between the two layers. The coincidence pair between two layers is determined by certain criteria. The criterion for hit time difference is set to be ± 15 ns. To obtain the criterion for the hit position, we study the hit position difference of the first layer and the second layer. The both of hits should be from the same positron penetrating the two layers, so we made a selection of hits 16 μs after the muon arrival time. The selection is similar to the one we made in establishing the criteria for clustering.

The hit position difference of the two hits from single penetrating positron is shown in Fig. 4.19. The number of hits is the sum of 25700 pulses. The probability of 3×3 area around the center amounts to 33% of the clusters in total. 5×5 area has 55% of probability and 7×7 area has 75% of probability. 9×9 area has 87% of

probability, and 11×11 area has 91% of probability. Unlike the hits making a cluster, the hits making a coincidence in two layers have a tendency to be separated. Thus we regard two hits as a coincidence hit if the hit time difference of the two is within 15 ns and the hit positions are within 9×9 area.

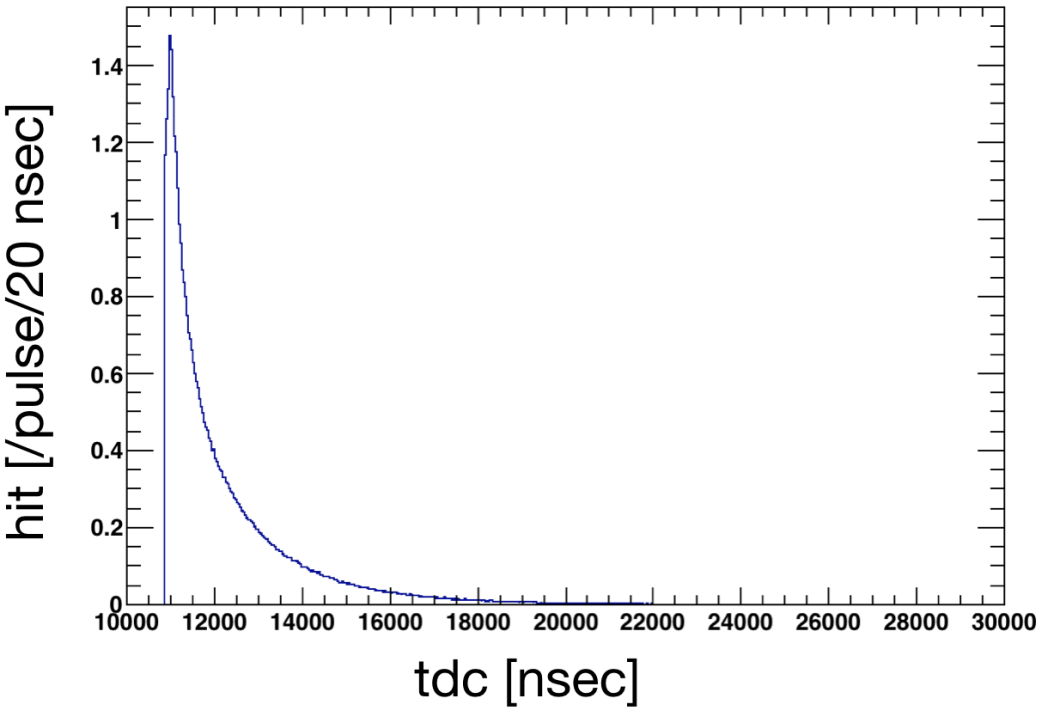

Figure 4.20: Time spectrum after taking the coincidence.

Figure 4.20 shows the time spectrum after taking the coincidence. The hit number is normalized by the number of the pulse.

4.2.5 Time-Dependent Signal

One can determine the true counts of the detector after the coincidence. The signal is written as

$$S = \left(\frac{N_{\mathrm{ON}} - N_{\mathrm{OFF}}}{N_{\mathrm{OFF}}} \right) \tag{4.2}$$

as defined in the section before, where the N_{ON} is the counts when the microwave is on, and N_{OFF} is the counts when the microwave is off. The obtained time-dependent signal when the microwave frequency is on resonance is shown in Fig. 4.21. The signal clearly deviates from the zero. We also obtain the time-dependent signal when the microwave is very far from the resonance, 1.2 MHz away. The off-resonance signal is shown in Fig. 4.22. The signal is consistent with the zero.

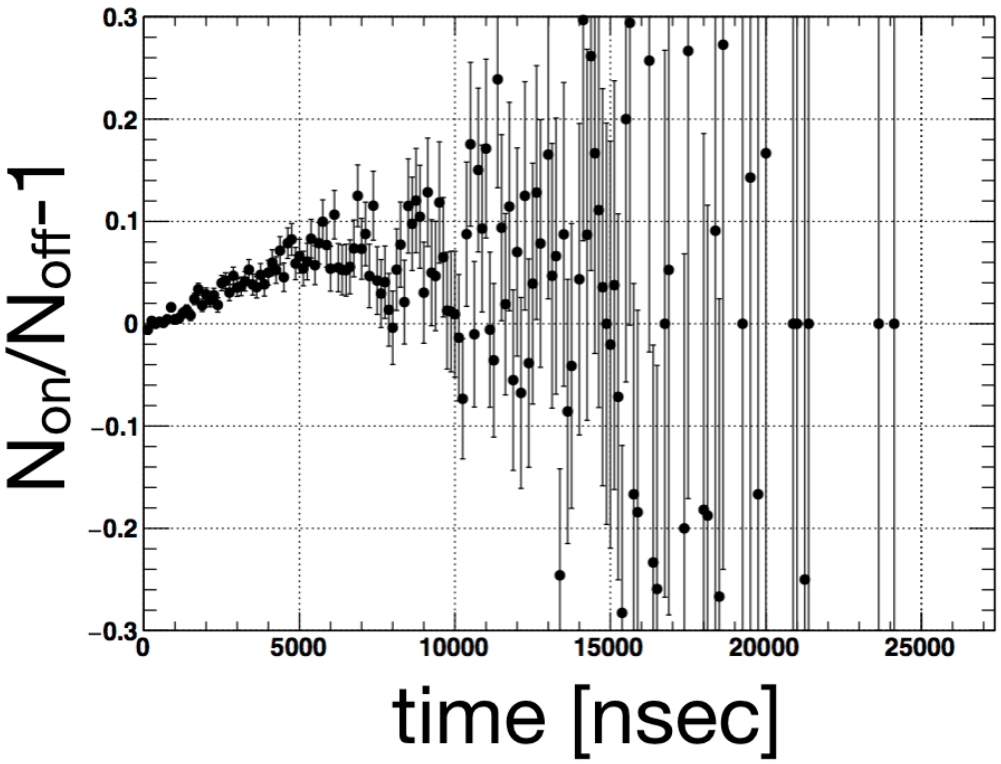

Figure 4.21: Time-dependent signal when the microwave is on resonance. The horizontal axis shows the elapsed time after muon arrival. The vertical axis is the signal. Non is defined as the number of hits when the microwave is ON while Noff as the number of hits when the microwave is OFF.

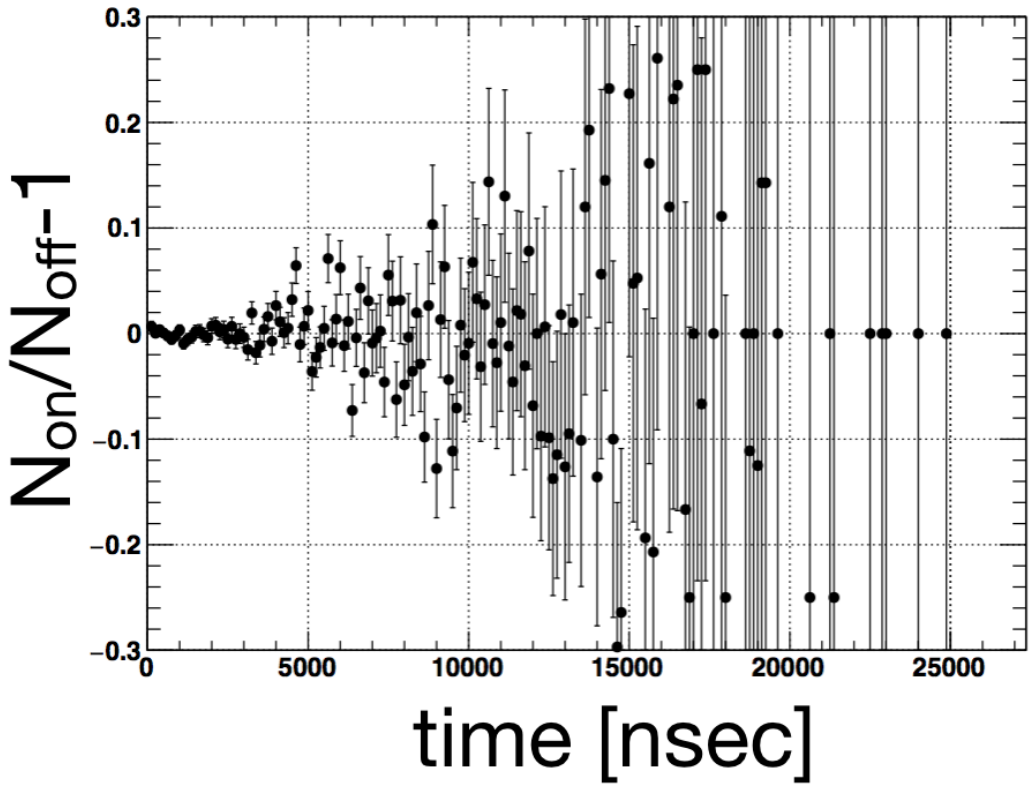

Figure 4.22: Time-dependent signal when the microwave frequency is far from the resonance (-1.2 MHz). The horizontal axis shows the elapsed time after muon arrival. The vertical axis is the signal. Non is defined as the number of the hits when the microwave is ON while Noff as the number of the hits when the microwave is OFF.

4.2.6 Resonance Line

By integrating the number of hits when the microwave is on and compare them to the integrated counts when the microwave is off, we can obtain the resonance line. As discussed in Chap. 2, we used the old muonium method, so we integrated the positron counts in a certain time window, to obtain the narrower resonance line. In this analysis, we integrated the signal in the time interval from 2 μs to 6 μs. Some of the data sets in 0.4 atm are not appropriate for the old muonium method since the microwave power was higher than the optimum. These data sets were primarily used for the search of the optimal power. These data sets were analyzed using the conventional method, i.e., the positron signal was integrated over the all time interval.

We use the theoretical resonance line shape as the fitting function. The resonance line for the conventional method is shown in Eq. 2.83 and the resonance line for the old muonium method is in Eq. 2.84. To correct the microwave power variation run by run, we rewrite the microwave parameter b in the fitting function as

$$b = b_{\rm ave} R_{\rm run}, \tag{4.3}$$

where $b_{\rm ave}$ is the average microwave parameter, which is treated as a free parameter in the fitting, and the $R_{\rm run}$ is a run-dependent scaling factor, which is determined by the measurement of the microwave cavity characteristic. The $R_{\rm run}$ parameter is fixed in the fitting.

The χ^2 function for the fitting is

$$\chi^2 = \sum_{\rm i} \left[\frac{S_{\rm exp}(\omega_{\rm i}) - S_0 S_{\rm th}(\omega_{\rm i})}{\sigma(\omega_{\rm i})} \right]^2, \tag{4.4}$$

where $S_{\rm exp}(\omega_{\rm i})$ is the experimental signal, $S_{\rm th}(\omega_{\rm i})$ is the theoretical signal, $\sigma(\omega_{\rm i})$ is the statistical uncertainty, S_0 is the scaling factor.

The obtained resonance curve when the Kr pressure is 0.3 atm is shown in Fig. 4.23. The vertical axis is the signal defined as in Eq. 4.2. The horizontal line is the frequency offset from 4 463 302 kHz. One can clearly see more signal when the microwave is on-resonance, and less signal as the microwave frequency is set to be far. The fitting result is shown as the red line in the figure. The fitting program is based on the CERN MINUIT package [81].

We have also conducted the measurements at other gas pressures. Fig. 4.24 shows the result from the measurement with Kr pressure 0.4 atm. The red line indicates the resonance line fit.

Table 4.1 shows the summary of the results of the center frequency obtained by the fit to each data sets. The data in 1.0 atm (run number 07) is from the previous measurement by MuSEUM [55].

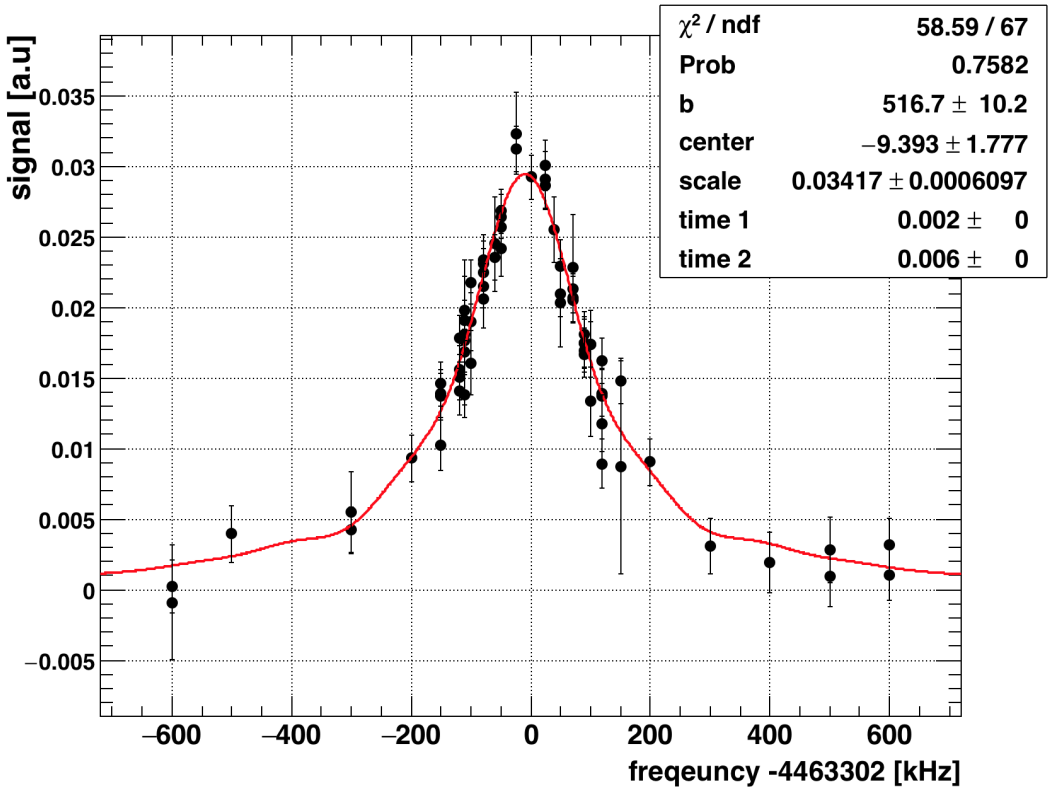

Figure 4.23: The resonance line observed at 0.3 atm.

4.2.7 Gas Pressure Extrapolation

To obtain the frequency of the muonium hyperfine structure interval at vacuum, one need to extrapolate the obtained results in several pressure points, as described in Fig. 4.25. There is a systematic effect from the uncertainty of the pressure gauge, which will be discussed in the latter section.

We obtain two resonance curves at 0.3 atm and four resonance curves at 0.4 atm. Combined with the result obtained by the pilot measurement at 1.0 atm, we have seven datasets at various pressures in total. The data points at each pressures are averaged (Fig. 4.26 and Fig. 4.27). We correct the gas density at $T = 0\,^{\circ}\mathrm{C}$, and extrapolate the results to the value at the zero density, as shown in Fig. 4.28. The fitting function is

$$f(D) = f(0)(1 + aD + bD^2), \tag{4.5}$$

where D is the gas density of the krypton at $0\,^{\circ}\mathrm{C}$. Here we use amagat as the unit of the density[1]. The temperature correction is discussed in the next chapter. There is a small quadratic term b in the pressure dependence of the frequency, which was measured by precursor experiment [20]. The parameter was fixed to the previously

[1]amagat is the unit of the density normalized to the density of the gas at 1 atm, $0\,^{\circ}\mathrm{C}$.

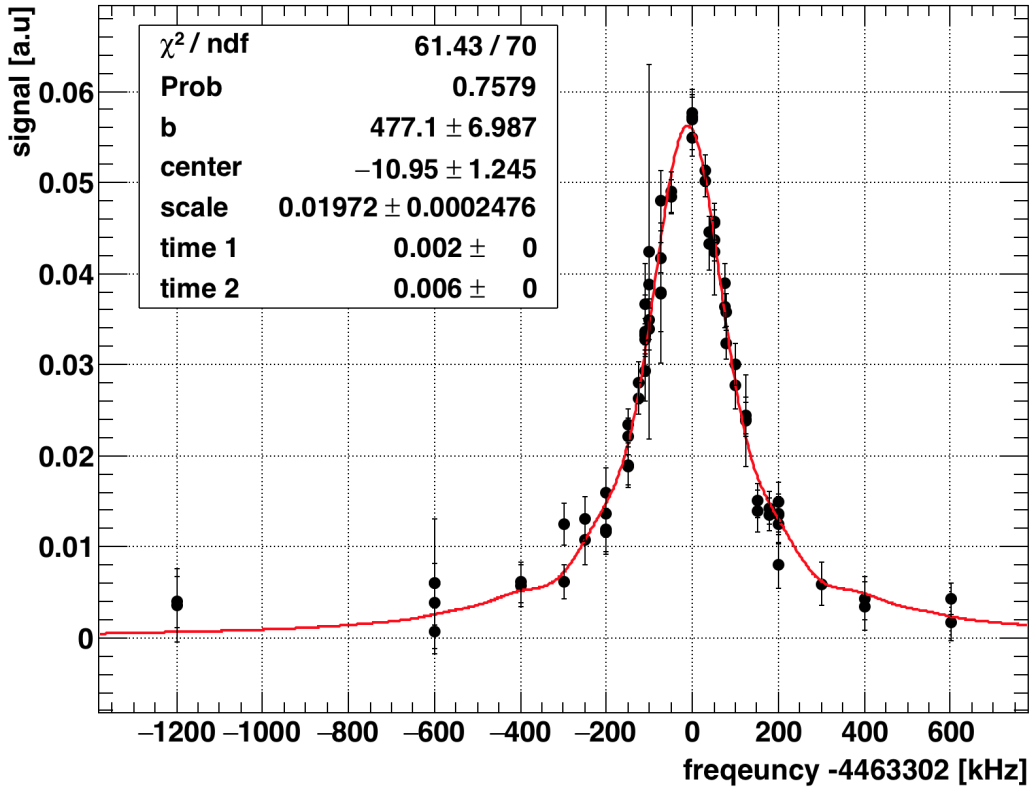

Figure 4.24: The resonance line obtained with krypton gas pressure 0.4 atm.

measured value,

$$b = (9.7 \pm 2.0) \times 10^{-15}\ \text{Torr}^{-2} \tag{4.6}$$

$$= (5.7 \pm 1.3) \times 10^{-9}\ \text{atm}^{-2}. \tag{4.7}$$

There is a small quadratic term b in the pressure dependence of the frequency. The effect of the uncertainty from the quadratic term is discussed in the later section.

The obtained MuHFS frequency in vacuo is

$$\Delta\nu_{\text{fit}} = 4.463\ 3055(23)\ \text{GHz}, \tag{4.8}$$

Table 4.1: Data Summary. Summary of the fit results for obtained resonance lines.

Run number	Gas pressure	Center Frequency [kHz]	Uncertainty [kHz]
01	0.4 atm	4 463 279.57	7.02
02	0.4 atm	4 463 293.10	8.90
03	0.4 atm	4 463 287.81	9.57
04	0.4 atm	4 463 291.17	1.24
05	0.3 atm	4 463 292.57	1.79
06	0.3 atm	4 463 288.43	5.04
07	1.0 atm	4 463 265.84	3.10

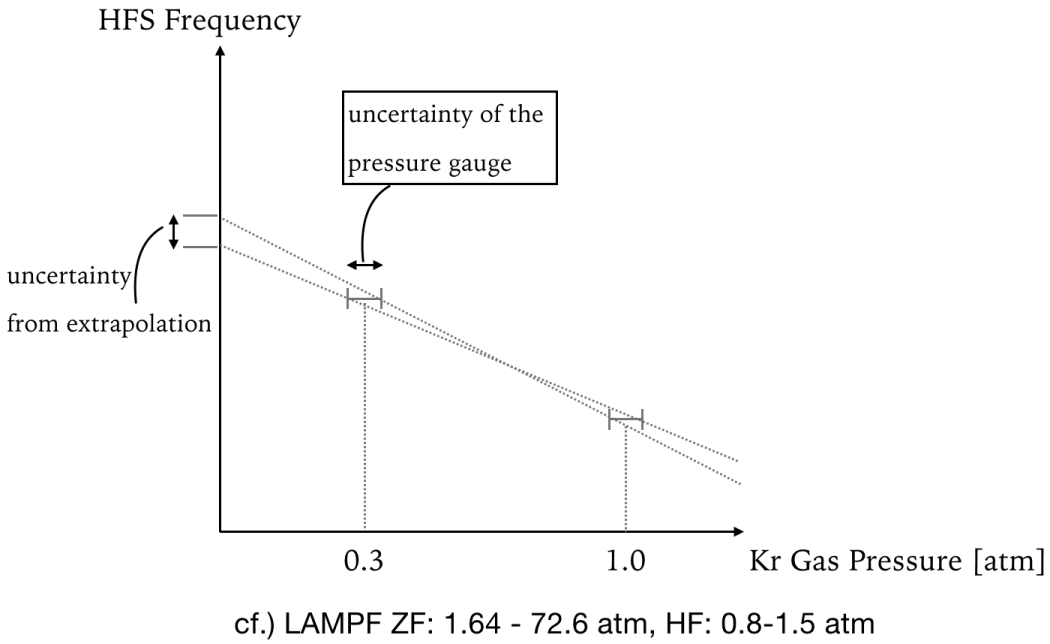

Figure 4.25: Concept of the gas pressure extrapolation and the systematic uncertainty from the precision of the gauge.

where the number in parentheses indicates the statistical uncertainty from the extrapolation. The obtained linear pressure dependence term a from the fit is

$$a = -(9.3 \pm 1.2) \times 10^{-6}\ \mathrm{atm}^{-1}. \tag{4.9}$$

The linear dependence a_{pre} obtained by the precursor experiment in high field at LAMPF [51] is

$$a_{\mathrm{pre}} = -(1.0627 \pm 0.0024) \times 10^{-8}\ \mathrm{torr}^{-1} \tag{4.10}$$

$$= -(8.077 \pm 0.018) \times 10^{-6}\ \mathrm{atm}^{-1}. \tag{4.11}$$

We also note that the hydrogen hyperfine pressure shift in krypton was also investigated by optical pumping [82], and yielded a similar value,

$$a_{\mathrm{H-HPS}} = -(1.04 \pm 0.02) \times 10^{-9}\ \mathrm{torr}^{-1} \tag{4.12}$$

$$= -(7.9 \pm 0.2) \times 10^{-6}\ \mathrm{atm}^{-1}. \tag{4.13}$$

The result obtained by our measurement is consistent with the value obtained at LAMPF within 2σ. We can also obtain the frequency in vacuum by using the data obtained by LAMPF [20] (Fig. 4.29), and the result is

$$\Delta\nu_{\mathrm{comb}} = 4.463\ 3029(8)\ \mathrm{GHz}, \tag{4.14}$$

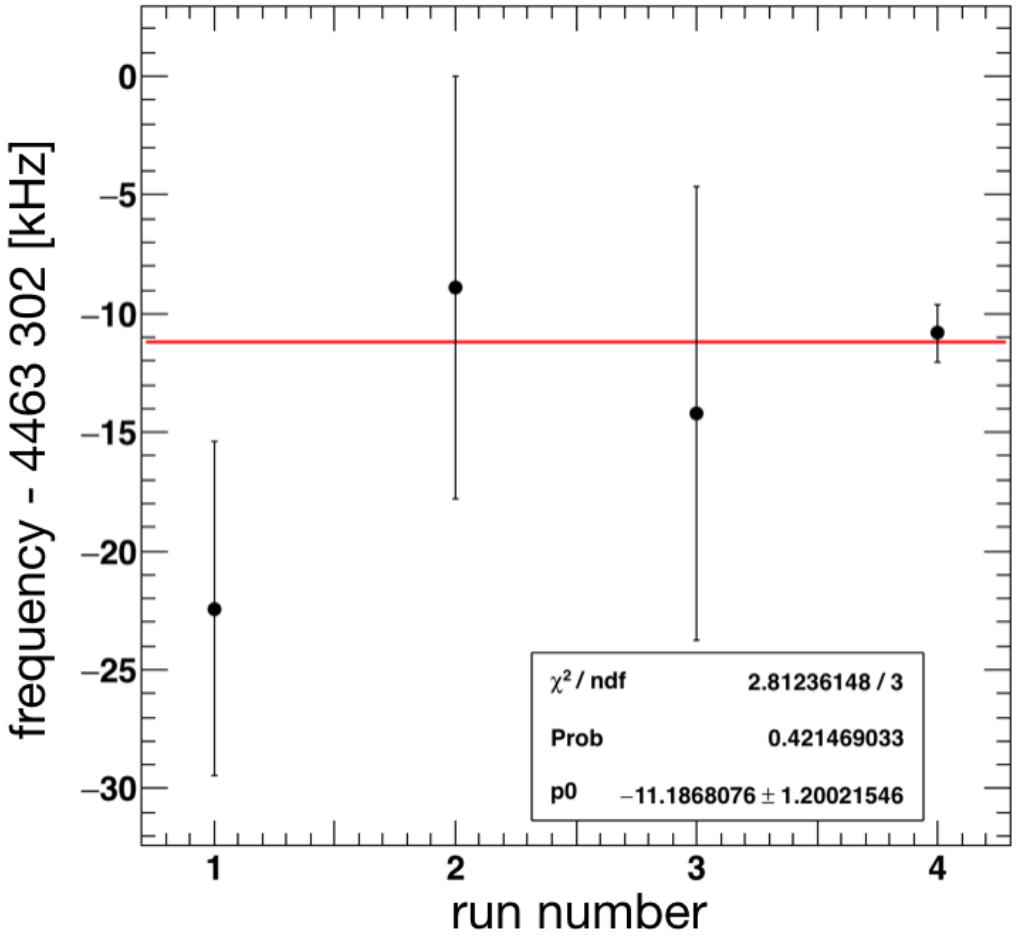

Figure 4.26: Averaging data points at 0.4 atm. The data points are the fitting result of the each run, and the red line is the averaged value.

where the number in parentheses indicates the statistical uncertainty (1σ) from the extrapolation, which is smaller than the case of the previous case. The obtained linear pressure dependence term a from the fit is

$$a = -(8.2 \pm 0.5) \times 10^{-6}\ \mathrm{atm}^{-1}. \tag{4.15}$$

The obtained quadratic pressure dependence term b from the fit is

$$b = (6.6 \pm 0.9) \times 10^{-9}\ \mathrm{atm}^{-2}. \tag{4.16}$$

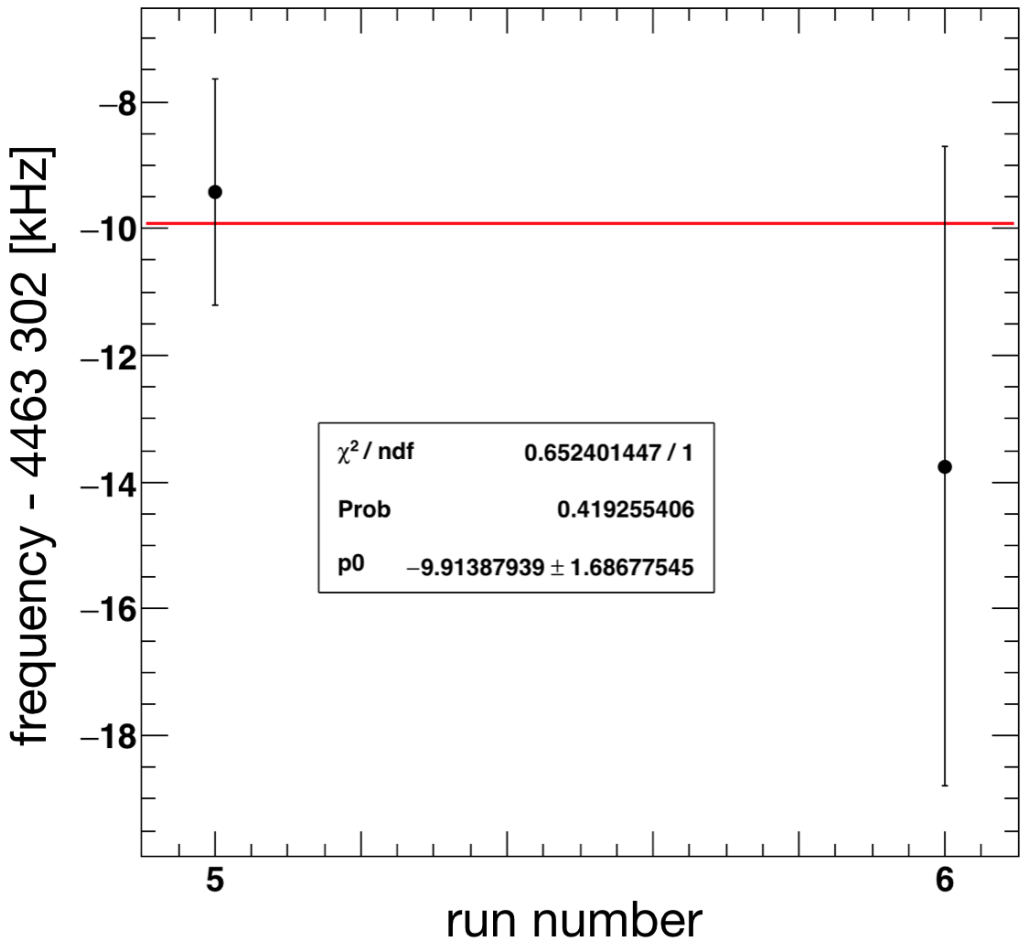

Figure 4.27: Averaging data points at 0.3 atm. The data points are the fitting result of the each run, and the red line is the averaged value.

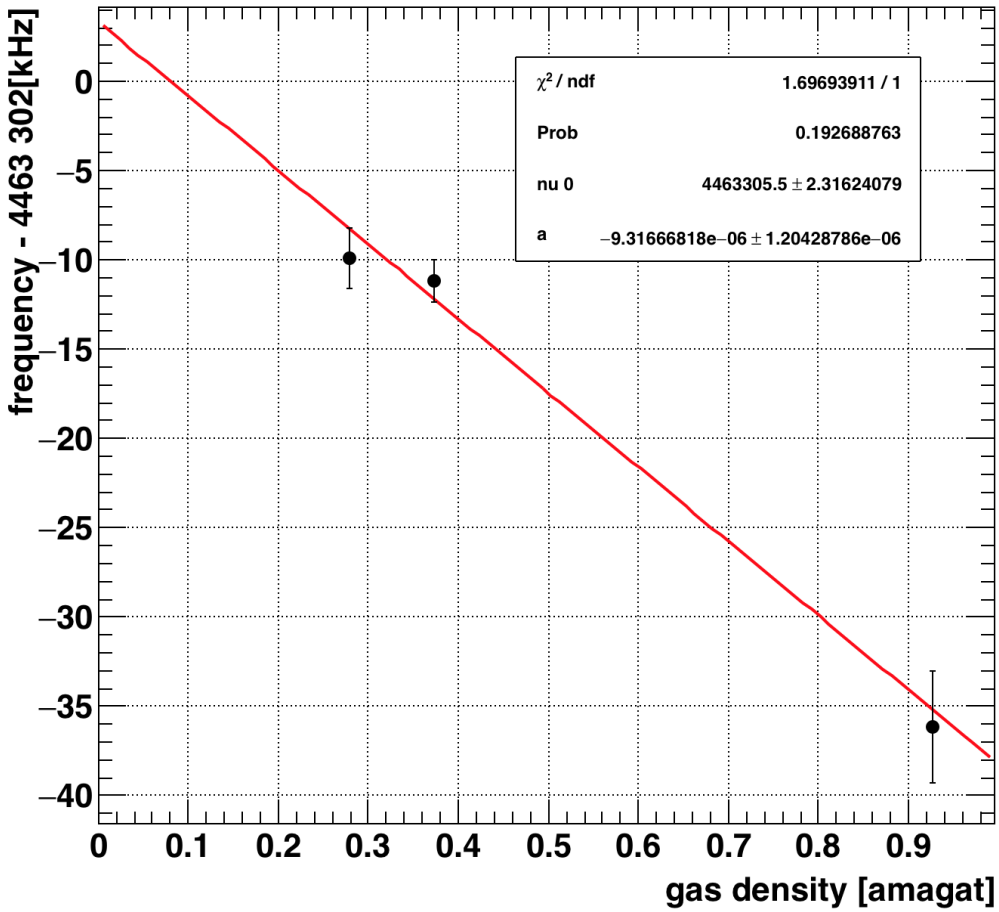

Figure 4.28: Gas pressure extrapolation. The data points are the result of the spectroscopy in various pressures. The red line is fit result by the function $f(D) = f(0)(1 + aD + bD^2)$ where b is fixed to the value obtained by the previous measurement, $b = 5.7 \times 10^{-9}$ atm^{-2}.

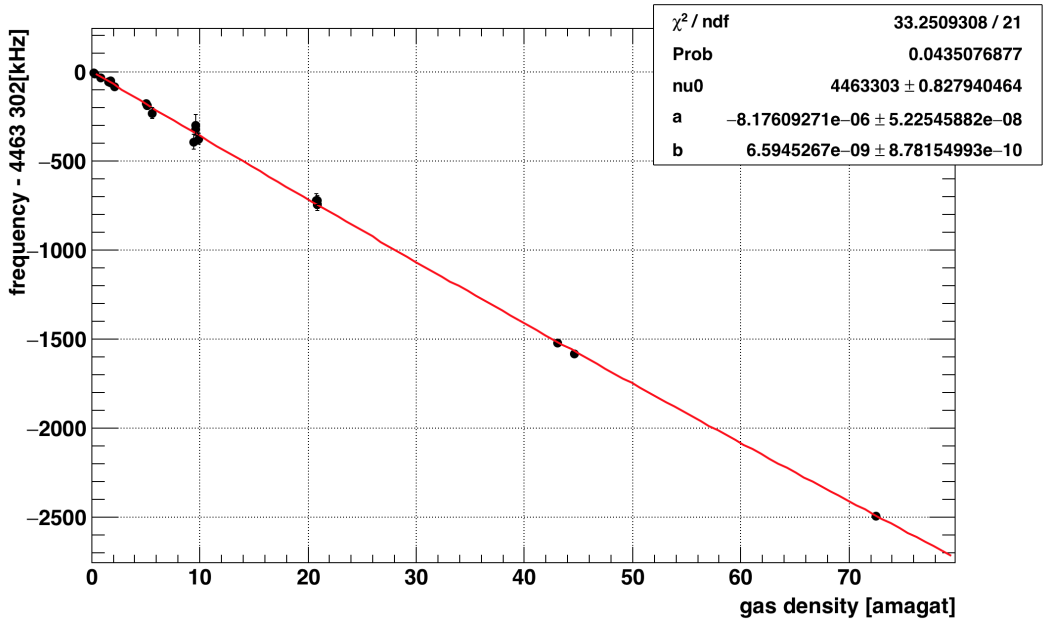

Figure 4.29: Gas pressure extrapolation combined with LAMPF data [20]. The red line is fit result by the function $f(D) = f(0)(1 + aD + bD^2)$.

Chapter 5

Result

5.1 Discussion of the Systematic Uncertainty

5.1.1 Gas System

The collision of a muonium atom with Kr atoms can shift the hyperfine frequency. The general review of the HFS pressure shift in gas has been reviewed by Happer in [83]. The two-body collision between Kr and Mu, which cause the frequency shift which is linearly dependent on the pressure. There is three-body interaction whose effect is proportional to the square of the krypton density.

The gas pressure was monitored by the capacitance gauge on the gas handling panel every ten seconds, while the temperature was monitored every second. The averages of these readings are taken for the resonance line.

Temperature

First, the pressure at $T = 0\,^{\circ}\mathrm{C}$ is calculated from the real gas equation

$$(P + \frac{a_v}{V^2})(V - b_v) = RT \tag{5.1}$$

where P is the pressure, V is the molar volume, R is the molar gas constant. The van der Waals constants a_v, b_v are [84],

$$a_v = 2.325 \text{ bar L}^2/\text{mol} \tag{5.2}$$

and

$$b_v = 0.0396 \text{ L/mol}. \tag{5.3}$$

Using the equation above, we calculate the pressure at $T = 0\,^{\circ}\mathrm{C}$. The correction is already implemented in the figures and results in Sec. 4.2.7. Figure 5.1 shows the temperature in a day. There are some effect on the gas temperature from the temperature from the experimental hall. The systematic effect of the temperature variation is included in the variation of the gas pressure, which will be discussed in the next section.

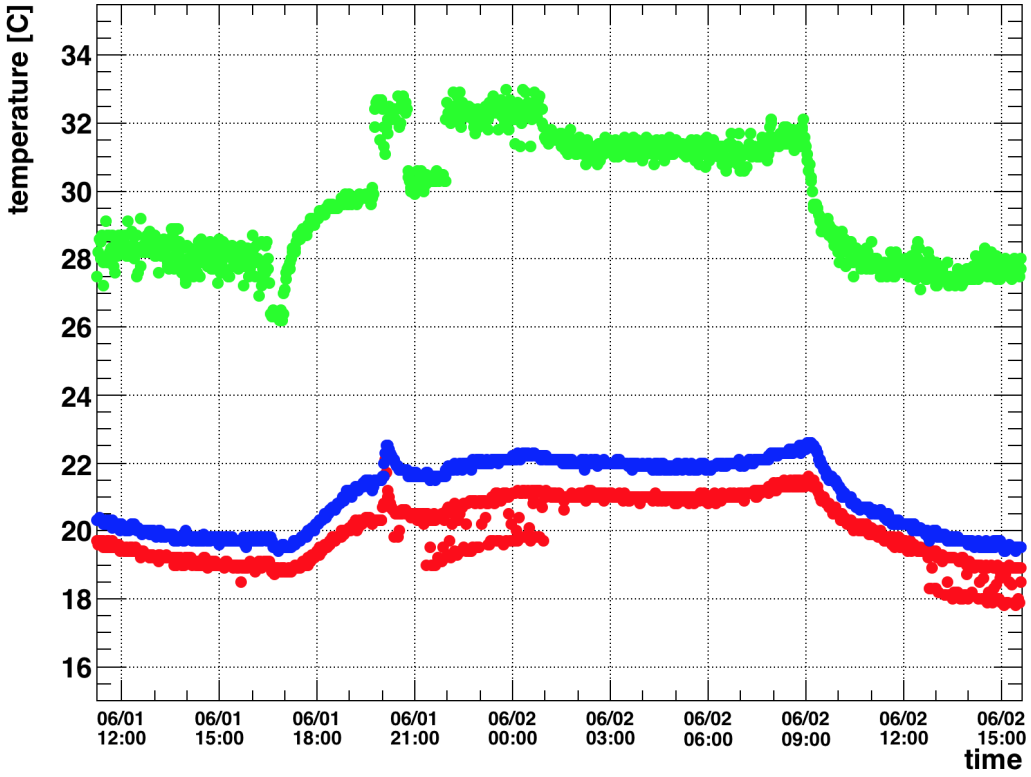

Figure 5.1: Temperature variation. The green points are the temperature in the experimental hall. The red points are the data in the magnetic shield and out of the gas chamber. The blue points indicate the gas temperature in the gas chamber. Due to the cooler for detectors, the temperature in the shield is lower than those in the experimental hall. There is a rise in temperature in the experimental hall after 5 p.m. (17:00) when the coolers in the hall are stopped automatically. As a consequence, the gas temperature also rises after some time. The temperatures decline after 9 a.m. when the coolers are activated. The cooler inside the shield was always on during the data taking.

Gas Pressure Fluctuation

Figure 5.2 shows the typical fluctuation of the monitored gas pressure. During the measurement, typically ± 100 Pa fluctuation at maximum in a day was observed. This fluctuation includes the temperature drift. We correct the change from the temperature variation and calculate the residual gas pressure variation. Figure 5.3 shows the distribution of the corrected gas pressure during the two days of 0.4 atm measurement. The standard deviation is 68 Pa, and for the other measurements, the standard deviation is smaller than 68 Pa. We account the pressure shift resulting from the 68 Pa change as the systematic uncertainty, i.e., 24 Hz.

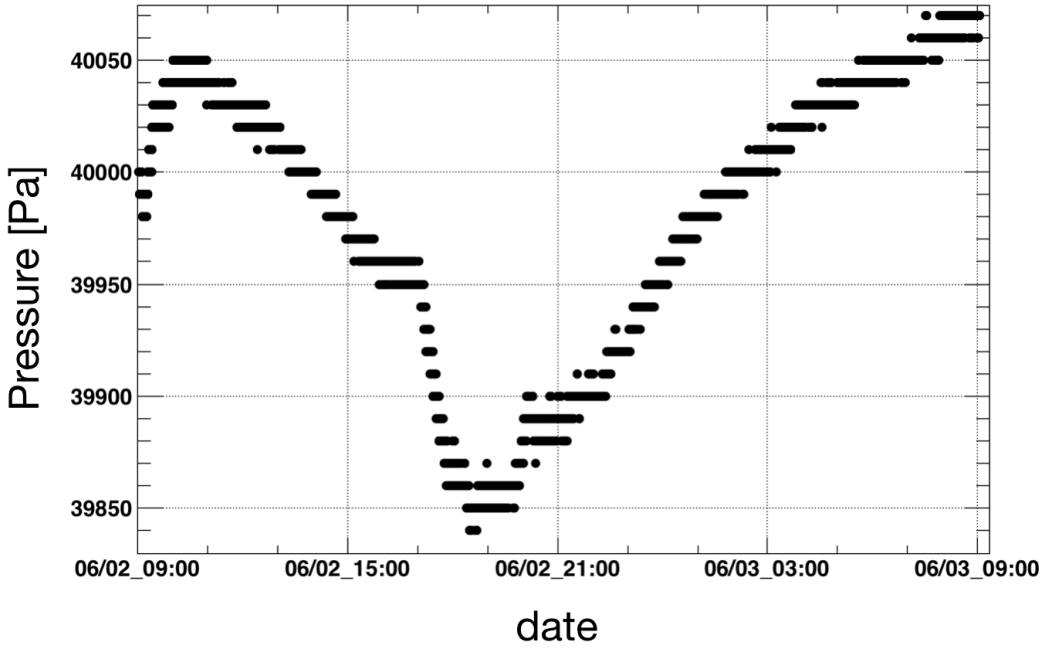

Figure 5.2: Gas pressure variation in one day monitored by the capacitance gauge. The variation includes the change due to the temperature variation.

Uncertainty in the Gas Pressure Gauge

We used the capacitance gauge which has an accuracy of 0.2% full scale. Thus we have the uncertainty in gas pressure $\delta P = 0.002$ atm. We reanalyze the gas pressure extrapolation after a shift $\pm\delta P$ is introduced to the data set and obtain

$$\delta\nu_{\delta P} = \pm 79 \text{ Hz}. \tag{5.4}$$

We conclude the systematic uncertainty is 79 Hz. In the future, this uncertainty is readily improved by using a pressure gauge with an accuracy of 0.01%.

Uncertainty from the Quadratic Term

There are quadratic term arising from the three-body interaction of Mu and Kr. We use the most precise measurement of the parameter [20] for the fit of $\Delta\nu_{\text{fit}}$,

$$b = (9.7 \pm 2.0) \times 10^{-15} \text{ Torr}^{-2} \tag{5.5}$$

$$= (5.7 \pm 1.3) \times 10^{-9} \text{ atm}^{-2} \tag{5.6}$$

The effect of the uncertainty in the expression above is estimated by reanalysing the gas pressure extrapolation using different parameters for b,

$$b_{\text{upper}} = 7.0 \times 10^{-9} \text{ atm}^{-2} \tag{5.7}$$

$$b_{\text{lower}} = 4.4 \times 10^{-9} \text{ atm}^{-2}. \tag{5.8}$$

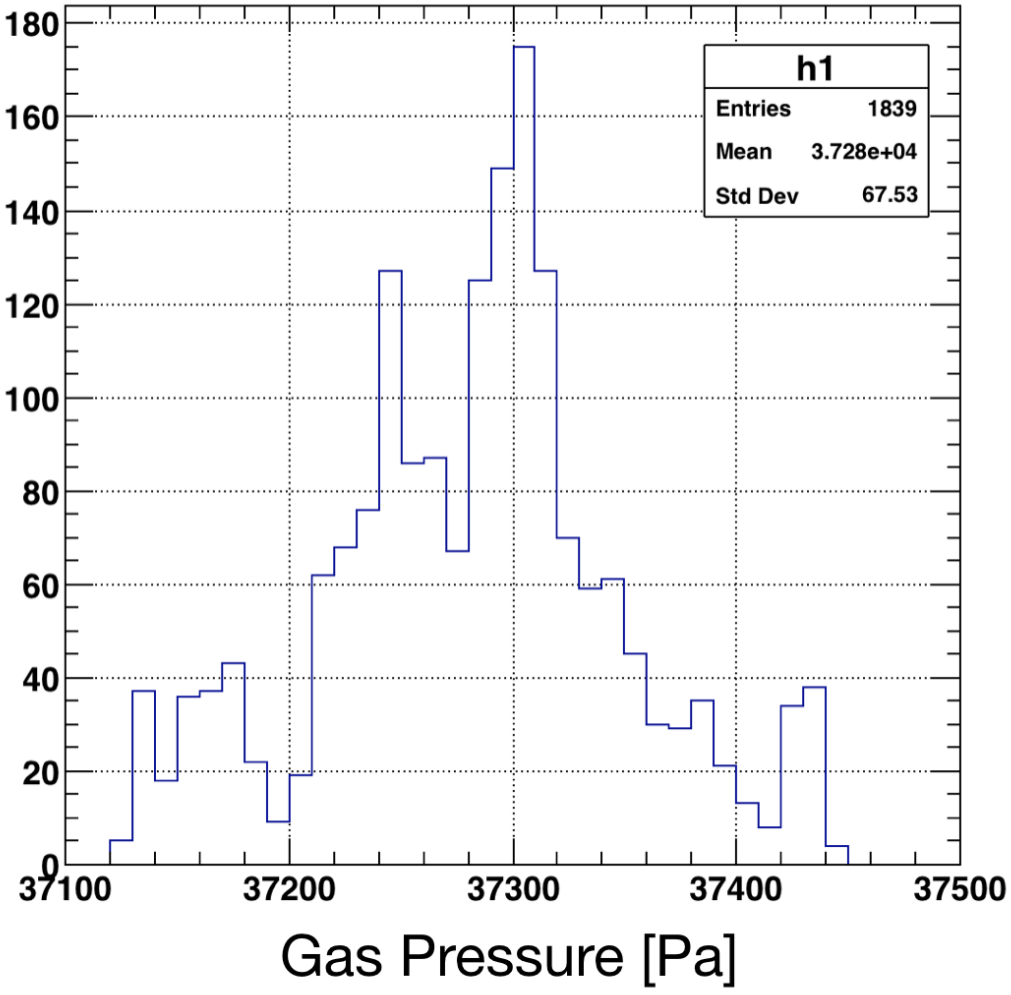

Figure 5.3: Gas pressure variation after the temperature correction. The standard deviation of the gas pressure is accounted as the source of the systematic uncertainty.

The deviation from the original result $\Delta\nu_{\rm fit}$ is ± 2 Hz. Note that the uncertainty is smaller than the corresponding uncertainty at the precursor experiment [19] by a factor of two, since we succeeded in the measurements at lower krypton pressures.

Gas Impurities

Gas impurities were measured by QMASS before the experiment. The gas inside the chamber was exchanged after 24 hours. The contamination of H_2 and O_2 after 24 hours was estimated to be at most 1 ppm. The muonium HFS shift in hydrogen was estimated by Liu in [51] to be

$$\frac{\partial \Delta\nu}{\partial P_H} \approx 16 \text{ kHz/atm}. \tag{5.9}$$

The 1 ppm contamination of hydrogen in 1 atm krypton gas corresponds to the frequency shift of 0.016 Hz, and it is negligible.

5.1.2 Microwave

Signal Generator and Frequency Reference

The signal generator used in this experiment has a reference OCXO, and its frequency is calibrated with a precision of 10^{-8}, 45 Hz. Frequency drift from aging is less than 10^{-9} per day, which is negligible. We account 45 Hz as the corresponding systematic uncertainty for MuHFS. In the future, a frequency reference using GPS (Global Positioning System) will ameliorate the uncertainty. We abdicated the installation of the GPS antennae on the outer wall and the signal cable through a hole on the wall for the experimental hall No.2, where the experimental area D2 is located, due to the severe limitation from radiation safety in the hall. For the new beamline H1 in the experimental hall No. 1, the installation of the GPS antennae and the signal cable is ongoing.

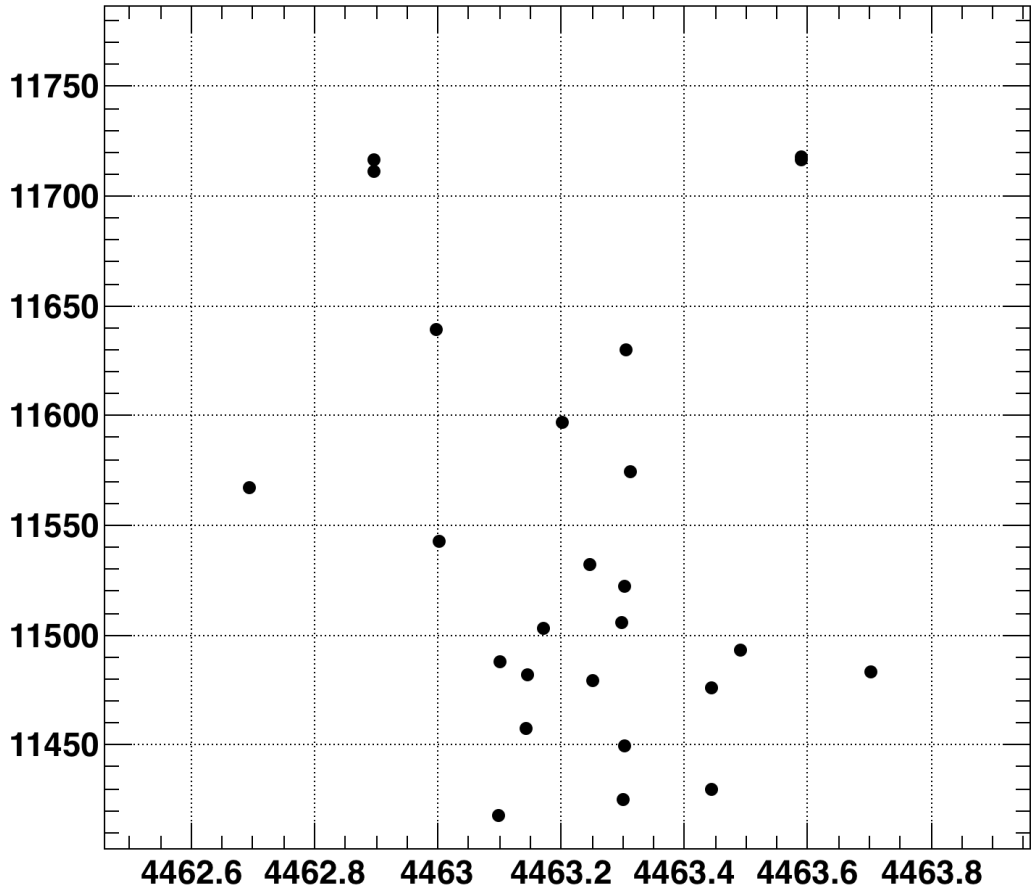

Figure 5.4: Q values for different frequencies. Due to the thermal expansion of the cavity from microwave power or other factors, Q value varies in time, and two measurement result in the same frequency are not always identical, although the fluctuation is small ($\pm$ 1.5%).

Microwave Power Drift

In the measurement, we spent approximately 20 minutes or less for each frequency point, and then move on to the next frequency. If the microwave power changes for different microwave frequencies, the effect would distort the resonance line shape, and shift the center of the resonance. The typical microwave drift during the time (20 min) was 1%. By randomly choosing the sequence of the frequency points, we can suppress the shit caused by the power drift. The systematic uncertainty caused by the power drift is estimated to be 60 Hz by the numerical simulation of the resonance line shape with the power drift of 1% per frequency point. In the future experiment, the systematic uncertainty can be suppressed by the feedback of the microwave power, and by realizing the shorter measurement period for each frequency point.

5.1.3 Magnetic Field

The magnetic field was measured before the beam time and typical value of the field strength is 1 mG. This corresponds to the shift of $\Delta\nu_{14}$ ($\Delta\nu_{34}$) by 1.4 kHz (-1.4 kHz), which is relatively small to the natural linewidth 145 kHz. The effect is symmetric and we conclude the effect is negligible.

5.1.4 Muon Beam

Beam Intensity Fluctuation

The muon beam intensity fluctuation between the beam pulses with microwave ON and the beam pulses with microwave OFF may cause the change in the signal height and may shift the signal center. The microwave is switched ON and OFF for each pulse (25 Hz) in the measurement, and drastically suppresses the systematic uncertainty caused by the beam intensity fluctuation. This is one of the major accomplishment of the measurement in 2018. In J-PARC, proton beam power is measured by the accelerator division. The typical intensity drift of the beam is 0.1% for ten minutes, and we assume the intensity drift in two pulses (in 80 ms) is negligibly small. In the future, an online beam monitor using very thin scintillation fibers can realize another method of the beam intensity measurement [54].

Muon Beam Profile

Change of the muon beam profile (e.g., a slight shift of the muon beam profile center) during the microwave frequency scan result in the change of the microwave field strength felt by muoniums, and this changes the resonance line shape. We made the pre-measurement of the beam profile change in time using the beam profile monitor described in Appendix A. No significant change of the profile observed with

the monitor's resolution of ±0.6 mm. This amounts to an effective change of the microwave power by 0.1%, corresponding to the 6 Hz uncertainty from the shift of the resonance center.

5.1.5 Others

Electric Field

There are several studies about the dependence of the hydrogen HFS interval on an external electric field, [85, 86, 87, 88]. For the 1.4 GHz of the hydrogen HFS, the theoretical and the experimental values for the shifts $\delta\nu_{\mathrm{H}}$ with E in volts per meter are

$$\vec{E} \parallel \vec{B} \quad \text{Expt.} \qquad \delta\nu_{\mathrm{H}} = (-8.37 \pm 0.84) \times 10^{-14} \qquad E^2\mathrm{Hz} \tag{5.10}$$

$$\text{Theory} \qquad \delta\nu_{\mathrm{H}} = -8.47 \times 10^{-14} \qquad E^2\mathrm{Hz} \tag{5.11}$$

$$\vec{E} \perp \vec{B} \quad \text{Expt.} \qquad \delta\nu_{\mathrm{H}} = (-8.45 \pm 0.20) \times 10^{-14} \qquad E^2\mathrm{Hz} \tag{5.12}$$

$$\text{Theory} \qquad \delta\nu_{\mathrm{H}} = -8.24 \times 10^{-14} \qquad E^2\mathrm{Hz}. \tag{5.13}$$

Assuming the fractional shits for the hydrogen HFS and the MuHFS are the same, we can estimate the shift for MuHFS,

$$\delta\nu = -2.6 \times 10^{-13} E^2\mathrm{Hz}. \tag{5.14}$$

It is thus negligible for the current precision of the experiment.

Bloch-Siegert Term

In the section of the theory of the resonance line shape, we neglect one of the two components of the microwave term, one rotating clockwise and one rotating counter-clockwise. The neglected term can shift the resonance line center and this term was first calculated by Bloch and Siegert [89], thus being called the Bloch-Siegert term. The shift was also derived by Shirley [90]. The 1st order shift expressed in angular frequency is

$$\frac{b^2}{\omega} \tag{5.15}$$

where b is the microwave b parameter also used in Chap. 2, ω is the angular frequency of the transition.

If the microwave b parameter is $b = 200$ kHz, then the frequency shift caused by the Bloch-Siegert term $\delta\nu_{\mathrm{BS}}$ for MuHFS (frequency = 4.463 GHz) is

$$\delta\nu_{\mathrm{BS}} = \frac{1}{2\pi} \frac{(200\ \mathrm{kHz})^2}{(2\pi \times 4.463\ \mathrm{GHz})} = 0.2\ \mathrm{Hz} \tag{5.16}$$

and we conclude it is negligible compared to the precision of the current experiment.

As derived in [90], the 2nd order shift is suppressed by a factor of $b^2/4\omega^2 = 10^{-11}$, and it is also negligible.

Off Resonance Term

There is another term which was neglected in the section of resonance line shape (Sec. 2.4), the off resonance term. The detailed discussion of the effect by neglecting the term can be found in [91]. The frequency shift $\delta\nu_{14}$ and $\delta\nu_{34}$ by neglecting the term can be calculated as below,

$$\delta\nu_{14} = \left(\frac{b_{14}}{2\pi}\right)^2 \left[\frac{1}{\nu_{12}-\nu_{14}} - \frac{1}{-\nu_{34}-\nu_{14}}\right] \tag{5.17}$$

$$\delta\nu_{34} = \left(\frac{b_{34}}{2\pi}\right)^2 \left[\frac{1}{-\nu_{34}-\nu_{23}} - \frac{1}{-\nu_{34}-\nu_{14}}\right], \tag{5.18}$$

and if we substitute $b = 200$ kHz, the shifts $\delta\nu_{14}$ and $\delta\nu_{34}$ amount to -0.1 Hz and 0.1 Hz, respectively. Therefore we can conclude the systematic uncertainty related to the term is negligible.

Blackbody Radiation

For the cesium atomic clocks using microwave, one of the important systematic uncertainties is the Stark shift caused by the Blackbody Radiation (BBR). The shift is discussed both experimentally and theoretically in pieces of literature [92, 93], the correction is estimated to be the order of 10^{-14} [94, 95]. Thus we conclude the effect is negligible for the current case of the MuHFS.

5.2 Result

In conclusion, we developed a new microwave cavity to measure the MuHFS at low Kr pressure points, i.e., 0.3 atm and 0.4 atm. To obtain the MuHFS frequency in vacuo, we applied pressure extrapolation. Pressure extrapolation was conducted in two ways; one is the extrapolation using data sets at J-PARC only and the other is the extrapolation using the linear term obtained by the precursor experiment in high field at LAMPF [51]. From the first way of the extrapolation, we obtain,

$$\Delta\nu_{\text{fit}} = 4.463\ 3055(23)\ \text{GHz}, \tag{5.19}$$

and

$$a = -(9.3 \pm 1.2) \times 10^{-6}\ \text{atm}^{-1}. \tag{5.20}$$

The systematic uncertainty in total is 112 Hz. Table 5.1 is the summary of the systematic uncertainty. The most dominant source of the systematic uncertainty is the precision of the gauge, which can be ameliorated by using a gauge with better precision. The second largest uncertainty (Power drift) can be suppressed by the feedback of the microwave power and water cooling of the cavity. The third largest term (Frequency reference) will be improved by using GPS as the reference.

Table 5.1: Summary table of the systematic uncertainty. The figure in a parenthesis indicates the systematic uncertainty of the combined result of our data set and the previous measurements at LAMPF [52].

Contribution	Uncertainty [Hz]
Pressure Gauge	79(127)
Pressure Fluctuation	24
Quadratic Term	2(0)
Frequency Reference	45
Power Drift	60
Muon Beam	6
Others	< 1
Total	112(150)

From the second way of the extrapolation, we obtain

$$\Delta\nu_{\mathrm{comb}} = 4.463\ 3029(8)\ \mathrm{GHz}. \tag{5.21}$$

The total systematic uncertainty, in this case, is 150 Hz. The value of the systematic uncertainty for a pressure gauge in the previous measurement in LAMPF was 100 Hz [52], so we account $\sqrt{100^2 + 79^2} = 127$ Hz as the systematic uncertainty.

Figure 5.5 shows the summary plot of our results (the red point is for our result only, the blue point is the combined result of our data and LAMPF data), the theoretical value (gray band), and the result obtained by precursor experiments at LAMPF (black points). The point $\Delta\nu_{\mathrm{LF}}$ shows the result of the precursor experiment in very weak field [20], and the point $\Delta\nu_{\mathrm{HF}}$ indicates the result of the precursor experiment in high field [19]. Our results were consistent with theoretical value and the results of the precursor experiments.

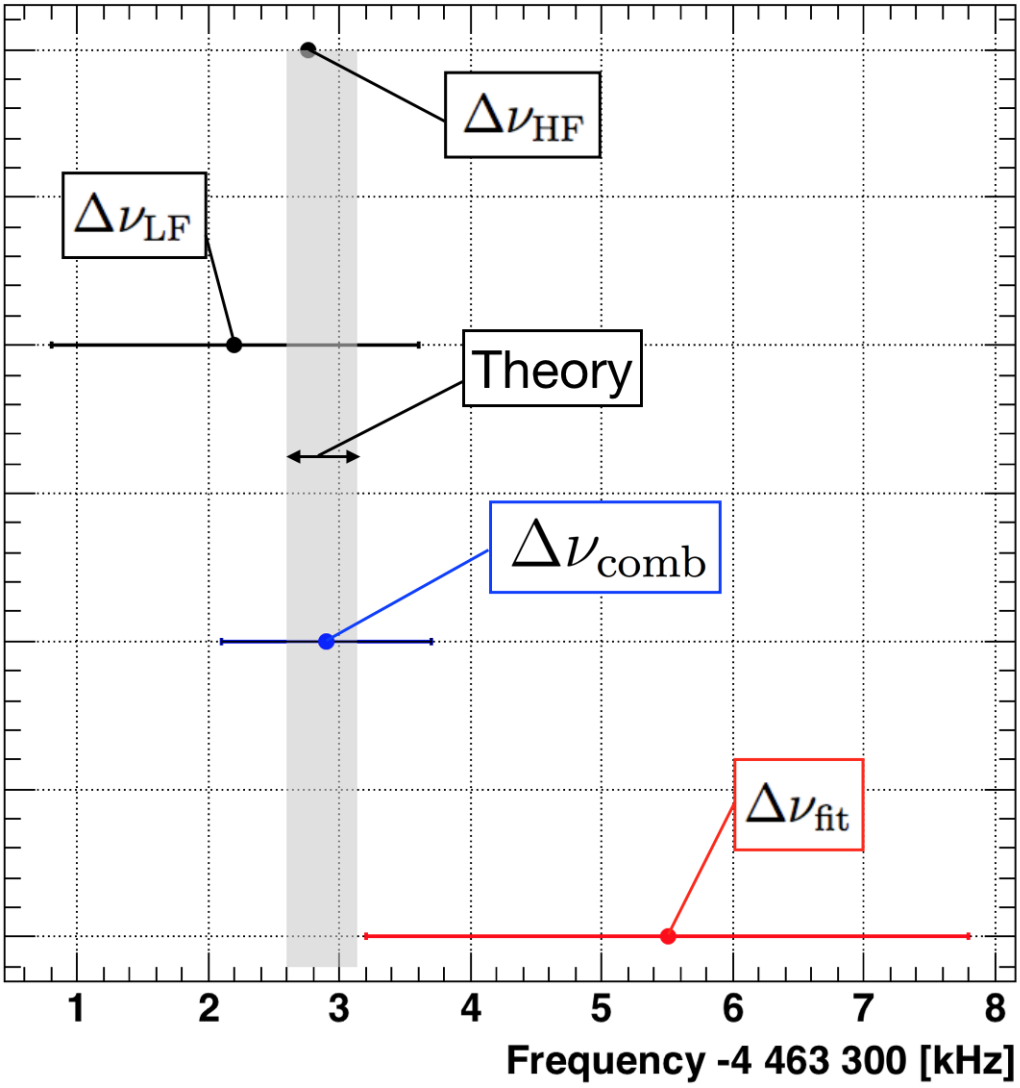

Figure 5.5: Summary plot of our results. The red point is for our result only, the blue point is the combined result of our data and LAMPF data. The gray band shows the theoretical value, and the black points are the result obtained by precursor experiments at LAMPF. Our results were consistent with theoretical value and the precursor experiment.

Chapter 6

Conclusion and Outlook

6.1 Conclusion

In conclusion, we measured the MuHFS at Kr pressure points 0.3 atm, 0.4 atm. Combining the results with the data at 1.0 atm, which was obtained previously by the MuSEUM group, we extrapolate the results from these data sets to obtain the MuHFS frequency in vacuo. The obtained value is

$$\Delta\nu_{\rm fit} = 4.463\ 3055(23)\ \text{GHz}, \tag{6.1}$$

where the number in the parenthesis is the statistical uncertainty in 1σ and the systematic uncertainty was estimated to be 112 Hz. As shown in Fig. 5.5, the result is consistent with the precursor experiments at LAMPF and the theoretical calculation.

The linear pressure dependence term a of the MuHFS is determined to be

$$a = -(9.3 \pm 1.2) \times 10^{-6}\ \text{atm}^{-1}. \tag{6.2}$$

It is consistent with the linear dependence $a_{\rm pre}$ obtained by the precursor experiment in high field at LAMPF [51];

$$a_{\rm pre} = -(8.077 \pm 0.018) \times 10^{-6}\ \text{atm}^{-1}. \tag{6.3}$$

We also made a combined analysis of our data and LAMPF data, obtaining

$$\Delta\nu_{\rm comb} = 4.463\ 3029(8)\ \text{GHz}, \tag{6.4}$$

which is also consistent with the previous measurements and the theory. We also obtained linear and quadratic term of the pressure dependence from the combined data,

$$a = -(8.2 \pm 0.5) \times 10^{-6}\ \text{atm}^{-1} \tag{6.5}$$

and

$$b = (6.6 \pm 0.9) \times 10^{-9}\ \text{atm}^{-2}. \tag{6.6}$$

The result of the quadratic term is consistent with the previous measurement [20],

$$b = (5.7 \pm 1.3) \times 10^{-9}\ \text{atm}^{-2}. \tag{6.7}$$

6.2 Outlook

6.2.1 Systematic Uncertainty

Table 5.1 is the summary of the systematic uncertainty. The most dominant source of the systematic uncertainty is from the precision of the capacitance pressure gauge (79 Hz). The precision of the gauge is 0.2%. This systematic uncertainty can be ameliorated by using a gauge with better precision. One of the candidates of such pressure gauge is RPM4-AD (by Fluke Calibration), which has a precision of 0.2% and it is commercially available. If we use the gauge, the uncertainty will be suppressed to be 8 Hz.

The second largest uncertainty is power drift (60 Hz). This systematic uncertainty is caused by the drift of the microwave power during the scan of the resonance line. Typically it took 20 minutes for the measurement at one frequency point. The fluctuation of the microwave power during the time is 1%. Microwave feedback can suppress such fluctuation to 0.02%. Also, we can suppress the uncertainty by reducing the time consumed for the resonance line scan. The future systematic uncertainty is estimated to be 1 Hz.

The third largest term (Frequency reference, 45 Hz) is from the uncertainty of the frequency reference in the microwave signal generator. It will be improved by using the GPS as the reference of the microwave frequency. GPS can suppress the uncertainty less than 1 Hz. Table 6.1 shows the summary of the prospect of systematic uncertainty in the future experiment.

Table 6.1: Summary table of the future prospect of the systematic uncertainties.

Contribution	Uncertainty [Hz]
Pressure Gauge	8
Pressure Fluctuation	2
Quadratic Term	0
Frequency Reference	1
Power Drift	1
Muon Beam	6
Others	< 1
Total	10

6.2.2 Statistical Uncertainty

In this thesis, we used data obtained with the muon intensity $5{\times}10^6$ μ^+/s in three days. Most statistics are gained by the two data set using old muonium method, obtained in two days. For experiments in the future, a new beamline (H-Line) under

construction will enhance the available number of the muons per second by a factor of ten. Also, the proton beam power will be upgraded from 500 kW to 1 MW, so a factor of 20 improvements in total is expected. The new beamline is a dedicated facility for the fundamental-physics experiments using muons, and MuSEUM expects more than 100 days of physics-run with the new beamline. With 100 days of run in the H-Line, a factor of $\sqrt{20 \times 100/2} = 32$ improvement of the statistical uncertainty is feasible, so the measurement with the statistical uncertainty 800 Hz/31 = 25 Hz is achievable. Additional studies, such as the improvement of the Signal-to-Noise ratio, can ameliorate the statistics further.

Figure 6.1 shows the summary of the uncertainties of the precursor experiments at LAMPF (gray bar) and our result (red), as well as the combined result (blue) and the prospected result with H-Line (magenta). Note that the uncertainty is statistical only.

Improvements in the analysis method may contribute to the suppression of the statistical uncertainty. The averaging of the results obtained from the old muonium method with narrower time windows (e.g., averaging the result of the old muonium signals at 2-3 μs, 3-4 μs, 4-5 μs, and 5-6 μs.) is one of the candidates. Another promising candidate for the analysis method is the time-differential method. The time-differential method is a method which obtains the resonance frequency by fitting the time-dependent signal (shown in 4.21), without fitting the resonance line itself. The method is discussed elsewhere in detail [55].

The separated oscillating field (SOF) method (Ramsey interferometry method) is another promising method for reducing the statistical uncertainty [52, 96], since it will give a narrower resonance line than the conventional method as well as the signal height will be doubled. In the method, one applies two separated microwave field so the cavity filling time $\tau = Q/\omega$ should be smaller than muon lifetime. In the case of $\tau = 100$ ns, the Q factor should be lower than 2800, and one must apply microwave with a higher power. This may cause an additional source of systematic uncertainty by heating due to the power loss at the surface of the cavity.

6.2.3 High field

This thesis focused on the measurement at a very weak field, but high field measurement will play an important role in the MuSEUM project, especially in terms of the synergy with muon g-2. The measurement in high field expects a higher statistics than the measurement in low field, since decay positrons are guided along the beam axis by the Lorentz force in the magnetic field, which is applied parallel to the beam axis, and they are more likely to hit the detector.

In high field, we can measure the MuHFS by sweeping the magnetic field strength as well as by sweeping the microwave frequency. These two different measurement methods can contribute to the reduction of the systematic uncertainty.

There is an additional systematic uncertainty source for high field measurement, one from the applied magnetic field. For the determination of the muon magnetic moment, the magnetic field becomes the dominant source of systematic uncertainty. Preparation of a magnetic field with a uniformity of 1 ppm [97] and precise magnetometers using Nuclear Magnetic Resonance (NMR) [98] can suppress systematic uncertainty. Recent measurement using a prototype of NMR magnetometer yield a precision of 18 ppb [99], which is promising for the measurement of the muon magnetic moment with unprecedented precision. The estimated systematic uncertainty in high field is 2 ppb for HFS and 20 ppb for the muon magnetic moment [97].

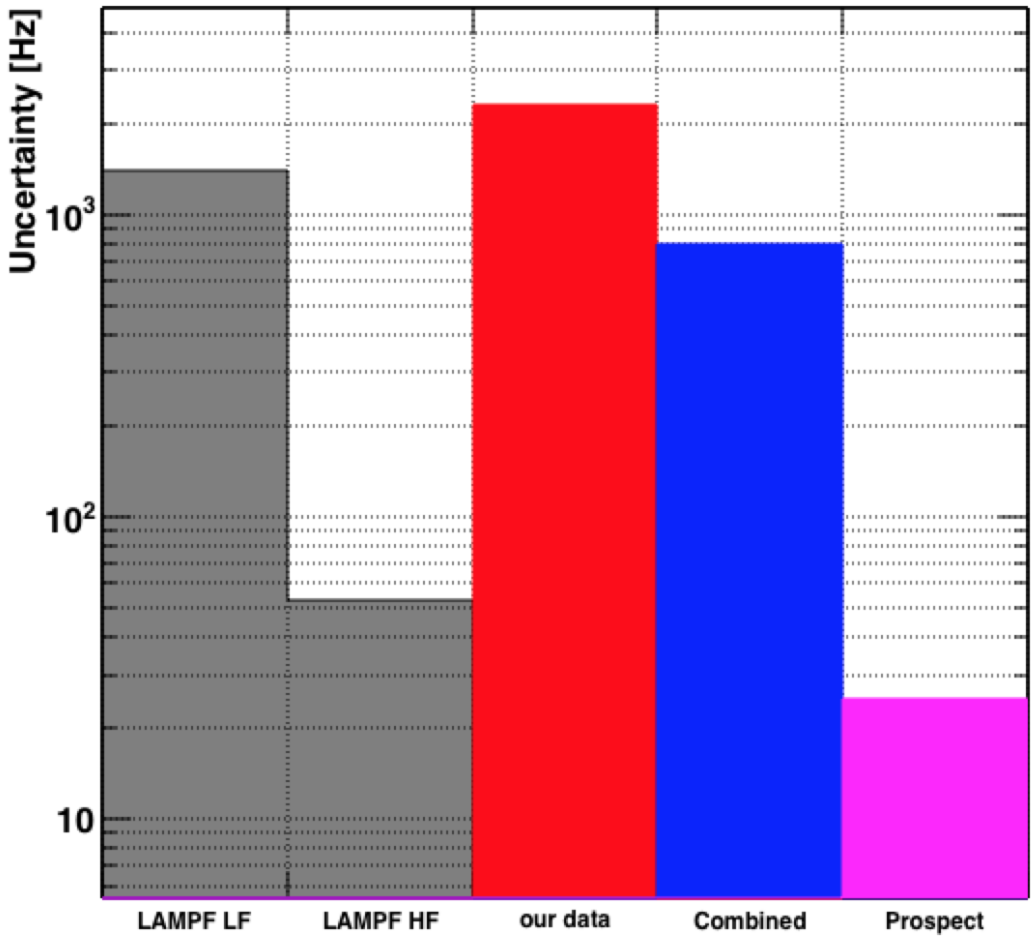

Figure 6.1: Statistical uncertainties of the previous and current experiments, in addition to the future prospect. The gray bars indicate the uncertainty of the previous experiments at LMAPF. The red and blue bars are the uncertainties of the result from our data and the combined result, respectively. The magenta bar is the prospect of the uncertainty in an experiment with H-Line 100-days run (25 Hz).

Appendix A

Beam Profile Measurement

A.1 Introduction

In this appendix, we discuss the measurement of the muon beam profile or the beam stopping distribution in the krypton gas target. The prototype of the measurement system is described elsewhere [100]. The data was used for the validation of the stopping distribution simulation using GEANT4 [79]. We discuss the measurement procedure including the apparatus for the profile measurement in Sec. A.2, and the result in Sec. A.3. The simulation validated here was used in the discussion of the new cavity in Sec. 3.5.2.

A.2 Measurement Procedure

A.2.1 Setup

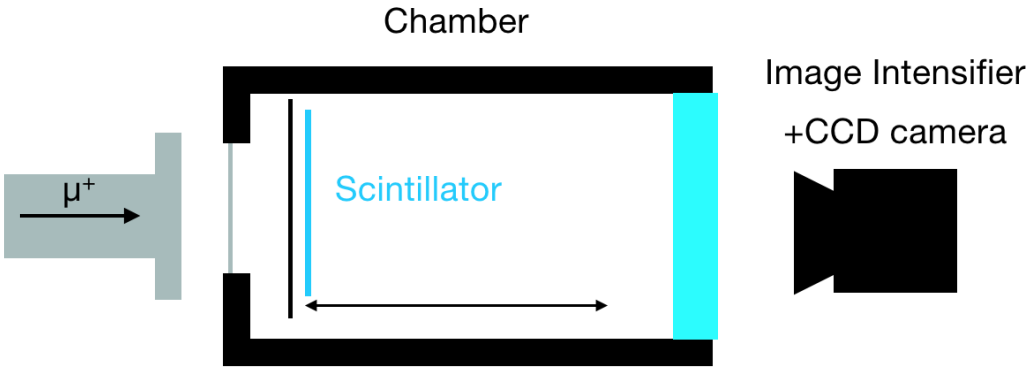

Figure A.1: A schematic diagram of the beam profile measurement.

We developed a measurement system, which consists of a profile measurement chamber, a scintillator, a Charge-Coupled Device (CCD) camera, and ancillary apparatus. Figure A.1 shows the schematic diagram of the beam profile measurement.

The chamber contains krypton gas and the scintillator, and its scintillation light is amplified by an image intensifier (IIF) before captured by the CCD camera. From the image obtained by the CCD camera, we determine the cross-sectional profile of the muon beam, as well as the light yield. One can move the position of the scintillator along the muon beam axis (longitudinal axis). After the move, the CCD captures the image again. We can also determine how many muons are stopped in the region between the first position of the scintillator and the second position of the scintillator, by taking the difference of the light yields of the two positions. By measuring at several positions, we can determine the muon longitudinal stopping distribution in the gas.

A beam profile chamber made for this measurement (Fig. A.2) has the same dimension (diameter, longitudinal length) as the chamber for muonium spectroscopy. The chamber and its foil are also made of aluminum. The chamber surface was anodized (alumite coating) which prevents the scintillation light from scattering at the chamber surface, and this suppresses the background photons due to the scattering.

Inside the profile chamber, there is no microwave cavity, instead, there is a piece of black paper, which has a similar density (0.0257 g/cm^2 compared to the Cu foil's 0.0223 g/cm^2) and thickness as the foil for the cavity. We call it a "dummy foil" and Fig. A.3 shows the picture of the dummy foil attached to the upstream flange of the profile measurement chamber. The black paper was selected as the dummy foil so that it suppresses the light scattering.

In addition to the dummy foil, we place a disk-shaped scintillator in the chamber. The scintillator is attached to a screw. An actuator outside the chamber can rotate the screw, and move the scintillator position. The CCD camera is also moved by another actuator, in order to keep the distance between the scintillator and the camera the same so the scintillator is always placed at the focal point of the CCD camera. The scan range covered by the scintillator is 300 mm.

Figure A.4 shows the chamber and the beam duct. There is a gap between the flange foil of the chamber and the beam duct. The gap is 11 cm, which is 1 cm longer than the gap of the spectroscopy chamber and the beam duct, due to the interference of the support of the chamber and the duct.

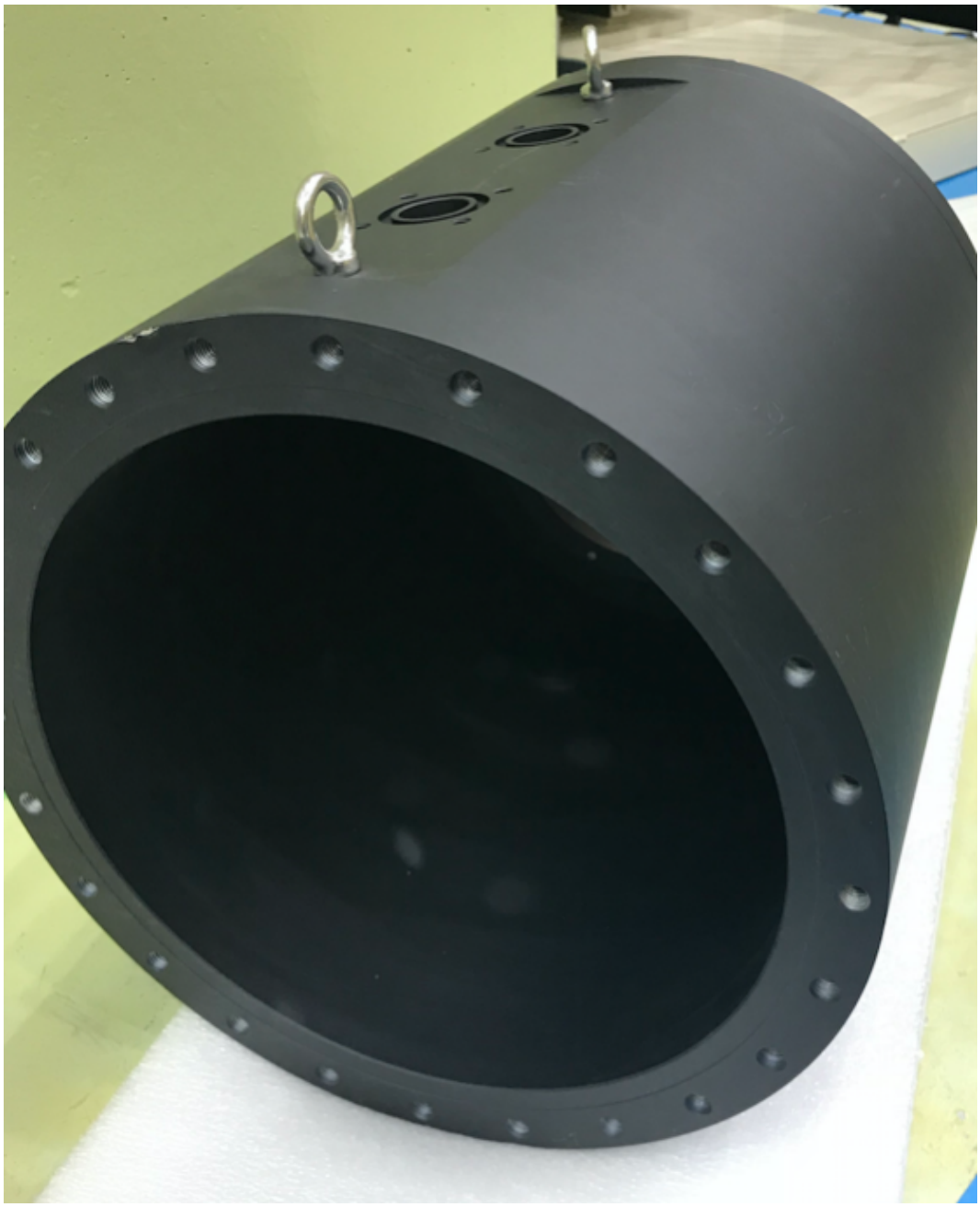

Figure A.2: A chamber for beam profile measurement.

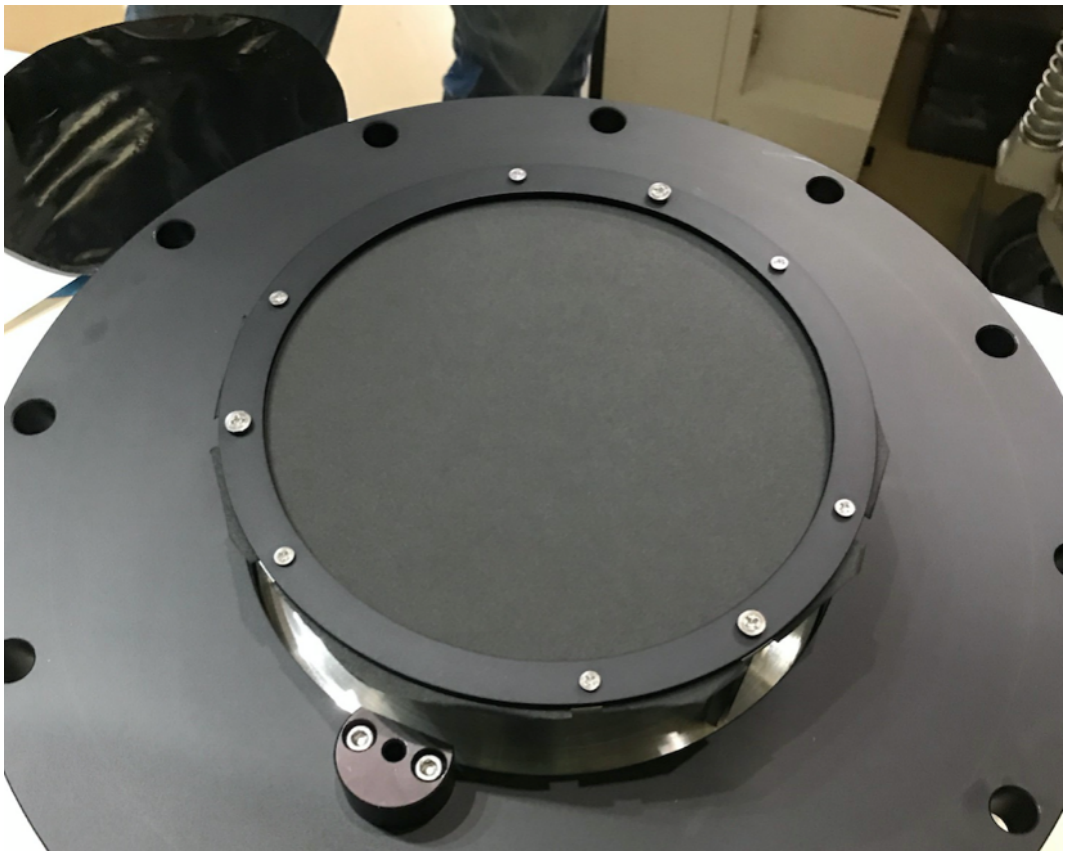

Figure A.3: Dummy foil for beam profile measurement.

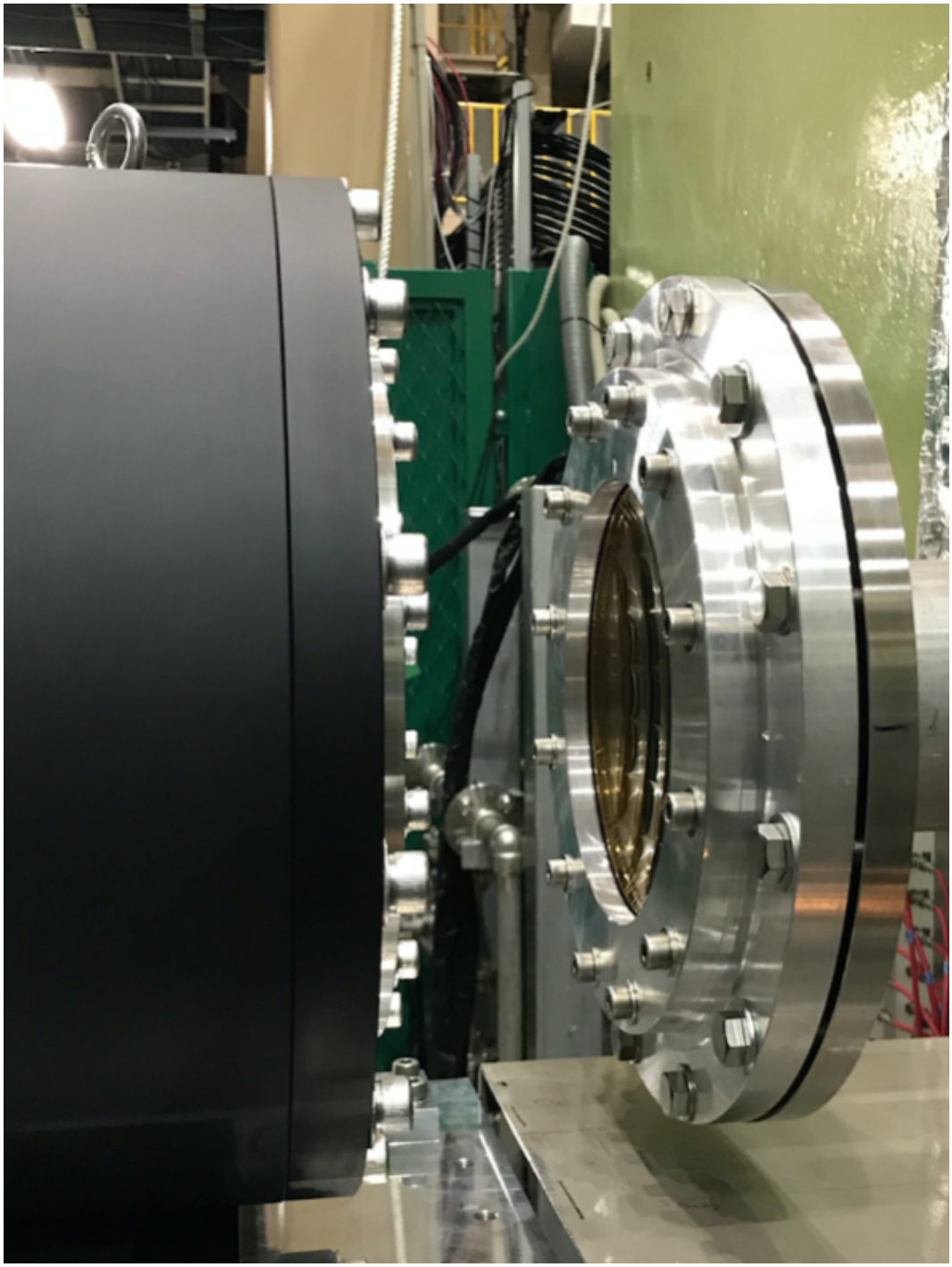

Figure A.4: The beam profile measurement chamber and the beam duct.

A.3 Result

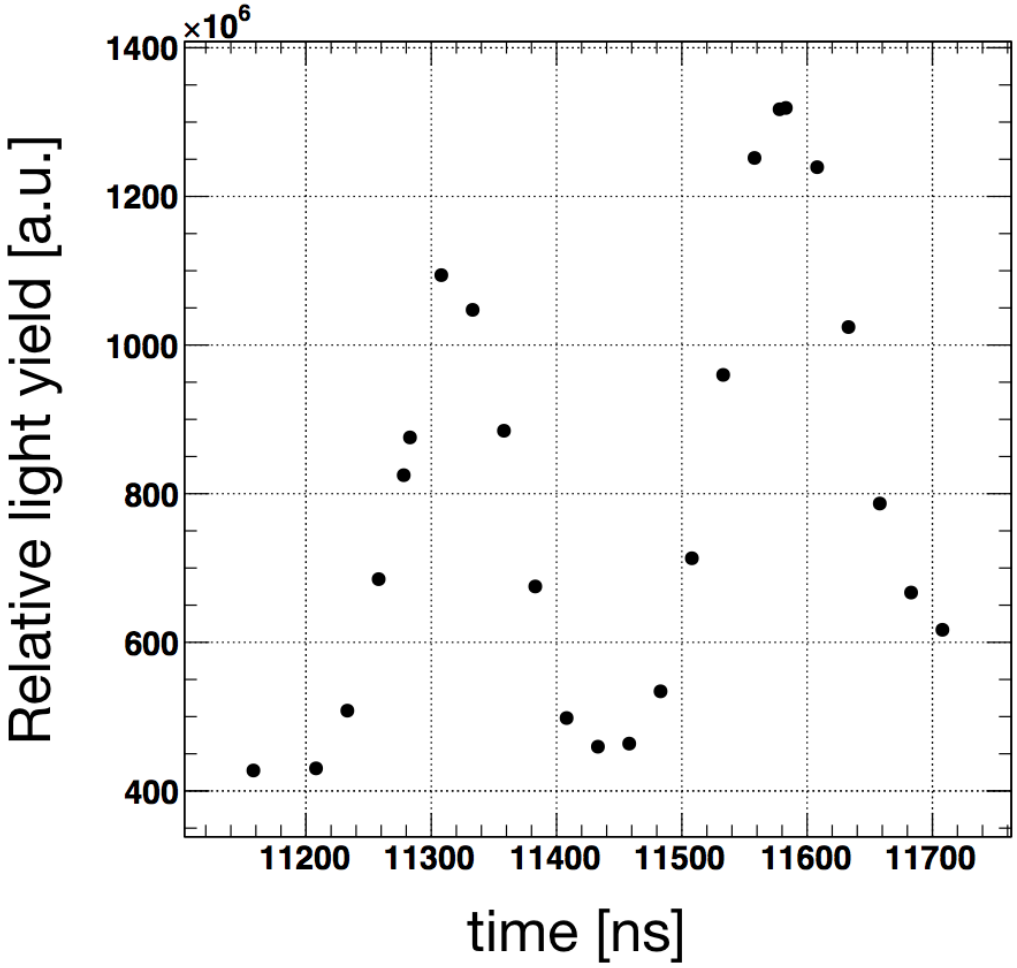

Figure A.5: The beam timing scan result.

The measurement was conducted at experimental area D2, the same experimental area as the spectroscopy measurement. At that time of the profile measurement (December 2017), the beam operation was so-called single pulse mode, and the beam power was 300 kW. Note that for the spectroscopy measurement, the beam operation was double pulse mode, meaning the beam was separated to two pulses. Each pulse has a 100 ns bunch width, and the two pulses are separated by 600 ns. The difference in the operational modes does not affect the muon beam profile. We measured the beam profile at two different conditions, the krypton gas pressure at 1.0 atm and the muon beam momentum 27.4 MeV/c, and the pressure at 0.3 atm and the momentum 26.0 MeV/c.

In the IIF, there is the gate amplifier for reducing the background photons. The gate is opened for 100 ns. The gate is triggered by the signal synchronized with the RF applied on the accelerator. The gate timing is adjustable by varying the

delay for the signal from the accelerator. Figure A.5 shows the light yield for the different delay time. There are two peaks at 11300 ns and 11580 ns. The first peak corresponds to the prompt positron pulse. The second peak is the muon peak. The time difference is consistent with the estimated time-of-flight from the muon momentum. From this plot, we decided to adjust the delay to 11580 ns.

We measure the muon beam profile by taking several "shots" for each scintillator positions. A "shot" is an accumulated image of the scintillation light for typically 30 seconds. As mentioned above, the gate is open for 100 ns per one beam pulse, whose repetition rate is 25 Hz. Therefore one shot is the integral of the light obtained by the CCD in 100 ns $\times$ 25 Hz $\times$ 30 sec = 75 μs exposure. Typically, we took 10 shots per scintillator position.

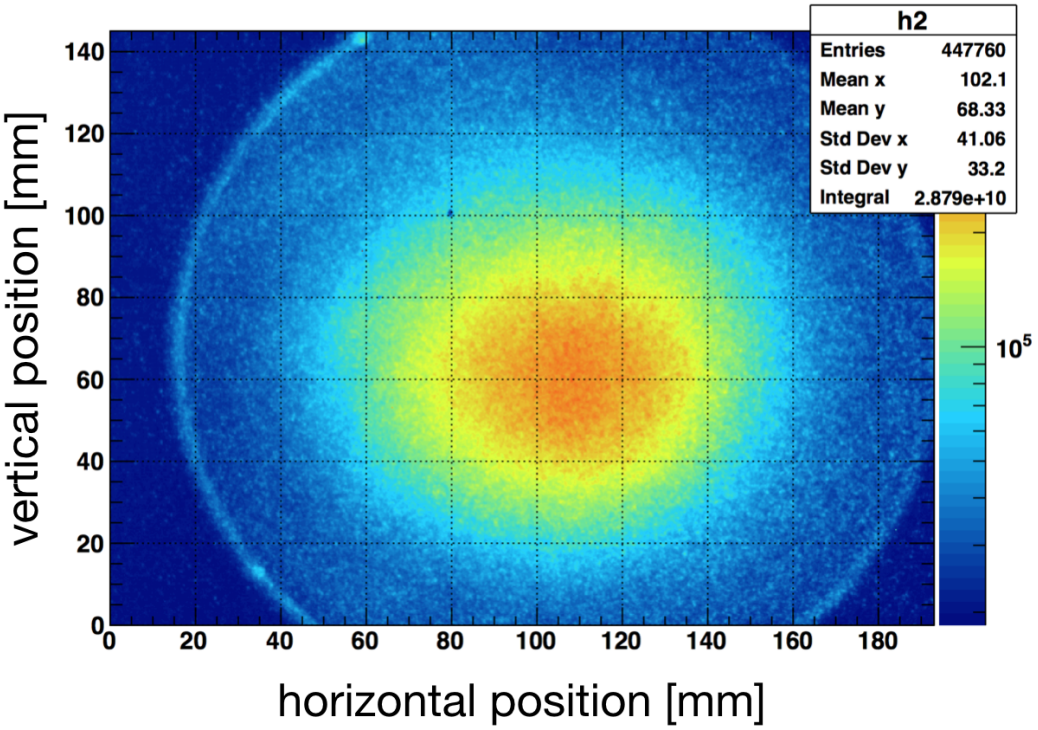

Figure A.6: Typical cross-sectional beam profile.

Figure A.6 shows the typical beam profile obtained by the CCD camera. The profile was obtained when the scintillator is placed at the most upstream position. The background photons are well suppressed by the anodized wall of the chamber and the black dummy foil, so we can clearly see the edge of the disk-shaped scintillator and the muon beam profile.

Figure A.7 shows the zoomed view of the typical image of the CCD camera. There is a pixel which has an unreasonably high photon yield ("noisy"), or other pixels have very low yields compared to the surrounding pixels (dead pixels). These pixels were omitted from the analysis, and it does not affect the result.

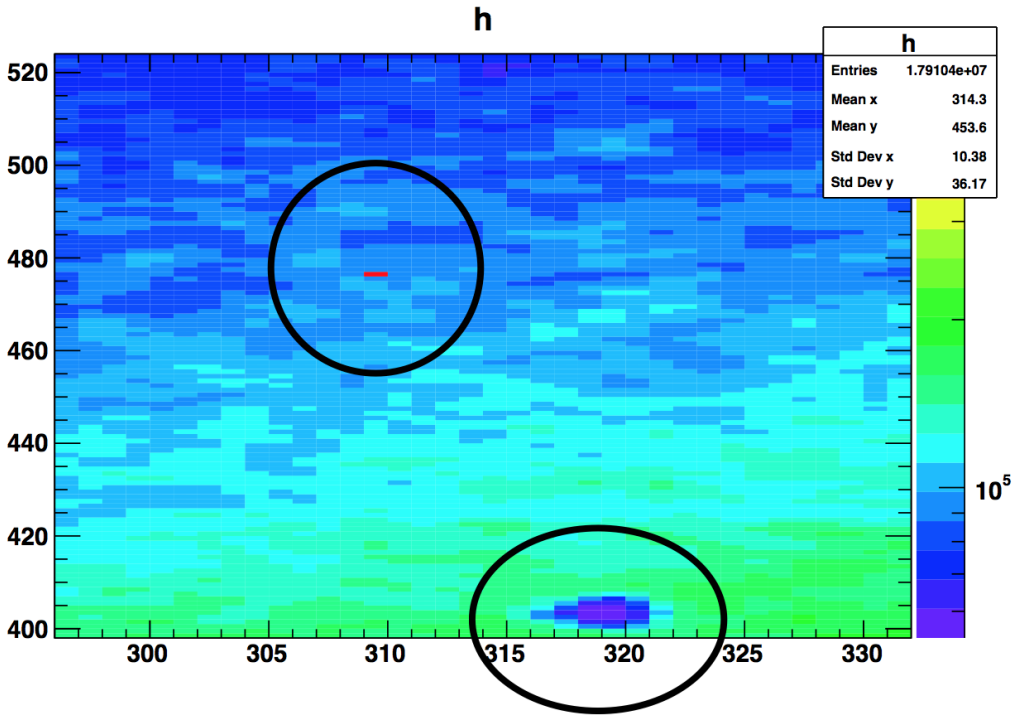

Figure A.7: An example of the noisy pixel and the dead pixel, indicated by the black circles.

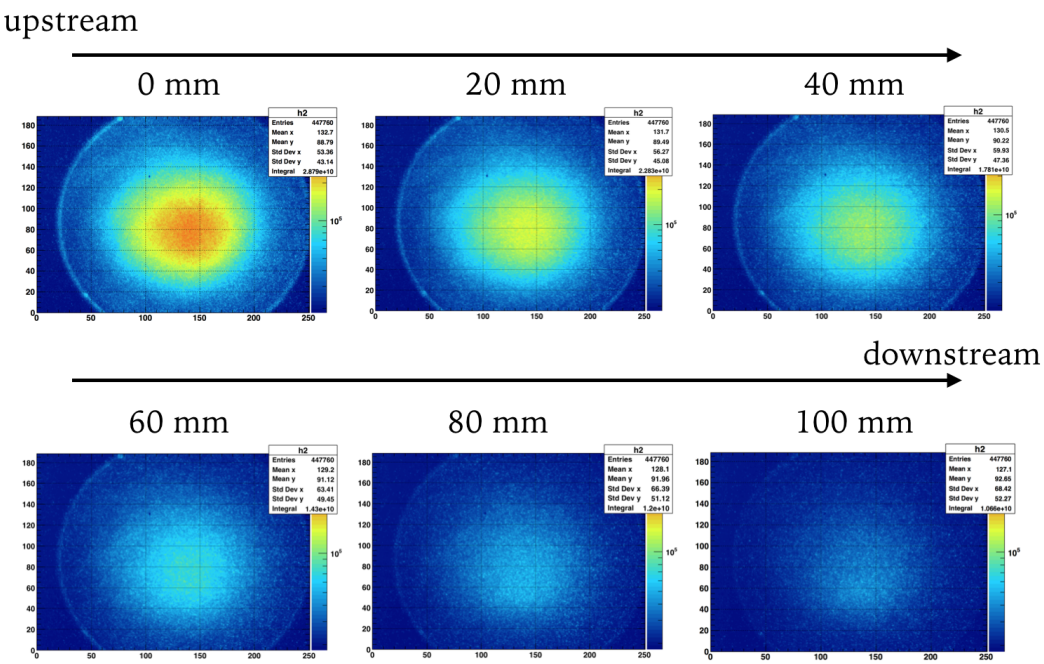

Figure A.8: Beam profiles from upstream to the downstream.

Figure A.8 presents the change of the beam profile for different scintillator positions. There is a steady decrease of the light yield as the scintillator moves to downstream positions, meaning fewer muons hit the scintillator. The bottom right profile in the figure shows the image of the beam profile when the scintillator is 100 mm away from the cavity entrance, i.e., the dummy foil. Note that the profile center looks slightly shifted compared to the upper left figure. The cause of this shift may be attributed to the background positrons (the positrons are considered to have a different vertical profile since there is the deflection from the Wien filter described in Sec. 3.2), or the actual shift of the muon beam profile. Figure A.9 shows the beam profile of prompt positrons, meaning the obtained profile when the trigger delay was adjusted to 11300 ns, instead of 11580 ns. The profile of the prompt positrons have a shifted center in the same direction, but the horizontal projection of the profile in Fig. A.10 presents the fact that the profile of the positrons (blue line) is further deviated from the center compared to the profiles of muons (red or yellow lines). The profile difference suggests that the deviation of the beam profile at 100 mm position is likely to be caused by the actual shift of the muon beam profile.

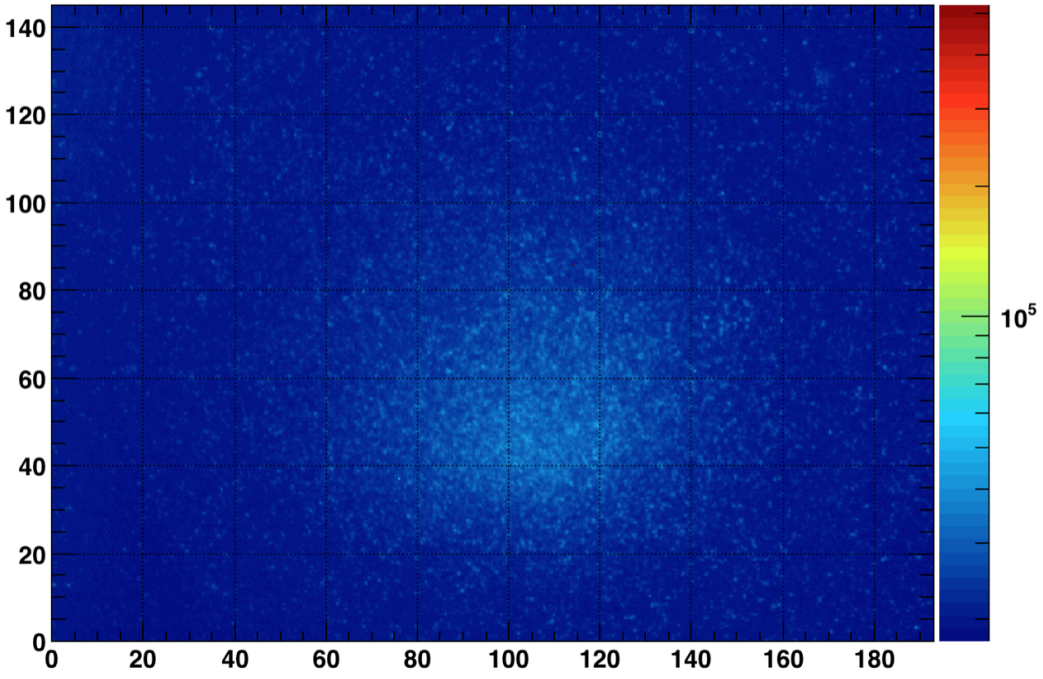

Figure A.9: Cross-sectional distribution of the prompt positrons. Due to the vertical deflection caused by the Wien filter, the vertical center is shifted downward.

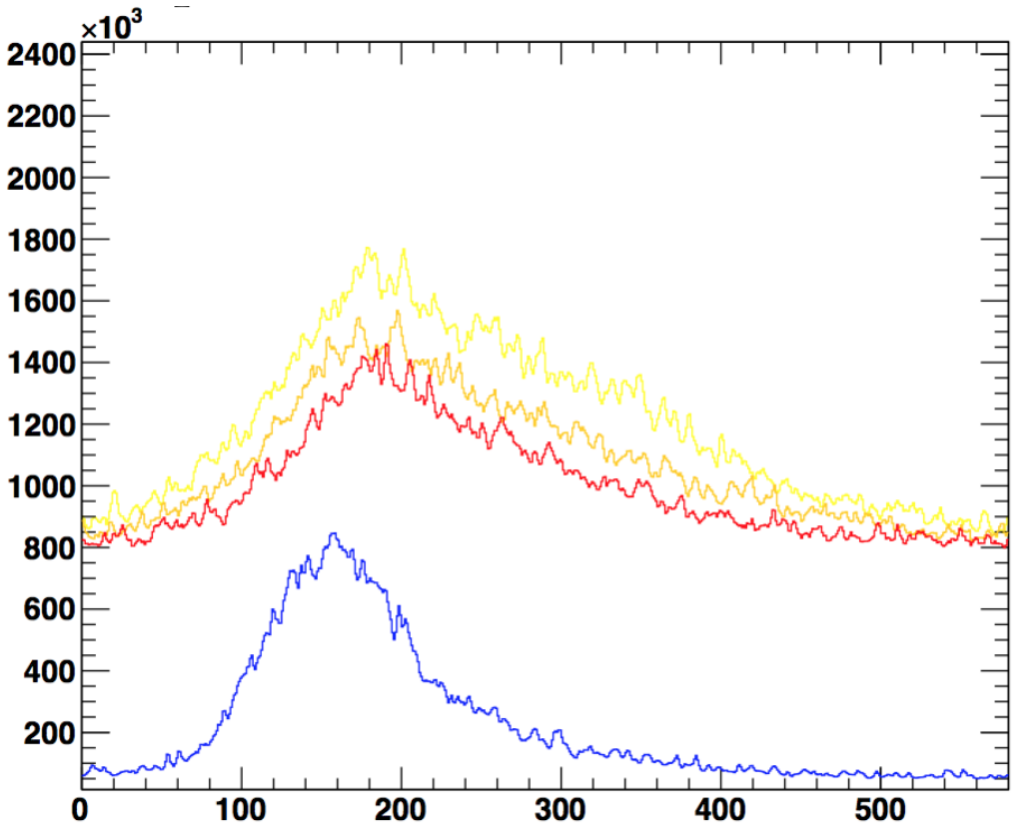

Figure A.10: Comparison of the vertically projected profiles of the positrons and muons. Red, orange, and yellow lines represent the muon profile, and the blue represents the profile of the positrons.

In order to obtain the beam width and center, we fit the beam profile with the two-dimensional Gaussian. For the fitting, we have to define the error of the light yield for each pixel of the CCD camera. Figure A.11 shows the correlation between the light yield of a pixel and the standard deviation of the light yield. The red line is the fit result using the following equation,

$$\sigma_{\mathrm{ly}} = A\sqrt{(Y - B)/G} \tag{A.1}$$

where the σ_{ly} is the standard deviation of the light yield, A is the scaling parameter, Y is the light yield, B is the offset or shift parameter, and G is the gain of the IIF. In the fitting, A, B, and G are the free parameters. In the figure, A is denoted as "scale". B is expressed as "shift", and G is written as "gain". We use the standard deviation determined from the light yield, based on the equation and the parameters obtained by this fitting.

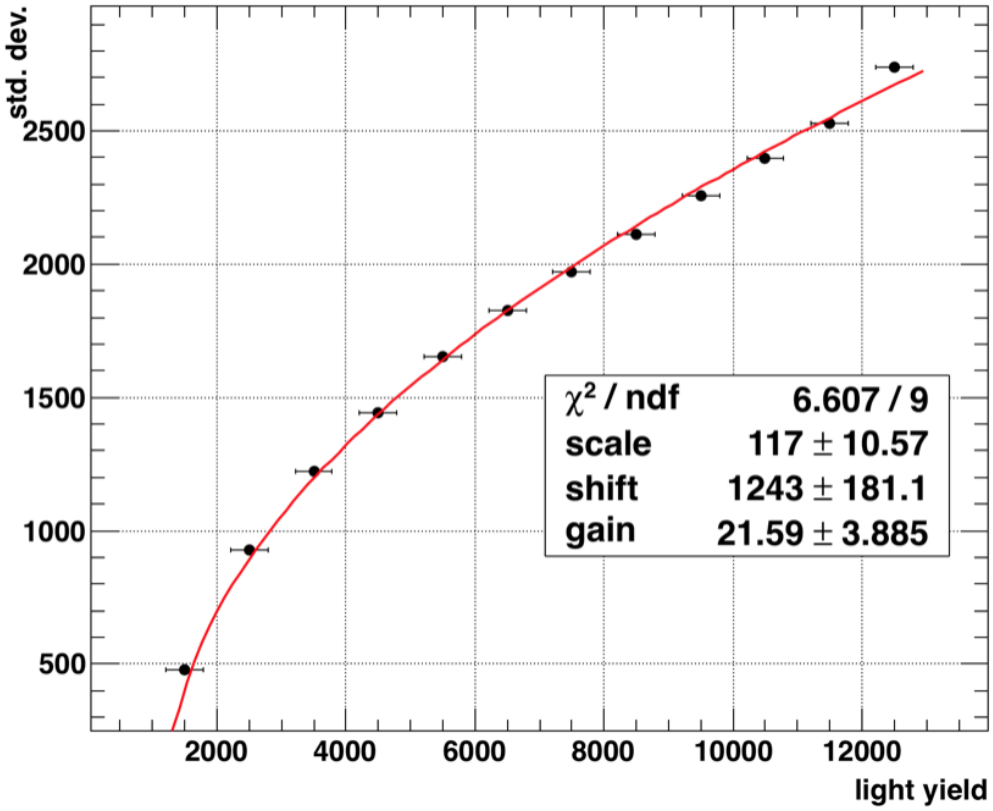

Figure A.11: Correlation of the light yield and the standard deviation of the yield

The fitting of the beam profiles can be done in several ways. We can fit the two-dimensional profile with a two-dimensional Gaussian, and obtain the (vertical and horizontal) center and the width. Also, we can first project the 2D profile to horizontal and vertical axes, and then fit the projected profile with one-dimensional Gaussian. The latter way is less statistically powerful, but the result is easy to understand. Also, there are two ways of the fitting; one can fit each shot of the CCD camera, or fit the accumulated image of the several shots.

Figure A.12 is the horizontal center of the beam profile determined by several fit results. The horizontal axis is the scintillator position, and the vertical axis is the horizontal center of the beam profile. Black circle points indicate the result obtained by 2D-fitting of the accumulated image. Pale-violet square points represent the results obtained by the one dimensional-fitting (1D-fitting) of each shot. Green square points are the results of the 1D-fitting of the accumulated image. The points not shown in the figure were omitted due to the failure of the fit. All the points are in the very small region (4.6 $\pm$0.6 mm), and we conclude the horizontal center of the beam profile does not significantly change for different scintillator position.

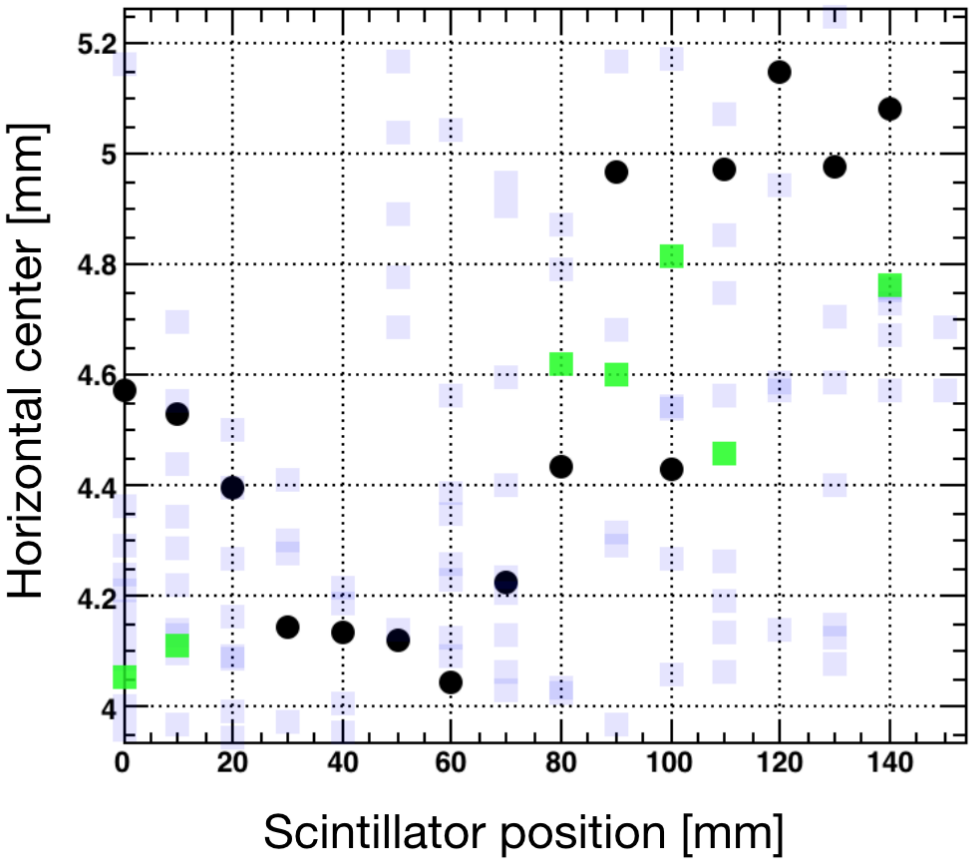

Figure A.12: Horizontal center of the muon cross-sectional distribution.

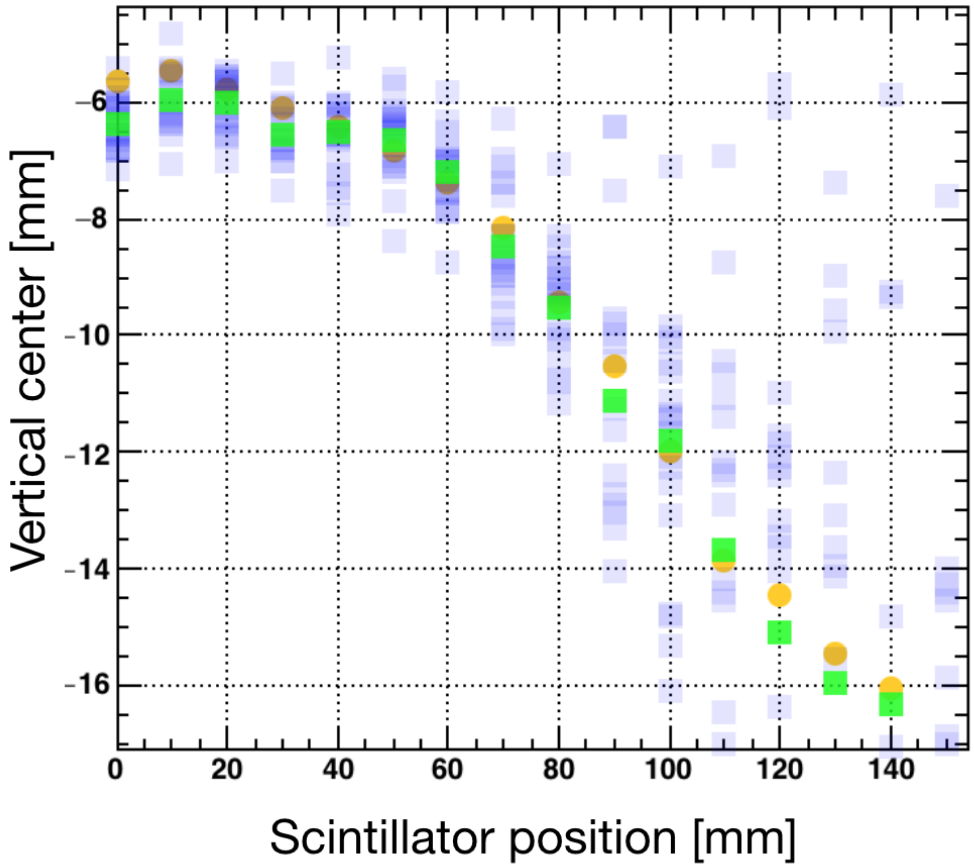

Figure A.13: Vertical center of the muon cross-sectional distribution.

Similarly, the vertical center obtained by the fitting is shown in Fig. A.13. The horizontal axis is the scintillator position, and the vertical axis is the vertical center of the beam profile. Orange circle points indicate the result obtained by 2D-fitting of the accumulated image. Pale-violet square points represent the results obtained by the 1D-fitting of each shot. Green square points are the results of the 1D-fitting of the accumulated image. Due to the lack of statistics, the results obtained by the 1D-fitting of each shot fluctuate. Different fitting methods indicate a similar tendency; for the downstream scintillator position, the muon beam profile deviates downward. This tendency is qualitatively explained by the Wien filter. The Wien filter's $E \times B$ field acts as a particle selector as well as a momentum selector; the muons are deflected according to the slight difference in its momentum. The higher the momentum a muon has, the lower position in the vertical axis the muon occupies. For the downstream position of the scintillator, only more energetic muons arrive at the scintillator. As the consequence, the beam profile in downstream is shifted downward.

Figure A.14 shows the vertical and horizontal widths of the beam profile. The beam width becomes wider as the scintillator moves away from the cavity entrance, mainly due to the multiple scattering of the muon beam with Kr atoms and beam

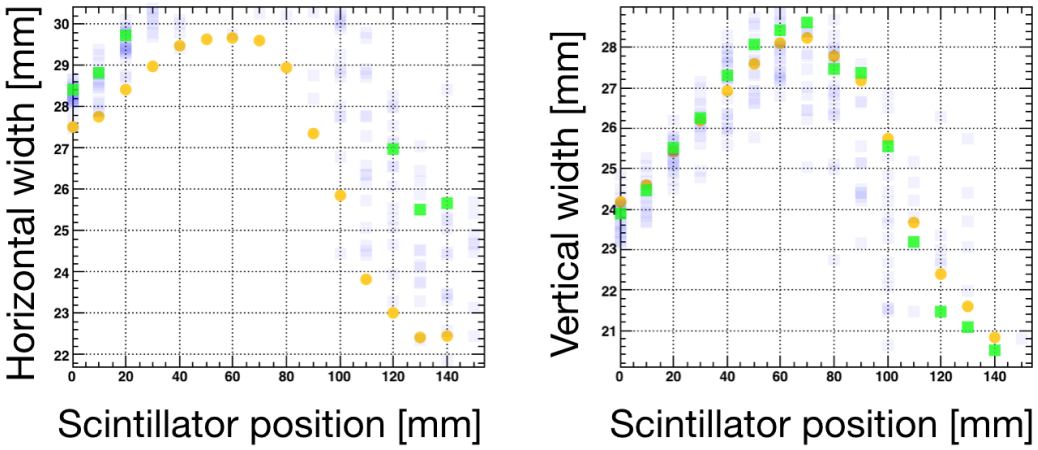

Figure A.14: Vertical and Horizontal widths of the cross-sectional muon distribution

defocusing. At a certain point, the tendency changes and the beam width become narrower. This is due to the correlation of the beam momentum and the position of the beam.

Figure A.15 shows the light yield of the scintillator for different positions. There is less light yield for the scintillators away from the cavity entrance since more muons are stopped in the Kr gas before hitting the scintillator. Roughly speaking, we can deduce the muon stopping distribution in the longitudinal axis, by taking the difference of the light yield for adjacent scintillator positions. One should notice, however, that to determine the number of the muons stopped in the region between the two scintillator positions, we should correct the difference of the muon energy for different scintillator positions.

Figure A.16 presents the average muon energy for different positions, calculated by GEANT4. We used this result to correct the light yield and then determined the muon distribution based on the corrected light yield. The figure shows the muon average energy when Kr pressure is 1 atm.

Figure A.17 shows the longitudinal muon distribution in 1 atm Kr gas, with beam momentum p=27.4 MeV/c. Most likely the muons stop around 30 mm from the cavity entrance. Figure A.18 shows the muon distribution in 0.3 atm Kr gas, with beam momentum p=26.0 MeV/c (indicated as black points). For the comparison, the distribution in 1.0 atm is also shown (red points). The distribution in 0.3 atm is broader than the distribution in 1.0 atm.

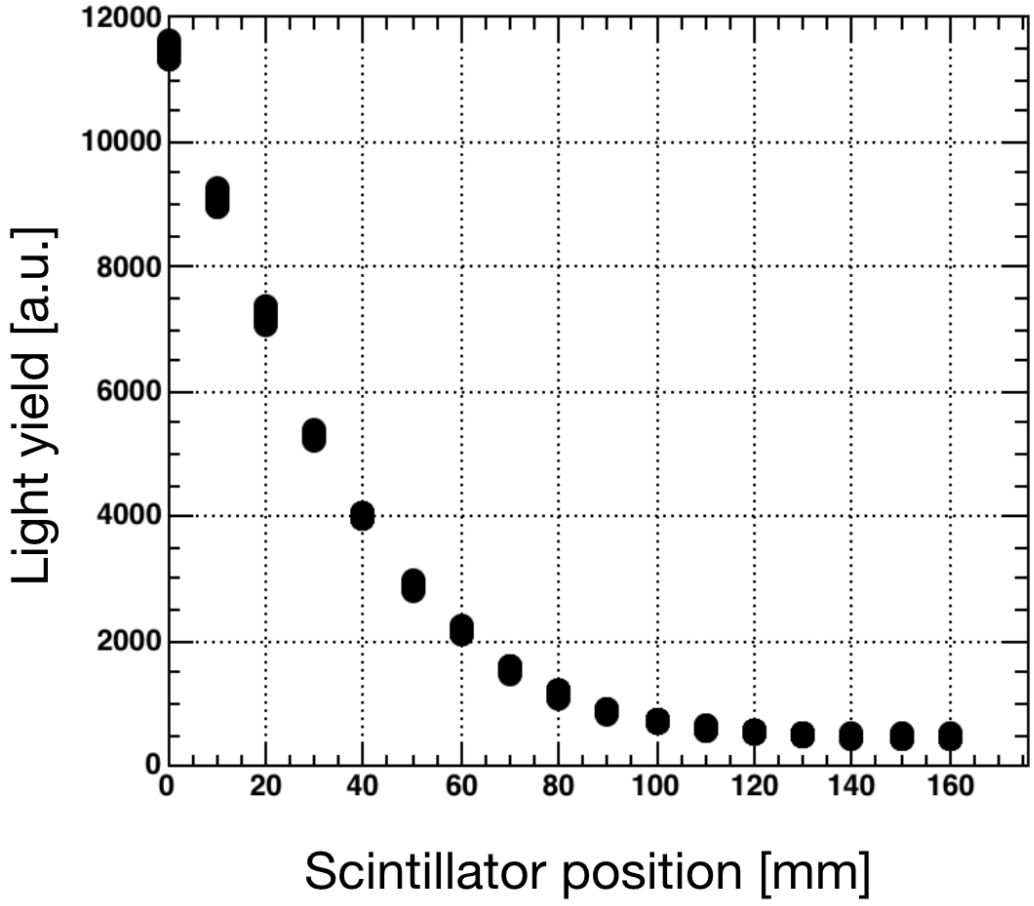

Figure A.15: Light yield for different scintillator positions.

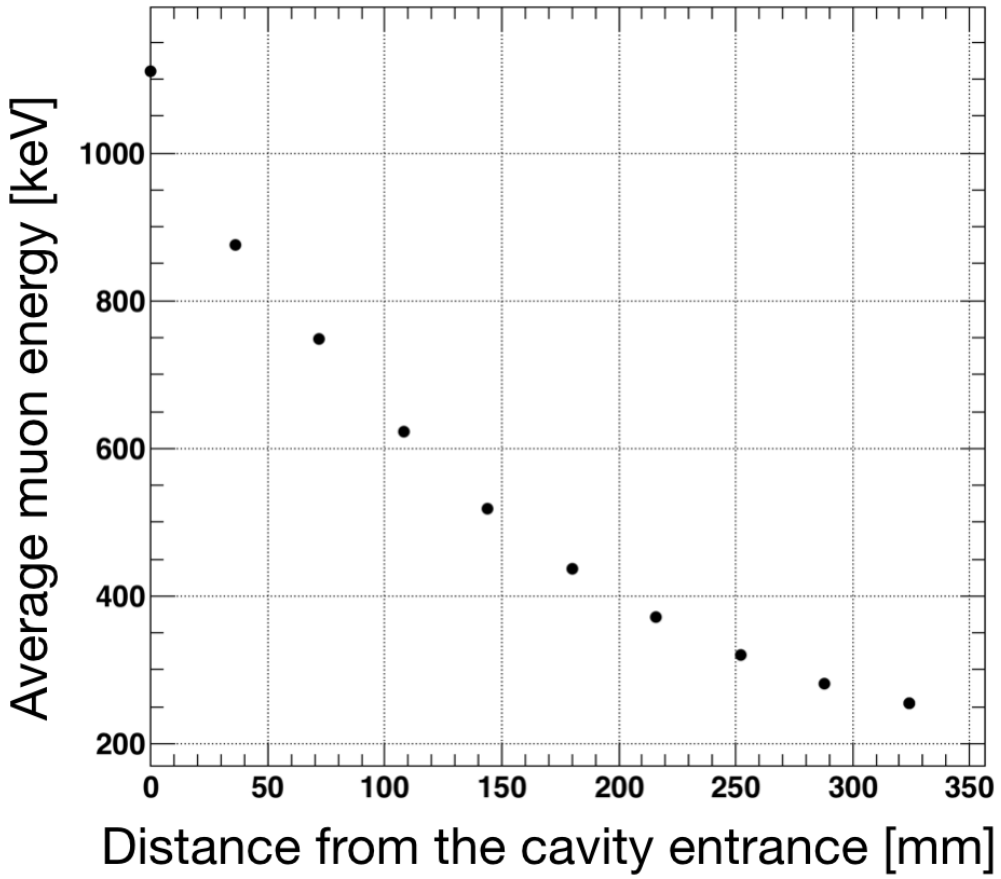

Figure A.16: Simulated average muon energy for different scintillator positions.

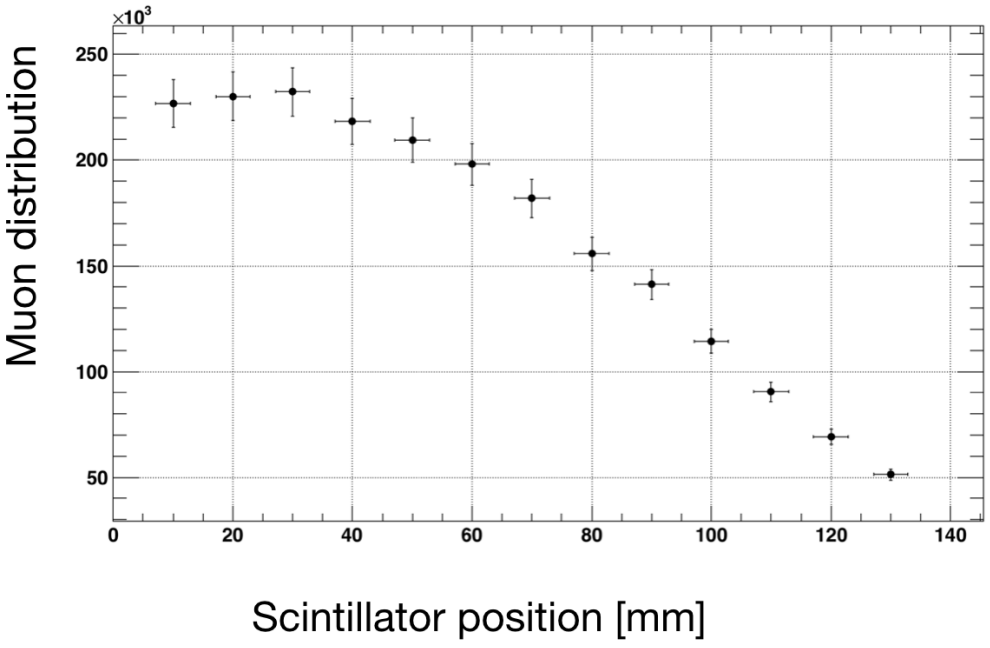

Figure A.17: Longitudinal muon distribution in 1 atm krypton

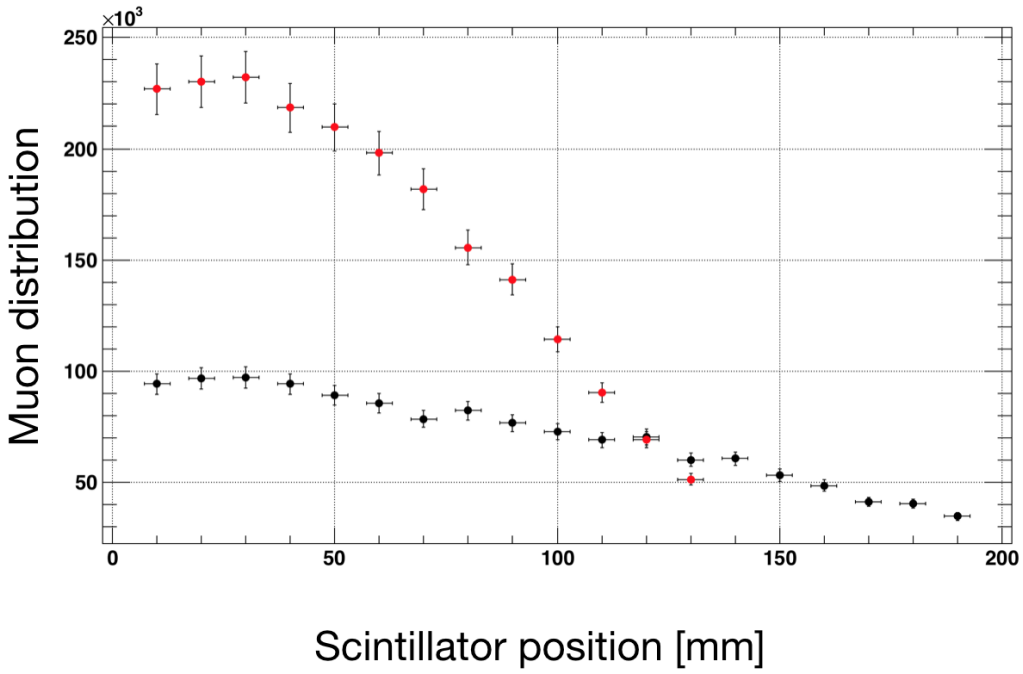

Figure A.18: Comparison of the longitudinal muon distribution in 0.3 atm krypton (black) and the distribution in 1.0 atm krypton (red). Muon distribution is broader with lower gas pressure.

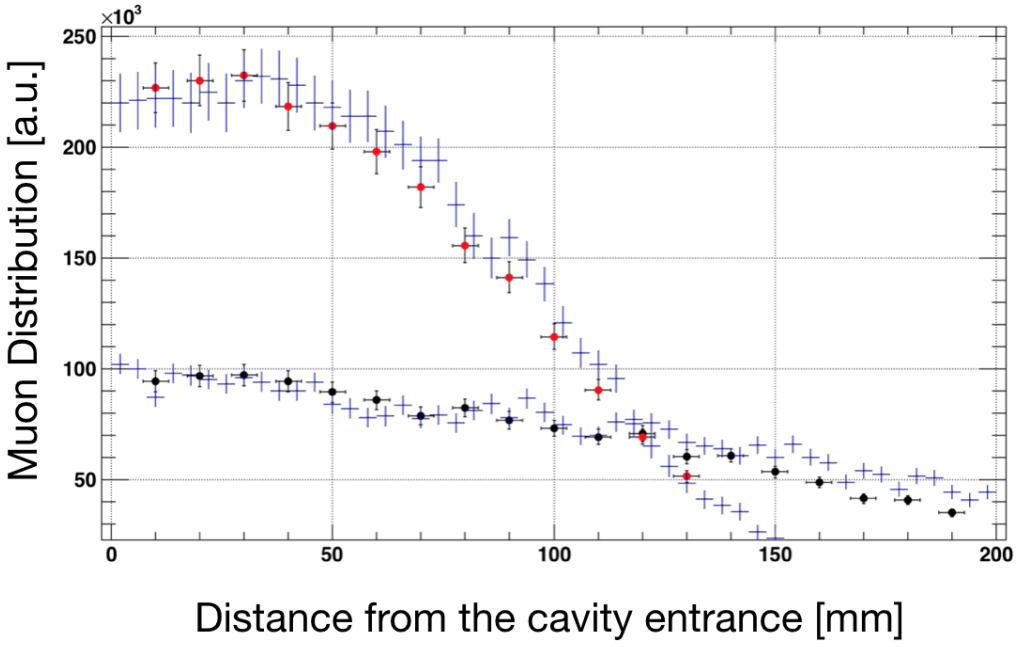

Figure A.19: Comparison of simulated beam distribution and data. Black or red points are measured value by the beam monitor. Blue plots indicate the simulated distribution.

Figure A.19 shows the comparison of the obtained data by the beam profile monitor and the result of the simulation using GEANT4. There is a consistency between the data and the simulation. We used this data as the validation of the GEANT4 simulation, and we modified the geometry of the apparatus for the spectroscopy and then simulated results shown in Sec. 3.5.2.

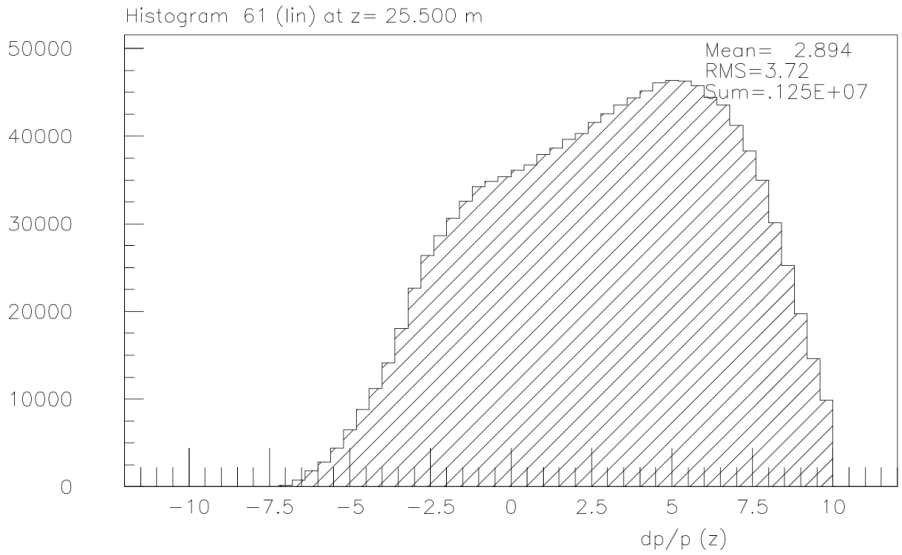

Figure A.20: Initial beam momentum distribution [101]

Figure A.20 presents the initial beam momentum distribution at the end of the beam duct we used for the simulation in GEANT4. This shape is qualitatively explained by the effect of beam line magnets and the muon production; the momentum acceptance of the magnets shapes the momentum distribution like a trapezoid-shape, and the number of the surface muons N obeys the momentum p dependency $N \propto p^{2.5}$, so the resulting momentum distribution is a skewed trapezoid in the figure.

Bibliography

[1] G. Aad, *et al., ATLAS collaboration*, Phys. Lett., B716, 1 (2012) [page 12]

[2] S. Chatrchyan, *et al., CMS collaboration*, Phys. Lett., B716, 30 (2012) [page 12]

[3] D. Hanneke, S. Fogwell, and G. Gabrielse, Phys. Rev. Lett., 100, 120801 (2008) [page 12]

[4] R. H. Parker, *et al.,* Science, 360, 191 (2018) [page 12]

[5] G. W. Bennett, *et al.*, Phys. Rev. D73, 072003 (2006) [page 12], [page 14], [page 17]

[6] N. Bohr, Phil. Mag. 6. 26, 151, 1 (1913) [page 13]

[7] P. A. M. Dirac, Proc. of the Royal Soc. A, 126, 260 (1930) [page 13]

[8] W. E. Lamb, and R. C. Retherford, Phys. Rev. 72, 241 (1947) [page 13]

[9] H. A. Bethe, and E. E. Salpeter, "Quantum Mechanics of One- and Two-Electron Atoms", (Springer, 1957) [page 13]

[10] L. Essen, *et al.*, Nature, 229, 110 (1971) [page 13], [page 15]

[11] C. G. Parthey, *et al.*, Phys. Rev. Lett., 107, 203001 (2011) [page 13]

[12] F. Nez, *et al.*, Phys. Rev. Lett., 69, 2326 (1992) [page 13]

[13] R. Pohl, *et al.*, Nature, 466, 213 (2010) [page 13]

[14] A. Antognini, *et al.*, Science, 339, 417 (2013) [page 13]

[15] A. Beyer, *et al.*, Science, 358, 79 (2017) [page 13]

[16] H. Fleurbaey, *et al.*, Phys. Rev. Lett., 120, 183001 (2018) [page 13]

[17] P. J. Mohr, D. B. Newell, and B. N. Taylor, " CODATA 2014" , Rev. of Mod. Phys., 88, 035009 (2016) [page 13], [page 32], [page 35], [page 36]

[18] M. I. Eides, arXiv, 1812.10881 (2018) [page 13]

[19] W. Liu, *et al.*, Phys. Rev. Lett., 82, 711 (1999) [page 14], [page 18], [page 24], [page 50], [page 115], [page 120]

[20] D. E. Casperson, *et al.*, Phys. Lett. B59, 397 (1975) [page 14], [page 24], [page 105], [page 107], [page 111], [page 114], [page 120], [page 122]

[21] K.A. Olive *et al.* (Particle Data Group), Chin. Phys. C38, 090001 (2014) (URL: http://pdg.lbl.gov) [page 14], [page 17], [page 52]

[22] L. Essen, *et al.*, Metrologia, 9, 128 (1973) [page 15]

[23] J. R. Sapirstein and D.R. Yennie, "Quantum Electrodynamics", edited by T. Kinoshita, 560, (World Scientific, Singapore, 1990)t [page 15]

[24] P. Crivelli, Hyperfine Interact., 239, 49 (2018)
See also, P. Crivelli, LEAP2018, Paris, (2018)
(URL: `https://indico.cern.ch/event/657512/contributions/2926894/`
) [page 16]

[25] M. I. Eides, and V. A. Shelyuto, Phys. Rev. D89, 111301(R) (2014) [page 16]

[26] A. Ishida, *et al.*, Phys. Lett. B734, 338 (2014) [page 16]

[27] F. Jegerlehner and A. Nyffeler, Phys. Rep. 477, 1 (2009) [page 17]

[28] K. Hagiwara *et al.*, J. Phys. G38, 085003 (2011) [page 17]

[29] M. Davier, *et al.*, Eur. Phys. C71, 1515 (2011) [page 17]

[30] M. Davier, *et al.*, Eur. Phys. C77, 827 (2017) [page 17]

[31] A. Keshavarzi, D. Nomuta, and T. Teubner, Phys. Rev. D97, 114025 (2018) [page 17]

[32] J Holzbauer, Jour. of Phys.: Conf. Ser. 770 012038 (2016) [page 17]

[33] M. Otani, JPS Proc. Conf., 8, 025008 (2015) [page 18]

[34] D. Colladay, and V. A. Kostelecký, Phys. Rev. D58 116002 (1998) [page 19]

[35] A. H. Gomes, V. A. Kostelecký, and A. J. Vargas, Phys. Rev. D90 076009 (2014) [page 19]

[36] V. W. Hughes, *et al.*, Phys. Rev. Lett., 87, 111804 (2000) [page 19], [page 21]

[37] S. G. Karshenboim, Phys. Rev. Lett. 104, 220406 (2010) [page 19], [page 22]

[38] Y. V. Stadnik, Phys. Rev. Lett. 120, 223202 (2018) [page 19]

[39] K. P. Jungmann, Jour. of the Phys. Soc. of Japan, 85, 091004 (2016) [page 23]

[40] L. Willmann, *et al.,* Phys. Rev. Lett., 82, 49 (1999) [page 23]

[41] K. Horikawa, and K. Sasaki, Phys. Rev. D53, 560 (1996) [page 23]

[42] V. W. Hughes, *et al.*, Phys. Rev. Lett., 5, 63 (1960) [page 23]

[43] W. E. Cleland, *et al.*, Phys. Rev. Lett., 13, 202 (1964) [page 24]

[44] V. W. Hughes, Annu. Rev. Nucl. Sci., 16, 445-470 (1966) [page 24]

[45] P. A. Thompson, *et al.,* Phys. Rev. Lett., 22, 163 (1969) [page 24]

[46] R. D. Ehrlich, *et al.,* Phys. Rev. Lett., 23, 513 (1969) [page 24]

[47] R. De Voe, *et al.,* Phys. Rev. Lett., 26, 213 (1970) [page 24]

[48] D. Favart, *et al.,* Phys. Rev. A, 8, 1195 (1973) [page 24]

[49] D. E. Casperson, *et al.,* Phys. Rev. Lett., 38, 1504 (1977) [page 24]

[50] F. G. Mariam *et al.,* Phys. Rev. Lett., 49, 993 (1982) [page 24]

[51] W. Liu, Ph.D. Thesis, Yale University, (1997) [page 25], [page 26], [page 40], [page 107], [page 115], [page 119], [page 122]

[52] D. E. Casperson, Ph.D. Thesis, Yale University, (1976) [page 27], [page 120], [page 124]

[53] S. Kanda, Proc. of Sci. (INPC2016) 170 (2017) [page 29], [page 30]

[54] S. Kanda, Ph.D. Thesis, the University of Tokyo (2017) [page 29], [page 30], [page 80], [page 81], [page 82], [page 117]

[55] S. Nishimura, Ph.D. Thesis, the University of Tokyo (2018) [page 30], [page 31], [page 104], [page 124]

[56] S. G. Karshenboim, Phys. Rep. 422, 1 (2005) [page 32], [page 36]

[57] E. E. Salpeter, and H. A. Bethe, Phys. Rev. 84, 1232 (1951) [page 32]

[58] E. E. Salpeter, Phys. Rev. 87, 328 (1952) [page 32]

[59] G. Breit, and R. E. Meyerott, Phys. Rev. 72, 1023 (1947) [page 32]

[60] W. E. Caswell, and G. P. Lepage, Phys. Lett. B167, 437 (1986) [page 32]

[61] T. Kinoshita, and M. Nio, Phys. Rev. D53, 4909 (1996) [page 32]

[62] P. Labelle, G. P. Lepage, and U. Magnea, Phys. Rev. Lett. 72, 2006 (1994) [page 32]

[63] V. A. Yerokhin, and U. D. Jentschura, Phys. Rev. A81, 012502 (2010) [page 34]

[64] S. G. Karshenboim, V. G. Ivanov, and V. M. Shabaev, Jour. of Exp. and Theo. Phys., 90, 59 (2000) [page 34]

[65] J. Mondéjar, J. H. Piclum, and A. Czarnecki, Phys. Rev. A81, 062511 (2010) [page 34]

[66] M. I. Eides, H. Grotch, and V. A. Shelyuto, Phys. Rep 342, 63 (2001) [page 34]

[67] D. Nomura, and T. Tubner, Nuc. Phys. B867, 236 (2013) [page 35]

[68] S. G. Karshenboim, V. A. Shelyuto, and A. I. Vainshtein, Phys. Rev. D78, 065036 (2008) [page 35]

[69] M. I. Eides, Phys. Rev. A53, 2953 (1996) [page 35]

[70] S. G. Karshenboim, Z. Phys. D36, 11 (1996) [page 35]

[71] P. J. Mohr, and B. N. Taylor, "CODATA2002" Rev. of Mod. Phys., 77, 1 (2005) [page 35]

[72] S. G. Karshenboim, and V. G. Ivanov, Can. Jour. Phys. 80, 1305 (2002) [page 36]

[73] D. C. Walker, "Muon and Muonium Chemistry" (Cambridge University Press, Cambridge, 1983) [page 40]

[74] D. G. Fleming, R. J. Mikula, and D. M. Garner, Phys. Rev. A26, 2527 (1982) [page 40]

[75] V. Tishchenco, *et al.*, Phys. Rev. D87, 052003 (2013) [page 41]

[76] Y. M. Belousov, *et al.*, Jour. of Russ. Laser Research, 31, 421 (2010) [page 42], [page 43], [page 44]

[77] W. Higemoto, *et al.*, Quant. Beam Sci. 1, 11 (2017) [page 54], [page 56]

[78] S. Seo, private communication, 2018 [page 58], [page 60], [page 62], [page 63]

[79] S. Agostinelli, *et al.*, Nuc. Inst. and Inst. A506 250 (2003) [page 74], [page 126]

[80] R. Brun and F. Rademakers, NIM A389, 81-86 (1997), (see also URL: `http://root.cern.ch/`) [page 83]

[81] F. James, and M. Roos, Comput. Phys. Commun., 10, 343 (1975), (see also URL:`http://seal.web.cern.ch/seal/snapshot/work-packages/mathlibs/minuit/`) [page 104]

[82] E. S. Ensberg, and C. L. Morgan, Phys. Lett. 28A, 106 (1968) [page 107]

[83] W. Happer, Rev. of Mod. Phys. 44, 169 (1972) [page 112]

[84] R. C. Weast, *CRC handbook of chemistry and physics* 74th ed. (Boca Raton, Fla. : CRC Press, 1993) [page 112]

[85] E. N. Fortson, D. Kleppner, and N. F. Ramsey, Phys. Rev. Lett. 13, 22 (1964) [page 118]

[86] P. G. H. Sandars, Proc. Phys. Soc. 92, 857 (1967) [page 118]

[87] P. C. Gibbons, and N. F. Ramsey, Phys. Rev. A5, 73 (1972) [page 118]

[88] J. G. Stuart, D. J. Larson, and N. F. Ramsey, Phys. Rev. A22, 2092 (1980) [page 118]

[89] F. Bloch, and A. Siegert, Phys. Rev. 57, 522 (1940) [page 118]

[90] J. H. Shirley, Phys. Rev. 138B, 979 (1965) [page 118]

[91] H. Salwen, Phys. Rev., 99, 1274 (1955) [page 119]

[92] S. Ulzega, *et al.,* arXiv, physics/0604233v2 (2006) [page 119]

[93] A. Godone, *et al.,* Phys. Rev. A71, 063401 (2005) [page 119]

[94] T. P. Heavner, *et al.,* Metrologia, 42, 411 (2005) [page 119]

[95] J. Guéna, *et al.,* IEEE Trans. Ultrason. Ferroelect. Freq. Contr., 59, 391 (2012) [page 119]

[96] W. Kells, *et al.,* Il Nuovo Cimento, 35A, 289 (1976) [page 124]

[97] P. Strasser, *et al.,* Hyperfine Interact, 237, 124 (2016) [page 125]

[98] P. Strasser, *et al.,* EPJ Web of Conf., 198, 00003 (2019) [page 125]

[99] H. Yamaguchi, *et al.,* IEEE Trans. Appl. Supercond., 29, 9000904 (2019) [page 125]

[100] T. U. Ito, *et al.,* NIM A754, 1 (2014) [page 126]

[101] N. Kawamura, private communication, 2018 [page 144]

Acknowledgements

First and foremost, I would like to express my deepest gratitude to my collaborators in MuSEUM. It has been a great experience to work on this project for the last six years. I am indebted to my adviser, Prof. Yasuyuki Matsuda, who has always been insightful and patient. His erudite and curiosity-driven personality inspired me countless times, and I learned many from conversations with him. One of the most significant benefits of working on this research program is to work with Prof. Koichiro Shimomura, who is the spokesperson for this project. Without his constant guidance, the work presented here would never have happened. He encouraged me to attend conferences and workshops in Japan and abroad, and this allowed me to learn a lot, not only in physics research; I have learned about different cultures and values.

I am also grateful to Dr. Hiroyuki A. Torii for many valuable discussions during this study. He was not only a knowledgeable physicist; he is also an entertaining lecturer with outstanding pedagogical skills. Having Attended his lectures several times, I became more careful with how to convey my ideas to others. I also mention that he is also an enthusiastic learner of languages. He kindly helped me with my English writing, and propitiously I had some chances to enjoy his informal mini-lectures on other languages or linguistics. I also owe an immense debt to Dr. Patrick Strasser. His work on the monitoring system and the gas handling system with great care was crucial for this research. He also assisted me by correcting my errors on writing many times. He is often the first person to notice errors in the experimental setting, and this prevented us from wasting a large portion of the allocated beamtime.

I was very fortunate to work with Dr. Kazuo S. Tanaka, who once was a fellow student in our lab and the first person to earn Ph.D. in this project. When I joined this project, he always helped me and encouraged me. He had made a significant effort on the design of the gas chamber and the microwave system, and he was always open to my questions even after he left for another experiment. His advice based on his experience was always insightful. I am further indebted to Dr. Sohtaro Kanda, who has specialized knowledge on the positron counters. He was also my fellow student with patience and excellent skills of tutoring other students. Without him, I could not finish this long and cumbersome study. He is also a very sophisticated

person, and I am also thankful to him for recommending me good books and films. I would like to thank Dr. Shoichiro Nishimura for his excellent work on his detector and the data acquisition system. He has helped me with his exceptional skill of computing, and his careful work on the resonance line shape theory. He is also the best person to take a data-taking shift with. The four of us shared very happy moments and toughest moments in this project together, and I cherish every single moment with them.

Many thanks are due to Mr. Toya Tanaka, Mr. Shun Seo, and Mr. Daisuke Yagi for their vital roles in the experiment. Since Mr. Toya Tanaka joined our team, he has always been helpful. Without his work on the monitoring system for the gas pressure and the magnetic field, this work would never have been completed. I would like to thank Mr. Shun Seo for his exceptional contributions to the resonance line shape theory. He pointed out many mistakes in my draft of the part. Also, I appreciate his work on the measurement of the residual magnetic field and his comment on the analysis of the measurement. Mr. Daisuke Yagi kindly helped a sub-project on the neutron background measurement at the experimental areas. His tireless effort enabled us to complete both the development of a detector and the measurement. I sincerely hope his success in his new position.

I also would like to thank other collaborators. Dr. Ken'ichi Sasaki tutored my first research project in MuSEUM, and he taught me many things, even how to solder. Unfortunately, I could not keep working on the NMR system due to the overall plan of the project, but he always kindly assisted me even after I left. Dr. Tsutomu Mibe is not only a great collaborator but also the spokesperson of the g-2 collaboration at J-PARC. He invited me to workshops on related topics several times and gave me some chance to learn the topics. Dr. Naritoshi Kawamura helped us with his knowledge on the beamline and neutron detectors. Dr. Akihiro Koda is always open to my questions and assisted me when I have some difficulties, especially during the measurement of beam distribution. He and Dr. Kenji M. Kojima have worked on the development of the Kalliope readout board and the data acquisition system, on which our detector system relies. Dr. Yoshinori Fukao has helped us develop the detectors and the beam monitoring system. The beam profile measurement system is based on a system developed by Dr. Takashi U. Ito. Dr. David Kawall's advice based on his experience on the precursor experiment at LAMPF was indispensable for this research. I am deeply indebted to Dr. Yutaro Sato, Dr. Takashi Yamanaka, Mr. Hiromasa Yasuda, and Mr. Takumi Ito for their great effort to make the data-taking process successful.

The best thing I had when I was an undergraduate student is to have Prof. M. K. Kubo as my adviser at the International Christian University. There were no labs on particle physics, but he allowed me to join his radiochemistry lab and even encouraged me to do this research project. His questions and comments on my

research in the lab seminars were always critical. Without him, I could not have had this career and this incredible experience at MuSEUM.

I am indebted to all members of Matsuda Lab. Unfortunately, I had no chance to work with Dr. Naofumi Kuroda, but my all research activity was supported by his help on the infrastructures of the lab, such as the computing system and the e-mailing system. I was fortunate to have warm-hearted and hardworking labmates. Mr. Yoshitaka Higashi and I entered the lab in the same year, and we share good memories off and on work. Mr. Takehiro Mizutani taught me how to visit KEK and the basic things about this research. Mr. Takuya Matsudate helped me on computing, and he gave me a toaster when he left the lab, without which my breakfast would become more impoverished. I could not have a chance to work with Mr. Ryoma Nishi, Mr. Markus Fleck, Dr. Minori Tajima, Dr. Hiroki Nagahama, and Dr. Takashi Higuchi, but I always enjoyed chatting with them and talking about physics at coffee time.

This research program is supported by great efforts by all members of the J-PARC accelerator team and the muon division. This work is supported by Grant-in-Aid for JSPS Fellows No. 16J03151.

Last but not least, I would like to thank my family and friends for their support and encouragement over the years. It was a great pleasure to spend three years at ICU and a year at the University of California, Irvine. I would like to thank all members of the math class of 2014. My thoughts are always with Mr. Takuya Tokihisa and his family. I thank Mr. Kaito Kikuchi and Mr. Hiroaki Tanaka who kindly invited me to study statistics together. What I learned with them became the foundations for the research presented here. My thanks go to Asumi Oka, Remi Akada, Keisuke Usui, Koji Ota, Ryota Kobayashi, Naoto Hirashige, Megumi Kishi, Arisa Teshima, Kazuki Uematsu, and Hitomi Iwasa, who brought much happiness to my life. I would like to thank my parents, Tomoko and Hideaki Ueno for their unconditional love and selfless support, and my sister Atsuko, whose warm personality always cheered me up. I also thank my grandmothers, Ruriko Ueno and Satoe Hosoda, for allowing me to pursue my dream and leave my hometown. Life can be difficult sometimes, but having this family makes me feel I am not alone. I dedicate this thesis to my grandfathers, Michio Ueno, and Masaharu Hosoda.